From fundamental interactions in solution to the design of hybrid plyoxometalate-based materials

Nancy Watfa

Thèse En Cotutelle

Pour obtenir le grade de Docteur délivré par

L'UNIVERSITE DE VERSAILLES SAINT QUENTIN-EN-YVELINES

Et

L'Université Libanaise

Ecole Doctorale des Sciences et de Technologie

Spécialité :

Chimie Inorganique

Présentée Par:

Nancy Watfa

Sujet de la Thèse:

De l'étude fondamentale des interactions en solution à la conception de matériaux hybrides à base de Polyoxométallates

Date de Soutenance: 20 Mai 2015
Devant le Jury Composé de:

Pr. T. Parac-Vogt	Université de Leuven	Rapporteur
Dr. F. Camerel	Université de Rennes	Rapporteur
Pr. T. Mallah	Université de Paris-Sud	Examinateur
Pr. N. Steunou	Université de Versailles	Examinateur
Pr. E. Cadot	Université de Versailles	Co- Directeur de thèse
Dr. S. Floquet	Université de Versailles	Directeur de thèse
Pr. D. Naoufal	Université Libanaise	Directeur de thèse
Dr. A. Hijazi	Université Libanaise	Co- Directeur de thèse

Acknowledgements

At the end of my thesis I would like to thank all the people who contributed in some way to this work and made this thesis an unforgettable experience for me. First and foremost, I would like to thank the members of jury for their acceptance to evaluate my work: **Prof. Tatjana Parac-Vogt, Dr. Franck Camerel, Prof. Nathalie Steunou, and Prof. Talal Mallah.**

I would like to express my deepest thanks to my two supervisors, **Pr. Emmanuel Cadot** and **Dr. Sébastien Floquet** for accepting me in their group. Their guidance, patience, and immense knowledge over the last three years were invaluable and key motivations throughout my Ph.D.

The experience and the enthusiasm **Emmanuel** has for his research was contagious and motivational for me, his insight has shaped my thinking as a young researcher and immeasurably improved my work. Many obstacles were encounter during this long journey and **Emmanuel** has always told me to never give up because there is always a solution and nothing is impossible, it was like that at the end.

Sébastien gave me this nice opportunity and experience to continue my Ph.D. study which I would count this as one of the best decisions I've made in my life. I have been extremely fortunate to have had him as my guide in the essential tasks of improving my research, I appreciate all his ideas and contributions of time. He has been extremely generous and always searching for grants and funding to make my Ph.D. experience easier.
For both, thank you for your forward-looking in your willingness to involve me in conferences, sharing your experience, opinion and being kind and very helpful when reviewing those early first paper draft.

Thank you **Mohamed Haouas,** you were very helpful and patient, always taking the time to explain me and answer all my questions about NMR spectroscopy. You are always very motivated and every time I discuss with you I have the feeling that everything is going well. Working with you was a great experience.
I would like to thank my supervisors in Lebanon **Pr. Daoud Naoufal** and **Dr. Akram Hijazi** for giving me the chance to continue. They have given me the freedom to decide what is best for me during the last three years and supporting me when it was possible.
I also owed many thanks to **Dr. Emmanuel Terrazi**, **Pr. Claude Piguet** and Dr. **Laure Guénée** (University of Geneva, Switzerland) for their collaboration on the liquid crystal

properties and **Pr. Carlos Bo** and **Dolores Melgar** (ICIQ, Spain) for their computational studies.

During my stay at Versailles, I have had the pleasure to work and learn with good and talented researchers. **Nathalie Leclerc** and **Catherine Roch** have treated me like a younger sister and I am grateful for the simple advice and encouragement they gave me at every critical moment, thank you for taking care of me and I really love both of you very much. **Corine Simonnet** was always up for talking and providing me with a lot of information about food, culture and so on during lunch time. I am very impressed of the way **Anne Dolbecq** treats everything with care, and hope to someday be as assertive as she is. I really enjoyed the funny time I spent with **Marc Lepeltier** in the train where we talked in science, politics, television or really anything else and I have always admired his clear-sightedness and his candor. I am also forever indebted to **Eddy Dumas** who really supported me when I was at my lowest, and restored my faith in myself. **Olivier Oms** was so joyful and I appreciate the artistic taste of **Pierre Mialane**.
My sincere thanks also goes to **Jérome Marrot** for all his attempts to record X-ray structure to **Veronique Delahaye** for her kind help in all the administrative process.

My good memories of lab would not be complete without the many friends and colleagues who have enriched my work through stimulating conversation, insightful comments, assistance with source materials, keeping me calm and above all constant support. I must in particular express my gratitude to my lovely and honest friend **William** who was always supportive and taking care of me, **Ali** with his lovely family (**Randa and Larine**) thank you for all your help and all the weekends that we spent together**,**. I am also grateful to **Mohammed Ali, Guillaume, Iman, Loïc, Felicia, Maya, Leticia, Muhamad, Karima, Khawla, Hoan, Fedila, Hala, Damien, Racha, Zahra, Hawraa, Fatmi, Kamel, George, Batoul, Alaa, Hamza, Alexender, Christian, Olivier, Amani** and **Suzy.** I wish you all the best.
I cannot forget my university colleagues who I started this long journey and I had the great pleasure of studying chemistry with them. **Sahar**, **Farah**, **Hanan**, **Fatima**, **Hiba**, **Fatima**, **Samah** and **Rosa** thank you for making the early beginning funny, full of happiness and incredible moments which will be stucked in my mind forever.
I have made some amazing friends who have made these last 3 years some of the best of my life. A special shoutout to my room-mate **Ihsan** and **Amal**, who I first consider as my sisters

Thank you for always being there, from the good to the bad.
To my **dad**, who gave me the best start in life, sacrificed to make sure I grew up in a comfortable and loving home. I love you so much, you are the best , thank you for instilling in me a great work ethic, your encouragement while made all the difference in shaping who I am and where I am today. My only dream is to make you proud of me my lovely daddy.
To my **Mom**, thank you for being cooperative, trusting me, instilling in me compassion, sense of humor, love for people. You are a great mum I love you so much.

To my sisters, **Linda**, **Zainab** and **diana,** you three mean the world to me. It is not fair and enough to thank you in few lines but what I can say: we've been through a lot together with happiness and sadness, and I wouldn't be the person I am today without you being there scarifying and supporting me, and calling me out when I need it. The real happy and funny moments are with you my dear, and I'm so grateful that we're as close as we are. I love you more than life itself. I am really lucky to have the kindest sisters in the whole world!!!!
I would like also to thank also my family including my aunts, my uncles and Hassan's family including his lovely parents and all his family members: **Hasnaa**, **Zeina**, **Fatima, Ragida**, **Fatima**, **Abbass**, **Ali, Assad**, **Mohamed**, and **Ali** and all their cute children.
Special thank goes to my lovely aunt **Jamola** who I lost this summer, I just want to tell you that I miss you so much and this work is dedicated to your soul.

Finally, to my soul mate **Hassan,** whom cares little about acknowledgements but is deserving of them anyways. For 3 years you have been a constant pillar of support, always encouraging when times were hard. We've experienced awesome and inspiring events like having our beautiful engagement. We've also each struggled with finding our own direction and purpose. Luckily, we have one another for guidance through those hard times. You are always there to pick me up when I struggle, and I hope to be there as much for you also. Without you, this journey would have been impossible. Thank you and I love you and really proud of you.

It is fun to look back at the people who have filled my life and supported or encouraged me for the past 27 years. This Ph.D would not have been possible without them, and there are so many that I must apologize for the people I've inevitably forgotten.

Nancy Watfa

Abstract

Herein, we report the use of ^{1}H DOSY NMR methodology to track the interaction between an inorganic multireceptor capsule, referring to the well-defined spherical Keplerate-type $\{Mo_{132}\}$ ion and a series of organic cation (including tetraalklylammonium). The obtained results reveal a strong dependence of the self-diffusion coefficient of the cationic guests balancing from the solvated to the plugging situations. Quantitative analysis of the data based on two-site exchange regime, involving the 20 independent $\{Mo_9O_9\}$ receptors of the capsule ,allowed determining the stability constants associated to the plugging process of the pores. Surprisingly, the affinity of the capsule for a series of cationic guests increases continuously with its apolar character. Such observations evidence that the major factor dictating selectivity in the trapping process is mainly the so-called "hydrophobic effect".

Further investigation focused on the design of Keplerate-based materials where the ammonium cations was replaced by imidazolium cations. The obtained materials were characterized in the solid state by FT-IR, TGA and elemental analysis. These materials exhibit liquid crystalline phase as evidenced by polarized optical microscopy and DSC, however, folding of the alkyl chain prohibit the formation of well organized mesophase. Finally, this strategy was extended to cyclic $[Na_2K_2\{Mo_4O_4S_4(H_2O)_3(OH)_2\}_2(P_8W_{48}O_{184})]^{32-}$ which was isolated as DODA or imidazolium salt. Solid state NMR evidence the well organization of the solid. The obtained materials exhibit smectic A liquid crystalline phase and packed as hexagonal lamellar arrangement in the solid state.

Resume en francais

La première partie de ce mémoire concerne l'étude en solution de systèmes à base de POMs et de cations organiques de polarité/taille variables. Ainsi, l'étude des interactions entre un anion Keplerate noté $\{Mo_{132}\}$ et une large série de cations organiques (composée d'ions alkyl ammonium AA) a nécessité la mise en place d'une méthodologie spécifique utilisant la RMN DOSY de ^{1}H. La méthode s'est révélée particulièrement efficace et a permis non seulement de mettre clairement en évidence l'existence d'interactions anion-cation fortes mais aussi l'extraction des constantes d'association à partir d'un traitement quantitatif des données. Cette étude révèle que le facteur qui domine le processus d'association anion-cation résulte d'un « effet hydrophobe » directement lié au caractère apolaire du cation organique et polaire du solvant. Les constantes de stabilité sont en accord avec des interactions plutôt fortes. Par

ailleurs, une expérience spécifique a permis de titrer les 20 pores présents à la surface de l'ion Keplérate, montrant ainsi la spécificité du processus d'association.

La seconde partie de ce mémoire concerne la conception de matériaux à base de Képlerate en jouant sur la nature des cations imidazolium qui lui sont associés. Les phases solides ont été caractérisées par spectrométrie infrarouge, analyse élémentaire, EDX et analyse thermogravimétrique. Ces études montrent que dans certaines conditions, ces systèmes se affichent un comportement type cristal liquide.

La troisième partie s'intéresse spécifiquement aux interactions ionique et/ou van der Waals à l'origine de phénomènes de structuration. L'anion cyclique $[Na_2K_2\{Mo_4O_4S_4(H_2O)_3(OH)_2\}_2(P_8W_{48}O_{184})]^{32-}$ (noted **1**) a été isolé à l'état solide sous la forme de sels de DODA (dioctadécyl-diméthyl-ammonium) ou d'imidazolium. L'analyse structurale de ces phases par RMN MAS de ^{1}H, ^{13}C et ^{31}P montre sans ambigüité l'organisation des chaines alkyles. Ces résultats croisés avec la microscopie optique polarisée, l'analyse thermique différentielle et la diffraction des rayons X aux petits angles montrent clairement la formation de phases mésomorphes lamellaires dont l'espacement est directement lié à la longueur des chaines alkyles.

Publications

The following articles were published or submitted as a result of work undertaken over the course of this PhD programme.

"Hydrophobic effect as a driving force for host-guest chemistry of a multireceptor keplerate-type capsule" **N. Watfa**, D. Melgar, M. Haouas, F. Taulelle, , A. Hijazi , D. Naoufal, J. B. Avalos, S. Floquet, C. Bo, E. Cadot, *J. Am. Chem. Soc.* **2015,** 137**,** 5845.

"Synthesis, characterization, and tuning of the liquid crystal properties of ionic materials based on the cyclic polyoxothiometalate $[\{Mo_4O_4S_4(H_2O)_3(OH)_2\}_2\ (P_8W_{48}O_{184})]^{36-}$". **N. Watfa**, S. Floquet, E. Terazzi, M. Haouas, W. Salomon, V.S. Korenev, F. Taulelle, L. Guénée, A. Hijazi, D. Naoufal, C. Piguet, E. Cadot, *Soft Matter.*, 2015, 11, 1087.

"Synthesis, characterization and study of liquid crystals based on the ionic association of the keplerate compound $[Mo_{132}O_{372}(CH_3COO)_{30}(H_2O)_{72}]^{42-}$ and imidazolium cation" **N. Watfa**, S. Floquet, E. Terazzi, W. Salomon, L. Guénée, A. Hijazi, D. Naoufal, C. Piguet, E. Cadot, *Inorganics*, **2015**, 3, 246.

"Selective encapsulation of tetramethylammonium cations within the cavity of the Keplerate-type ion compound" **N. Watfa**, S. Floquet, M. Haouas, F. Taulelle, , A. Hijazi , D. Naoufal, E. Cadot. (to be submitted).

Other works

"Crystal and Molecular Structure of Dicesium bis(malonato)-di-m-sulphido-bis[oxomolybdate(v)] dihydrate: $Cs_2[Mo_2O_2S_2(malonate)_2(H_2O)_2].2H_2O$." M. Abou Fadel, **N. Watfa**, S. Floquet, J. Marrot, M. Awada, A. Hijazi, D. Naoufal, E. Cadot, *J. Struct. Chem*.**, 2014**, 55(8), 1419.

"Functionalization of the Keplerate type-cluster "Mo_{132}" by dicarboxylate ligands. Synthesis and NMR studies in solution." T. L. Loan Lai, M. Awada, S. Floquet, C. Roch-Marchal, **N. Watfa**, J. Marrot, M. Haouas, F. Taulelle, E. Cadot. (Accepted in Chemistry- A European Journal).

Table of contents

General Introduction

General Introduction

Polyoxometalates (POMs) are often described as discrete anionic metal-oxide clusters whose unrivalled structural and chemical diversity provides many interesting properties and applications in the fields of catalysis, optics, magnetism, medicine and biology. In the past decade, many recent efforts have focused on POM-hybrid materials providing additional properties and functions due to the synergistic interactions between the POM and the organic components. One of the simplest hybrid systems is based on the ionic association between inorganic POM and the organic components. This type of association depends on the nature of interactions existing in the solution. Based on the inorganic/organic complementarity and on nature of the solvent, the POM-cation interactions can lead to pre-association in the form of ion pairs in its simplest form but also they can provoke the self-assembly of POM into complex structures as micelles or blackberry. Finally, in the solid state POM-hybrid materials may adopt liquid crystal and ionic liquid properties.

For the development of POM-hybrid materials, it is fundamental to understand first the nature of the interactions between the hydrophilic POM ions and hydrophobic organic cations. In this work, we used DOSY NMR methodology to elucidate some of the fundamental POM-cation interactions that are critical for designing POM-hybrid materials. The manuscript is divided into three main parts.

Chapter I. An overview of different families of polyoxometalates and their structural diversity is first presented. Then some examples of the host-guest chemistry of the POM based structure are introduced with the special emphasis on the Keplerate-type $\{Mo_{132}\}$ capsule which is the main topic of the coming chapters, however this part also proposes an examination of the main recent results about POM-cation interaction in solution. Finally, we ended this chapter by presenting a brief review of the hybrid-surfactant systems based on polyoxometalates.

Chapter II. ^{1}H NMR DOSY methodology is applied to track the interactions between the Keplerate ion noted, $\{Mo_{132}\}$, and a large series of organic cations (composed of alkyl ammonium AA). This method seems to be an efficient tool not only to evidence the strong ion-cation interaction but also to extract quantitative data, such as the stability constants. This study reveals that the interaction is specifically related to the 20 $\{Mo_9O_9\}$ pores paneling the surface of the spheroidal Keplerate ion and demonstrates that the dominant factor of the

plugging process comes from hydrophobic effect where the stability constants are nicely correlated with the apolar character of the cations.

Chapter III. This chapter concerns the design of Keplerate-based materials by exchanging the simple ammonium countercations by organic cations such as imidazolium cations. These materials were characterized in the solid state by FT-IR, elemental analysis, EDX and TGA. This study reveals that in certain conditions, the obtained materials exhibit liquid crystal properties. As the hydrophobic surface of surfactant-encapsulated Keplerate materials increases its solubility in organic solvent and thus extends its scope of application, we were interested to investigate the ion-trapping properties of the Keplerate capsule by transfer of cations from the aqueous to the organic phase. The last part of this chapter described our attempts to prepare Keplerate-based silica materials by modified sol-gel process. The obtained materials were characterized in the solid state and two hypotheses were proposed concerning the organization within the silica matrix i) a cation covalently involved within the silica matrix or ii) a cation interacting by H-bonds with the silanol groups at the surface of the matrix.

Chapter IV. The last part interests specifically with the ionic and/or van der Waals interactions which are at the origin of some structuration phenomena. The highly charged cyclic anion $[\{Mo_4O_4S_4(H_2O)_3(OH)_2\}_2(P_8W_{48}O_{184})]^{36-}$ (noted **1**) was isolated in the solid state in the form of $DODA^+$ and imidazolium salts. The structural analysis by ^{1}H, ^{13}C, ^{31}P solid state NMR reveals the self-organization of the alkyl chain within the solid. These results were supported by Polarized Optical Microscopy, Differential Scanning Calorimetry, and Small-Angle Xray Diffraction, which clearly evidence the formation of well organized lamellar mesophases with a geometric parameter directly related to the length of the alkyl chain.

Chapter I
Introduction

Chapter I: Introduction

I. Supramolecular chemistry in Nature and beyond

Simplicity and complexity are two main terms to describe nature's approach, that is, nature usually uses simple and identical building blocks to build highly complex structures of great biological importance. Of particular example, the protein apoferritin, responsible for iron transport, is self-assembled from twenty-four identical subunits creating an assembly with octahedral symmetry and an internal cavity of over 230 nm^3 and can hold up to 4500 iron atoms as hydrous ferric oxide (Figure 1).[1] Such assemblies are not based on covalent interactions but weak supramolecular interactions such as hydrogen bonding, π–π interactions, van der Waals interactions and electrostatic interactions to glue these subunits together.

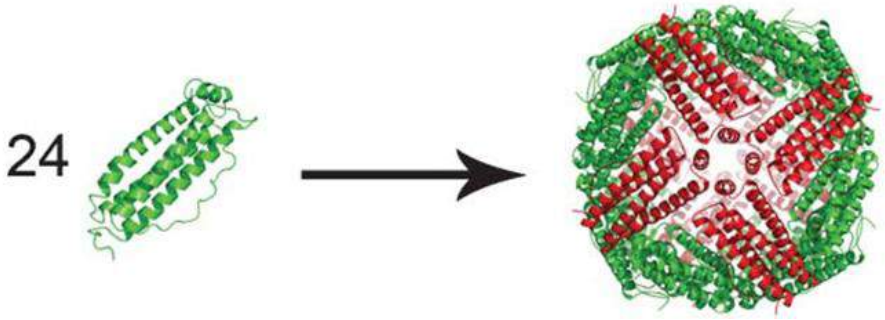

Figure 1: Twenty-four identical subunits self-assemble to form the protein apoferritin. The assembled protein has octahedral symmetry and a large interior cavity. Reproduced from reference [1].

Jean-Marie Lehn, winner of the 1987 Nobel Prize, defined supramolecular chemistry as "the chemistry of molecular assemblies and of the intermolecular bond." However, a suitable definition can be expressed in a simpler form as the "chemistry of the non-covalent bond", as this field of chemistry is multidisciplinary and is not restricted to the area of organic or inorganic chemistry, but also it includes the biochemical structures of Nature's complexes.
Understanding and controlling such non covalent interactions are the driving forces for many research areas ranging from biology, traditional organic chemistry and inorganic coordination chemistry or physical chemistry. As biological systems often provide inspiration, organic and inorganic chemistry are essential for the synthesis of the designed supramolecular components and physical chemistry is required to fully understand their properties to design functioning devices ready for application in our real world. Thus Mimicking the nature's complexes accompanied by the desire to design molecular electronic devices for data storage and transfer were one of the fueling point for researchers in this domain. In organic chemistry, the main problem is that synthesis of supramolecular organic objects is time-consuming and

quite complicated. Besides, due to the linear nature of hydrogen bonds, the curvature occurring within spheroidal topology has to be considered, which can be problematic. In contrast, inorganic chemistry which can be considered as an alternative, offer great opportunities to design complex architectures which should be tricky to build from organic multistep synthesis. Whether considering pure inorganic assemblies or combined with "programmed" organic ligands (coordination chemistry), the coordination modes of the transition metals are versatile enough to provide an access to a large variety of complex architectures arising from the self-assembly processes through one-pot reactions with nearly quantitative yields.

A large variety of supramolecular systems have been assembled using the metal–ligand interactions as the basic "algorithm" for the programmatic routine of the self-assembly process. The rational design of such complexes has been reviewed widely.[2] Raymond's group reported one of the best characterized metal–ligand supramolecular clusters based on the $[M_4L_6]$ tetrahedral assembly where M = Al^{III}, Ga^{III}, In^{III}, Ti^{IV}, Ge^{IV} or Fe^{III}, and L corresponds to a ditopic ligand (L = N,N-bis(2,3-dihydroxybenzoyl)-1,5-diaminonaphthalene) (Figure 2).

The highly anionic and hydrophobic character of the $[M_4L_6]$ host allows exclusive encapsulation of monocationic species such as apolar organic cations, e.g. $[NMe_4]^+$ and $[NEt_4]^+$ as well as organometallic sandwich complexes, e.g. $[Cp_2Fe]^+$, $[Cp_2Co]^+$, and $[CpRu(C_6H_6)]^+$ ($Cp=\eta_5\text{-}C_5H_5$) [3] which in turn lead to an enhancement of the catalytic activity for a wide variety of reactions such as selective C-H bond activation or hydroalkoxylation reaction.[4]

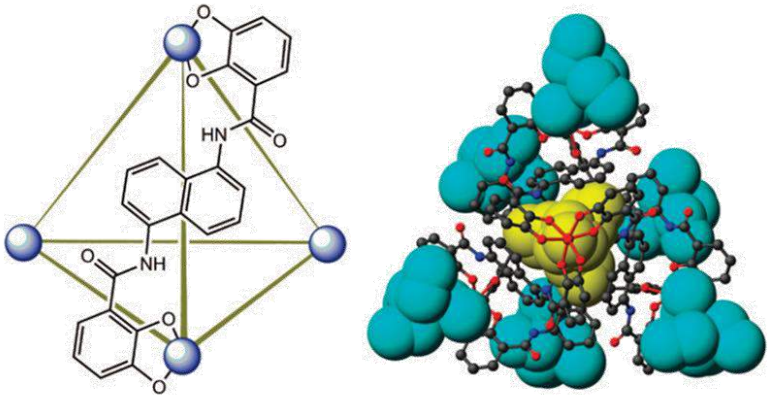

Figure 2: Left: Schematic of the $[Ga_4L_6]^{12-}$ assembly. Right: Model from the crystal structure $K_5(NEt_4)_6[NEt_4@Fe_4L_6]$ showing encapsulated (yellow) and ion-associated (blue) NEt_4^+ molecules. Reproduced from reference [3].

An attractive approach in the field of supramolecular coordination chemistry has been pioneered by Fujita's group, in which they use crystallized molecular capsules able to carry out specific chemical reactions.[5] In such cases, the encapsulated guests are characterized structurally by single-crystal X-ray diffraction analysis. The remarkable reaction acceleration is due to the concentration increase and the high chemio-selectivity due to some strictly regulated orientations of the substrates in the cavity.[5] The $[Pd_6L_4]^{12+}$-based cage systems constitute nice examples (where L is 2,4,6-tri(4-pyridyl)-1,3,5-triazine). The $[Pd_6L_4]^{12+}$ anion is an octahedral capsule with alternate closed and open faces formed from square-planar Pd^{2+} ions (the vertices) and tris(4-pyridyl) triazine ligands (the faces) as shown in Figure 3. The self-assembling of this capsule was achieved in the presence of acenaphthylene, forming the host-guest system capsule-(acenapththylene)$_2$ complex.[6] X-Ray diffraction study showed the acenaphthylene guest disordered over three positions within the cage. Furthermore, ultraviolet irridation of this host-guest assembly led to a [2+2] photodimerization, with the formation of the syn-product observed via X-Ray diffraction (Figure 3).[6]

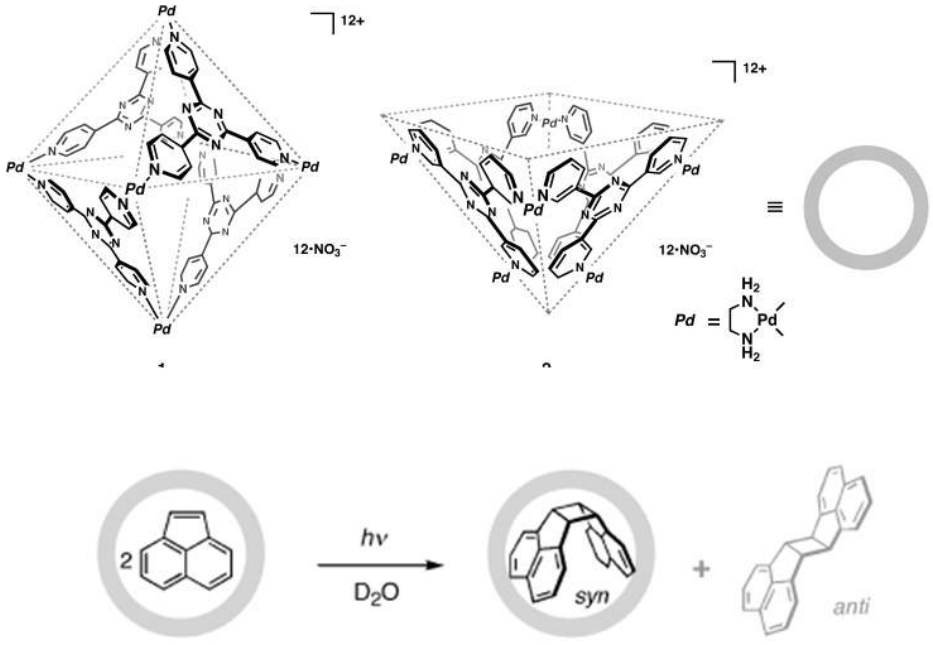

Figure 3: top: two capsules $[Pd_6L_4]^{12-}$ formed in the presence of acenaphthylene; bottom: [2+2] photodimerization of acenaphthylene within cage $[Pd_6L_4]^{12-}$. Reproduced from Reference [6].

In addition, to other numerous examples of organic-inorganic capsules available, there is also a family that really lies in the realm of supramolecular inorganic chemistry, known as the polyoxometalates (abbreviated POMs). POMs are formed from condensation process and give

a wide variety of structures having a number of metal centers ranging from 2 to 368 matching the protein size as shown in Figure 4. The following sections provide an introduction to this family, with a special focus on their supramolecular properties.

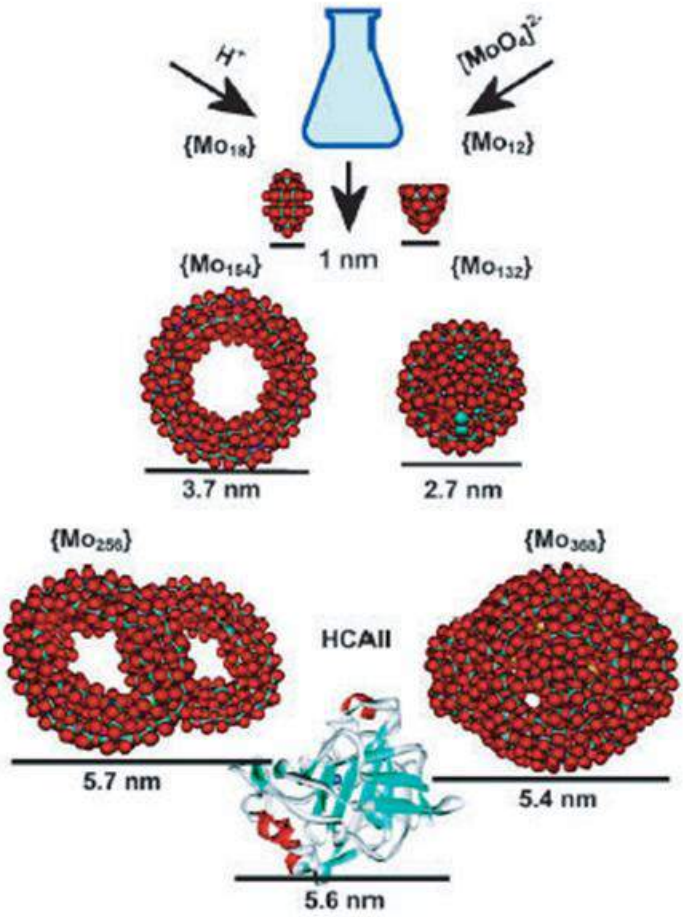

Figure 4: Representation of some structures of giant polyoxometalates. All are synthesized under "one pot" acidic reaction conditions, from the condensation of small anions to the giant clusters. These clusters are compared (to scale) with the protein Human Carbonic Anhydrase II . Reproduced from Reference [7].

II. Polyoxometalates' Generalities

II.1 Historical background and Definitions

POMs are often described as polynuclear metal oxide building blocks whose unrivalled structural and chemical diversity have provoked a tremendous amount of scientific research ranging from fundamental studies [8] to industrial applications.[9-10] This field is even getting more and more important from year to year. One must not be surprised and it is not by chance that some of the famous chemists as Scheele, Berzelius, Werner and Pauling were interested in this field.

Historically, in 1826 Berzelius noticed that acidification of ammonium molybdate solution with phosphoric acid lead to the formation of a yellow precipitate.[11] This was the first description of a polyoxometalate compound now known as the ammonium salt of the phosphomolybdate ion $(NH_4)_3[PMo_{12}O_{40}]$. In the development of POMs chemistry, the structural determination methods such as single-crystal X-ray diffraction technique have played a crucial role allowing the discovery of numerous complex POM arrangements. In 1933, J. F. Keggin reported the structure of the 12-phosphotungstic acid which had been solved by the interpretation of powder-X-ray diffraction images.[12] Since then, this type of compound is often generically referred to the "Keggin" structure.

II.2 Polycondensation processes / POMs formation

POMs compounds include in their structure metal centers usually in their highest oxidation state such as (Mo^{VI}, W^{VI}, V^{V}, Nb^{V}, Ta^{V}). Under acidic conditions, the basic oxo-anions MO_4^{n-} are able to condense through successive steps to yield negatively charged polynuclear metal-oxide. The condensation process results in the formation of $\{MO_p\}$ polyhedra (p = 4-7) connected through edge-shared or corner-shared junctions in the $[M_xO_y]^{m-}$ polynuclear framework (see scheme 1). Then, the overall structure of POM is represented by a set of linked polyhedra, where the metal M occupies the "center" of the polyhedron and the oxygen atoms define the corners. The formation of polynuclear POMs from acidic condensation of basic tetraoxometalate ion can be written by the following equation:

$$x\ MO_4^{n-} + z\ H^+ \rightarrow [M_xO_y]^{m-} + z/2\ H_2O \qquad (1)$$

The pH corresponds to a crucial parameter for the formation of the polycondensed species which are generally observed before the formation of the infinite oxide MO_3 (in the case of M^{VI} metallic cations). Concerning the nature of the metal, the high-valent molybdenum (VI) and tungsten (VI) are probably the most prominent in POM chemistry while POMs containing vanadium (IV/V), niobium (V) or tantalum (V) constitute an intensive growing area.[13] There are a lot of factors that play an important role in directing the self-assembly process such as (i) the concentration of the reagents, (ii) the pH, (iii) the temperature, iv) the ionic strength, v) the solvent... The chemical nature of the reagents is also important: i) the type of metal-oxide ions used as precursor, (ii) the type of acid used for the acidic condensation, (iii) the presence of assembling group or any additional ligands; (iv) the use of reducing agent crucial for the synthesis of mixed valence systems, such as Mo^{V}/Mo^{IV} or V^{IV}/V^{V} systems.[14]

II.3 Classification of polyoxometalate structures

The large number of compounds in polyoxometalate chemistry can be broadly divided into two sub-classes: the isopolyoxometalates and heteropolyoxometalates. The following sections aim to examine, in more detail, some structural relationships between the archetypical polyoxometalate compounds belonging to the main families such as molybdate, tungstate and vanadate.

II.3.1 Isopolyoxometalates $[M_xO_y]^{n-}$

Isopolyoxoanions are composed of only metal oxide frameworks without the presence of internal heteroatom/heteroanion. Thus, they are considered less stable compared to their heteropolyoxoanion counterparts.[14] However, some of them exhibit a high charge density on their surface which confers a basic character for some oxygen atoms. Such a properties enable them as good candidates for their use as building blocks with interesting physical properties.[15] Isopolyoxometalate ions are generally obtained from acidification of the tetraoxometalate ions used as precursors as written in equation (1).

II.3.1.a Structural description of the Lindqvist polyoxoanion $[M_6O_{19}]^{n-}$

The Lindqvist ion corresponds to a hexametalate arrangement of general formula $[M_6O_{19}]^{n-}$ and contain generally metals of group 5 or 6. It is made up of six $[MO_6]$ polyhedron linked together by edge-shared mode where each metal center bears one terminal oxygen atom and shares four μ_2-bridging oxo ligands with the other adjacent metal centers (Figure 5). The compounds $[Nb_6O_{19}]^{8-}$, $[Ta_6O_{19}]^{8-}$, $[Mo_6O_{19}]^{2-}$, and $[W_6O_{19}]^{2-}$ have been isolated. Structural characterizations (either X-ray diffraction or spectroscopic methods) reveal that they retain approximately the O_h symmetry.[16]

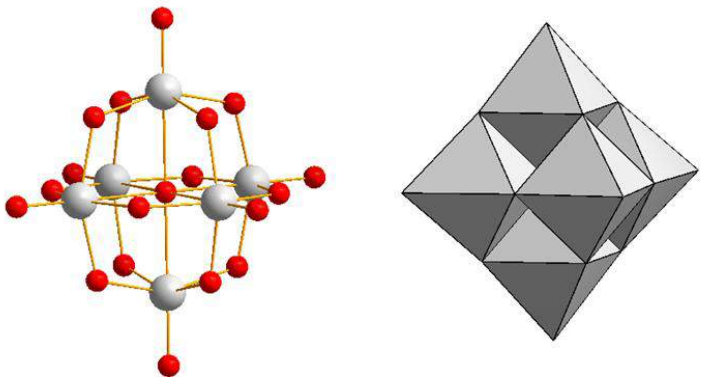

Figure 5: Structural representations of the $[M_6O_{19}]^{n-}$ Lindqvist anion, Left: Ball-and-stick representation. Right: Polyhedral representation showing the six edge-sharing octahedra which lend the cluster its overall octahedral symmetry. Colour scheme: M, light gray (polyhedra); O, red.

Depending on the overall charge of the Linqvist ion, the oxygen atom at the surface are able to coordinate metallic cation. For instance, the oxygen atoms of the highly charged niobate cluster exhibits nucleophilic properties at the origin of the binding of many transition metals such as copper, cobalt or nickel at the surface of the POM.

II.3.1.b Decavanadate polyoxoanion $[V_{10}O_{28}]^{6-}$

Other examples of isopolyoxometalate compounds are found in the vanadates subclass. These species are obtained from the acidification of the metavanadate species giving first a series of metavanadate ions (at pH > 6) and then the decavanadate polyoxoanion $[V_{10}O_{28}]^{6-}$ which is obtained at pH 6. Depending on the acidity of the solution the decavanadate anion exists under different protonation state such as $[H_nV_{10}O_{28}]^{(6-n)-}$ where n ranges between 2 and 4. The structure of the $[V_{10}O_{28}]^{6-}$ anion can be viewed as an extension of lindqvist structure described above. It composes of two fused $[V_6O_{19}]^{8-}$ which share two $[VO_6]$ octahedra (Figure 6).

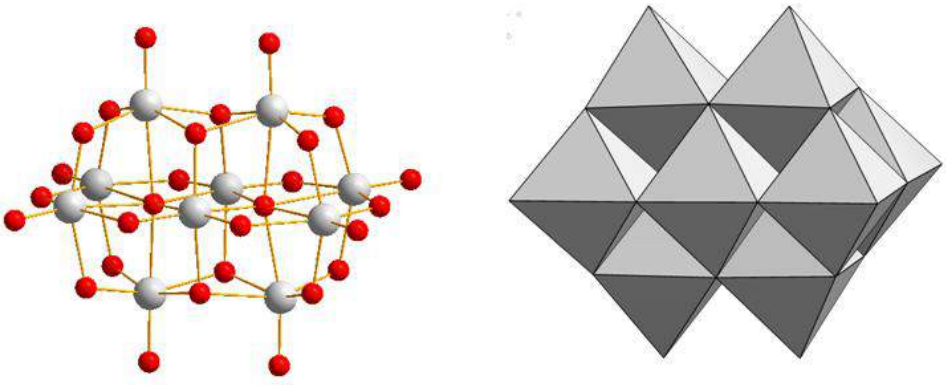

Figure 6 : Structural representations of the $[V_{10}O_{28}]^{6-}$ decavanadate anion. Left: Ball-and stick representation . Right: Polyhedral representation. Colour scheme: V, light gray (polyhedra); O, red

II.3.2 Heteropolyoxometalates $[X_xM_yOz]^{n-}$

Heteropolyanions are of general formula $[X_xM_yO_z]^{n-}$ and contain one or more heteroatoms (X) which belong generally to the p-block of the periodic table, e.g. Si, Ge, P, As or S. These heteratoms are generally present as oxo-ions in the synthesis medium, such as silicate, arsenate or phosphate and are known to direct the condensation processes of the metalates ions. Depending on the geometry of the heterogroup such as tetrahedral, trigonal or octahedral, a wide structural variety of heteropolyoxometalates can be obtained. Among the most prominent structures of heteropolyoxometalates, the Keggin and the Wells-Dawson

anions including their derivatives are highly illustrative of this class of compounds. They will be discussed below in this section.

II.3.2.a Structural description of the archetypical saturated ion

The Keggin anion $[XM_{12}O_{40}]^{n-}$. The Keggin anions are of general formula $[XM_{12}O_{40}]^{n-}$ where M = W or Mo, and X corresponds to the heteroatom, usually Si or P. The arrangement is based on a central $[XO_4]$ tetrahedron surrounded by twelve $[MO_6]$ octahedra. These twelve octahedra are arranged into four $[M_3O_{13}]$ triads in which the three octahedra are linked by edge-shared junctions. These triads are symmetrically linked together *via* corner-shared junctions surrounding the central heteroatom X (Figure 7). The Keggin arrangement is highly symmetric and retains the idealized T_d symmetry. However, in the solid state, the molybdenum Keggin anion exhibits a lower symmetry close to the chiral group *T* due to small displacements of the Mo atoms out of the mirror planes crossing the four $\{M_3O_{13}\}$ units.[16]

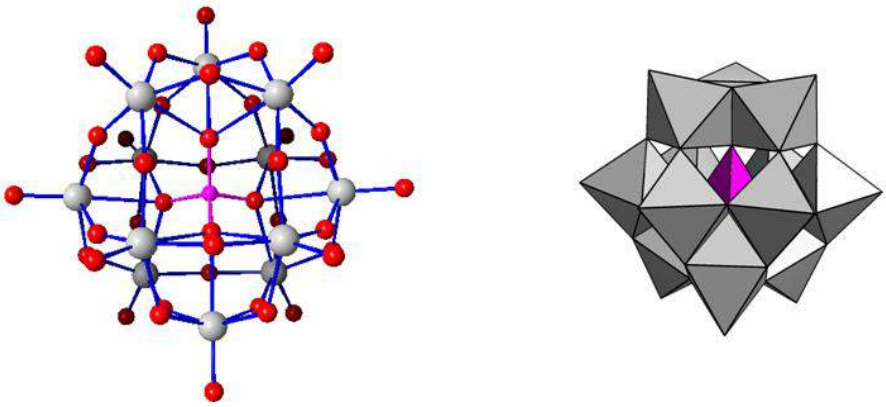

Figure 7: Representation of the Keggin anion. Left: Ball-and-stick representation showing the tetrahedral coordination of the central heteroatom. Right: Polyhedral representation showing the twelve $\{WO_6\}$ octahedra and central tetrahedron (highlighted in pink). Colour scheme: M, light gray, (polyhedra); P, pink (central tetrahedron); O, red.

The Keggin structure described in Figure 7 correspond to the α isomer and four isomers can be deduced from the α arrangement. They correspond to the formal Baker-Figgis isomers and are named β, γ, δ, and ε isomeric forms.[17] They are obtained formally through rotation of 60° of one, two, three and four $\{M_3O_{13}\}$ units of the α-isomer. The isomers of the Keggin structure are shown in Figure 8. The α isomer is probably the most popular and common ion. It exists as molybdate or tungstate and exhibits the highest stability compared to the other isomers. The β-isomer exists also as tungstate or molybdate while the γ-isomer exists only as heteropolyoxotungstate. The ε arrangement is known as reduced Mo(V) metal-oxide arrangement and δ isomer exists only as a polyhydroxoaquo complexe of Aluminium(III).

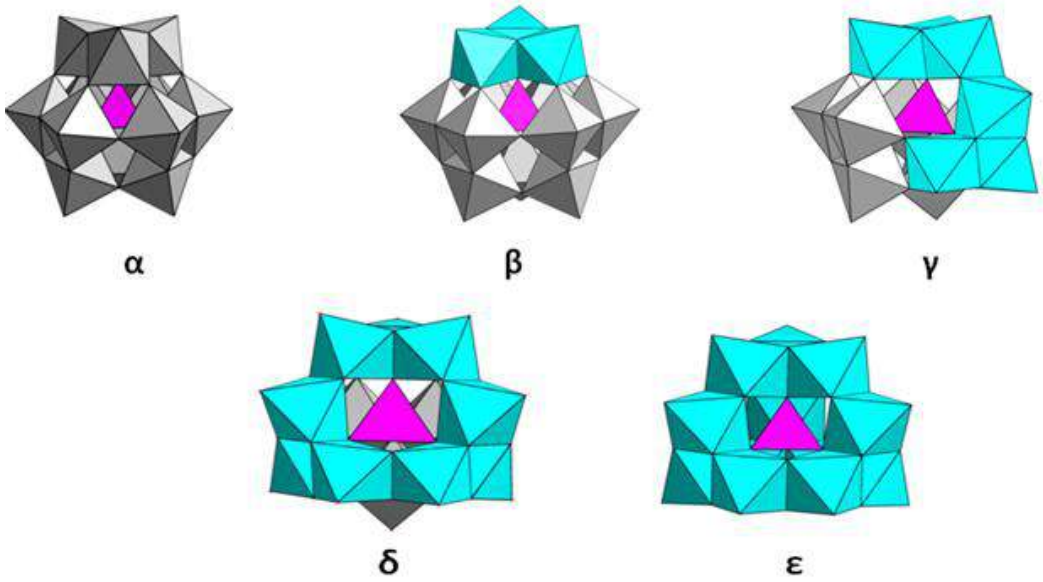

Figure 8: Polyhedral representation of the different isomers of the α-keggin structure.

The Wells-Dawson polyoxoanion $[X_2M_{18}O_{62}]^{n-}$. Dawson polyoxoanions are of general formula α-$[X_2M_{18}O_{62}]^{n-}$ where M = W or Mo and X = P or As. Structurally, the cluster is made up of two $\{XM_9O_{34}\}$ moieties, each deriving from the keggin arrangement through the removal of three adjacent octahedra (see Figure 9). These two subunits are symmetrically linked together through six quasi-linear M-O-M corner-shared junctions to give a D_{3h} arrangement, called the α isomer. The successive rotation of the two apical $[M_3O_{13}]$ caps by 60º allows the generation of isomers, also in this case the α isomer corresponds to the most stable one.[18]

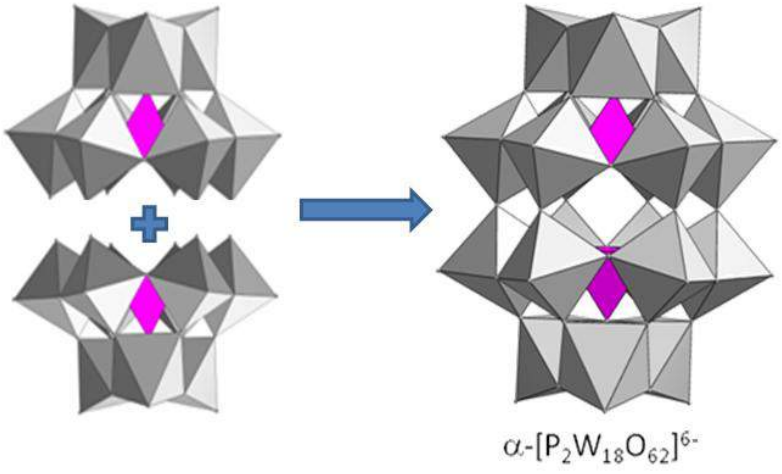

Figure 9: Polyhedral representation of the α-$[X_2M_{18}O_{62}]^{n-}$ Colour scheme: M, gray , (polyhedra); P, pink (central tetrahedron).

II.3.2.b Lacunary heteropolyoxotungstates

- **Lacunary structures derived from the Keggin polyoxoanion**

Heteropolytungstates with the keggin struture, e.g. $[SiW_{12}O_{40}]^{4-}$, are known for their ability to form polyvacant arrangements where one or several metallic centers have been removed. The resulting clusters are called vacant or lacunary polyanions. Such complexes are generated through controlled basic hydrolysis of keggin-anion allowing to induce the hydrolytic cleavage of the M-O bonds and to remove selectively one, two or three metal centers from the parent anion.[16] Formation of vacant species corresponds to a general behavior in the POM chemistry, observed in many chemical POM systems, but probably the best known POM system is the silicotungstate whose the relationships between polyvacant species and their related isomers give a complex interconversion scheme (see Figure 10).[19] These processes lead to the formation of undecatungstate ($\{SiW_{11}\}$), decatungstate ($\{SiW_{10}\}$), and nonatungstate ($\{SiW_9\}$) lacunary structures and their related isomers β, γ or δ (Figure 10).

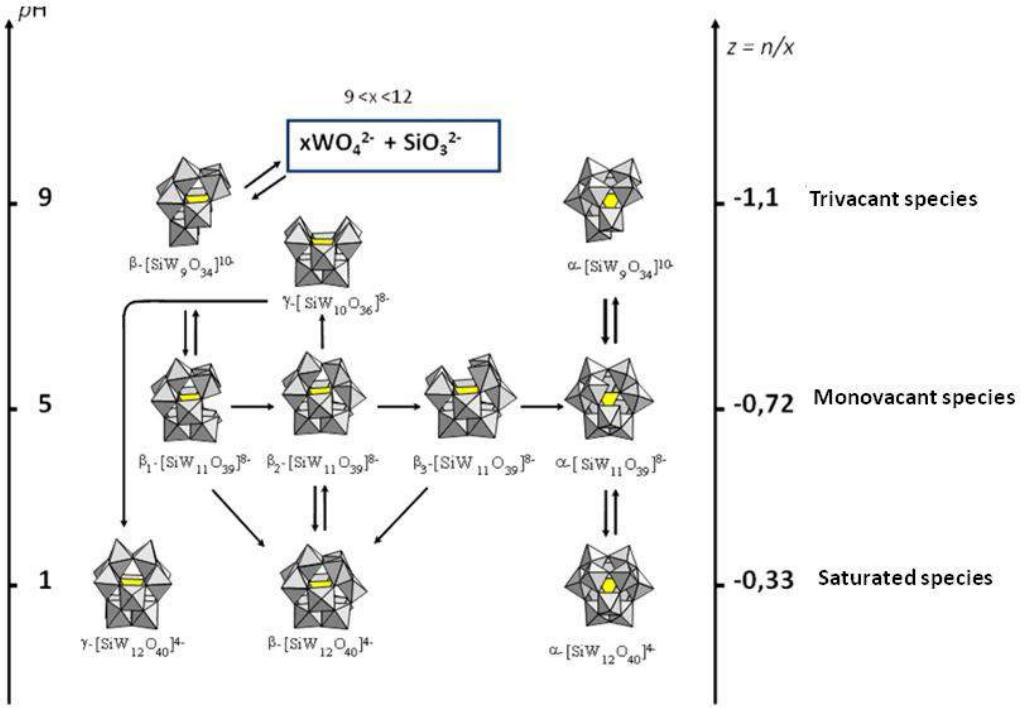

Figure 10: Interconversion relationship within the silicotungstate system.

- **Lacunary structures derived from the Wells Dawson polyoxoanion**

Typically, the saturated Dawson anion is stable in solution up to approximately pH = 5. However, above pH = 5, a partial hydrolysis occurs to yield derived lacunary species where

one or more metal centers are selectively removed. Such a partial hydrolysis of the saturated wells Dawson anion is similar to that occurs with Keggin derivatives. In the case of the Dawson clusters, however, all the stable lacunary species are derived from the α-isomer of the $\{X_2W_{18}\}$ anion.[19] Three defect species can be produced and isolated in this way, corresponding to a mono-, tri- and hexavacant species with formula $[\alpha_1\text{- or } \alpha_2\text{-}X_2W_{17}O_{61}]^{10-}$, $[\alpha\text{-}X_2W_{15}O_{56}]^{12-}$, and $[\alpha\text{-}H_2X_2W_{12}O_{48}]^{12-}$, respectively (Figure 11).

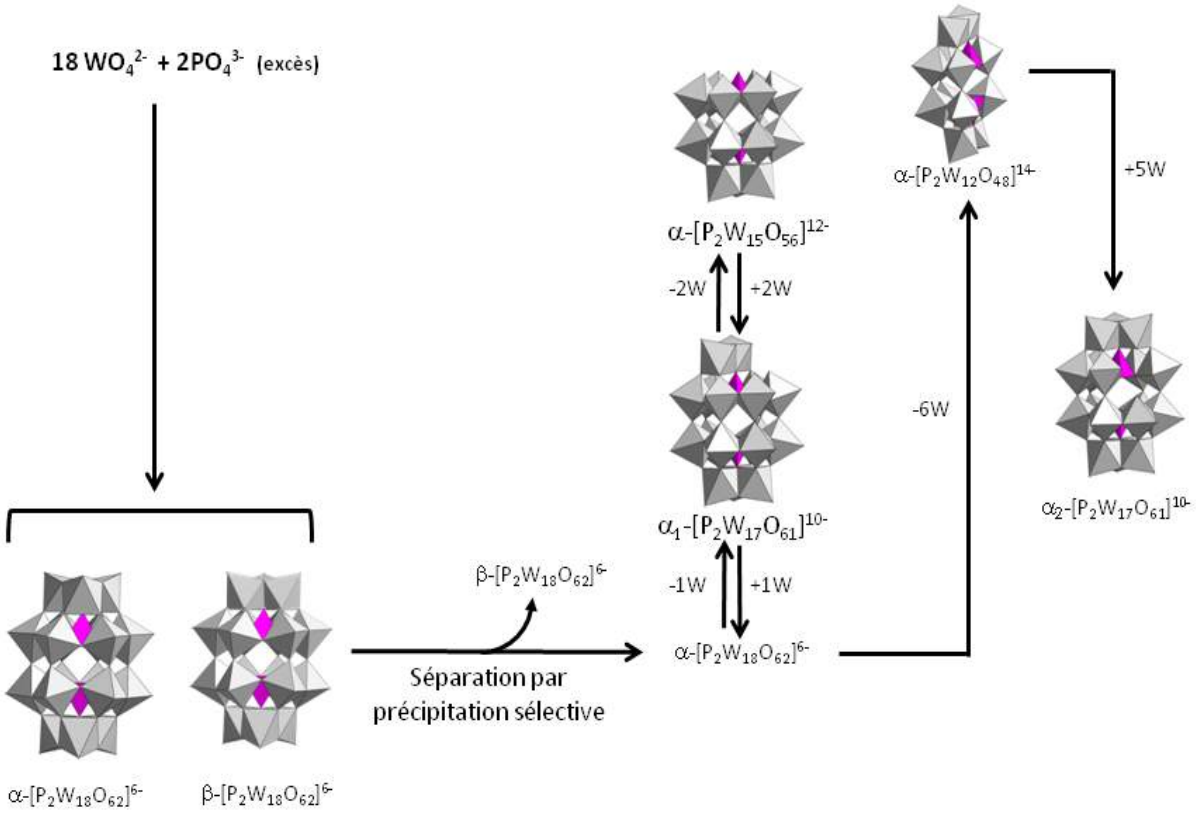

Figure 11 : Different lacunary species of the $[P_2W_{18}O_{62}]^{6-}$ Wells Dawson ion.

The structural diversity of POMs is enormously increased by the ability of their lacunary species to act as multidentate ligands and to coordinate a wide variety of cations either mononuclear species M^{n+} belonging to the transition elements (d- or f-elements) or preformed cationic clusters such as $\{Mo_2O_2E_2\}^{2+}$ (with E = O or S) or $\{Mo_3S_4\}^{4+}$. Thus, the POM-cation combinations allow the construction of many mixed metal polyoxoanions as well as larger, more complex POM structures. Depending on the nature of the combination, interesting properties will be emerged such as structural, electronic,[20] magnetic[21] or catalytic properties.[22] In this section, some examples of the extended coordination ability of Keggin as well as wells Dawson derivated species will be shown .

II.3.2.c *Coordination of lacunary polyoxometalates with metallic cation*

A lot of examples have demonstrated the ability of lacunary polyoxometalates derivatives to coordinate cationic species. In this context , Kortz *et al*. reported the inclusion of Ru^{II} center within the α-isomer of $\{GeW_{11}\}$ to give $[Ru^{II}(DMSO)_3(H_2O)\alpha\text{-}GeW_{11}O_{39}]^{6-}$ where the coordination sphere of Ru^{II} is filled by two oxo groups belonging to the POM moiety and additionally completed with three DMSO molecules and one water molecule (Figure 12a).[23] In 2007, Dolbecq *et al.* reported the coordination of the trivacant anion α-$\{SiW_9\}$ coordinated to four Co^{II} centres whose coordination spheres are filled with μ_2-bridging acetate and hydroxo ligands, giving the $[(A\text{-}\alpha\text{-}\ SiW_9O_{34})Co_4(OH)_3(CH_3CO_2)_3]^{8-}$ species (Figure 12b).[24]

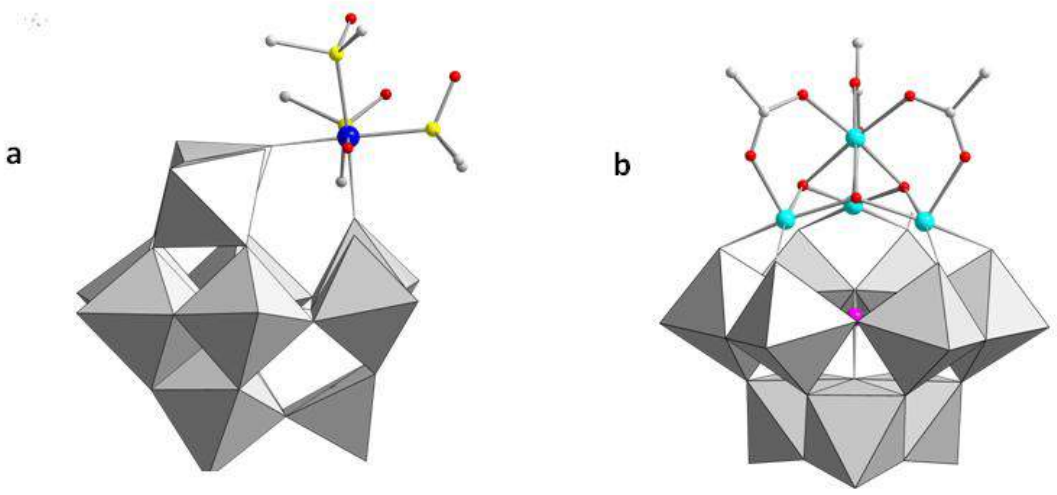

Figure 12: (a) Combined polyhedral ball-and- stick representation for $Ru^{II}(DMSO)_3(H_2O)\alpha\text{-}GeW_{11}O_{39}]^{6-}$, (b) $[(A\text{-}\alpha\text{-}\ SiW_9O_{34})Co_4(OH)_3(CH_3CO_2)_3]^{8-}$. Color scheme: W, gray polyhedral; Si, pink; O, red; C, grey; S, yellow; Co, turquoise; Ru, blue.

In the same way, the lacunary Dawson species were also functionalized with organic groups or transition metal clusters. The functionalizing of the α_2-$\{P_2W_{17}\}$ monolacunary anion with an organosilyl group ($O[Si(CH_2)_3SH]_2$) *via* the four oxygen atoms lining the mono-lacunary site of the cluster leads to the hybrid species $[\alpha_2\text{-}P_2W_{17}O_{61}(O[Si(CH_2)_3SH]_2)]^{6-}$ (Figure 13a).[25] Gouzerh *et al.* demonstrate that the six vacancies of the $\{P_2W_{12}\}$ anion can be filled by six Fe^{III} centres involved within the metal-oxo core $\{Fe_6O_8\}^{2+}$. Three additional Fe^{III} centres are then grafted on the $\{Fe_6O_8\}^{2+}$ core through bridging oxo ligands. The coordination spheres of the nine resulting Fe centres are filled with seven terminal or bridging acetate ligands to give the $[H_4P_2W_{12}Fe^{III}{}_9O_{56}(OAc)_7]^{6-}$ anion (Figure 13b).[26]

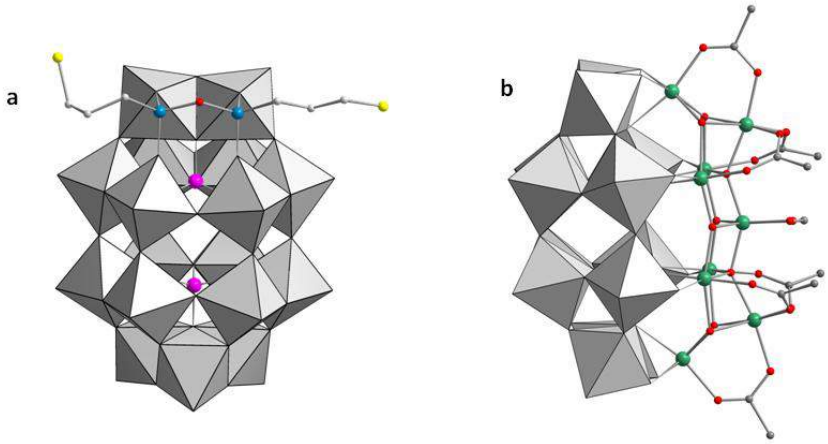

Figure 13: (a) Combined polyhedral ball-and-stick representation for $[\alpha_2\text{-}P_2W_{17}O_{61}(O[Si(CH_2)_3SH]_2)]^{6-}$. (b) $[H_4P_2W_{12}Fe^{III}{}_9O_{56}(OAc)_7]^{6-}$. Color sheme: W, gray polyhedral; P, pink; O, red; C, grey; S, yellow; Si, blue; Fe, green.

There are extensive literature reports on studies of lanthanide ions containing POMs due to the interesting structural and physicochemical properties of such mixed compounds. A lot of groups investigated the mixed metal POM-based lanthanide by multinuclear NMR spectroscopy.[27] For example Qu *et al.* reported the synthesis of several polyanions of the type $[Ln(\beta_2\text{-}SiW_{11}O_{39})]^{13-}$ (*Ln* = La, Ce, Pr, Nd, Sm, Gd, Er) fully characterized by multinuclear NMR in solution while structural data were missing. [28] In the following of this work, Kortz *et al.* reported structural investigations of the monolacunary β_2-Keggin family $[Ln(\beta_2\text{-}SiW_{11}O_{39})_2]^{13-}$ (*Ln* = La, Ce, Sm, Eu, Gd, Tb, Yb, Lu) by using single-crystal XRD as well as ^{183}W NMR spectroscopy in solution (Figure 14a).[29] Pope and Francesconi were interested by the interaction of lanthanide ions with the lacunary Dawson derivatives. For example, Francesconi reported the europium-containing Dawson dimer $\{Eu_2(H_2O)_3(\alpha_2\text{-}P_2W_{17}O_{61})\}_2$, where the two POM subunits are bridged by two Eu^{2+} ions (Figure 14b).[30]

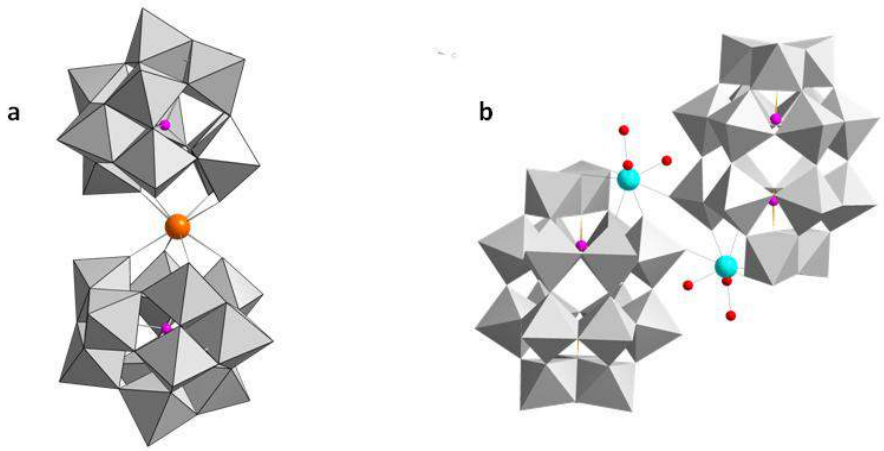

Figure 14 : a) Combined polyhedral ball-and-stick representation for $[La(\beta_2\text{-}SiW_{11}O_{39})_2]^{13-}$. (b) $\{Eu_2(H_2O)_3(\alpha_2\text{-}P_2W_{17}O_{61})\}_2$. Color scheme: W, gray polyhedral; P, Si, pink; O, red; La, orange; Eu, turquoise.

II.3.2.d *Coordination of lacunary POMs with polynuclear cationic cores :*

Cadot *et al.* used the "magic building block" $\{M_2S_2O_2\}^{2+}$ (M = Mo or W), a stable preformed cationic precursor, to react with anionic polyoxometallates. The first isolated heteropolyoxothioanion was obtained from the addition of the $\{M_2S_2O_2\}^{2+}$ (M = Mo or W) on the divacant γ-$[SiW_{10}O_{36}]^{8-}$ anion.[31] The structure of the resulting product γ-$[SiW_{10}Mo_2S_2O_{38}]^{6-}$ clearly shows the filling of the divacancy of the anion resulting in four Mo–O–W bridges through a desolvation process of the aqua cation (see Figure 15a). This strategy was extended to monovacant anions, derived from Keggin or Dawson structures giving the dimeric species $[(PW_{11}O_{39})_2(Mo_4S_4O_4(H_2O)_2)]^{10-}$ and $[(P_2W_{17}O_{61})_2(Mo_4S_4O_4(H_2O)_2)]^{16-}$, respectively (see Figure 15b).[32-33] Unique coordination properties toward metallic cations were observed for trivacant lacunary species due to the stereo-chemical difference of the six terminal oxygen that constitute the coordinating centers of the trivacant anions. Especially, coordination of $\{Mo_2O_2S_2\}^{2+}$ to the trivacant [A-α-$PW_9O_{34}]^{9-}$ leads to a pillar-like compound in which two $\{PW_9\}$ subunits are assembled by three parallel $\{Mo_2O_2S_2(H_2O)_2\}$ linkers (Fig.15c).[34] However, the presence of an additional central {P=O} group within the $[O_6]$ crown in the B-type trivacant anion [B-$P_2W_{15}O_{56}]^{12-}$ favors the formation of a spectacular planar tetrameric arrangement (Fig. 15d).[35]

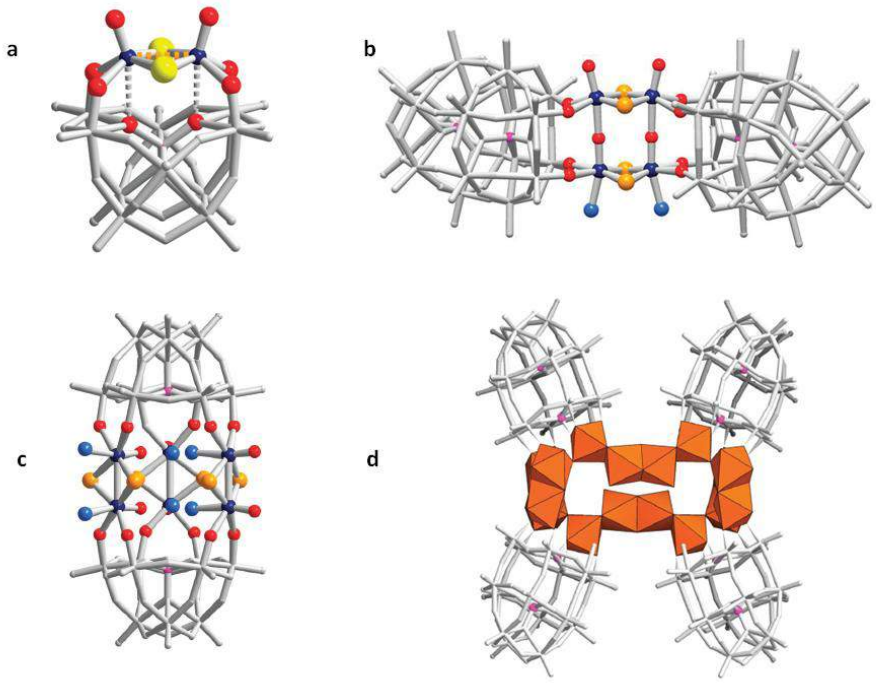

Figure 15: **(a)** Structural representation of γ-$[SiW_{10}Mo_2S_2O_{38}]^{6-}$, (b) $[(P_2W_{17}O_{61})_2(Mo_4S_4O_4(H_2O)_2)]^{16-}$, (c) $[(PW_9O_{34})_2(Mo_2O_2S_2(H_2O)_2)_3]^{12-}$, (d)$[(H_2P_2W_{15}O_{56})_4\{Mo_2O_2S_2(H_2O)_2\}_4\{Mo_4S_4O_4(OH)_2(H_2O)\}_2]^{28-}$. Color code: heteropolyoxotungstate subunits, grey sticks; $\{Mo_2O_2S_2\}$ linkers, orange polyhedra; Mo, blue sphere; S, yellow spheres; O, red spheres; light blue spheres ;water molecule, light blue spheres. Reproduced from reference [35].

Such an approach has been then successfully extended by to the trinuclear cation $\{Mo_3S_4\}^{4+}$ where a unique family of hybrid chalcogenide cluster-incorporated polyoxometalates (POM) has been obtained (Figure 16). shows some particular examples of this family including $[EW_{15}Mo_3S_4(H_2O)_3O_{53}]^{9-}$ (E = As, Sb).[36]

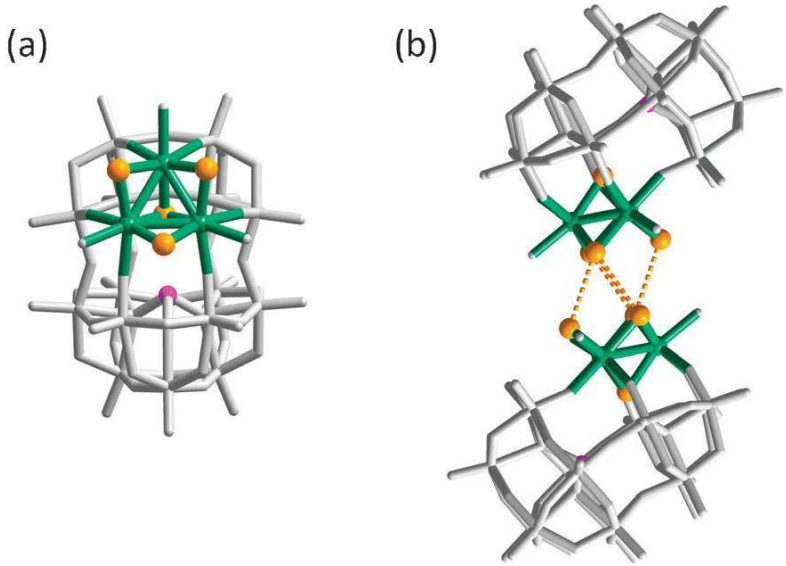

Figure 16: Structure of the $[AsW_{15}Mo_3S_4(H_2O)_3O_{53}]^{9-}$anion. (a) Isolated species showing the presence of the $\{Mo_3S_4(H_2O)_3\}$ as a constitutional trimetallic unit; (b) view of the dimeric arrangement observed in the solid contacts. Color code: grey sticks=$\{AsW1_5\}$ framework; green sticks=$\{Mo_3S_4\}$ core; yellow spheres = S atoms. Reproduced from reference [35].

II.3.2.e Hollow and ringed large POMs arrangements

POMs show the tendency to form ringed crown or spheroidal type structures.[37] Such a tendency results from the polycondensation processes occurring in aqueous solution and can be explained by a dominant factor: the ring or spheroidal assembly minimize the propensity for further self-aggregation by allowing the minimal interaction with the solvent. The heteropolyoxotungstates give some nice examples of such kind of assemblies.

The Preyssler anion. The Preyssler anion $[M^{n+}P_5W_{30}O_{110}]^{(15-n)-}$ is one of the first example of heteropolytungstophosphate with an internal cavity. It was reported for the first time by Preyssler [38] and structurally characterized through single-crystal X-ray diffraction by Pope and co-workers 15 years later.[39] The Preyssler anion is composed by five $\{PW_6O_{22}\}^{9-}$ units disposed in a cyclic arrangement with an internal cavity occupied by an encrypted cation (originally sodium) (Figure 17). This inner Na^+ cation appears disordered over two close positions and can be replaced under hydrothermal conditions by other cations of similar size such as lanthanides or actinides.[40] This ability to capture lanthanide/actinide cations from aqueous solutions allow envisioning the use of such anions for treatment of the nuclear

wastes. Cations that have already been incorporated into the internal cavity are trivalent lanthanides, such as La^{3+}, Ce^{3+}, Nd^{3+} and Eu^{3+} also tetravalent actinides, such as U^{4+}. [41] The Preyssler anion is also known for its catalytic and redox properties. Antonio and co-workers demonstrated by electrochemical studies the ability of the $[P_5W_{30}O_{110}]^{15-}$ and derivatives to stock reversibly a great number of electrons.[42]

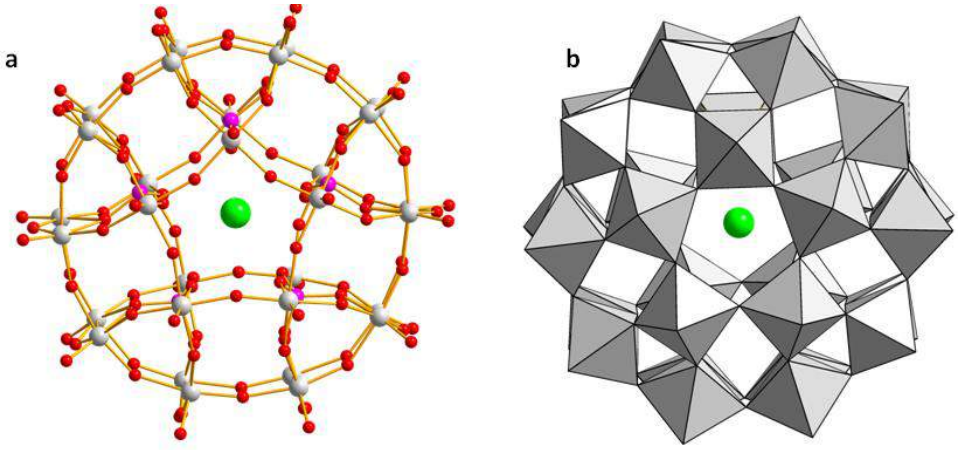

Figure 17: Representations of the Preyssler-type anion $[NaP_5W_{30}O_{110}]^{14-}$: (a) Ball-and-stick representaiton.(b) polyhedral representation showing the sodium ion sits in the central closed circle). Color scheme: W, gray (polyhedral); P, pink; O, red; Na, green.

The superlacunary crown-type $[P_8W_{48}O_{184}]^{40-}$. The $[P_8W_{48}O_{184}]^{n-}$ anion represents a unique example of macrocyclic arrangement. It was first isolated by Contant and Téze in 1985.[43] The $\{P_8W_{48}\}$ macrocycle results of the cyclic condensation of four hexavacant $[\alpha\text{-}H_2P_2W_{12}O_{48}]^{12-}$ anion used as precursor in the condition of synthesis (abbreviated as $\{P_2W_{12}\}$). The metal-oxo framework of crown-type $\{P_8W_{48}\}$ assembly exhibits the nominal D_{4h} symmetry. However, the structural characterization showed the presence of four potassium cations statistically disordered over eight positions within the 1 nm-sized cavity. These four potassium ions are expected to play important templating role in the mechanism formation of the macrocycle by directing within a convergent process the condensation of the $\{P_2W_{12}\}$ subunits (Figure 18) and by lowering the repulsive interactions of the exposed, nucleophilic, inner-ring oxygen surface. The $\{P_8W_{48}\}$ ion appears stable over a broad pH range, a remarkable behavior for such a polylacunary cluster.[44] The $\{P_8W_{48}\}$ ion has been denominated as "superlacunary" anion because of its ability to develop challenging host-guest chemistry and then its possibility to include a large number of metallic centres within the cavity. Some examples will be given in section III.

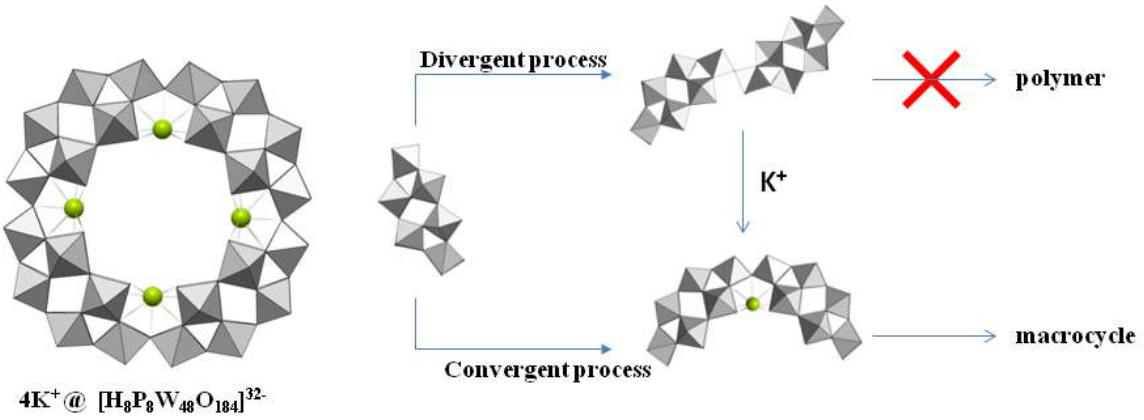

Figure 18: Schematic view showing the importance of potassium cations in the cyclization process resulting in the formation of the $\{P_8W_{48}\}$ anion. Color scheme: W, gray(polyhedral); K, green.

II.3.3 Molybdenum blue and keplerate structures

The condensation of molybdates under reducing conditions in solution brought amazing examples of multifunctional and highly complex molecular nano-objects up to protein size. The control of the reducing conditions under acidic conditions enables the linking of metal-oxide building blocks available from the constitutional (and virtual) dynamic libraries. In this section, we will highlight the fantastic development of the giant-metal oxide chemistry which is dominated by a common structural feature corresponding to the transferable pentagonal $\{(M)(M_5)\}$ group, as an important building block in the formation of these extended supermolecules.

II.3.3.a Mystery of "molybdenum blue" and discovery of the Bielefeld giant wheels

"Molybdenum blue" solutions exist in Nature: e.g. near Idaho Springs, Colorado, and Ouray, Utah,[45] where they result from dissolution of the amorphous mineral ilsemannite (approximate formula $Mo_3O_8.nH_2O$) formed by partial oxidation of molybdenite (MoS_2). Famous chemists as Scheele and Berzelius were the first to study the "molybdenum blue" solution. The latter reported the first formula ($Mo_5O_{14}.nH_2O$) for the blue powder isolated from such solutions. In 1995, an important step has been accomplished which revealed that beyond these blue solutions lies a stunning bouquet of outstanding clusters, including the torus-shaped $\{Mo_{154}\}$ and $\{Mo_{176}\}$-type species, as well as the hedgehog-shaped $\{Mo_{368}\}$-type one.[45]

The story of unveiling this mystery started with the isolation of some crystals from a molybdenum blue solution which was prepared using hydroxylamine as reducing agent.[15, 46]

The crystal structure analysis showed a unique giant $\{Mo_{154}\}$-type wheel containing 14 NO ligands [15] but the isolation of the compound as pure crystalline phase was restricted by severe problems of crystallization. By simple replacement of 14 $\{MoNO\}^{3+}$ by 14 $\{MoO\}^{4+}$ units - the crystallization problems were solved leading to a straightforward and high yield synthesis of the crystalline $\{Mo_{154}\}$ giant compound allowing the complete determination of the formula.[46] Structurally, $\{Mo_{154}\}$-type compound exhibits a ring-shape arrangement, which consists of 140 $\{MoO_6\}$ octahedra and 14 pentagonal bipyramids of the type $\{MoO_7\}$, forming the three types of basic building blocks $\{Mo_8\}$,$\{Mo_2\}$ and $\{Mo_1\}$. A slight change in the experimental conditions such as lowering pH (pH<1) and a concentration increase in molybdate lead to the formation and isolation of a larger wheel-shaped cluster $\{Mo_{176}\}$.The $\{Mo_{176}\}$ cluster can be roughly described as a hexadecamer with two extra $\{Mo_8\}$, $\{Mo_2\}$ and $\{Mo_1\}$ units (Figure 19). Using ascorbic acid as a reducing agent,[47] the $\{Mo_{176}\}$undergoes an unique nucleation process to form $\{Mo_{36}O_{96}(H_2O)_{24}\}$ clusters/fragments which has been structurally identified within the cavity like a hub-caps and resulting in the formation of an extraordinary $\{Mo_{248}\}$-type cluster.[47]

The interesting chemical properties of these wheel type species make them as good candidates for further study in different domains of science. For example, such mixed valence compounds are recognized for their rich electrochemistry due to the presence of Mo^{VI}/Mo^{V} centres;[48] their nanometer-sized cavities lined by the wheel-like metal-oxo framework constitutes promising structural hosts for organic or inorganic guest molecules;[49] These very large inorganic molecules exhibits unique electronic properties such as nano-sized semi-conductor due to the of high density of states in the HOMO/LUMO region leading to a small band gap.[48]

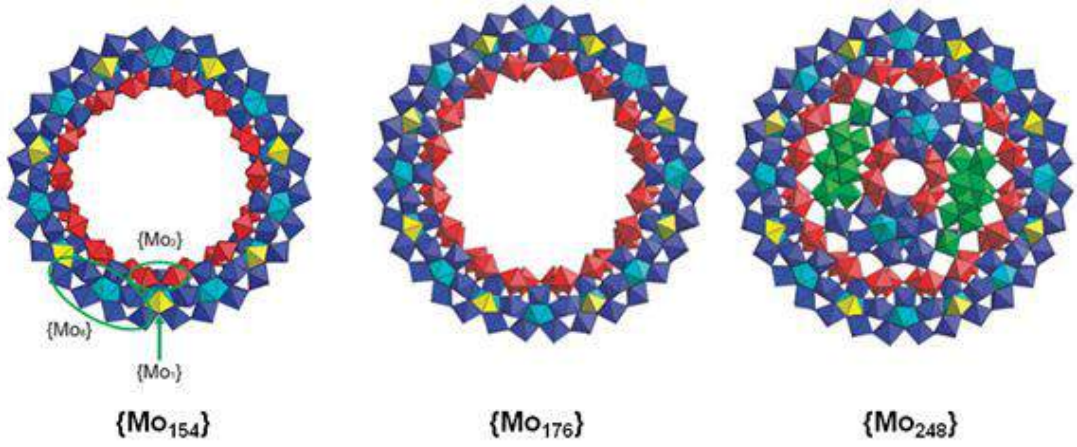

Figure 19: Polyhedral representation of the $\{Mo_{154}\}$, $\{Mo_{176}\}$ and $\{Mo_{248}\}$ clusters. Color code: ($\{Mo_8\}$ blue and cyan, $\{Mo_2\}$ red, $\{Mo_1\}$ yellow). Reproduced from Reference [45].

II.3.3.b From giant wheels to giant spheres

The extension of the structural types and topologies in the chemical world corresponds to a continuing challenge for the chemists. In the POMs chemistry, the chemist manipulates an extraordinary collection of polyhedra, arranged as primary building blocks which composed the so-called "virtual dynamic library", offering many accessible structural combinations. From a theoretical point of view, formation of spherical objects is possible from the curveted connection of 12 pentagonal motifs.[45] Such a topology has been found in chemistry with the illustrative example of the C_{60} fullerene. Based on the expertise gained from the discovery of the giant wheels, Mùller and his group succeeded to create the most marvelous highly symmetric ball-shaped structures, named "Keplerate".

The spherical capsule with the abbreviated formula $[M^{VI}_{72}M^{V}_{60}]$ with M = Mo or W type cluster can be obtained by addition of preformed $\{Mo_2{}^{V}O_4(aq)\}^{2+}$ [50] or $\{Mo_2{}^{V}O_2S_2(aq)\}^{2+}$ units [51] to an acidified solution of molybdates while the addition of mononuclear linker, eg. Fe^{3+}, Cr^{3+} or VO^{2+}, leads to the formation of the smaller $[M^{VI}_{72}M^{V}_{30}]$ type keplerates.[52] In geometrical terms, this type of capsule can be described as $(Pentagon)_{12}(Linker)_{30}$; Pentagon $\{M^{VI}(M^{VI})_5\}$ which consists of a central pentagonal bipyramidal MoO_7 unit sharing edges with five MoO_6 octahedra. Then, these twelve pentagonal units are held together by 30 linkers ={$Mo_2E_2O_2$} with E = O or S to give the overall inorganic backbone of the capsule (Figure 20).[53] It is interesting that the $\{Mo^{V}_2\}$ building unit can only be formed in the presence of stabilizing bidentate ligands as acetate. Furthermore, these dimolybdic units are suspected to direct the formation of the $\{(Mo)(Mo_5)\}$ pentagons, which do not exist as an independent unit. Based on such a topology, molecular porosity arises from the Keplerate arrangement. The mentioned type capsules $[M^{VI}_{72}M^{V}_{60}]$ and $[M^{VI}_{72}M^{V}_{30}]$ exhibit 20 $\{M_9O_6E_3\}$ rings distributed on the spheroidal surface of the capsule. The diameter of these aperture depends on the nature of the linker i.e mono or dinuclear cationic unit. The larger pores are formed by three $\{Mo_2\}$ and three $\{Mo_1\}$ units and can be described from the lining components such as $\{Mo_9O_6E_3\}$. Their diameters reach about 6.5 Å, thus lining a large crown perimeters interesting for host-guest chemistry. Actually, these pores have receptor properties similar to those of the classical crown ethers. Thus, sphere-surface chemistry with such multi-receptors opens new insigths in the context of supramolecular chemistry. This point is discussed in detail in the following sections .

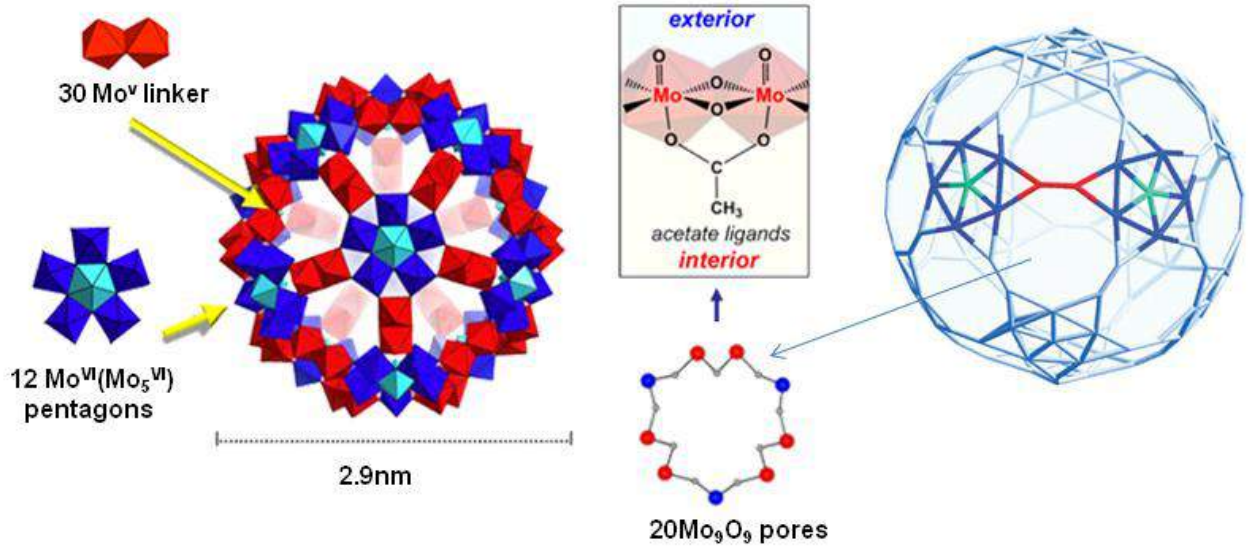

Figure 20: Polyhedral representation and wire frame notation of {Mo_{132}} showing the building blocks and define the pore of the capsule. Reproduced from reference [54].

II.3.3.c {Mo_{368}} Clusters: a hybrid topology between wheel- and ball-shaped clusters.

Going deep in the dream of mimicking nature's complexes, *Muller et al.* have reported the largest molecular cluster comparable to the size of hemoglobin, with an approximate diameter of 6 nm. It contains 368 metal atoms formed by the linking of 64 {Mo_1}, 32{Mo_2}, and 40{$Mo(Mo_5)$}-type units with the formula [$H_xMo_{368}O_{1032}(H_2O)_{240}(SO_4)_{48}$].[55-56] The overall structure of the cluster is exceptional, as it incorporates two oppositely curved surfaces, i.e., a positive surface that goes through an inflexion point to a negative surface. The resulting cluster resembles the shape of a lemon (Figure 21). On the other hand, the Mo-blue mixed-valence {Mo_{368}}-type cluster was (preferably) obtained only in the presence of Na^+ and SO_4^{2-} ions. This is a direct evidence that the reaction pathways leading to the giant ‘‘blue-type’’polyoxomolybdates are dependent not only on the pH value and on the reducing conditions but also in some cases upon the presence of specific components.

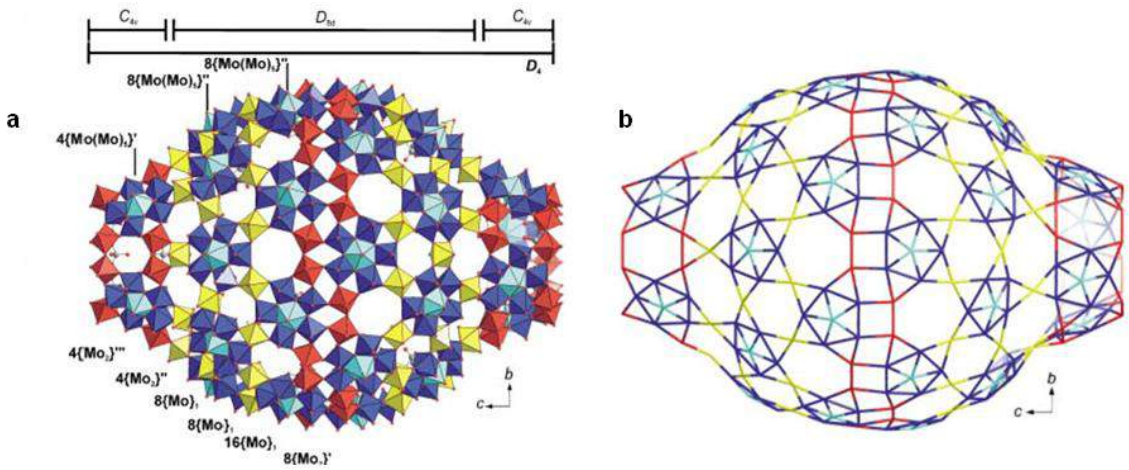

Figure 21 : Polyhedral representation and wire frame notation of $\{Mo_{362}\}$. Reproduced from Reference [56].

III. Host-guest chemistry of POM based superclusters: From the basic model to the multi-receptor system.

Ion pairing in aqueous solution orchestrates a variety of vital processes occurring in nature and in several areas of science including Polyoxometalates chemistry.[57] POMs are highly charged anions and are normally associated with charge-balancing cations, although these are sometimes omitted from structural analysis as being "silent" components. However, it seems that assembly of POMs, their redox activity and catalysis properties in aqueous solution are greatly influenced by POM-cation associations. Understanding the interactions of POMs with their cations has become a subject of both fundamental and practical interest, as it is important for the development of challenging POM-based supramolecular engineering concept toward ionic recognition, dynamic or inclusion of guest. Last but not least, it is also important for the successful utilization of these species as homo- or heterogeneous catalysts,[58] as molecular materials with optical,[59] magnetic properties[60] or as materials for selective capturing of cations such as lanthanides and actinides.

III.1 Polyoxometalates as Crowns and Cryptates

The genesis of supramolecular chemistry may be tracked back to the pioneering work of J. Pedersen, Jean Marie-lehn and Donald J. Cram. They shared the 1987 Nobel Prize in chemistry for their work on the discovery and application of some very special multi-dentate macrocyclic molecule called crowns and cryptands.

1. Crown ethers (or crowns) are a group of macrocyclic polyethers in which the ethereal group are separated by two methylene (CH_2-) groups. Crowns are known to bind metal ions, ammonium and alkyl-ammonium. This type of ligands is known to be flexible

and can be distorted to optimize the host-guest geometry. For smaller cations, such as sodium, the [18]crown-6 distorts and wraps itself around the metal to maximize favourable electrostatic interactions.

2. Cryptands effectively moved the crown ethers into the third dimensions. Cryptands are cage-like bicyclic molecules. They have been found to complex group 1 and 2 metal cations with very large stability constants, higher than those of analogous crown ethers.

The high stability constants have been attributed to different contributing factors. Once bound in the cryptand cavity, the cation is poorly solvated leading to a positive variation of entropy due to desolvation processes at the binding site and at the cation. In addition, the receptor's structure of the cryptands required only few adaptative distortions to accomodate the metal ions than those for the crowns ethers, thus giving favorable enthalpic contributions.

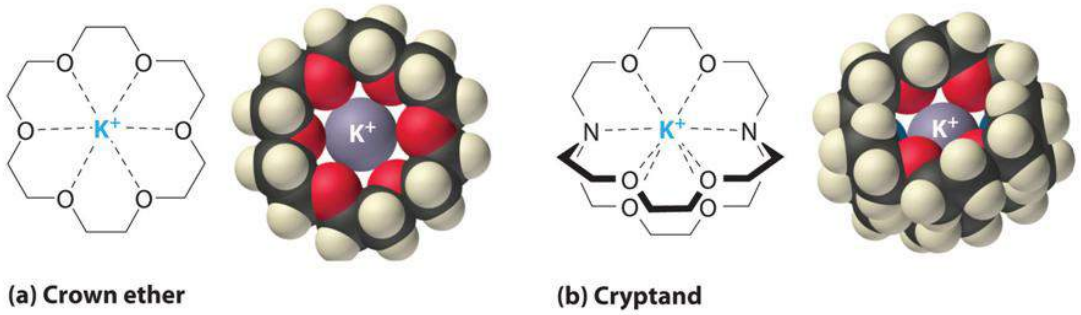

Figure 22: (a) The potassium complex of the crown ether [18]-crown-[6]. Note how the cation is nestled within the central cavity of the molecule and interacts with lone pairs of electrons on the oxygen atoms. (b) The potassium complex of 2,2,2-cryptand, showing how the cation is almost hidden by the cryptand.

Such types of design is also possible with polyoxometalate clusters due to their ability to form highly structured and well-organized metal-oxo frameworks. As such, several examples of POMs clusters are known where the POM structure behaves as inorganic cryptates or as crown-ether-like moiety.

Starting with the interaction of alkali and alkaline-earth metals with basic POM systems such as the γ-$[SiW_{10}O_{36}]^{8-}$ anion, it has been shown that the stability of this polyanion in aqueous solution is strongly dependent on the nature of the counterion. The solution containing potassium, rubidium, or cesium ions allows stabilizing the divacant γ-$[SiW_{10}O_{36}]^{8-}$ anion; in contrast, lithium and sodiums solutions induce a slow conversion of the γ-$[SiW_{10}O_{36}]^{8-}$ anion into the monovacant species β-$[SiW_{11}O_{39}]^{8-}$.[61] The stability constant of the complex $[MSiW_{10}O_{36}]^{(8-n)-}$ (M = alkali or earth-alkaline metal) has been determined through

potentiometric measurements. The results shown in Figure 23 revealed that the stability constant *K* increases with the size and the charge of the cation. This illustrates the contribution of electrostatic interaction as well as the steric effects on the host-guest stability. These results can be compared to that obtained from α-$[MSiW_{11}O_{36}]^{(8-n)-}$ complexes where the stability constant decreases as the size of the cations M^{n+} increases.[61] This different behavior can be related to the size of the cavity, differing from the divacant to the monovacant anion. In α-$[SiW_{11}O_{39}]^{8-}$, the size of the cavity is small and better fits with the smallest cations such as Li^+. In contrast, the aperture of the γ-$[SiW_{10}O_{36}]^{8-}$ structure is larger leading to a better host-guest complementarity with the larger.

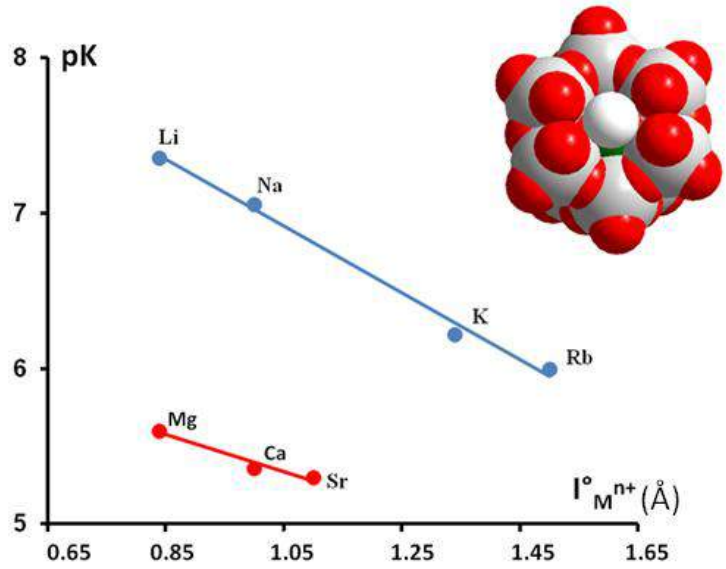

Figure 23: Variation of pK value as function of the metallic radii for alkali and alkaline earth-metals. The picture represents a possible space-filling model of $MSiW_{10}O_{36}^{7-}$ complexes.

Another nice example of POM-based cryptate is the big cyclic polyanion $[As_4W_{40}O_{140}]^{28-}$. Host-guest chemistry of inorganic cryptates, such as $[As_4W_{40}O_{140}]^{28-}$ has been extensively investigated.[62] Hervé *et al.* described the cyclic polyanion $[As_4W_{40}O_{140}]^{28-}$ as a central site S_1 and four external coordination sites S_2 in which proper radius ions might be incorporated. The study of $\{As_4W_{40}\}$ in the presence of ammonium and transiton metals reveals that ammonium occupies the central site S_1 and the metal centres located on the other four site S_2. Robert *et al.* in 1980 determined the structure of cobalt substituted anion $[NH_4\{Co(H_2O)\}_2$-$As_4W_{40}O_{140}]^{23-}$.[63] Actually, the structure analysis reveals that the coordination of two Co^{2+} ions by the site S_2 leads to geometrical modification (or distortion) of the two other adjacent sites S_2 (noted S_2'). Such an observation in the solid state has been studied in solution, showing that only two Co^{II} cations are selectively crypted, as a result of an allosteric effect

through a conformational change of the ligand $\{As_4W_{40}\}$from D_{2d} to C_{2v} symmetry (Figure 24).

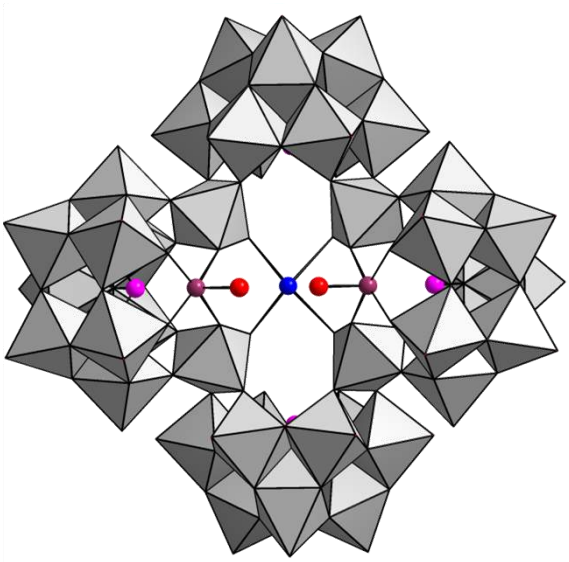

Figure 24: Combined polyhedral ball-and- stick representation of $[NH_4\{Co(H_2O)\}_2\text{-}As_4W_{40}O_{140}]^{23-}$. Color code: W, gray (polyhedral); As, pink; O, red; Co, dark red; N, blue.

Cronin *et al.* reported a range of alkali and alkaline-earth metal complexes based on the $\{W_{36}\}$ cluster.[64] The $[H_{12}W_{36}O_{120}]^{12-}$ ion has a triangular topology and it made up of three $\{W_{11}\}$ subunits linked together by $\{W_1\}$ as shown in Figure 25. The $\{W_{11}\}$ subunit consists of a ring of six basal W positions and another W in the center of this ring, the other four W atoms are located on apical positions. Each W site of $\{W_{11}\}$ and $\{W_1\}$ has a distorted octahedral geometry (Figure 25). The cluster cavity is lined by six WO_6 moieties which map exactly the contour of the 18-crown-6 cavitand. Based on this, Cronin investigated the host-guest chemistry of $\{W_{36}\}$ with different alkali and alkaline earth metals. Single crystal X-ray diffraction of the compounds with $\{Rb@W_{36}\}$and$\{Sr@W_{36}\}$ showed the central cavity incorporates Rb^+ and Sr^+ at full occupancy. However, for $\{Cs@W_{36}\}$ the central site is not fully occupied by the cesium ion, while additional electron densities were found and assigned to *outer* Cs positions between two $\{W_{11}\}$ subunits. The central guest position can also be occupied by an ammonium cation, bound to the cavity through electrostatic interactions and hydrogen bonding. These complexes demonstrate that the $\{W_{36}\}$ anion can act as inorganic "crown ether", but in this case, high selectivity could be expected mainly due to the rigidity of the inorganic backbone. However, the Cronin report suffers from the lack of any solution studies, necessary to get relevant insights about the receptor properties of the $\{W_{36}\}$ species.[64]

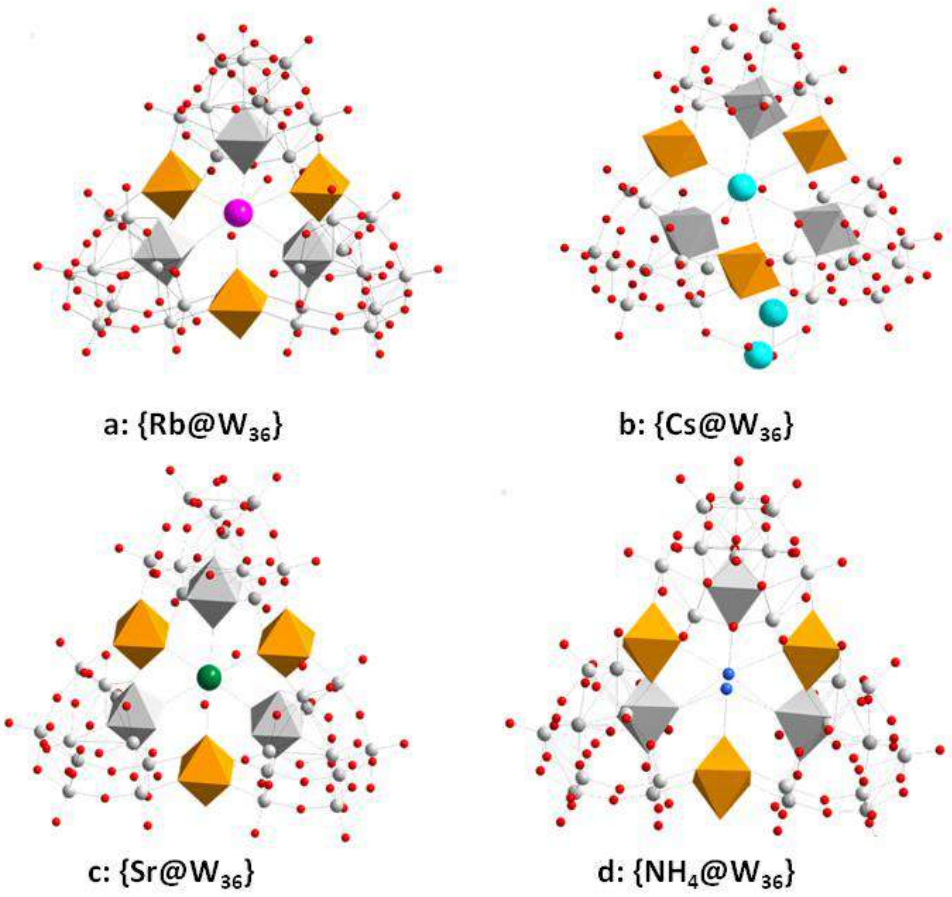

Figure 25: Representation of W_{36} complexed with different cations. Color schema: $\{W_{11}\}$cluster, gray polyhedral; $\{W_1\}$cluster, orange polyhedral; Rb, pink; Cs, tourqoise; Sr green; N,blue .

Another example of POM-based crown is the macrocyclic $[H_7P_8W_{48}O_{184}]^{33-}$ anion (noted $\{P_8W_{48}\}$, able to encapsulate various transition metal or alkali metal ions in the central crown-shaped cavity of about 1 nm in diameter. There are numerous recent literature examples such as the copper-containing $[Cu_{20}\text{-}X(OH)_{24}(H_2O)_{12}(P_8W_{48}O_{184})]$ species (X= Cl^-, Br^-, I^-) (Figure 26) reported by Kortz *et al.* [65] Structural analysis showed that the oxo-groups lining the cavity of the $[H_7P_8W_{48}O_{184}]^{33-}$ backbone do actually interact with transition-metal ions in aqueous medium. The encapsulation process have been extended to other transition metals e.g., Co^{2+}, Mn^{2+}, Ni^{2+},V^{5+} and organoruthenium-based complexes.[66] In this context, Floquet *et al* . reported on the integration of two $[Mo_4O_4S_4(OH)_2(H_2O)_3]^{2+}$ units acting as handles on the surface of the $\{P_8W_{48}\}$ ion.[67] A detailed description of this compound will be given in chapter IV.

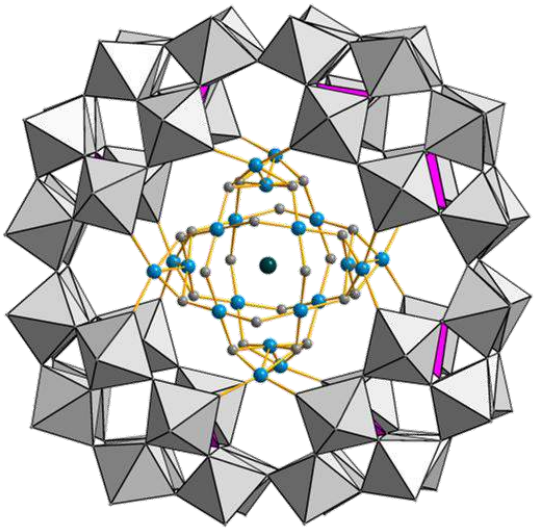

Figure 26: Combined polyhedral ball-and- stick representation of $[Cu_{20}\text{-}Br(OH)_{24}(H_2O)_{12}(P_8W_{48}O_{184})]^{25-}$ Color code: W, gray(polyhedral); P, pink; O, gray; Cu, turquoise; Br, green.

III.2 POM-capsule as multireceptors

Muller *et al.* demonstrated interesting supramolecular inorganic chemistry by structural investigation of the highly charged cluster $[H_3Mo_{57}V_6(NO)_6O_{183}(H_2O)_{18}]^{21-}$ as a mixed ammonium-potassium salt. The cluster is made up of three large $\{Mo_{17}\}$ fragments linked by six vanadium (V^{IV}) centers and three $\{Mo^{V}_{2}\}$ type units. The geometry of the cluster generates external holes able to bind positively charged species (Figure 27).[68] The interesting result is that two $\{Mo_3V_3O_6\}$ crown-ether-like pores and the functional groups of the six external holes of the cluster can interact differently with potassium and ammonium ions. Three different sites discriminating for the K^+/NH_4^+ cations are shown in Figure 27. The first one involves the $\{Mo_3V_3O_6\}$ pores which are occupied by ammonium cations, interacting through O···H-N hydrogen bonds (Figure 27a). It can be worth noting that the N···O distances reveal to be similar to those observed in the related ammonium-[18]crown-6 host-guest species. The second type of positions involves the three equatorial positions occupied by potassium ions (Figure 27b). Each cation is coordinated to four symmetry-equivalent terminal oxygen atoms of two neighboring $\{Mo_{17}\}$ units, which leads to the formation of two $\{K@Mo_4O_6\}$ crown-ether-like complexes. Finally, additional NH_4^+ ions were found slightly above the six $\{Mo_4VO_6\}$ rings. These ammonium ions interact with four bridging and two terminal oxygen cluster atoms through hydrogen bonds (N···O=3.14–3.28 Å; Figure 27).[57]

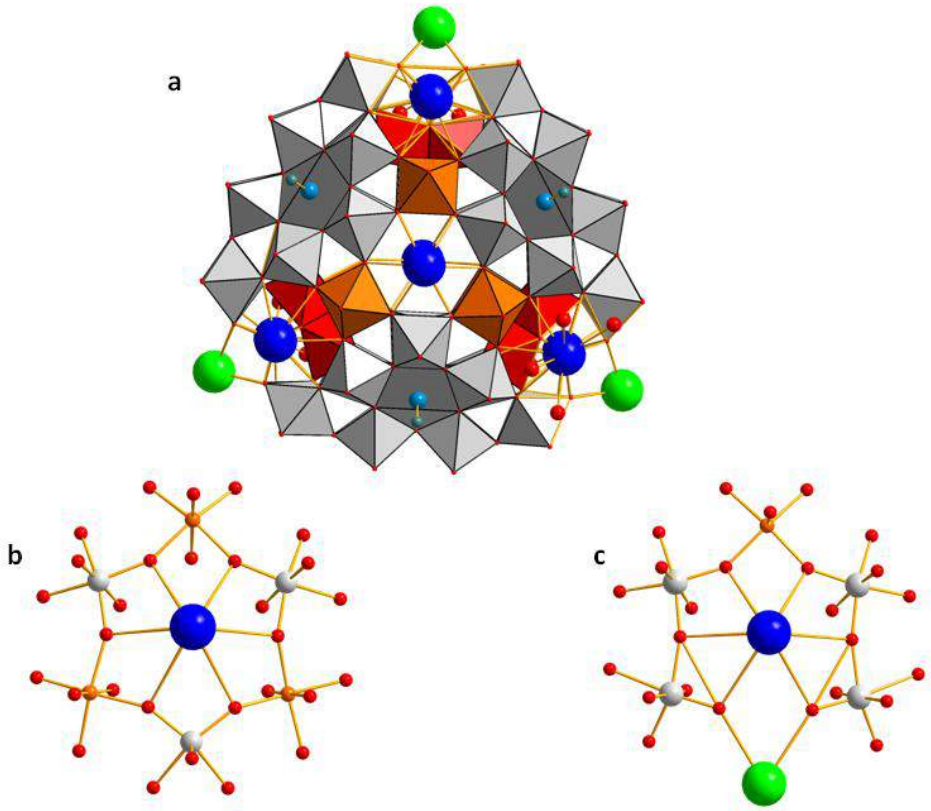

Figure 27: a) Polyhedral ball-and-stick representation of $(NH_4^+/K^+)@[H_3Mo_{57}V_6(NO)_6O_{183}(H_2O)_{18}]^{21-}$. b) Ball-and-stick representation of $\{Mo_3V_3O_6\}$ pore containing an ammonium cation. c) $\{Mo_4VO_6\}$ rings formed by four skeletal bridging and two terminal oxygen atoms linked to Mo and V centers. N···O distances: 3.14–3.28 Å. Color code: $\{Mo_{17}\}$ units, gray polyhedral; $\{Mo_2\}$ groups, red polyhedral; VO_6 orange polyhedral; K, green; N, blue.

Cadot *et al.* reported the discoid-type $[\{Mo_{17}O_{52}(OH)_4(H_2O)_6\}_3\{Mo_2O_2S_2(H_2O)_2\}_6]^{6-}$ cluster (abbreviated as $\{Mo_{63}S_{12}\}$ hereafter) which is structurally related to the previously described cluster $[H_3Mo_{57}V_6(NO)_6O_{183}(H_2O)_{18}]^{21-}$ anion where both arrangements share the same $\{Mo_{17}\}$ building blocks. However, the main difference between both clusters corresponds to the presence of six $\{Mo_2O_2S_2\}^{2+}$ linkers in the $\{Mo_{63}S_{12}\}$ instead of the six $\{V^{IV}O\}^{2+}$ groups.[69] The presence of the longer $\{Mo_2O_2S_2\}^{2+}$ linking groups in the cluster results in the expansion of the active anionic pockets, allowing in turn to exciting supramolecular properties with tetramethylammonium cations. X-ray diffraction analysis reveals the presence of two types of environment for NMe_4^+ within the cluster. The first one include three NMe_4^+ ions occupying the three peripheral pockets, that is outlined by two neighboring $\{Mo_{17}O_{52}(OH)_4(H_2O)_6\}$ building blocks. Each interaction site is formed by the terminal oxygen and the external sulfur atoms of the $\{Mo_2O_2S_2(OH_2)_2\}$ and only weak host-guest interactions have to be considered due to the quite long distances between methyl C atoms and POM's oxo groups (C-O = 3.88-3.56 Å). The second type involves a single NMe_4^+ ions encapsulated within the central cavity close to one water molecule. Three methyl groups of

this central NMe_4^+ cation are positioned at the bottom of the cavity (Figure 28) and interact with the terminal oxo group through weak hydrogen bonding and stronger electrostatic interactions. The remaining methyl group, oriented toward the center of the cavity, is located close to the inner water molecule as an interesting ion-dipole cluster $\{NMe_4^+\text{-}OH_2\}$. The presence of the integrated NMe_4^+ cations has also been confirmed by multi-^{1}H NMR spectroscopic experiments which will be highlighted in Chapter II.

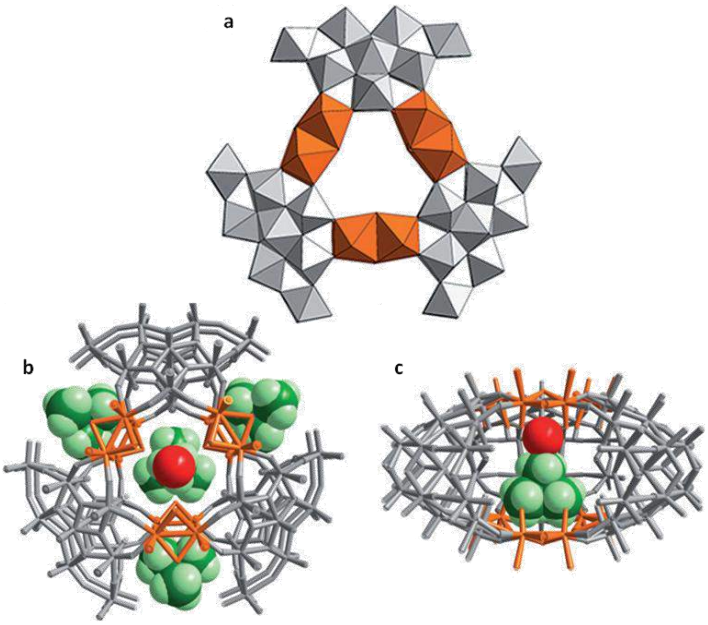

Figure 28: a) Polyhedral representation of $\{Mo_{63}S_{12}\}$ showing the three $\{Mo_{17}\}$ building(gray polyhedral) and six $\{Mo_2O_2S_2\}^{2+}$ linkers(orange polyhedral). b) The central pocket containing one NMe_4^+ cation (green spheres) and a water molecule (red sphere), and the three peripheral pockets with trapped NMe_4^+ cations. b) Side view focusing on the central $\{NMe_4^+\cdots OH_2\}$ ion-dipole arrangement. Reproduced from reference [69].

Large polyoxometalates such as Keplerate-type capsule provide ideal frameworks to extend the idea of "super-supramolecular chemistry" due to the presence of accessible inner channel and flexible crown-ether-types pores. It is possible to change the capsule's basic properties as the charge, the hydrophobicity or hydrophilicity by changing the internal anionic ligands or inorganic one. This can be achieved by changing the corresponding acid used in the one-pot synthesis method [51, 70] or by post-functionnalization procedures based on chemical exchange of a variety of ligands such as carboxylates,[54] carbonates,[71] sulfates [72] . The studies of the substitution of the 30 inner acetate ligands in $\{Mo_{132}\text{-}Ac\}$ by various organic substrates demonstrate the great flexibility of these $\{Mo_9O_9\}$ pores capable to exchange bulky substrates. All these multi-scale properties offer various interesting options for the investigations of the Keplerate-type capsule as "polytopic supramolecular multireceptors"

Muller *et al.* investigated the host-guest chemistry of the Keplerate capsules using different cations. An important result was found in the case of the smaller keplerate capsule $\{W_{72}Fe_{30}\}$ cluster where the 20 crown ether type $\{Fe_3W_3O_6\}$ pores are plugged by 20 NH_4^+ ions through hydrogen bonds. X-ray diffraction analysis showed that the NH_4^+ cations are fixed in the planar $\{Fe_3W_3O_6\}$ pores by the formation of N-H···O hydrogen bonds (N···O ca. 3.1 Å) comparable to those found within the [18]crown-[6] ligands.[73]

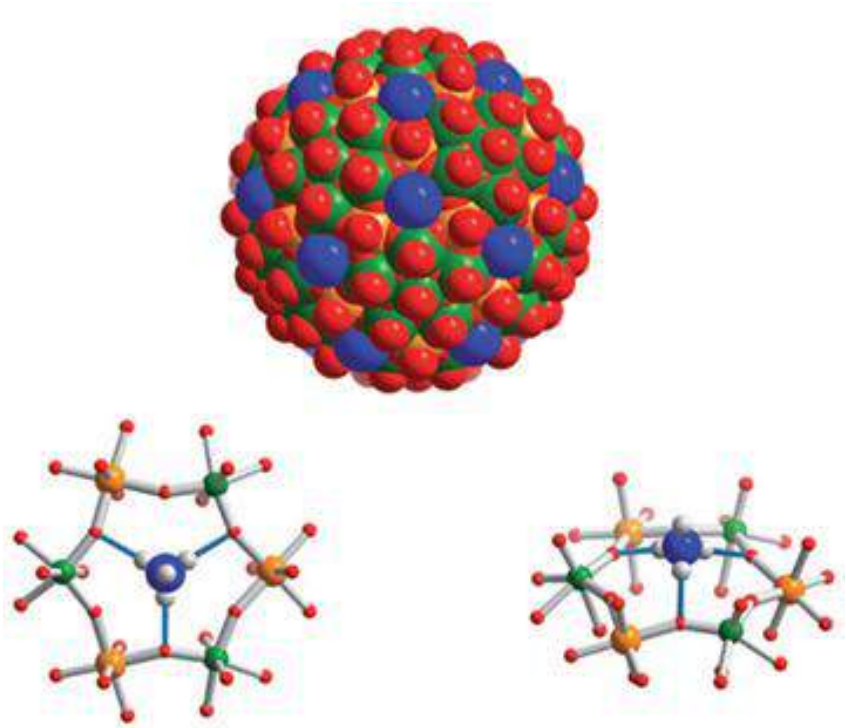

Figure 29: Top: Space-filling of NH_4^+@$\{W_{72}Fe_{30}\}$ highlighting the complementarity between the $\{Fe_3W_3O_6\}$ pores and the NH_4^+cation. Bottom: Two views of the pores situation (N blue, H light gray, Fe orange,W green, O red). Reproduced from reference [69].

Similarly, Műller *et al.* demonstrated that the 20 $\{Mo_9O_9\}$ pores of the $\{Mo_{132}\}$-type capsules have the appropriate size to be plugged noncovalently by organic guests such as guanidinium cations. The reaction of the $\{Mo_{132}$-sulfate$\}$ capsule with guanidinium sulfate allows the isolation of dark-brown crystals. X-ray diffraction study reveals that the guanidinium cations $[(NH_2)_3C]^+$ fit perfectly into the $\{Mo_9O_9\}$ pores, interacting with the bridging oxygen atoms of the binuclear $\{Mo_2\}$ units, through hydrogen bonds.[74] By the same way, this plugging process was extended to other cations such as formamidinium cations and protonated urea, showing that both interact similarly with the pores through hydrogen bonding.[75] It is worthy to mention that all these studies of the plugging process were done in the solid state using the X-ray diffraction structures, thus giving no quantitative information about the strength of these host-guest interactions in solution.

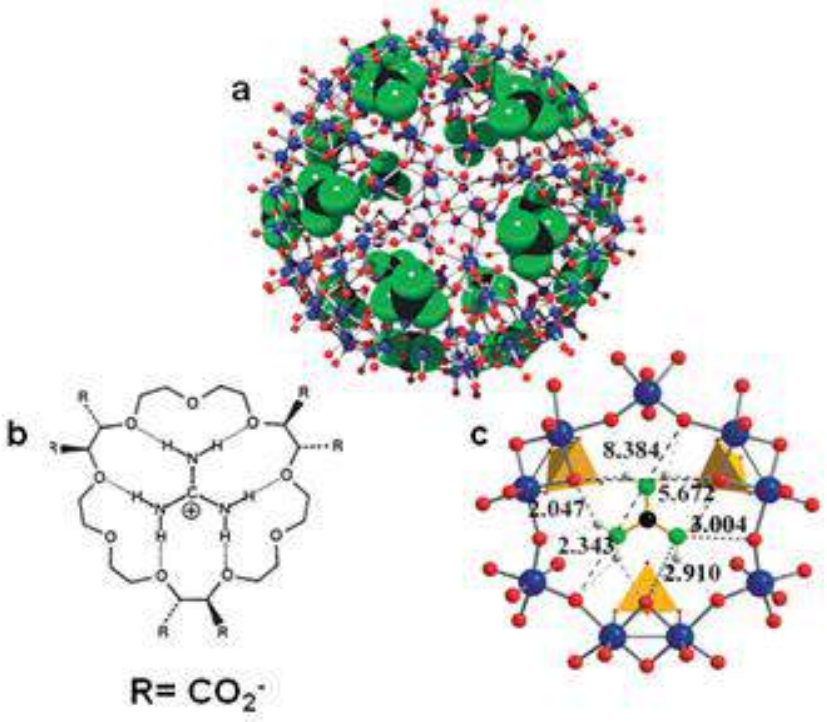

Figure 30: a) Top: $[\{(NH_2)_3C^+\}_{20}@\{Mo_{132}\}$ capsule. Bottom: Comparison of two receptors with the same guanidinium cation guest, (a) $GuaH^+$ with the [27]-O_9 macrocyclic polyether and (b) $guaH^+$ with one of the 20 $\{Mo_9O_9\}$ pores of the $\{Mo_{132}\}$ Keplerate ion. (colour code: Mo blue, O red, C black, N green, and $\{SO_4^{2-}\}$ ligands yellow tetrahedra). Reproduced from reference [45].

III.3 Cation-POM interactions in action

The study of the interactions between the counterion and POM ions is still a point of interest for a lot of chemists. In his famous book, Pope noticed that some POMs exhibits some special binding sites able to develop strong interactions with counterions. By electrochemical studies, Weinstock and co-workers observed that close ion pairing exists in dilute solutions for Keggin anions.[76] Recently, Bo *et al.* used molecular dynamics simulations to reveal direct contact ions pairing between monovalent cations and Keggins in more concentrated solutions,[77] while Antonio *et al*. confirmed experimentally ions pairing contact between the Lindqvist POM $[Nb_6O_{19}]^{8-}$ ion and monovalent counterions in aqueous solution.[78]

III.3.1 Direct measurement of Contact ion pairing in aqueous solution

In this work, Antonio *et al.* show that small angle X-ray scattering measurements (SAXS) of the Lindqvist $[Nb_6O_{19}]^{8-}$ ion in aqueous solution provides models for the ion pairs formation in aqueous solution.[78] The results of calculations on the atomic small-angle X-ray scattering (SAXS) intensities Ia (Q) versus the magnitude of the scattering vector Q ($Å^{-1}$) show that the calculated radius of gyration Rg for the 25-atom bare cluster anion, $[Nb_6O_{19}]^{8-}$ is 3.0 Å and that for the $8A^+$ ion-paired neutral clusters, $A_8[Nb_6O_{19}]$, are 3.5 , 3.6 and 3.6 Å for A=Rb, Cs

and K, respectively. The average experimental Rg values were obtained by fitting the SAXS data of three series of solutions constituted of the potassium, rubidium, and cesium $[Nb_6O_{19}]^{8-}$ salts dissolved either in 3M tetramethylammonium hydroxide (TMAOH) solution or in their corresponding 3M alkali metal hydroxide (AOH, A= K, Rb, Cs) media. In TMAOH solutions, in which the A^+ ions are diluted relative to the TMA cation, the experimental R_g radii are consistent with the value calculated for the bare anion (3.0 Å) showing that in such conditions, no direct anion-cation contact. On the other hand, in AOH solutions with large excess in A^+ ions, the experimental Rg values are equivalent to the Rg radii calculated for direct ion-paired $A_8[Nb_6O_{19}]$ species in the solid state (3.5–3.6 Å). The fair agreement between the calculated and experimental results provides direct evidence for contact ion pairing in aqueous solution between the hexaniobate and alkali metal ions.[78]

III.3.2 Self assembly in dilute solution : Blackberry formation

Giant polyoxometalate macroions demonstrate unique solution behaviors as they behave differently from small simple ions (as described by the Debye-Huckel theory) because the macroions cannot be treated as point charges or large, insoluble colloidal suspensions. Instead, they tend to self-assemble into single-layered, hollow, spherical "blackberry" structure. The most important point is the driving forces behind the assembly process which bring the like-charged macroions together and overcome the electrostatic repulsion. In attempt to understand this intriguing phenomenum, Tianbo liu did a simple experiment where the formation of blackberries was studied as function of solvent mixture. The important result showed that the $\{Mo_{132}\}$ blackberries were detected in 1.0 mg mL^{-1} water–acetone mixed solvents containing 3–70 vol% acetone (see Figure 31).[79] However, only discrete $\{Mo_{132}\}$ clusters were found in solutions for *out of range* solutions i.e. containing < 3 vol% or >70 vol% in acetone. In these limit solutions, the high or low charge density of the discrete macroanions cancels the formation of the blackberry aggregates.[79] This result confirms the importance of the charge density upon the blackberry formation and rules out the contribution of the van der Waals interactions as unique driving force for the blackberry formation. As the water content increase, the effective charge density of the macroions increased, which should increase the electrostatic repulsion between individual $\{Mo_{132}\}$ macroanions. Strikingly, this is precisely in these conditions that the macroions self-assemble to form blackberry Thus the behavior of the $\{Mo_{132}\}$ capsule in water/acetone solutions exemplifies that the role of the counter ions in solution is of prime importance in the solution behavior of the macroions and

that the blackberries formation should arise from a subtle balance between electrostatic and van der Waals interaction involving solvent and the POM surface.

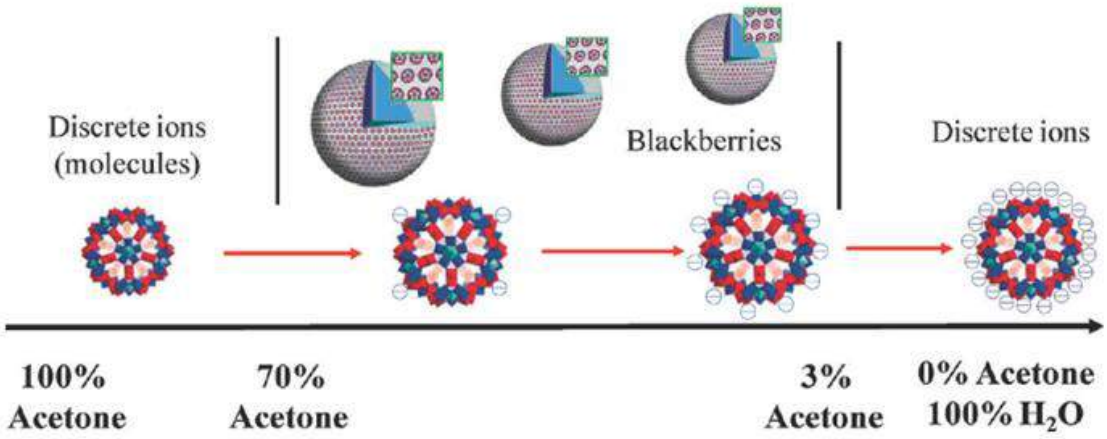

Figure 31: Transition from discrete macroions (molecules) to blackberries, then to discrete macroions due to the change of solvent content for $\{Mo_{132}\}$ in water–acetone mixed solvents. Reproduced from reference [79].

There are several ways of tuning the blackberry size. Cationic surfactants with long alkyl chains can interact with macroanions stoichiometrically and therefore be used to decrease accurately the effective charge at the surface of the macroion. The $\{Mo_{72}V_{30}\}$ cluster does not show self-assembly behavior in dilute aqueous solution, probably due to its high charge density, favoring the anion-anion electrostatic repulsions.[80] Introducing a small amount of water-soluble cationic surfactants, such as cetyltrimethylammonium bromide (CTAB), trimethyltetradecylammonium chloride (CTAT), dodecyltrimethylammonium bromide (DTAB) or octyltrimethylammonium bromide (OTAB) leads to decreasing of the charge density of macroions allowing blackberry formation (Figure 32).[80]

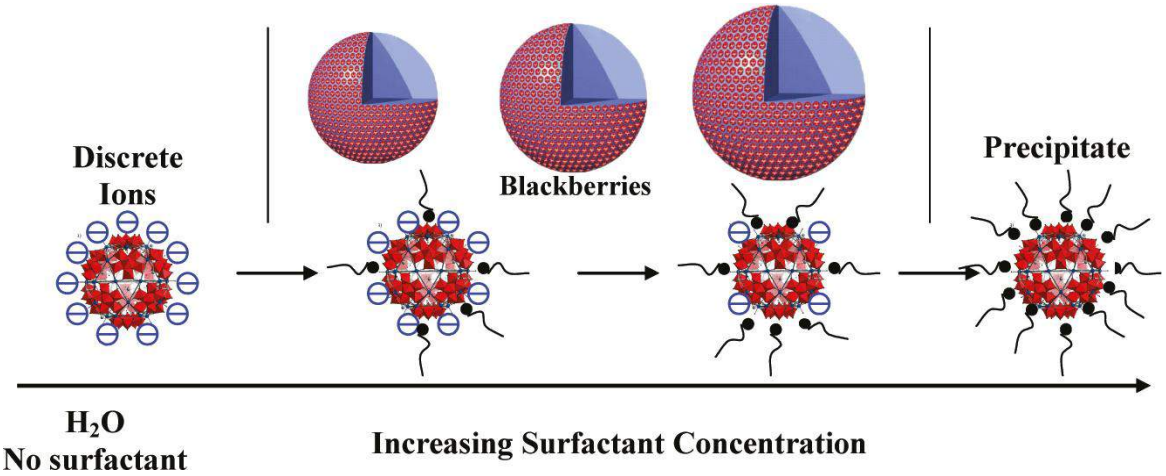

Figure 32: Blackbeery formation of $\{Mo_{72}V_{30}\}$ cluster upon gradual introducing of alkyltrimethylammonium halide cationic surfactants. Reproduced from reference from reference [80].

So, such solution behaviors allow to state that such amphiphilic couterions are not completely free in the solution but rather closely associated with the macroions. Such associations should shield partially the negative charges of the macroions and thus should originate a couterion-mediated attraction between macroions.

III.3.3 Templating effect through ion-pairing

Counter cations through their weak electrostatic interactions with POM clusters seem to be not silent and can have an "active" influence upon the self-assembly process. Depending on the nature of the counter cations and the ionic strength, different architectures can be obtained using lacunary polyoxometalates and the $[Mo_2O_2S_2]^{2+}$ linker as building blocks. In this respect, *Cadot et al* reported the formation of three different modular architectures such as hexamer, tetramer, and dimer based on the common trivacant ligand $[B\text{-}AsW_9O_{33}]^{9-}$(denoted POM) and the ditopic cation $[Mo_2O_2S_2]^{2+}$ (denoted L). This series of clusters $\{POM_6L_9\}^{36-}$, $\{POM_4L_6\}^{24-}$ and $\{POM_2L_3\}^{12-}$ display the same stoichiometry however their conditions of formation differ mainly by the nature and the concentration of the alkali-metal cations (from Li^+ to Cs^+) (Figure 33).[35]

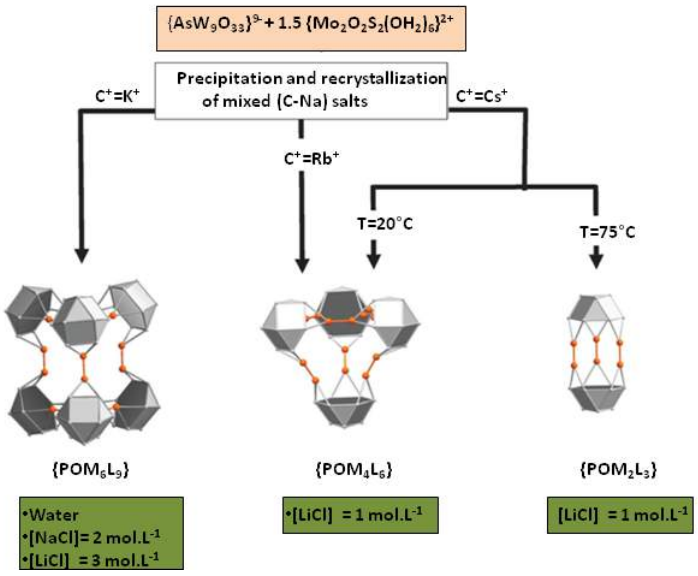

Figure 33: Schematic view of the conditions of formation of the anions $\{POM_2L_3\}$, $\{POM_4L_6\}$ and $\{POM_6L_9\}$ with POM =$\{AsW_9O_{33}\}$ and L = $\{Mo_2O_2S_2\}$. Reproduced from reference [35].

To get a better understanding of the effect of the counterions upon the self-assembling process, the ''angle of approach'' between the reactive units has been considered. It corresponds to the angle between the two vectors representing the orientation of the $\{Mo_2O_2S_2\}$ linkers and that of the POM subunit, respectively. The $\{Mo_2O_2S_2\}$ linker is defined by a vector crossing both the Mo atoms and along the Mo–Mo bond, while the POM

ligand is characterized by a vector normal of the plane delimited by the six crown oxygen atoms as shown in (Figure 34) .

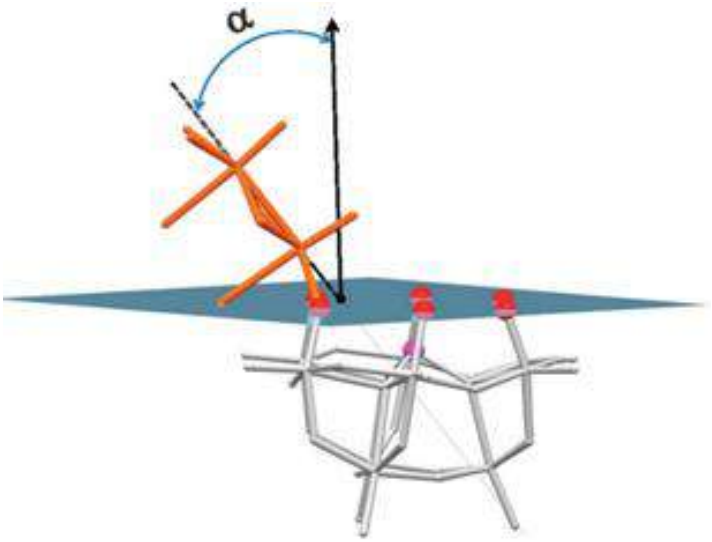

Figure 34: Schematic view showing the angle of approach a between the linker $\{Mo_2O_2S_2\}$ and the vector normal of the plane delimited by the six crown oxygen atoms of the POM ligand. Reproduced from reference [35].

The largest cations (Rb^+ and Cs^+) associated to weak ionic strength induce the closure of the angle observed for the tetra- and dimodular species. For the dimer, the three α angles are equivalent and close to zero while they are significantly opened for the tetramodular arrangement, α = 35.2 ± 2°, close to the idealized value of 35.3°. However, for polarizing cations with smaller ionic radius, such as Li^+, Na^+ and K^+, electrostatic interactions within the ionic aggregate should induce some steric congestions in the vicinity of the coordinating centres leading to large angles of approach and to higher modularity arrangement such as found in the hexameric$\{POM_6L_9\}$species.[35]

III.3.4 Investigation of the plugging process of capsule pores through uptake/ transport of cations of in solution

The $\{Mo_{132}\}$ capsule can be regarded as artificial inorganic cell where it can transport cations as Li^+ from the bulk solution into the cavity. It has been shown that internal Li^+ ions can be replaced by adding Na^+ and K^+ ions, and completely by Ca^{2+} ions (see Figure 35).[81] Such cation uptake/release can be controlled by pore closing/opening thus offering a nice proof for the host-guest interaction in solution involving the 20 pores of the host.

Li^+ ion uptake/release processes have been investigated for the capsule$[(CH_3)_2NH_2]_{44}Li_{28-n}$ - $[Li_nMo_{132}O_{372}(SO_4)_{30}(H_2O)_{72}]$ (noted **1**) by means of ^7Li NMR spectroscopy with DMSO as solvent. The NMR measurements at room temperature show one sharp signal at ∂ = -1 ppm

attributed to solvated Li cations, and two broad resonances centered at ∂ = -1.67 and -3 ppm attributed to Li^+ ions located on different inner sites (Figure 35). Addition of increasing amounts of formamidinium hydrochloride to a solution of **1** in DMSO results in the suppressing of the Li^+ exchange processes which is finally blocked when the 20 pores are closed (Figure 35a).[82]

Furthermore, variable-temperature NMR experiments reveal that temperature increase of solution of **1** leads to coalescence of the ^7Li NMR resonances until the final disappearance of all the upfield peaks at T = 343 K (Figure 35), indicating a variety of fast exchange processes between the different Li^+ species at the different sites. However in the presence of formamidinium cations, the coalescence process is totally blocked up to 363 K (see Figure 35b) thus giving a nice evidence that formamidinium cations act as appropriate plugs for the capsule and then cancel any exchange between the interior and the exterior of the $\{Mo_{132}\}$ capsule.

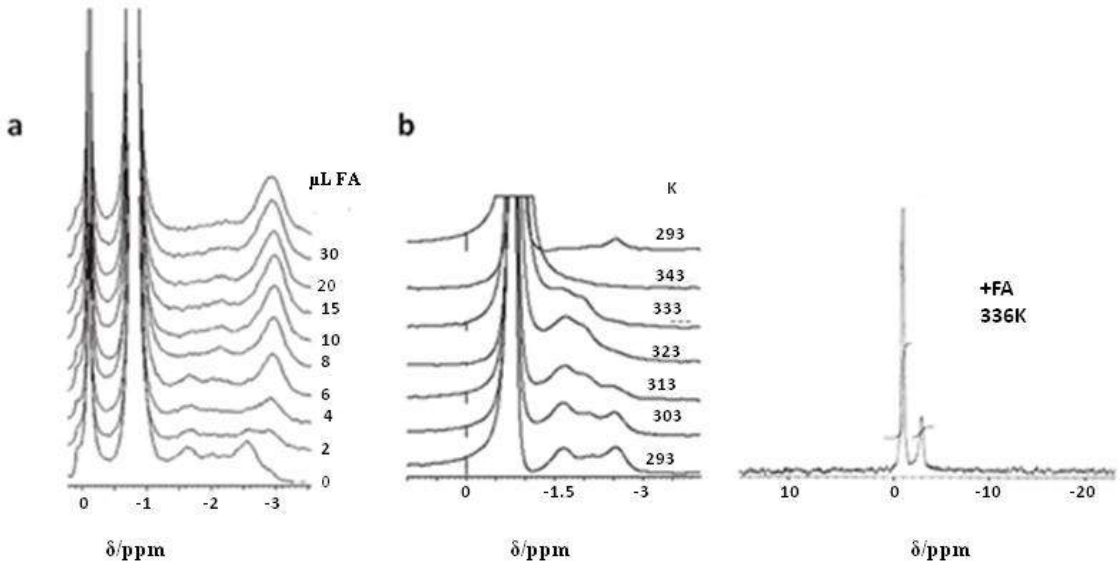

Figure 35: a) ^7Li NMR spectra of $[(CH_3)_2NH_2]_{44}Li_{28-n}$ -$[Li_nMo_{132}O_{372}(SO_4)_{30}(H_2O)_{72}]$ in DMSO measured after the addition of increasing amount of formamidinium hydrochloride (FA). b) Left: ^7Li NMR spectra of $[(CH_3)_2NH_2]_{44}Li_{28-n}$ -$[Li_nMo_{132}O_{372}(SO_4)_{30}(H_2O)_{72}]$ in DMSO upon heating. Right: spectrum measured at 336k after addition of FA. Reproduced from reference [82].

Nevertheless, such qualitative experiments need quantitative data about the relative efficiency/affinity of the plugs and this is quite challenging to investigate deeply this plugging process and to provide quantitative information about the strength of this host-guest interaction, especially required for a better understanding of the capsule in action either for cation transport or catalysis under confined conditions.

IV. Hybrid Surfactant systems with inorganic constituents.

Amphiphilic molecules are one of the advanced technological materials with wide spread applications and properties. The most important properties of amphiphiles are certainly due to their surfactant behavior surfactants which are characterized by a unique antagonist combination, that is, an ionic (or polar) and water-soluble head group attached to a hydrophobic alkyl tail. The tendency of surfactant to alter the interface energy by minimizing the water-alkyl and and by maximizing the water-head group interfaces is at the origin of their well-known self-organization processes ranging from micelles to lyotropic phases and depending on wide variety of parameters such as concentration, molecular structure of surfactant, presence of additives, concentration, solvent….[83]

Practically, most of the surfactant systems are organic in nature with commonly ammonium head group. However, it is of great importance to prepare surfactant with alternative head-group having multicharge, redox-active, magnetic or catalytic properties as those of transiton metals. A lot of examples for metal-containing amphiphiles are already reported and can be considered to belong to the field of metallomesogenic systems. In this context, Molard *et al.* obtained clustomesogens compounds possessing switchable magnetic/luminescence properties by combining the cluster $[Re_6Se_8(CN)_6]^{n-}$ (n = 3, 4) with tetraalkylammonium cations functionalized with cyanobiphenyl groups.[84] POMs with their diverse properties are also relevant candidates to move these hybrid to higher levels of complexity.

D. G. Kurth and D. Volkmer were among the first to associate POMs with cationic surfactants to give discrete surfactant encapsulated clusters (SECs).[85] Generally, Surfactant Encapsulated Clusters (SECs) can be prepared according to two different methods: through single-phase co-precipitation, or through a two-phase ion-exchange process. The surfactant shell improves the stability of the polyoxometalate and increases the solubility of POMs in non polar and aprotic solvents. In this section we will focus on the hybrid materials based on cooperative electrostatic interactions between anionic POM and cationic surfactants.

Due to the structural diversity of POMs and surfactants, the self assembling behavior of SECs include numerous diverse aggregation structures. Lixin Wu reported that introduction of DODA into polyoxometallates such as the $[Eu(H_2O)_2SiW_{11}O_{39}]^{5-}$ species or the Keggin α-$[SiW_{12}O_4]^{4-}$ ion forms hybrid materials which aggregate into remarkable stable onion-like vesicles in organic solvents such as chloroform (Figure 36).[86] However, XRD experiments showed these assemblies fused into layers during the solvent evaporation to form lamellar

structures sandwiching POMs moieties between organic layers. Introducing the DODA cation into giant {Mo_{132}-acetate} or {Mo_{132}-sulfate}[87] lead to discrete and nearly core-shell spherical assemblies. Nevertheless, these SECs do not rearrange into layered structures but maintain their core–shell structure in the spherical assemblies. This may be due to the large 3 nm diameter of the Mo_{132} nanocapsule which is much larger than the 1.9 nm length of the DODA ions. In such cases, the {Mo_{132}} capsules should enable to drive the self-assembly process and then to break off the tendency of the DODA alkyl chains to form usual layered stacking arrangements.

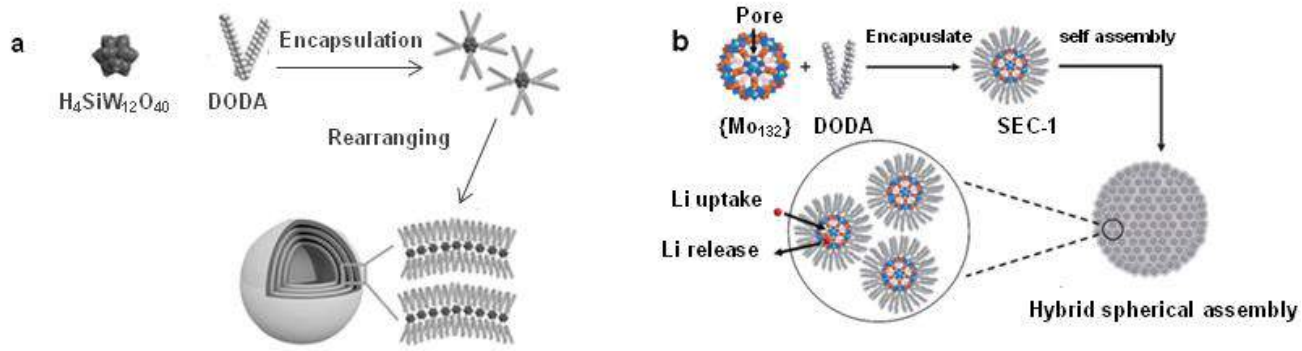

Figure 36: a) Assembly mechanism of $(DODA)_4SiW_{12}O_{40}$ and formation of onion like vesicles. b) Schematic illustration of the fabrication of SEC-1 assemblies, including an electrostatic encapsulation process and a polarity induced self-assembly process. Reproduced form reference [86] and [87].

In 2001, Polarz *et al.* examined the Mo_{176}-surfactant complexes. This system was considered as remarkable because TEM and SAXS experiments revealed 3D SEC superstructures consisting of hydrophilic POM cores and hydrophobic shells where the surfactants interact only at the periphery of the inorganic clusters.[88] In the same context, Cronin et al. demonstrated that encapsulation of Mo_{154} with DODA cations provides SEC material with interesting sorption properties of N_2 and CO_2 gases as well as catalytic properties (Figure 37).[89]

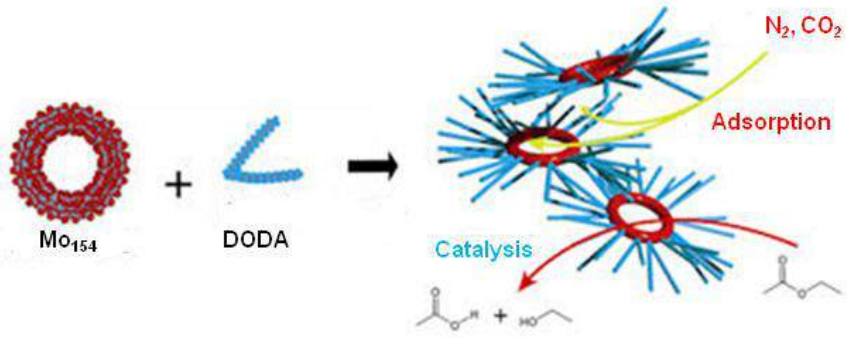

Figure 37: Protection of {Mo_{154}} ring by DODA cations and illustrating of the sorption process as well as catalytic reaction of the {Mo_{154}}-DODA system. Reproduced from reference [89].

The self-assemblies of these POM-surfactant associations are also capable to form stable and homogenous Langmuir–Blodgett (LB) films,[90] as reported by a lots of groups. We can mention Kurth *et al.* who reported stable LB films containing SECs, such as DODA-{$Mo_{57}V_6$}, DODA-{Mo_{132}}[91] and DODA-{Mo_{142}}.[92] Kortz prepared stable monolayers at the air-water interface with combinations of DODA and the {$Cu_{20}P_8W_{48}$} cluster (Figure 38).[93] As a common feature, these LB films are characterized by well-ordered lamellar structures.

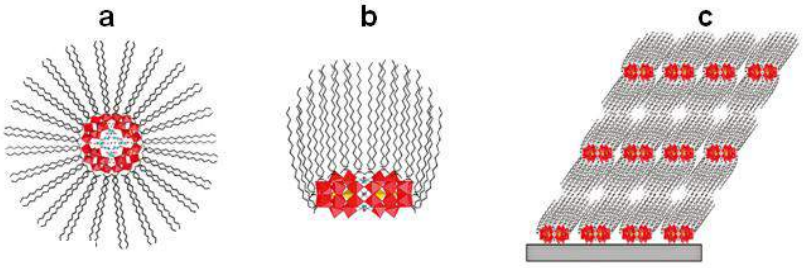

Figure 38: Schematic drawing of DODA-{$Cu_{20}P_8W_{48}$}. a) Core-shell structure in the solid state, b) arrangement at the water-air interface in the monolayer and c) packing structure of the LB film. Reproduced from reference [93].

In 2012, Bu *et al*. presented a novel organic-inorganic hybrid materials described as a POM-based star polymers (PSP). They fabricated PSP by encapsulation of a keplerate anionic core with 11'(N,N,N-trimethylammonium) undecanylisobutyrate terminated poly(styrene) (S_n^+, Br^-) with (n= 124, 169, 218, 290) chains stabilized by electrostatic interactions. Analysis of the BF-TEM, HAADF-STEM and EDX experiments allow to propose the picture presented in Figure 39 for the formed PSP structures: the S_n^+ chains were attached onto a keplerate core by electrostatic interaction where the inorganic cluster core was tightly encapsulated by a polymer chains, leading thus to spherical supramolecular structures.[94]

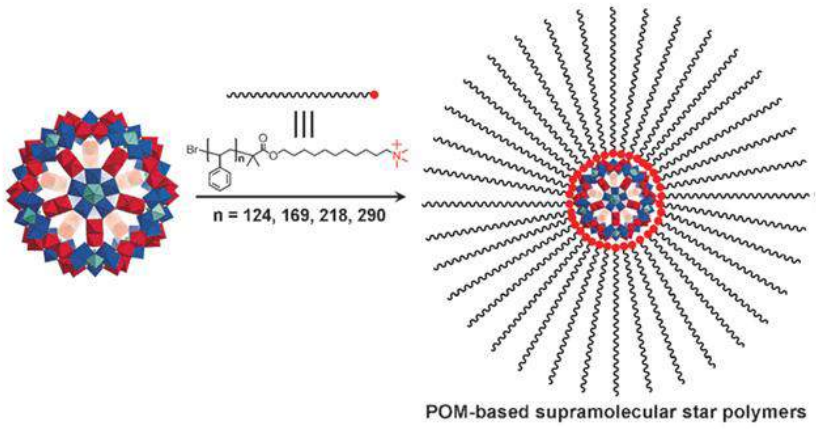

Figure 39: Schematic drawing of electrostatic combination of keplerate with cationic terminated poly(styrene). Reproduced from reference [94].

Surfactant- encapsulated Polyoxometalates towards a liquid crystal properties.

Liquid crystals are fascinating functional materials involved in many advanced technological applications such as low-power-consuming flat-panel displays (LCDs) which allowed the development of mobile data processing and communication. The unique feature of liquid crystal is that ordering develops while a high degree of mobility is retained, thus allowing to external stimuli-responsive behavior.

The work pioneered by Lixin Wu's group introduced a lot of examples of liquid crystalline behaviour in POM chemistry.[95-98] In 2005, Wu *et al.* introduced the $[Tb(SiW_{11}O_{39})_2]^{13-}$ species into LC surfactant matrix such as azobenzene-containing surfactant with the mesogenic group di[12-(4'-octyloxy-4-azophenyl)dodecyloxy]dimethyl-ammonium bromide (L1).[99] Such systems gave SECs with thermotropic liquid-crystalline behavior, fully studied by POM, DSC and XRD. DSC analysis revealed several phase transitions attributed to the formation of liquid crystal phases (Figure 40).[99]

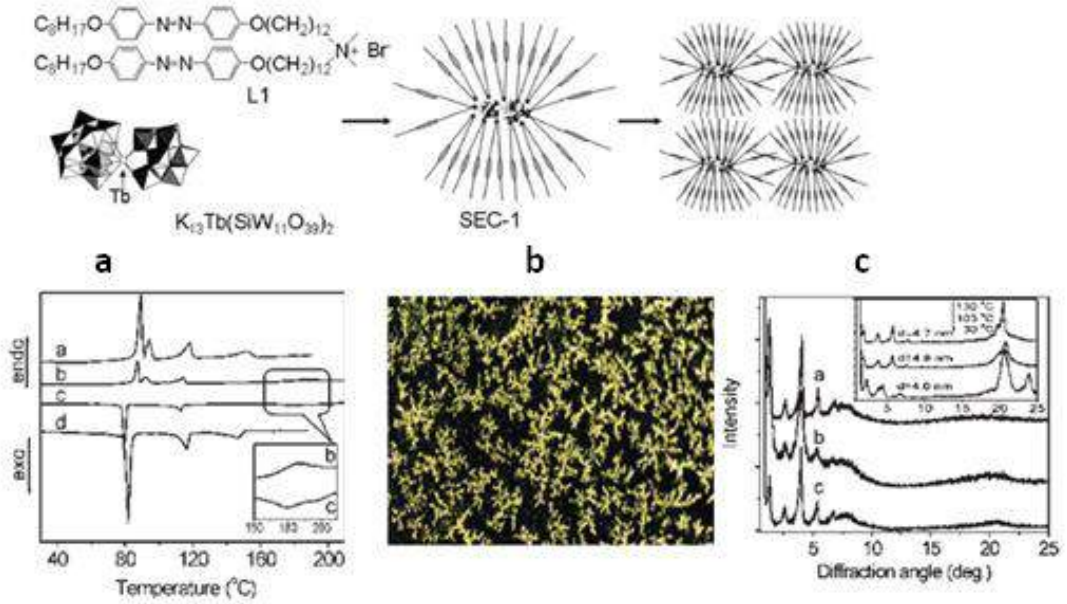

Figure 40: The schematic chemical structures of L1, PM-1, SEC-1 and proposed layered aggregates of SEC-1. DSC thermograms of SEC-1(a) POM of SEC-1 at 103°C. (b) Variable-temperature wide-angle X-ray diffraction (c). Reproduced from reference [99].

Wu *et al*. studied many POM/surfactant combinations varying systematically the length of the alkyl chain or the shape and charge density of the POMs. Analysis of the results shows that the shape of POM affects the overall packing arrangements. In case of elliptical cluster, lamellar structures are favored. Recently, Wu *et al.* demonstrated that the length of the alkyl chain affects also the self-assembly behavior where the encapsulation of α-$[SiW_{12}O_{40}]^{4-}$ with $[(C_nH_{2n+1})_4N^+]$ (n= 4, 6, 8, 10) shows that the shorter alkyl chain complexes tend to form

liquid crystalline phases with cubic supramolecular organization, whereas longer alkyl chains favor lamellar structures see Figure 41.[100]

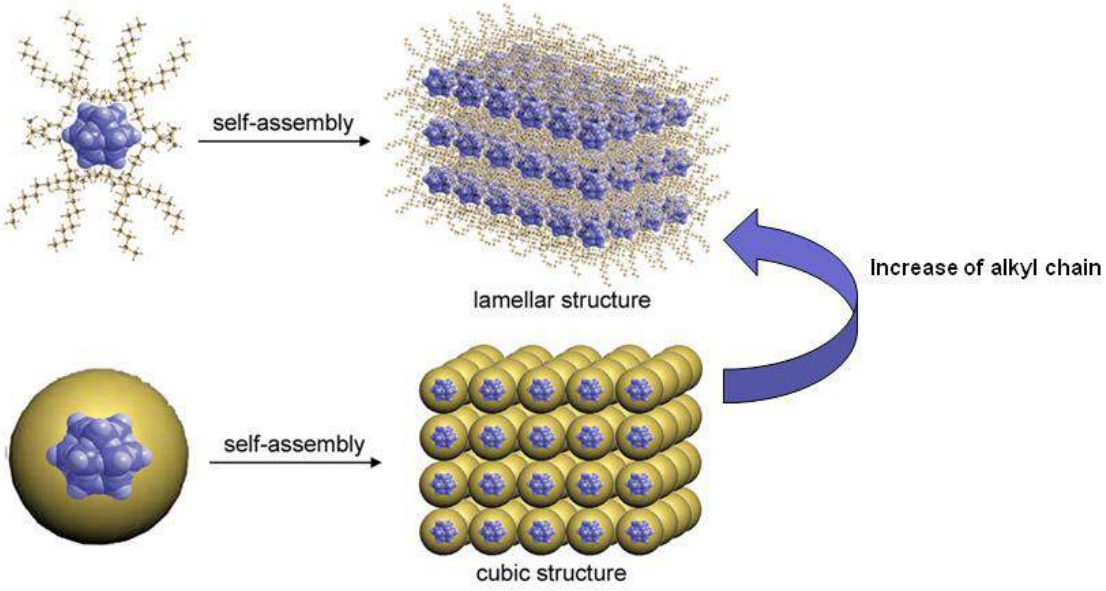

Figure 41: A schematic drawing of the self assembly of $[(C_nH_{2n+1})_4N]$-$[SiW_{12}O_{40}]^{4-}$ from a cubic to lamellar phase. Reproduced from reference [100].

V. Conclusion and outlook

Investigation and understanding the interactions of POMs with their cations is of critical signifiance from a fundamental point of view but also necessary to design POM-based systems relevant for further applications. Supramolecular host-guest chemistry of spherical Keplerate capsule is still unexplored, but as outlined above, many examples illustrate the plugging process of the 20 pores of the capsule only in solid state. Chapters 2-4 are aimed broadly at examining the fundamentals of the host-guest noncovalent interactions in $\{Mo_{132}\}$, using sophisticated NMR spectroscopy as DOSY to understand the driving force for such interaction. Then using such interaction to build POM-based supramolecular material with liquid crystals properties using simple cations for a better controlling and understanding of the self assembly process.

VI. References

[1] M. D. Pluth, K. N. Raymond, *Chem. Soc. Rev.* **2007**, *36*, 161-171.
[2] D. L. Caulder, R. E. Powers, T. N. Parac, K. N. Raymond, *Angewandte Chemie International Edition* **1998**, *37*, 1840-1843.

[3] D. H. Leung, D. Fiedler, R. G. Bergman, K. N. Raymond, *Angewandte Chemie International Edition* **2004**, *43*, 963-966.
[4] Z. J. Wang, C. J. Brown, R. G. Bergman, K. N. Raymond, F. D. Toste, *J. Am. Chem. Soc.* **2011**, *133*, 7358-7360.
[5] M. Fujita, K. Umemoto, M. Yoshizawa, N. Fujita, T. Kusukawa, K. Biradha, *Chem. Commun.* **2001**, 509-518.
[6] M. Yoshizawa, Y. Takeyama, T. Kusukawa, M. Fujita, *Angewandte Chemie International Edition* **2002**, *41*, 1347-1349.
[7] P. Gouzerh, M. Che, *Actual Chim.* **2006**, 9-22.
[8] J. M. Poblet, X. Lopez, C. Bo, *Chem. Soc. Rev.* **2003**, *32*, 297-308.
[9] N. Mizuno, K. Yamaguchi, K. Kamata, *Coord. Chem. Rev.* **2005**, *249*, 1944-1956.
[10] A. R. Gaspar, D. V. Evtuguin, C. P. Neto, *Ind. Eng. Chem. Res.* **2004**, *43*, 7754-7761.
[11] J. Berzelius, *Pogg. Ann. Phys. Chem.* **1826**, *6*, 369-380
[12] J. F. Keggin, *Proc. R. Soc. London, Ser. A* **1934**, *144*, 75-100.
[13] R. B. King, *Encyclopedia of Inorganic Chemistry, John Wiley & Sons: New York, , 6*, 1994.
[14] M. Hutin, M. H. Rosnes, D. L. Long, L. Cronin, in *Comprehensive Inorganic Chemistry II (Second Edition)* (Ed.: J. R. Poeppelmeier), Elsevier, Amsterdam, **2013**, pp. 241-269.
[15] A. Muller, E. Krickemeyer, J. Meyer, H. Bogge, F. Peters, W. Plass, E. Diemann, S. Dillinger, F. Nonnenbruch, M. Randerath, C. Menke, *Angew. Chem.-Int. Edit. Engl.* **1995**, *34*, 2122-2124.
[16] M. T. Pope, , *Heteropoly and Isopoly Oxometalates, Springer- Verlag, Berlin* **1983**.
[17] L. C. W. Baker, J. S. Figgis, *J. Am. Chem. Soc.* **1970**, *92*, 3794-3797.
[18] J. J. Borras-Almenar, E. Coronado, A. Müller, M. T. Pope, *Kluwer Academic Publishers, Dordrecht* **2003**, 33-54.
[19] A. Tézé, G. Hervé, *Inorganic Syntheses, John Wiley & Sons: New. York,* **1990**, *27*, 85.
[20] A. Müller, W. Plass, E. Krickemeyer, S. Dillinger, H. Bögge, A. Armatage, A. Proust, C. Beugholt, U. Bergmann, *Angew. Chem* **1994**, *125* 525-533.
[21] A. Müller, W. Plass, E. Krickemeyer, R. Sessoli, D. Gatteschi, J. Meyer, H. Bögge, M. Kröckel, A. X. Trautwein, *Inorg. Chim. Acta* **1998**, *271*, 9-12.
[22] T. B. Liu, E. Diemann, H. L. Li, A. W. M. Dress, A. Muller, *Nature* **2003**, *426*, 59-62.
[23] L.-H. Bi, U. Kortz, B. Keita, L. Nadjo, *Dalton Trans.* **2004**, 3184-3190.
[24] L. Lisnard, P. Mialane, A. Dolbecq, J. Marrot, J. M. Clemente-Juan, E. Coronado, B. Keita, P. de Oliveira, L. Nadjo, F. Sécheresse, *Chemistry – A European Journal* **2007**, *13*, 3525-3536.
[25] C. N. Kato, Y. Kasahara, K. Hayashi, A. Yamaguchi, T. Hasegawa, K. Nomiya, *Eur. J. Inorg. Chem.* **2006**, *2006*, 4834-4842.
[26] B. Godin, Y. G. Chen, J. Vaissermann, L. Ruhlmann, M. Verdaguer, P. Gouzerh, *Angew. Chem.-Int. Edit.* **2005**, *44*, 3072-3075.
[27] M. A. Fedotov, B. Z. Pertsikov, D. K. Danovich, *Polyhedron* **1990**, *9*, 1249-1256.
[28] L. Qu, Z. Niu, J. Liu, Y. Chen, B. Zhao, J. P. Gaodeng, *Xuexiao Huaxue Xuebao* **1991**, *12*, 1434.
[29] B. S. Bassil, M. H. Dickman, B. von der Kammer, U. Kortz, *Inorg. Chem.* **2007**, *46*, 2452-2458.
[30] C. Zhang, R. C. Howell, K. B. Scotland, F. G. Perez, L. Todaro, L. C. Francesconi, *Inorg. Chem.* **2004**, *43*, 7691-7701.
[31] E. Cadot, V. Béreau, B. Marg, S. Halut, F. Sécheresse, *Inorg. Chem.* **1996**, *35*, 3099-3106.
[32] J. Marrot, M. A. Pilette, F. Sécheresse, E. Cadot, *Inorg. Chem.* **2003**, *42*, 3609-3615.

[33] M.-A. Pilette, S. Floquet, J. Marrot, E. Cadot, *Eur. J. Inorg. Chem.* **2011**, *2011*, 3523-3528.
[34] V. Béreau, E. Cadot, H. Bögge, A. Müller, F. Sécheresse, *Inorg. Chem.* **1999**, *38*, 5803-5808.
[35] E. Cadot, M. N. Sokolov, V. P. Fedin, C. Simonnet-Jegat, S. Floquet, F. Secheresse, *Chem. Soc. Rev.* **2012**, *41*, 7335-7353.
[36] Y. Jeannin, J. Martin-Frere, *Inorg. Chem.* **1979**, *18*, 3010-3014.
[37] T. Boyd, S. G. Mitchell, D. Gabb, D.-L. Long, L. Cronin, *Chemistry – A European Journal* **2011**, *17*, 12010-12014.
[38] C. Preyssler, *Bull. Soc. Chim. Fr* **1970**, 30
[39] M. H. Alizadeh, S. P. Harmalker, Y. Jeannin, J. Martin-Frere, M. T. Pope, *J. Am. Chem. Soc.* **1985**, *107*, 2662-2669.
[40] M. R. Antonio, L. Soderholm, *Inorg. Chem.* **1994**, *33*, 5988-5993.
[41] M. Dickman, G. Gama, K.-C. Kim, M. Pope, *J. Clust. Sci.* **1996**, *7*, 567-583.
[42] M. R. Antonio, C. W. William, L. Soderholm, *J. Alloy. Compd.* **1998**, *271*, 846-849.
[43] R. Contant, A. Teze, *Inorg. Chem.* **1985**, *24*, 4610-4614.
[44] B. Keita, Y. W. Lu, L. Nadjo, R. Contant, *Electrochem. Commun.* **2000**, *2*, 720-726.
[45] A. Müller, P. Gouzerh, *Chem. Soc. Rev.* **2012**, *41*, 7431-7463.
[46] A. Muller, C. Serain, *Accounts Chem. Res.* **2000**, *33*, 2-10.
[47] A. Muller, S. Q. N. Shah, H. Bogge, M. Schmidtmann, *Nature* **1999**, *397*, 48-50.
[48] A. Muller, J. Meyer, E. Krickemeyer, E. Diemann, *Angew. Chem.-Int. Edit. Engl.* **1996**, *35*, 1206-1208.
[49] A. Tsuda, E. Hirahara, Y. S. Kim, H. Tanaka, T. Kawai, T. Haida, *Angew. Chem., Int. Ed.* **2004**, *43*, 6327-6331.
[50] C. Schaffer, A. M. Todea, P. Gouzerh, A. Muller, *Chem. Commun.* **2012**, *48*, 350-352.
[51] F. Bannani, S. Floquet, N. Leclerc-Laronze, M. Haouas, F. Taulelle, J. Marrot, P. Kogerler, E. Cadot, *J. Am. Chem. Soc.* **2012**, *134*, 19342-19345.
[52] A. Muller, S. Sarkar, S. Q. N. Shah, H. Bogge, M. Schmidtmann, S. Sarkar, P. Kogerler, B. Hauptfleisch, A. X. Trautwein, V. Schunemann, *Angew. Chem.-Int. Edit.* **1999**, *38*, 3238-3241.
[53] A. Muller, P. Kogerler, H. Bogge, *Struct. Bond.* **2000**, *96*, 203.
[54] A. Ziv, A. Grego, S. Kopilevich, L. Zeiri, P. Miro, C. Bo, A. Müller, I. A. Weinstock, *J. Am. Chem. Soc.* **2009**, *131*, 6380.
[55] A. Muller, B. Botar, S. K. Das, H. Bogge, M. Schmidtmann, A. Merca, *Polyhedron* **2004**, *23*, 2381-2385.
[56] A. Muller, E. Beckmann, H. Bogge, M. Schmidtmann, A. Dress, *Angew. Chem.-Int. Edit.* **2002**, *41*, 1162-+.
[57] A. Muller, F. L. Sousa, A. Merca, H. Bogge, P. Miro, J. A. Fernandez, J. M. Poblet, C. Bo, *Angew. Chem.-Int. Edit.* **2009**, *48*, 5934-5937.
[58] C. L. Hill, *Journal of Molecular Catalysis A: Chemical* **2007**, *262*, 2-6.
[59] L. E. Roy, D. Ortiz-Acosta, E. R. Batista, B. L. Scott, M. W. Blair, I. May, R. E. Del Sesto, R. L. Martin, *Chem. Commun.* **2010**, *46*, 1848-1850.
[60] J. M. Clemente-Juan, E. Coronado, A. Gaita-Arino, *Chem. Soc. Rev.* **2012**, *41*, 7464-7478.
[61] J. Canny, A. Teze, R. Thouvenot, G. Herve, *Inorg. Chem.* **1986**, *25*, 2114-2119.
[62] M. Leyrie, G. Herve, *Nouveau Journal De Chimie-New Journal of Chemistry* **1978**, *2*, 233-237.
[63] F. Robert, M. Leyrie, G. Herve, A. Teze, Y. Jeannin, *Inorg. Chem.* **1980**, *19*, 1746-1752.
[64] D. L. Long, O. Brucher, C. Streb, L. Cronin, *Dalton Trans.* **2006**, 2852-2860.

[65] S. S. Mal, U. Kortz, *Angew. Chem.-Int. Edit.* **2005**, *44*, 3777-3780.
[66] S. S. Mal, N. H. Nsouli, M. H. Dickman, U. Kortz, *Dalton Trans.* **2007**, 2627-2630.
[67] V. S. Korenev, S. Floquet, J. Marrot, M. Haouas, I. M. Mbomekalle, F. Taulelle, M. N. Sokolov, V. P. Fedin, E. Cadot, *Inorg. Chem.* **2012**, *51*, 2349-2358.
[68] A. Muller, P. Kogerler, C. Kuhlmann, *Chem. Commun.* **1999**, 1347-1358.
[69] V. S. Korenev, A. G. Boulay, M. Haouas, F. Bannani, V. P. Fedin, M. N. Sokolov, E. Terazzi, S. Garai, A. Müller, F. Taulelle, J. Marrot, N. Leclerc, S. Floquet, E. Cadot, *Chem.-Eur. J.* **2014**, *20*, 3097-3105.
[70] C. Schaffer, A. M. Todea, H. Bögge, O. A. Petina, D. Rehder, E. T. K. Haupt, A. Müller, *Chem.-Eur. J.* **2011**, *17*, 9634-9639.
[71] S. Garai, E. T. K. Haupt, H. Bogge, A. Merca, A. Muller, *Angew. Chem.-Int. Edit.* **2012**, *51*, 10528-10531.
[72] A. Müller, S. K. Das, S. Talismanov, S. Roy, E. Beckmann, H. Bögge, M. Schmidtmann, A. Merca, A. Berkle, L. Allouche, Y. S. Zhou, L. J. Zhang, *Angew. Chem.-Int. Edit.* **2003**, *42*, 5039-5044.
[73] A. M. Todea, A. Merca, H. Bogge, T. Glaser, J. M. Pigga, M. L. K. Langston, T. B. Liu, R. Prozorov, M. Luban, C. Schroder, W. H. Casey, A. Muller, *Angew. Chem.-Int. Edit.* **2010**, *49*, 514-519.
[74] A. Muller, E. Krickemeyer, H. Bogge, M. Schmidtmann, S. Roy, A. Berkle, *Angew. Chem.-Int. Edit.* **2002**, *41*, 3604-3609.
[75] A. Muller, L. Toma, H. Bogge, C. Schaffer, A. Stammler, *Angew. Chem.-Int. Edit.* **2005**, *44*, 7757-7761.
[76] V. A. Grigoriev, D. Cheng, C. L. Hill, I. A. Weinstock, *J. Am. Chem. Soc.* **2001**, *123*, 5292-5307.
[77] F. Leroy, P. Miro, J. M. Poblet, C. Bo, J. B. Avalos, *J. Phys. Chem. B* **2008**, *112*, 8591-8599.
[78] M. R. Antonio, M. Nyman, T. M. Anderson, *Angewandte Chemie International Edition* **2009**, *48*, 6136-6140.
[79] M. L. Kistler, A. Bhatt, G. Liu, D. Casa, T. B. Liu, *J. Am. Chem. Soc.* **2007**, *129*, 6453-6460.
[80] M. L. Kistler, K. G. Patel, T. B. Liu, *Langmuir* **2009**, *25*, 7328-7334.
[81] D. Rehder, E. T. K. Haupt, H. Bogge, A. Muller, *Chem.-Asian J.* **2006**, *1*, 76-81.
[82] A. Merca, E. T. K. Haupt, T. Mitra, H. Bögge, D. Rehder, A. Müller, *Chem.-Eur. J.* **2007**, *13*, 7650-7658.
[83] S. Landsmann, C. Lizandara-Pueyo, S. Polarz, *J. Am. Chem. Soc.* **2010**, *132*, 5315-5321.
[84] Y. Molard, A. Ledneva, M. Amela-Cortes, V. Circu, N. G. Naumov, C. Meriadec, F. Artzner, S. Cordier, *Chem. Mat.* **2011**, *23*, 5122-5130.
[85] D. G. Kurth, P. Lehmann, D. Volkmer, H. Colfen, M. J. Koop, A. Muller, A. Du Chesne, *Chem.-Eur. J.* **2000**, *6*, 385-393.
[86] W. Bu, H. Li, H. Sun, S. Yin, L. Wu, *J. Am. Chem. Soc.* **2005**, *127*, 8016-8017.
[87] H. L. Li, Y. Yang, Y. Z. Wang, C. Y. Wang, W. Li, L. X. Wu, *Soft Matter* **2011**, *7*, 2668-2673.
[88] S. Polarz, B.Smarsly, M. Antonietti, *chem phy chem*, **2001**, *2*, 457-461.
[89] S.-i. Noro, R. Tsunashima, Y. Kamiya, K. Uemura, H. Kita, L. Cronin, T. Akutagawa, T. Nakamura, *Angewandte Chemie International Edition* **2009**, *48*, 8703-8706.
[90] T. Ito, H. Yashiro, T. Yamase, *Langmuir* **2006**, *22*, 2806-2810.
[91] D. Volkmer, A. Du Chesne, D. G. Kurth, H. Schnablegger, P. Lehmann, M. J. Koop, A. Muller, *J. Am. Chem. Soc.* **2000**, *122*, 1995-1998.

[92] M. Clemente-Leon, T. Ito, H. Yashiro, T. Yamase, E. Coronado, *Langmuir* **2007**, *23*, 4042-4047.
[93] Y. Y. Bao, L. H. Bi, L. X. Wu, S. S. Mal, U. Kortz, *Langmuir* **2009**, *25*, 13000-13006.
[94] Q. Zhang, L. He, H. Wang, C. Zhang, W. Liu, W. Bu, *Chem. Commun.* **2012**, *48*, 7067-7069.
[95] X. K. Lin, W. Li, J. Zhang, H. Sun, Y. Yan, L. X. Wu, *Langmuir* **2010**, *26*, 13201-13209.
[96] S. Y. Yin, H. Sun, Y. Yan, W. Li, L. X. Wu, *J. Phys. Chem. B* **2009**, *113*, 2355-2364.
[97] W. Li, S. Y. Yin, J. F. Wang, L. X. Wu, *Chem. Mat.* **2008**, *20*, 514-522.
[98] S. Y. Yin, W. Li, J. F. Wang, L. X. Wu, *J. Phys. Chem. B* **2008**, *112*, 3983-3988.
[99] W. Li, W. F. Bu, H. L. Li, L. X. Wu, M. Li, *Chem. Commun.* **2005**, 3785-3787.
[100] Y. Jiang, S. Liu, J. Zhang, L. Wu, *Dalton Trans.* **2013**, *42*, 7643-7650.

Chapter II
Hydrophobic Effect as a Driving Force For Host-Guest Chemistry of a Multi-receptor Keplerate type-Capsule

Chapter II- Hydrophobic Effect as a Driving Force For Host-Guest Chemistry of a Multi-receptor Keplerate type-Capsule

I. Keplerate Capsule in Action: From plugging to encapsulation of guest

Molecular recognition is defined as supramolecular noncovalent interaction between molecules or molecular patches. The host-guest chemistry of molecular capsules has proven to be important for molecular technological applications based on the selective recognition of chemical species in solution.[1] These applications include chemical sensing, molecular separations, encapsulated reaction chemistry, crystallization of drug-receptor adducts and host-guest catalysis. [2] One of the main challenges in supramolecular chemistry is the fully understanding of molecular recognition and the dissecting of the different forces that govern this recognition. This is critical in the design of host-guest systems with high selectivity and binding affinity and high catalytic efficiency.

The porous metal-oxide-based capsules known as 'Keplerate' capsule, described previously, have been shown to efficiently recognize a variety of cationic or neutral guests [3-4]. Importantly, the confined space within the capsule has an influence on the reactions taking place in the cavity. This was demonstrated by a recent example about the catalytic cleavage and formation of tert-butyl methyl ether.[5] In addition, this capsule can be regarded as artificial inorganic cells and can act as carriers allowing passive-ion transport into and out of the cavity.[6-7] Understanding of its solution behavior related to the presence of the 20 pores is a key feature in controlling and developing Keplerate-based supramolecular applications such as i) catalysis in confined conditions[5] or ii) catalysis at the surface of the capsule,[8] iii) ionic/ molecular recognition for ion trapping, iv) control of the spontaneous self assembly of "blackberry" aggregates and finally v) the design of keplerate based materials.[9]

The first quantitative analysis about this type of plugging process was reported by Cadot *et al*. In this report, they tracked the interaction of the NMe_4^+ cations with a sulphurated Keplerate containing 20 pores using ^1H NMR DOSY spectroscopic methodology. The ^1H NMR DOSY analysis allowed the determination of the stability constant of the host-guest association. The founded low value of the stability constant (K = 210 ± 20) reflects the weak interactions between the apolar NMe_4^+ ions and the pores, mainly based on very weak hydrogen bonds and electrostatic interactions.[10] These preliminary results were promising because various combinations can be studied, differing either by the nature of the pores $\{M_3Mo_3E_3O_6\}$

(M=Mo^{VI} or W^{VI}, E=O, S) of the used Keplerate or by the nature of the cationic guest. In this context, we aimed at the understanding the solution behavior of the oxo keplerate $\{Mo_{132}\}$ with a series of ammonium cations such as $Me_{4-x}NH_x^+$ with x = 0-4 as well as its interaction with other species in solution such as countercations. Pulsed- gradient spin-echo NMR methods have attracted increasing interest because they allow the measurement of self-diffusion coefficient of chemical objects with high accuracy. This techniques revealed to be powerful and decisive in the context of this work. Then, before presenting our obtained results, a brief literature review of the ^{1}H NMR DOSY methodology is first introduced.

II. Background to ^{1}H NMR DOSY spectrometry

Pulsed field-gradient (PFG) NMR spectroscopy has become a method of choice for measuring diffusion coefficients in both chemical and biological solutions due to its highly sensitivity to molecular displacements in the range of 10 nm - 100 µm as well as its non-invasive character.[11] Diffusion NMR spectroscopy is suitable for studying molecular dynamics and translational diffusion, thus giving the possibility to access to biological structural's details.[12] Recently, the application of this technique to measure biological transport was reviewed.[11] In the last few years, there is a significant potential to apply this technique in mapping intermolecular interaction in both chemical and biological solutions. In this section, we will introduce a brief and basic description of the NMR diffusion methods.

II.1 Concepts of Molecular Diffusion

II.1.1 Translational Diffusion in Isotropic Systems—"Free Diffusion"

The physical phenomenon of translational diffusion, which is one of the most important modes of molecular transport,[12] is the thermal motion. In 1828, Brown described self-diffusion as random translational motion of molecules which leads to their net displacement over time.[12] In 1960, Einstein established the following equation (Eq. 1) which gives the relationship between root mean square displacement, $\langle x^2 \rangle$, the self-diffusion coefficient, *D*, and the time t_d.

$$\langle \boldsymbol{x} \rangle^2 = \sqrt{\boldsymbol{nDt_d}} \qquad \text{(Eq.1)}$$

with n = 2, 4, or 6 for one-, two- or three dimensional diffusion process.[13]

It is well known that the diffusion coefficient is related to the molecular size and to the bulk viscosity as expressed by the Einstein–Smoluchowski equation Eq. (2),[11-12] where k_b is the

Boltzmann constant, T is the absolute temperature, f is the so-called hydrodynamic frictional coefficient, N is the Avogadro's number, and R is the gas constant.

$$D = \frac{K_b T}{f} = \frac{RT}{Nf} \qquad \text{(Eq.2)}$$

For a sphere moving in laminar flow, f is given by the Stokes equation (3):

$$f = 6\pi\eta r_h \qquad \text{(Eq.3)}$$

where η and r_h are the viscosity of the bulk, and the hydrodynamic raduis (stokes radius) respectively.

Combining equation (Eq.2) and (Eq.3) leads to the popular Stokes–Einstein equation Eq. (4)

$$D = \frac{K_b T}{6\pi\eta r_h} \qquad \text{(Eq.4)}$$

Based on Eq. (4), the measured diffusion coefficient will give information on the size and therefore on the specific interactions of the observed species with its close molecular environment. In case of homogeneous medium characterized by isotropic diffusion, the diffusion coefficient is directly correlated to the translational molecular displacement.

Rotational motions are also a form of self-diffusion but it will not be considered since this type of diffusion cannot be extracted from the PFG NMR methodology.

II.1.2 Other modes of diffusion: Restricted and Anisotropic Diffusion

For systems with barriers that prohibit free diffusion, the linear relation between the diffusion time and the mean displacement of the species is break off. In such cases, the increase of the diffusion time t_d does not lead to an increase in the displacement of the diffusion species. Actually, in such cases, restricted diffusion dominates and only an apparent diffusion coefficient can be obtained.[14] When the barriers that impose restrictions are uniformly distributed, an anisotropic diffusion can be determined. These two phenomena are less important in homogenous solutions.[15]

II.2 NMR Methods for Diffusion Measurement

II.2.1 The Modified Spin-Echo Experiment: The Pulse Field Gradients Spin Echo Experiment

Diffusion measurements are based on the fact that the position of NMR-active nuclei can be indirectly labeled by the magnetic field gradients using their larmor frequency. Pulsed gradient spin echo (PGSE) NMR technique is the most common approach to measure diffusion.[16] In this sequence, two identical gradient pulses are inserted, each with a duration period δ (Figure 1). At the beginning of the experiment, the net magnetization is oriented

along the z-axis which indicates that the ensemble of the spins are in thermal equilibrium. Then a 90° radio-frequency pulse is applied, so the magnetization rotates from the z-axis to the x-y plane. After that, the first pulse gradient of duration δ and of magnitude g is applied at t_1 and results in phase shifting for each spin according to the following equation (Eq. 5).

$$\Phi_i(\tau) = \gamma B_0\ \tau + \gamma G \int_{t1}^{t1+\delta} z_i\ (t) d_t \quad \text{(Eq. 5)}$$

The next step in the sequence is the application of 180° radio-frequency pulse followed by a second gradient applied at $t_1+\Delta$.

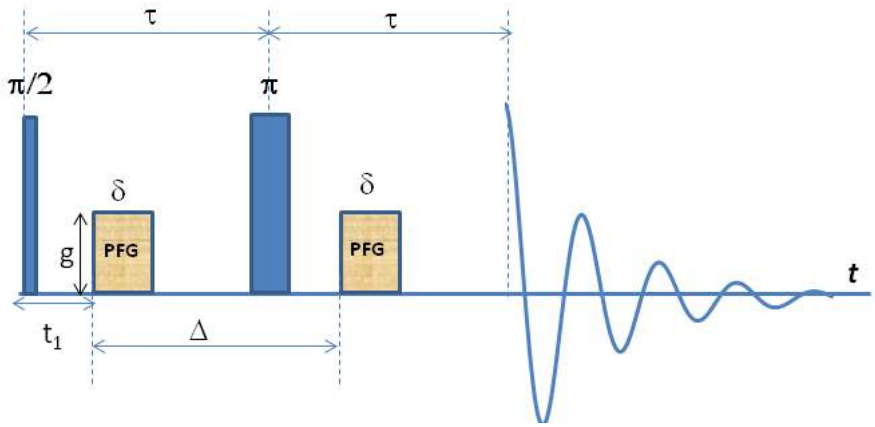

Figure 1: The PGSE pulse sequence. G is the amplitude of the pulsed gradient, δ its duration, and Δ the separation between the leading edges of the two equal pulsed gradients**.**

In the presence of diffusion, each species is located in a different position along z-axis at t_1 and $t_1+\Delta$ and is situated in a different magnetic field. The phase shift of each spin after the first period τ is different in magnitude from the phase shift of each spin after the second period τ. So, the phase angle fans out in this case and the obtained echo signal is smaller. The signal intensity is described by the following equation (Eq.6) where $I_{(2\tau,G)}$ and $I_{(2\tau,0)}$ are the signal and echo intensity, g is the pulsed gradient strength, Δ is the time separation between the pulsed-gradients, δ is the duration of the pulsed gradient, and *D* is the self-diffusion coefficient. Thus, the plot of $\ln(\frac{I_{(2\tau,G)}}{I_{(2\tau,0)}})$ versus the b parameter (see Eq.6) corresponds to a straight line with -D as the slope .

$$\ln(\frac{I_{(2\tau,G)}}{I_{(2\tau,0)}}) = -\gamma^2 G^2 \delta^2 \left(\Delta - \frac{\delta}{3}\right) D = -bD \quad \text{(Eq.6)}$$

Another NMR sequence is the stimulated Echo Diffusion Sequence (STE).[17] This sequence contains three 90° pulses with two gradients. The (PGSE) and (STE) were introduced before the advent of the diffusion ordered spectroscopy method (DOSY).

II.2.2 The DOSY Technique

An important requirement of the DOSY technique is the ability to discriminate diffusion coefficients even when signals of molecules overlap in the usual ^{1}D NMR spectrum. To achieve this, it is important to minimize spectral distortions originated from eddy currents induced from the gradient pulses. The best way to avoid the effects of eddy currents is to prevent their formation in the first place. However, they should remain significant, especially when strong gradient pulses are used with short delays. Therefore, the LED and bipolar LED sequences (shown in Figure 2) were introduced.[17] These two sequences have additional delay time (t_e) which make them less sensitive to eddy currents and then make them able to discriminate diffusion coefficients.[18]

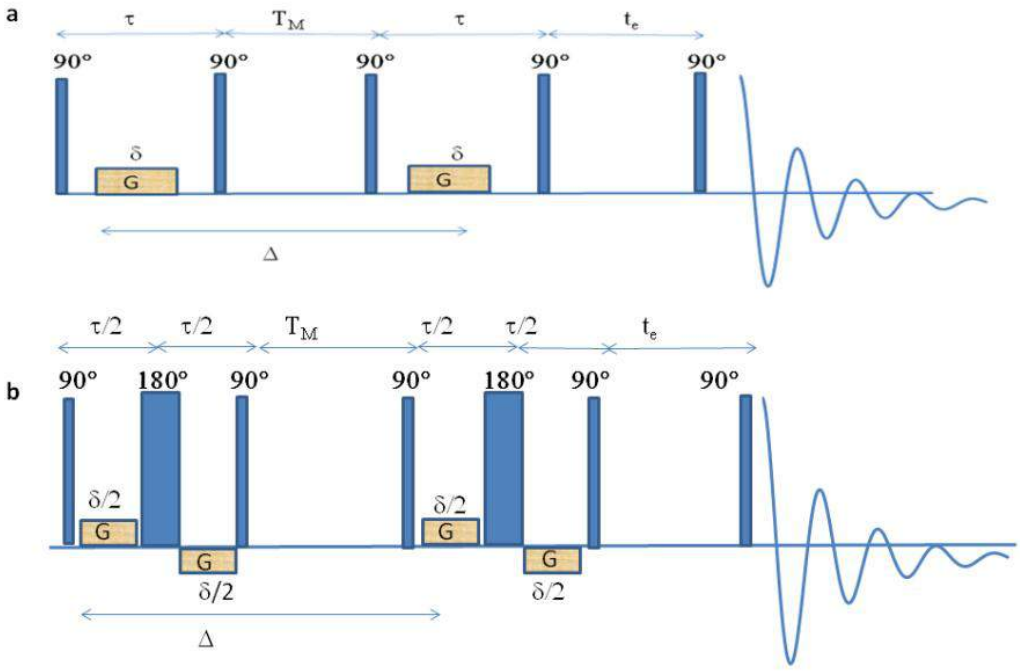

Figure 2: a) the LED pulse sequence, b) bipolar LED (BPLED) pulse sequence.

The diffusion experiments are displayed as a 2D matrix with chemical shifts plotted along one axis and diffusion coefficients plotted along the perpendicular axis (see Figure 3). The chemical shift information is obtained by Fast Fourier Transformation (FFT) of the time domain data while the diffusion information is obtained by an Inverse Laplace Transformation (ILT) of the signal intensity decay (Figure 3).

At a certain frequency, the data sets I(s), which describe the attenuation of this signal, is given by the following equation (Eq. 7) where $\lambda = D(\Delta-\delta/3)$ and $s = \gamma^2\delta^2G^2$.

$$I(s) = \int_0^\infty a(\lambda)\exp(-\lambda s)\,d(\lambda) \qquad \text{(Eq. 7)}$$

Based on equation 7 , $I(s)$ corresponds to the Laplace transform of the a(λ) function, the Laplace spectrum of the diffusion coefficients. Thus, the desired spectrum a(λ) is the inverse Laplace transform (ILT) of the decay function $I(s)$.

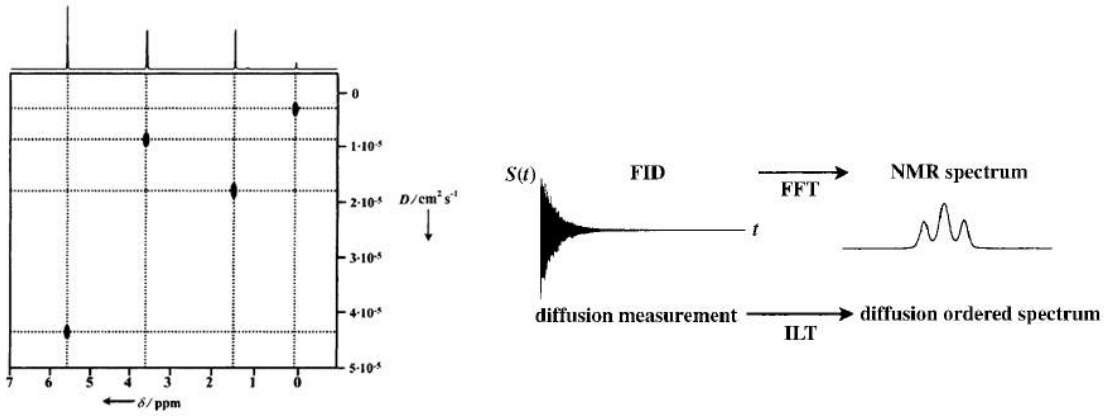

Figure 3: Left: 2D DOSY spectrum. Right: Comparison of FFT and ILT transformations.

II.3 DOSY NMR of Molecular association : From the diffusion coefficient to the association constant

Association constant is an essential parameter to quantify molecular association. Such a quantity can be determined by many different methods depending on the studied chemical system. Since diffusion coefficients can be directly obtained by NMR spectroscopy, it can be used in a similar way as chemical shifts to determine the stoichiometry and stability constant of many molecular associations.[19]

In the case of binding process in slow exchange regime on the time-scale of NMR, the diffusion coefficients can be determined for each distinct situation of the observed molecular species. In this case, numerical values of the stability constant K_s cannot be obtained from the individual self diffusion coefficient. On the contrary, if the binding process involves fast exchange on the time-scale of the NMR diffusion ($\Delta \gg (KD)^{-1}$), then the measured diffusion coefficients (D_{obs}) corresponds to the weighted average of the diffusion coefficients of the free and the complexed forms; thus, in this case, the fraction of species can be determined and the numerical value of the association constant K_s can be determined.[12]

The host−guest complexation is a dynamic process that can be described by Eq. 8:

$$H + G \rightleftarrows HG \qquad \text{Eq. 8}$$

Assuming fast exchange on the NMR time scale, the observed (measured) diffusion coefficient (D_{obs}) is used to calculate the bound fraction x, as expressed by the Eq.9:

$$D_{obs} = xD_{bound} + (1- x)\, D_{free} \qquad \text{Eq. 9}$$

In some favorable case (it will be the case with our Keplerate systems), the difference in sizes between the host and the guest is large. Based on this, we can approximate that D_{bound} of the guest should be similar to D_{free} of the host because the size of the host H should be nearly similar to the size of the HG adduct. In addition, Fielding has shown that when the ratio of the molecular weight between the host and the guest is about or greater than 10, D_{free} of the host H is not very different from D_{bound} of the HG host-guest. Consequently, an acceptable estimation of the association constant from a single point DOSY NMR measurements can be obtained.[20]

Actually, determination of the association constant by diffusion NMR measurements has a lot of advantages. So, this method is less prone to misinterpretation due to minor impurities compared to other methods based on UV or fluorescence spectroscopy.[21] Investigations of intermolecular interaction and the determination of association constants from the diffusion coefficients have been widely reported for molecular capsules or containers.[22]

Polyoxometalates compounds are, in some ways, the ideal candidates for DOSY NMR investigations since they retain large molecular size and thus exhibit large size difference with many guests. However, the use of DOSY NMR to characterize self-assembly and interactions of POM system in solution is still under-explored and the only few recent papers on ^{1}H DOSY NMR are witness for this topics.[23] The investigations of the supramolecular properties of giant POM as Keplerate concerned mainly solid state studies and suffer from the lack of any quantitative informations in the solution.[3]

Bridging the gap between solid state and solution studies and gaining insight into remarkable supramolecular properties listed above such as catalysis, ionic recognition, ion trapping , supramolecular aggregation (blackberries) require a detailed understanding of the fundamental host-guest interactions in Keplerate-type ions. In this chapter, the DOSY NMR is used to quantitatively probe the $\{Mo_{132}\}$ pores plugged by alkyl ammonium guests. The plugging process is found to be in competition with the other counterions in solution and the binding constant revealed to be related to the apolar character of the cations, thus highlighting the contribution of the hydrophobic effect within the overall process. The DOSY methodology was used to investigate the solution properties of Keplerate ions has been also extended to other POMs system thus showing the convenience of the method. Furthermore, the selective encapsulation of tetramethyl ammonium cation within the inner cavity of the $\{Mo_{132}\}$ ion was also investigated and suggests that the encapsulation is favored by the internal acetate ligands.

III. Results and discussion

III.1 Materials and methods

Reagents were obtained from commercial suppliers and used without further purification. The ammonium salt $(NH_4)_{42}[Mo_{132}O_{372}(CH_3COO)_{30}(H_2O)_{72}]\bullet 300H_2O\bullet 10NH_4CH_3COO$, noted $(NH_4)_{52}\{Mo_{132}\}$, was prepared according to the published procedure.[24] The lithium and sodium salts were obtained from $(NH_4)_{52}[Mo_{132}O_{372}(CH_3COO)_{30}(H_2O)_{72}].300H_2O.10\ CH_3COO$ through ions exchange process using acidic sulfonated resin DOWEX 50W in its Li or Na form, respectively. The resulting eluates were evaporated until dryness by rotating evaporator at 45°C. The corresponding salts were characterized by infrared and ^1H liquid NMR spectroscopies and their water content was determined by thermogragrimetric analysis.

The polyoxometalates used for this studies:

i.e. $H_4SiW_{12}O_{40}\bullet 12H_2O$,[25] $Na_{14}[P_5W_{30}O_{110}]\bullet 15H_2O$[26] and $K_{12}(NMe_4)[(AsW_9O_{33})_3(WO(OH_2))_3(Mo_2O_2S_2(H_2O)_4)]\bullet 20H_2O$,[27] were prepared according to the published procedure.

III.1.1 NMR Keplerate samples preparation

III.1.1.a Measurements of the self-diffusion coefficient (D_{obs}) of the S^+ cations at variable concentration in $Y_{52}\{Mo_{132}\}$ ($S^+ = H_{(4-x)}NMe_x^+$, Et-NMe_3^+, NEt_4^+ or Et-Me-imidazolium and $Y^+ = Li^+$, Na^+, NH_4^+) studies

A stock D_2O solution at 5 10^{-3} mol.L^{-1} in $Y_{52}\{Mo_{132}\}$ with a ratio $S^+/ Y_{52}\{Mo_{132}\}$ of about 3 was diluted in D_2O to get a series of NMR solutions in the 1.2 10^{-5} - 5 10^{-3} mol.L^{-1} range in $Y_{52}\{Mo_{132}\}$. The $S^+/ Y_{52}\{Mo_{132}\}$ ratio was determined experimentally through the ^1H NMR relative intensity of the S^+ and acetate resonances, using the 40 acetate ions as internal reference. The variations of the self diffusion of the cationic substrate S^+ as function of the concentration C° in $Y_{52}\{Mo_{132}\}$ are given in Figure 12.

III.1.1.b Pore titration experiment

A 2.4 10^{-3} mol.L^{-1} D_2O solution in $Li_{52}\{Mo_{132}\}$, a 1.2 10^{-1} mol.L^{-1} D_2O solution in NMe_4Cl and pure D_2O were mixed to get a series of NMR solutions with a fixed concentration at 1.2 10^{-3} mol.L^{-1} in $Li_{52}\{Mo_{132}\}$ and with a $S^+/ Y_{52}\{Mo_{132}\}$ ratio ranging from 0 to 50. The equivalent number of NMe_4^+ was determined experimentally for each solution from the ^1H NMR relative intensities, using the 40 acetate ions as internal standard. The results of the pore titration experiments are graphically shown in Figure 6.

III.1.1.c Measurements of the self-diffusion coefficient (*D*obs) of the NMe_4^+ ion at variable concentration in LiCl

A 5 10^{-3} mol.L^{-1} D_2O solution in $Li_{52}\{Mo_{132}\}$ containing about three equivalent of NMe_4^+, a 1 mol.L^{-1} LiCl D_2O solution and pure D_2O were mixed to get NMR solutions with a fixed concentration at 10^{-3} mol.L^{-1} in $\{Mo_{132}\}$ and with a variable concentration in LiCl ranging from 5 10^{-2} to 0.5 mol.L^{-1}. The variation of D_{obs} with the LiCl concentration graphically in Figure 7.

III.1.1.d NMe_4^+ encapsulation NMR study

Concentration effect study. A stock aqueous solution containing both $(NH_4)_{52}\{Mo_{132}\}$ at 5 mM and **NMe_4^+** at 15mM was first prepared. From this, another 6 solutions were prepared by dilution, obtaining therefore 7 NMe_4^+/$\{Mo_{132}\}$ 3:1 solutions with concentration ranging from 1.88 mM to 5 mM . Actual number of equivalents of NMe_4^+ was determined from ^1H NMR integrals.

At variable ratio NMe_4^+/{Mo_{132}} : In a glass vial, 560 mg (5mM) of $(NH_4)_{52}\{Mo_{132}\}$ was dissolved in 4 mL of D_2O. Another stock solution of 60mM NMe_4^+ in D_2O was prepared . For each titration point, different volumes of NMe_4^+ stock solution (0.25 mL, 0.5 mL, 1 mL, 1.5 mL,) was added to 0.5 mL of $(NH_4)_{52}\{Mo_{132}\}$ solution , the final volume was completed to 2 ml by D_2O. Then mixing the solution well before replacing the tube in the probe for the next measurement. Actual number of equivalents of NMe_4^+ was determined from ^1H NMR integrals.

III.1.2 NMR polyoxotungustate samples preparation

For (NMe_4)-$H_4SiW_{12}O_{40}$•$12H_2O$ and (NMe_4)-$Na_{14}[P_5W_{30}O_{110}]$•$15H_20$ solutions were prepared as previously, however the introduced equivalents of (NMe_4^+) was 0.88 and 2 respectively. For $K_{12}(NMe_4)[(AsW_9O_{33})_3(WO(OH_2))_3(Mo_2O_2S_2(H_2O)_4)]$•$20H_2O$ study: A stock solution containing $K_{12}(NMe_4)[(AsW_9O_{33})_3(WO(OH_2))_3(Mo_2O_2S_2(H_2O)_4)]$•$20H_2O$ at 5mM in D_2O was first prepared. Then we diluted to get a series of NMR with concentration ranging from 0 to 5 mmol.L^{-1}.

III.1.3 Physical measurements.

Infrared spectra were recorded on a Magna 550 Nicolet spectrophotometer, using KBr pellet.

Elemental analyses were performed by the service central d'analyses du CNRS, Vernaison, France and by the service d'analyses du CNRS, ICSN, Gif sur Yvette, France and by the Mikroanalytisches Labor Pascher, Remagen-Bandorf, Germany.

EDX measurements were performed on a JEOL JSM 5800LV apparatus.

TGA experiments were performed with a Seiko TG/DTA 320 thermogravimetric balance (5°C min^{-1}, under O_2).

^{1}H NMR spectra were recorded in D_2O. ^{1}H chemical shifts were referenced to TMS as external standard (δ = 0 ppm). NMR spectra were recorded on Bruker Avance 400 MHz spectrometer at room temperature (300 K) when it is not specified. For variable-temperature study, ^{1}H NMR spectra were acquired at seven temperatures between 299 and 342 K. Translational diffusion measurements were performed using Bruker's 'ledbpgs2s' stimulated echo DOSY pulse sequence including bipolar and spoil gradients. Apparent diffusion coefficients were obtained using an adapted algorithm based on the inverse Laplace transform and maximum entropy. Collection of the two-dimensional phase sensitive EXSY data included 16 transients per increment with a total of 1024 increments. A standard phase sensitive NOESY pulse sequence was used, preparation-90°-t_1-90°-t_m-90°-acquisition. The mixing time (t_m) was ranging from 50 to 500 ms and the recycle time was 1 s. The REOSY experiments were obtained using a standard phase sensitive pulse sequence, 16 scans per t_1 increment, 3 s recycle time, 1024 t_1 increments, and a mixing time ranging from 30 to 300 ms. The power level was 23 dB corresponding to 17 mW.

III.2 Evidence of the multi-receptor properties of the Keplerate-type capsule. Study of the interaction between NMe_4^+ and $Y_{52}\{Mo_{132}\}$

Before starting our investigations of the $NMe_4^+/Y_{52}\{Mo_{132}\}$ systems (Y = Li^+, Na^+ or NH_4^+), we performed several variable concentration DOSY experiments using aqueous NMe_4Cl and $(NH_4)_{52}\{Mo_{132}\}$ solutions in order to ensure that the observed variation of the diffusion coefficients was not caused by either self-aggregation of the initial components or by change in the viscosity of the solution. The obtained results show that the diffusion coefficient for pure NMe_4^+ ion is nearly independent upon the concentration in NMe_4Cl salt ($D°$ = 910 ± 30 $\mu m^2.s^{-1}$) and therefore rules out any changes in the viscosity of the solution in the studied concentration range. In addition, the self-diffusion coefficient of the $\{Mo_{132}\}$ capsule remains also quite constant (D^∞ = 115 ± 5 $\mu m^2.s^{-1}$) in the concentration range (10^{-4} - 5.10^{-3} $mol.L^{-1}$). Such a result allows to rule out any degradation or self-aggregation of our $\{Mo_{132}\}$ host. At this level, we are quite confident to state that any variation of the self-diffusion coefficient of

the guest must arise from host-guest interactions, the base for the accurate estimation of the host–guest stability constant.

III.2.1 Evidence of competition within the plugging process between the cationic guest NMe_4^+ and counter-ions Li^+, Na^+ or NH_4^+

The ^1H NMR spectra of the NMe_4^+-$Y_{52}\{Mo_{132}\}$ mixtures (Y = Li^+, Na^+ or NH_4^+) in aqueous solution show similar features in the range of used concentrations and reveal a broad resonance at 0.5 ppm attributed to the internal acetate coordinated to the $\{Mo_2O_4\}$ bridging units, a signal at 1.9 ppm assigned to solvated acetate ions and a narrow signal slightly dependent upon the concentration and ranging from about 3.0 to 3.4 ppm assigned to NMe_4^+ as shown in Figure 4**.** It should be noted that the linewidth of the NMe_4^+ signal remains almost constant for all the experiments ($\Delta\nu_{1/2}$ = 1-2 Hz) meaning that the transverse relaxation time T_2 is almost similar over the concentration range. In the high concentration domain, one can notice the appearance of two small and close additional peaks at 2.9 ppm which will be assigned and discussed in details in the following sections. 2D DOSY NMR technique was used to measure the self-diffusion coefficient *D* of each species. As usually observed, the encapsulated acetate ligands in the Keplerate capsule exhibit the lowest self-diffusion coefficient D = 115 ±5 $\mu m^2.s^{-1}$ while solvated acetate ions leads to higher *D* value (730 ± 30 $\mu m^2.s^{-1}$).[28] The main important feature of the DOSY spectrum is certainly the low value of the NMe_4^+ diffusion coefficient observed at $C°$ = 5 mmol compared to that of the solvated NMe_4^+ species ($D°$ = 910 ± 30$\mu m^2.s^{-1}$). In the presence of the $(NH_4)_{52}\{Mo_{132}\}$, the limit value of the self-diffusion coefficient of the NMe_4^+ ion is lowered down to 357 $\mu m^2.s^{-1}$. [28] This evidences a type of interaction between the small NMe_4^+ ion and the large keplerate capsule.

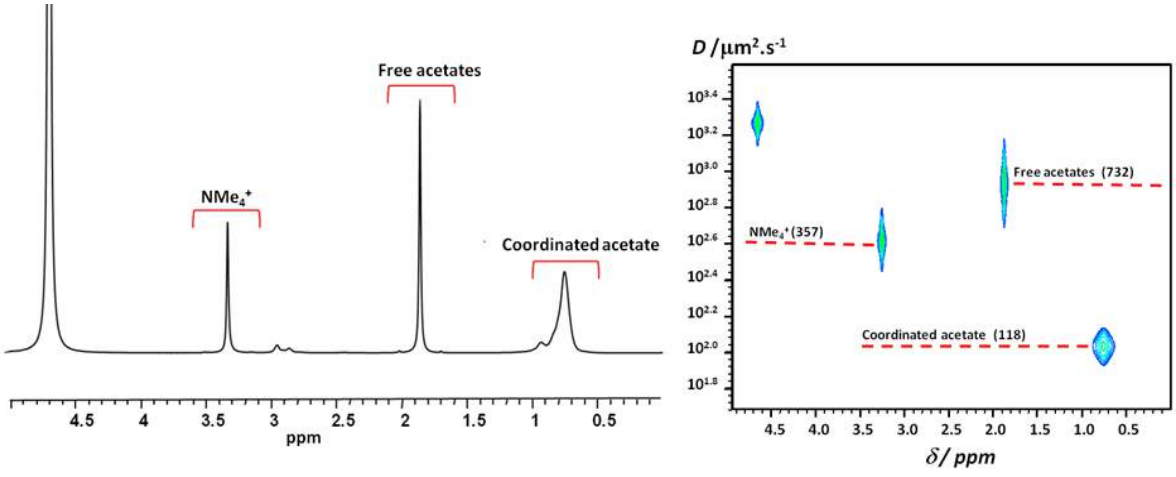

Figure 4: ^1H NMR spectra of $NMe_4^+$and $(NH_4)_{52}\{Mo_{132}\}$ in D_2O with NMe_4^+ /Mo_{132} = 3 and at $C°$ = 3 mmol/L. Left: 1D spectrum; Right: ^1H 2D DOSY.

From this observation, the first key question to be considered in our system was whether the counter ions contribute to this phenomenon. In other words, do the counter ions compete with NMe_4^+ ions in the vicinity of the Keplerate? Depending on the answer of the asked question, an appropiate host-guest binding model will be considered.

In this context, we measured the diffusion coefficient of the NMe_4^+ cation for different concentrations *C*° in the series $(Y)_{52}\{Mo_{132}\}$ Keplerate with Y = Li^+, Na^+ or NH_4^+. These experiments have been carried out at a fixed ratio $NMe_4^+/\{Mo_{132}\}$ = 3 varying the concentration *C*° in $Y_{52}\{Mo_{132}\}$ from 0 to 5.10^{-3} $mol.L^{-1}$. The results showing the variation of the self-diffusion coefficients (D_{obs}) versus *C*° are graphically shown in Figure 5.

Actually, when analyzing the *D* variations versus concentration, we found that changing the nature of the counterions from Li^+ to NH_4^+ increases gradually the limit value of the self-diffusion coefficients of the NMe_4^+ from 190 to 357 $\mu m^2.s^{-1}$ (see Figure 5). This highlight a competitive process at the binding sites between NMe_4^+ cations and the other counter ions present in solution *i.e.* NH_4^+, Na^+ or Li^+. Furthermore, comparison between the *D* limit value obtained with Li^+, Na^+ or NH_4^+ suggests that NH_4^+ behaves as a stronger competitor than Na^+ and Li^+ ions. Presumably, the size of ion and therefore, its charge density has a significant influence upon its interaction with the ionic capsule. Actually, we observed that this invoked competitive effect decreases as the size of the cation decrease in the following order $NH_4^+ > Na^+ > Li^+$.

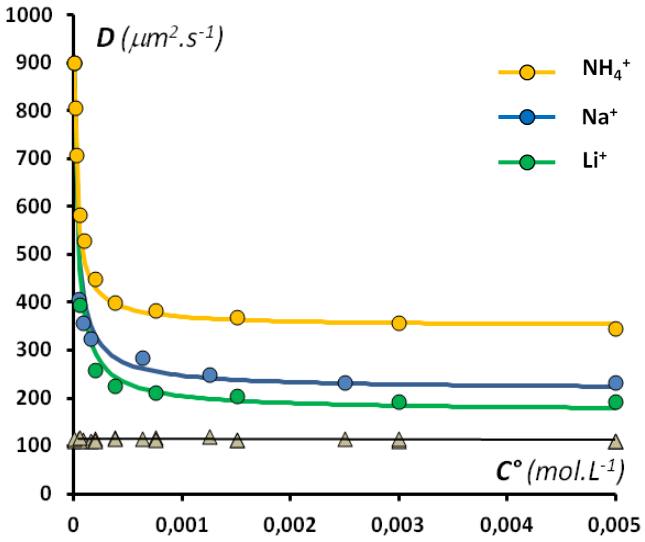

Figure 5: Variation of the self-diffusion coefficient (*D*) of the NMe_4^+ ions (circle) and of the inner acetate ligands (triangle) with concentration in $\{Mo_{132}\}$ (*C*°). ^1H DOSY experiments have been carried out at a fixed ratio $NMe_4^+/\{Mo_{132}\}$ = 3 using three different $Y_{52}\{Mo_{132}\}$ salts (Y = Li^+, Na^+ or NH_4^+). Experimental data (circles) fit nicely with those calculated (solid lines) using stability constants given Table 1.

III.2.2 The Binding Model

In the light of these previous results, the considered binding model must take into account the contribution of the counterions in the interaction process between the NMe_4^+ cations and the capsule. It could be achieved by considering the competition of both cations at the same binding site, as expressed by the cation exchange equilibrium: $*\text{-}Y + S^+ \rightleftharpoons *\text{-}S + Y^+$

where $*$ = binding site; S^+ = cationic guest and Y^+ = counter ions.

In a fast exchange regime on the NMR timescale, D_{obs} is the result of the average weight of the guest molecules in the free and complexed states (Eq. 9)

$$D_{obs} = xD^0 + (1-x)D^\infty$$

Where $D°$ and D^∞ correspond to the self-diffusion coefficient of the solvated (free) and trapped tetra-alkylammonium cation (noted TAA), respectively and x the fraction of free alkyl ammonium. As previously shown, a competitive complexation process involving NMe_4^+ and Y^+ at the binding site takes place. Then, the complexation process of a given substrate noted S^+ (with S^+ = TAA) should involve two equilibria in competition, involving the binding sites of the capsules (noted P), the counter-ions Y^+ and the substrate S^+. Assuming the twenty pores of the capsule are the binding sites for the cations either S^+ or Y^+ and that these twenty $\{Mo_9O_9\}$ pores are almost independent, the host-guest process can be expressed simply by equations (10) and (11). These two hypotheses will be justified in the following sections.

$P + Y \rightleftharpoons P\text{-}Y$ (Eq.10)

$P + S \rightleftharpoons P\text{-}S$ (Eq.11)

$K_Y = \frac{[PY]}{[P][Y]}$ (Eq. 12) and $K_S = \frac{[PS]}{[P][S]}$ (Eq. 13)

With P corresponding to a single $\{Mo_9O_9\}$ pore.

The following equations (14), (15) and (16) correspond to the conservation equations in *P*, *S* and Y, respectively.

$$20C° = [P] + [PS] + [PY] \quad \text{(Eq. 14)}$$

$$nC° = [S] + [PS] \quad \text{(Eq. 15)}$$

$$52C° = [Y] + [PY] \quad \text{(Eq. 16)}$$

where $C°$ is the concentration in Keplerate $\{Mo_{132}\}$ and *n* the equivalent number of cationic substrate per $\{Mo_{132}\}$ capsule. The number of equivalent in cationic substrate S is fixed to $n \approx 3$. In such conditions, and whatever the concentration $C°$, the amount of bound substrate PS remains weak compared to the sum *[P] + [PY]*. Then, the concentration *[PS]* can be

neglected with respect to the sum $[P]$ +$[PY]$. The equation (14) is then derived into equation (17):

$20C° = [P] + [PY]$ (Eq.17)

From equations (12), (16) and (17), the quadratic equation is established (18) :

$K_y[PY]^2 - \left(72C°K_y + 1\right)[PY] + 1040KyC°^2 = 0$ (Eq.18)

with $a = K_y$; $b = -\left(72C°K_y + 1\right)$; c = 1040 $KyC°^2$

where the suitable positive root *[PY]* of equation (10) is a function of K_y : $[PY]_{(Ky)}$. The concentration $[Y]_{(Ky)}$is then deduced from equation (16). For each concentration $C°$, $[PY]_{(Ky)}\ and\ [Y]_{(Ky)}$ can be calculated varying the K_y value.

Based on equation (13)

$nC° = [S] + [PS] \rightarrow [PS] = nC° - [S]$ (Eq. 19)

$K_Y = \frac{[PY]}{[P][Y]} \rightarrow [PY] = K_Y.[P][Y]$ (Eq. 20)

substitute eq (19) and (20) in eq. (14)

$20C° = [P] + [PS] + [PY]$

$20C° = [P] + nC° - [S] + K_Y.[P][Y] \rightarrow [P] = \frac{[S]+C°(20-\mathrm{n})}{1+[Y]K_Y}$ (Eq. 21)

substitute (19) and (21) in eq. (15)

$K_S = \frac{[PS]}{[P][S]}$ then a second quadratic equation (22) is established:

$-K_s[S]^2 - \left(K_y[Y]_{(Ky)} + 20C°K_s - nC°K_s + 1\right][S] + nC°\left(1 + K_y[Y]_{(Ky)}\right) = 0$ (Eq.22)

$a' = -K_s[S]^2$; $b' = -\left(K_y[Y]_{(Ky)} + 20C°K_s - nC°K_s + 1\right]; c' = nC°\left(1 + K_y[Y]_{(Ky)}\right)$

and the suitable positive square root *[S]* of equation (14) as a function of K_y and K_s is established . The concentration *[SP]* is obtained from equation (15) and the fraction x of the free substrate is given by equation (23) :

$x = \frac{[S]}{[S]+[SP]}$ (Eq.23)

allowing to the calculate self-diffusion coefficient $D_{calc.}$

$D_{calc} = xD^0 + (1 - x)D^\infty$ (Eq.9)

Practically, the limit values $D°$ and D^∞ used for calculations have been determined experimentally. They are given in Table 1. The equivalent number of substrate S (noted n and estimated about 3) is experimentally determined from the ^{1}H NMR intensity ratio of the signal of the 40 acetate ion and that of the substrate S. The procedure applied to extract the constants K_y and K_s was based on the optimal matching of the calculated and experimental self-diffusion coefficients data. The constants K_y and K_s were considered as parameters and varied until the

best agreement between experimental and calculated data. It is worth noting that the "plateau" observed for $C°>2.10^{-3}$ mol.L^{-1} depend mainly on the K_s/K_y ratio thus highlighting the competitive NMe_4^+/ Y^+ guest exchange process. Besides, the part in the low concentration domain ($C° < 2.10^{-3}$ mol.L^{-1}) depends mainly on the absolute value K_s where the dominant process corresponds to the equilibrium expressed by Eq. 11. Importantly, the calculated self-diffusion coefficients based on this model give very good fits over all the concentration range as shown in Figure 5. Thus this result provides direct evidence for the validity of our simple binding model and give indirect justification of the related hypotheses, such as i) cation competition at the binding site, ii) the binding sites behave independently. However, these results do not allow any information about the nature of the binding sites and their possible assignments to the twenty $\{Mo_9O_9\}$ pores. The stability constants extracted from the calculated curve shown in Figure 5 are given in Table 1. We found the following order for the stability constant $NMe_4^+ >> NH_4^+ > Na^+ > Li^+$. Such results are quite intriguing if we consider the apolar nature of the NMe_4^+ with respect to the others i.e. NH_4^+, Na^+, Li^+. At this moments, it seems too early to give a clear explanation for such a behavior due to the lack of sufficient information concerning the nature of the binding site and the influence of the apolar character of the guests. To gain more insights, we engaged a titration experiment in order to link the plugging process to the presence of the twenty pores. Furthermore, we varied systematically the apolar character of the cations within a large series of alkyl ammonium guest.

Table 1: Diffusion coefficient of NMe_4^+ with $Y_{52}[NMe_4+@\{Mo_{132}\}]$ salts and related stability constants of the multi-receptor Keplerate ions (C° = 5 mmol.L^{-1}) at 25 °*C* in D_2O.

	K_{NMe4^+} = 1500 ±200	
$Y_{52}[NMe_4^+ @\{Mo_{132}\}]$	D_{obs}	K_y
$Li_{52}[NMe_4^+ @\{Mo_{132}\}]$	193	65 ± 10
$Na_{52}[NMe_4^+ @\{Mo_{132}\}]$	230	130 ± 15
$(NH_4)_{52}[NMe_4^+ @\{Mo_{132}\}]$	357	370 ± 30

III.2.3 Pore titration experiment

The high binding constant value determined for NMe_4^+ ion in the presence of the Keplerate ion should reflect some specific interactions with the 20 pores of the capsule. In order to justify such an assumption, we carried out a pore-titration experiment using NMe_4^+ ion and $Li_{52}\{Mo_{132}\}$ as titrating and titrated reagents, respectively. This choice is logically justified by i) the high stability constant of the NMe_4^+ complexes (1), ii) the excellent solubility of the $\{Mo_{132}\}$ capsule in the presence of NMe_4^+/Li^+ cations allowing to investigate a large range of composition, iii) the lowest stability constant of the lithium cation which is expected to originate the weakest competition with the NMe_4^+ plugging process. NMR titrations were

carried out to measure the diffusion coefficients of NMe_4^+ in the presence of variable equivalent of NMe_4^+ ranging from 0 to 50 and at a fixed concentration $Li_{52}\{Mo_{132}\}$ ($1.2\ 10^{-3}$ $mol.L^{-1}$).

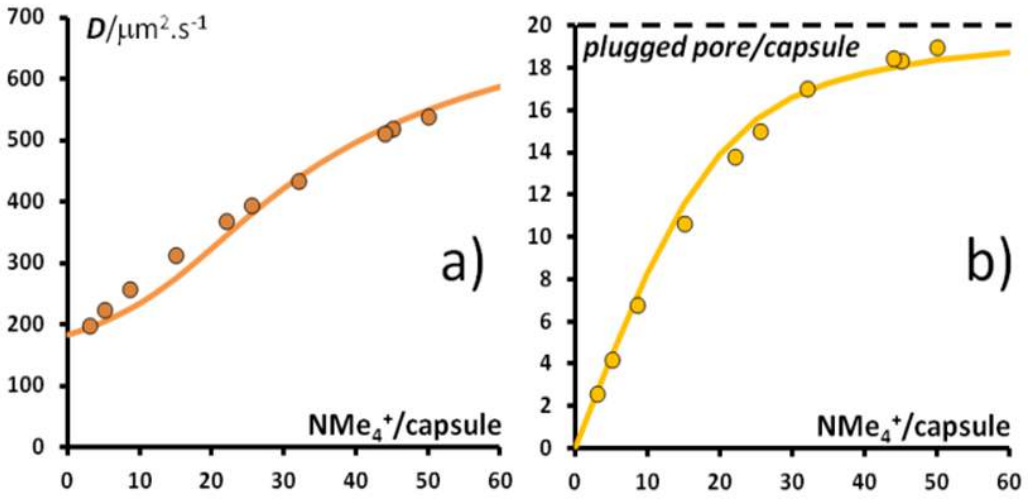

Figure 6: Titration pores experiment $xNMe_4^+ + \{Mo_{132}\}$: a) Variation of the self-diffusion coefficient (D) of the NMe_4^+ with $x = NMe_4^+/\{Mo_{132}\}$; b) Bound NMe_4^+ ions per capsule (plugged pores) versus $x = NMe_4^+/\{Mo_{132}\}$. For both curves, solid lines correspond to calculated data using stability constants K_s = 1550 and 65 for NMe_4^+ and Li^+, respectively (see Table 1).

The basic experimental results (D_{obs} versus $NMe_4^+/\{Mo_{132}\}$) are shown in Figure 6. Without any *priori* assumption based on the number of sites and on the binding constant value, we calculated the plugged fraction of NMe_4^+ using Eq. 9, and the ratio between plugging NMe_4^+ and $\{Mo_{132}\}$. Actually, this ratio corresponds to the number of pores plugged by NMe_4^+ within the capsule. As shown in Figure 6b , this number tends strikingly toward twenty as the NMe_4^+ concentration increases, then justifying plentifully the twenty pores involvement within equilibria (2) and (3). Furthermore, the calculated data obtained from the stability constants of NMe_4^+ (K_s = 1550) and Li^+ (K_y = 65) (Table 1) reveal to be fairly consistent with the experimental ones (Figure 6a and b) , showing that the multi-receptor properties of the capsule can be analyzed simply from a 20 independent-pores model. The calculated data obtained from our binding model require a specific mathematical treatment because some approximation used in previous calculations (see for example Eq. 17) cannot be considered here. The complete analytical treatment leading to calculated data shown in Figure 6a and 6b are given in Appendix (A1.II.2).

III.2.4 Influence of ionic strength upon the plugging process

Having proved that NMe_4^+ interacts strongly (K_s = 1550) and specifically with the 20 pores of the capsule, we aimed to probe (and thus confirm) the influence of the concentration in Li^+

cations on the Li^+/NMe_4^+ competition at the binding sites. When additional and substantial amount of LiCl (ranging from 0 to 0.6 mol/L) is added to a solution of $[3NMe_4^+@Li_{52}\{Mo_{132}\}]$ (5.10^{-3} $mol.L^{-1}$), the diffusion coefficient of the NMe_4^+ cation increases significantly from 200 to 700 $\mu m^2.s^{-1}$ as shown in Figure 7. Such an expected results confirm further the competition between cations. For high LiCl concentration, the NMe_4^+ cations are literally pushed away from the pore vicinty. Similar results have been reported by Raymond *et al.* who studied supramolecular interactions between tetrahedral cages and cationic guests.[29] The author gave similar explanation about variation of the diffusion coefficient of the guest moieties. The added salt disrupts the specific interaction of the NMe_4^+ with the pores causing the increase in the diffusion coefficient of the NMe_4^+ cation. Unfortunately, we were not able to carry out satisfying calculations of these experimental data. In such a case, the drastic variation of the ionic strength should be probably taken into account as activity correction calculation.

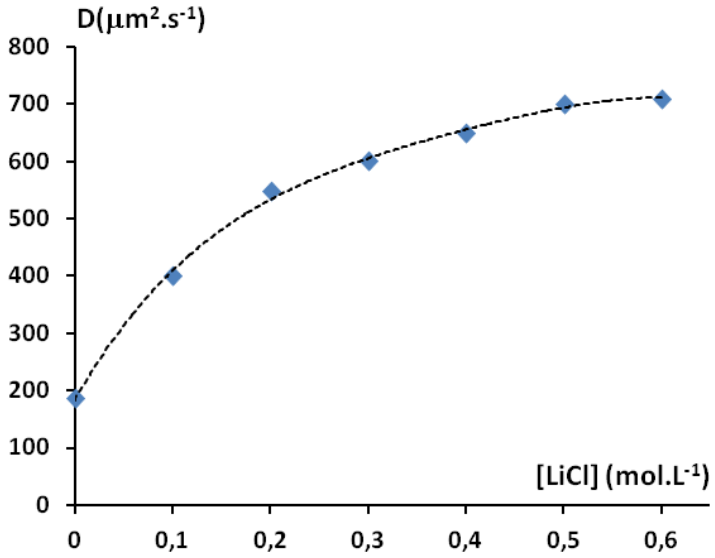

Figure 7: Diffusion coefficient of exterior NMe_4^+ as a function of the LiCl concentration.

III.2.5 A host-guest structural model

To confirm such an observation, we attempted to get a structural model from single X-ray diffraction study. In the presence of NMe_4^+, the $\{Mo_{132}\}$ Keplerate ion gave dark hexagonal well-shaped crystals. Unfortunately, these crystals were highly fragile and whatever the acquisition conditions, they produced only very weak and diffuse diffraction spots, unsuitable for any structural resolution. However, the existence of specific interaction can be supported structurally by a host-guest arrangement previously published by Pilette et *al.* which involves a NMe_4^+ ion and a single pore-model polyoxometalate (Figure 8).[27] This species consists of

three $\{AsW_9O_{33}\}^{9-}$ subunits linked together by three $\{O{=}W\text{-}OH_2\}^{4+}$ fragments. The POM framework lines a triangular cavity $\{W_9O_9\}$ which exhibits very close structural features that those observed for the $\{Mo_9O_9\}$ pores of the Keplerate ion (depicted in Figure 8).

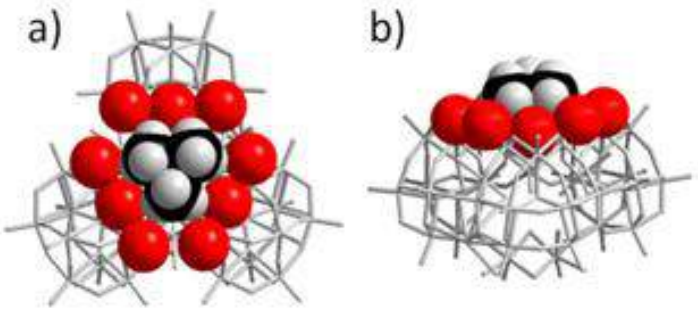

Figure 8: X-ray structure of a single-pore model showing the specific host-guest association between the NMe_4^+ cation and the $\{W_9O_9\}$ pore within a polyoxometalate (data obtained from ref.[27]). a) Top view along the C_3 axis ; b) side view highlighting the $\{W_9O_9\}$ pore filled by one methyl head.

Strikingly, a NMe_4^+ ion has been located within the central hole giving a host-guest arrangement which retains the C_{3v} symmetry with one methyl head within the hole. Surprisingly, the C-H•••O distances are long enough (3.4-3.6 Å) to exclude any hydrogen bonds formation as the prime factor of the host-guest stability. Then, the host-guest arrangement involving the $\{Mo_9O_9\}$ pores of the capsule and the Me_4N^+ is probably close to that represented in Figure 8. Such a similar close host-guest association within the $\{Mo_{132}\}$ capsule has been nicely supported by a pore-titration experiment (Figure 6b). Last but not least, the binding constant associated to the plugging process between a NMe_4^+ ion and the single pore-model polyoxometalate have been determined by using the same 1H DOSY NMR methodology (see below) and the data analysis leads to the stability constant *K*s = 20000. Such combined result i.e. structural analysis and solution study confirm the strong interaction between NMe_4^+ ions and the $\{W_9O_9\}$ pore.

III.2.6 Influence of the nature of the $\{Mo_9O_6E_3\}$ pore with E = O or S

Similar dependence of the NMe_4^+ self-diffusion coefficient upon the concentration has been already observed using the sulfurated derivatives of the $\{Mo_{132}\}$ capsule. The $Na_{38}K_{35}(NMe_4)_{3.5}[Mo_{132}O_{312}S_{60}(CH_3COO)_{30}(H_2O)_{72}]\bullet 200H_2O\bullet 3CH_3COO$ ion exhibit quite low affinity for NMe_4^+ ions highlighted by the stability constant *K*s = 210.[10] Thus changing the nature of the pore from $\{Mo_9O_9\}$ to $\{Mo_9S_3O_6\}$ leads to a drastic decrease of the stability constant from *K*s = 1550 ± 200 to 210 ± 20 while the main features of the capsule (ionic charge, size and shape) remain almost unchanged. This suggests that the binding constant and consequently the interaction of NMe_4^+ with the capsule are sensitive to the nature of the pore.

Such a result should be explained by the larger ionic radius of the sulfur atoms which reduced the inner space of the pore and then increases unfavorable steric effect for the NMe_4^+ plugging.

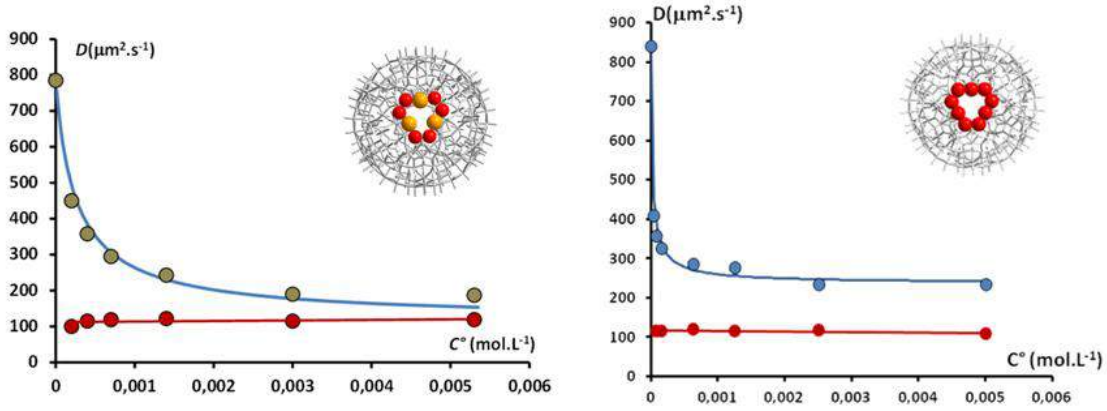

Figure 9: Variation of the self-diffusion coefficient (*D*) of the NMe_4^+ ions (yellow and blue circles) and of the inner acetate ligands (circle) with concentration in $\{Mo_{132}\}$ (*C*°) , Left: sulfurated keplerate, Right: oxo keplerate.

III.2.7 Molecular dynamic simulations

In collobration with Carlos Bo and Dolores Melgar (ICIQ, Spain), complementary insights about interactions between the Keplerate ion with its 42 counter-ions are obtained from molecular dynamics simulations. Calculations have been carried out on the system Keplerate, water and NMe_4^+ or NH_4^+ salts because the latter exhibit contrasted affinity for the Keplerate ion (see Table 2). The $\{Mo_{132}\}$ anion used in these theoretical investigations contains 30 inner formate ligands inside the capsule, instead of the acetates used in the experimental study. The total charge of the anion is the same in both, experimental and simulated cases and the exact nature of the inner medium of the capsules is expected to play no significant role in the overall dynamics of the capsule and the outer medium. The simulations have been carried out in a box of dimensions 7x7x7 nm^3 that contains one $\{Mo_{132}\}$ anion, the corresponding 42 counter-cations, and 11000 water molecules, leading to a density of 1.06 $g \cdot cm^{-3}$, and to a concentration in Keplerate $C°$ = 0.0048 $mol \cdot L^{-1}$. The used computational details are equivalent to those used in previous studies.[30-31] The analysis of the molecular dynamics simulations for NMe_4^+ and NH_4^+ demonstrates clearly that both ions interact differently with the capsule. Two representative snapshots of the dynamics scenario are given in Figure 10, together with the corresponding distribution of cations from the center of the capsule, g(r). According to the g(r) distribution, about 17 NMe_4^+ ions among the 42 are located in the vicinity of the capsule. Few of them corresponding to the closest region (r < 15 Å) plug perfectly the pore (see the center of the picture in Figure 10a), even showing exactly the same

host-guest arrangement as that observed from the X-Ray structure of the single-pore model mentioned above (Figure 8). A large number of NMe_4^+ cations remain close to the capsule surface for rather long time; some of them located just over the pores and preferentially oriented as the plugging ones (Figure 10a). These correspond to the second peak (15 < r < 17.7 Å) shown in Figure 10c and involve about 16 NMe_4^+ ions. The remaining cations observed at r > 17.7 Å did not show any specific attraction to the pore structure and simply remain close to the capsule due to its electrostatic interaction. Furthermore, none of the NMe_4^+ ions entered into the capsule. In the presence of NH_4^+, the scenario is quite different. Firstly, some of the ammonium cations enter the capsule, although they remain close to the pores, according to the first peak located at r = 11,25 Å which corresponds to the inner space just behind the metal-oxo framework (see Figure 10d). Some of the rest are located just at the pores (second peak in Figure 10d), while the remaining NH_4^+ ions are located close to the capsule surface but not as tightly bound to the latter as NMe_4^+ ions. The presence of clear and well-separated peaks in the distribution functions g(r) computed for both cations (see Figure 10 c-d) corresponds to different dynamic regimes correlated to diffusion coefficients.

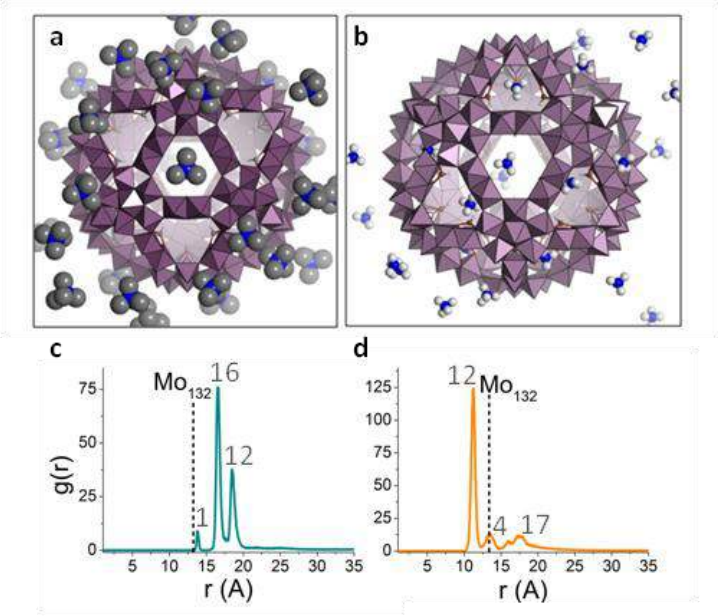

Figure 10. Upper part : snapshots of the MD simulations for NMe_4^+ (a) and NH_4^+ (b) counter-ions in the presence of the $\{Mo_{132}\}$ ionic capsule; Lower part: radial distribution functions for the (c) NMe_4^+ (blue), (d) NH_4^+ (orange) where the average number of cations associated to each peak has been indicated.

These different diffusion coefficients collected in Table 2, have been obtained by only considering ion trajectories such that the ion remains inside a given region around the peak for more than 90% of the time window used to determine the mean square displacement (100 ps). Bound cations are expected to diffuse and rotate with the capsule, and its measured diffusion coefficient should scale as r^2, according to:

$$D_{ion}(R) = D_{transl} + D_{rot}r^2 \qquad \text{(Eq.24)}$$

where D_{transl} is the diffusion coefficient of the center of the {Mo_{132}} capsule, and D_{rot} its rotational diffusion coefficient. The diffusion coefficients of the different components of the system as a function of r^2 are shown graphically in Figure 11. The behavior described in equation (24) should be limited to short simulation times, smaller than $\frac{L}{D_{transl}}$, estimated to be in the order of 5 ns for our system. The graph in Figure 11 shows clearly that diffusion coefficients associated to the center of the {Mo_{132}}, to the Mo atoms, and to the formate hydrogen atoms, as well as those associated to the cations belonging to the first two peaks in g(r) lay in a linear correlation, thus giving a clear indication that these components move together with the capsule. In contrast, free or loosely bound ions should exhibit diffusion coefficients expected to fall well above these correlations. This is exactly observed for ions belonging the region 3 (see Figure 11). Moreover, it is worth noting that the regression lines depend on the nature of the counterions *i.e.* NH_4^+ or NMe_4^+. The different behavior is due to the effect of the bound ions on the hydrodynamic drag including strongly bound ions and the surrounding water solvation shell.

Table 2. Regions considered for the MSD treatment and their related self-diffusion coefficient highlighting the different dynamic regimes.

NH_4^+		NMe_4^+	
Region	D($\mu m^2.s^{-1}$)	Region	D($\mu m^2.s^{-1}$)
1. R< 12.5 Å	112.37± 0.26	1. R< 15 Å	103.40± 0.41
2. 12.5 Å<R< 15Å	149.70± 1.3	2. 15 Å<R< 17.7Å	126.37± 0.28
3. 15Å<R< 22.5Å	908.30± 3.9	3. 17.7Å<R< 20Å	296.35± 0.81
4. R > 22.5 Å	1509.40± 1.0	4. R > 20 Å	851.6± 1.6

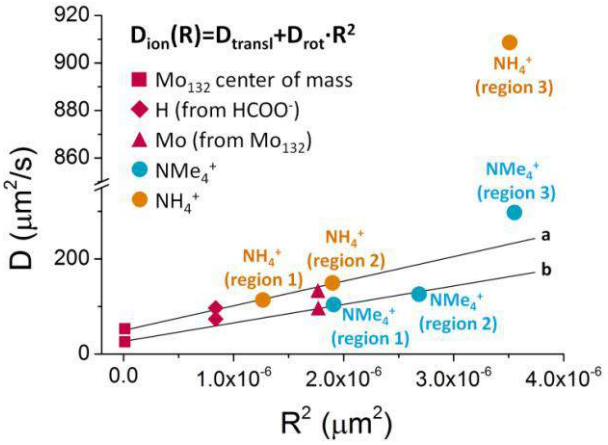

Figure 11: Regression of the self-diffusion coefficient data for different entities of the Mo_{132} capsule (center of mass, H and Mo atoms) (red) for two systems with different counter-cations: NH_4^+ (orange) and NMe_4^+ (blue). The results lay in straight line for each simulation (a for the NH_4^+ system and b for the NMe_4^+ system), which slope is, according to equation (4), the rotational diffusion coefficient (D_{rot}(a)= 5.13±0.16·$10^7 s^{-1}$; D_{rot}(b)= 3.87±0.15·$10^7 s^{-1}$).

Back to Figure 10c and 10d, we observe that some of the counter- cations are placed indeed very close to the capsule pores, forming a small peak for NMe_4^+ and NH_4^+ at the same distance from the center as the Mo atoms. However, for NMe_4^+, two high peaks nearby the capsule surface arise from a well defined distribution of cations. For NH_4^+, instead, the main peak at 11 Å corresponds to cations inside the capsule, while the distribution outside the capsule is much less structured than for NMe_4^+. The region 1 and 2 where the NH_4^+ ions are located either inside the capsule or in the pore give low *D* values, close to the experimental one measured for the capsule diffusion (see Table 2). For NMe_4^+ ions, region 1 comprises just one cation directly coordinated to the pore while 16 NMe_4^+ ions in the region 2 remain distributed nearby the capsule surface and located above the pores. Indeed, in this region, the average angle value between the N atoms of NMe_4^+ cations, the center of the capsule and the corresponding pore centroid is smaller than 10 degrees, indicating that all cations in this region are almost perfectly facing the pores, and that almost all pores are filled. In region 3, which is even further away the surface, NMe_4^+ and NH_4^+ cations behave differently. It is clear from the g(r) profiles and also from the diffusion coefficients that the ammonium cations interact with the capsule weakly than NMe_4^+.

III.2.8 Varying the apolar character of the cationic guest

In continuation with our keen interest on cation−$\{Mo_{132}\}$ interactions, and in an attempt to understand the nature of the driving force that governs the binding affinity of this host-guest recognition, the stability constant was determined for a wide series of other alkyl ammonium ions including the $Me_{4-x}NH_x^+$ series with x = 1-4, Me_3NR^+ (R= Et or Pr), NEt_4^+, and methylethylimidazolium cations (noted AA after).

- **series of alkyl ammonium ions (noted AA)**

For this study, the $(NH_4)_{52}\{Mo_{132}\}$ was used as precursor and the ^{1}H DOSY experiments of different cationic guests were carried at a fixed ratio AA/$\{Mo_{132}\}$ = 3 varying the concentration $C°$ in $\{Mo_{132}\}$ from 0 to 5.10^{-3} mol.L^{-1}. First, the ^{1}H NMR spectra of the AA - $\{Mo_{132}\}$ mixture in aqueous solution show exactly the same features of NMe_4^+ as discussed previously. The results obtained with the $Me_{4-x}NH_x^+$ series are shown in Figure 12 and those obtained with Me_3NR^+ (R = Et or Pr), NEt_4^+, and methylethylimidazolium cations are presented in Appendix (A2.1). The stability constant was obtained using similar methodology and calculations described above. Furthermore, the calculated self-diffusion coefficient D_{calc} using the stability constants (K_s and K_y = 370) is fairly consistent with the experimental ones

(Figure 12). All the obtained results are summarized in Table 3. These results show a continuous increase of K_s within the series $Me_{4-x}NH_x^+$. Besides, the stability constant increases further as the size (or the length) of the alkyl chains increases. The highest value was obtained for NEt_4^+ ion (K_s = 6500). The variation of the binding constant seems to reflect the apolar character of the cationic guests.

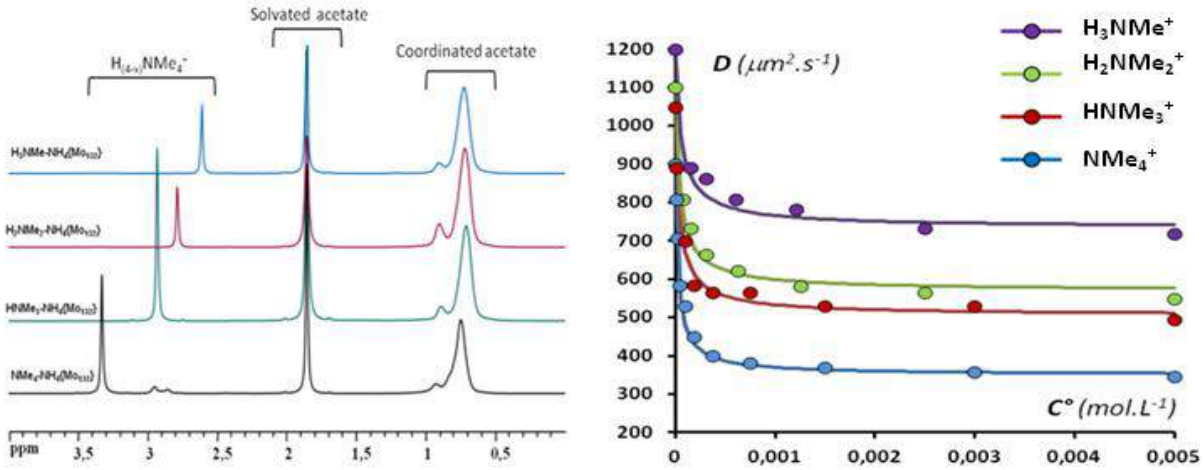

Figure 12: Left: ^{1}H NMR spectra of $H_{(4-x)}NMe_x^+$and $(NH_4)_{52}\{Mo_{132}\}$ mixture with $H_{(4-x)}NMe_x^+$ /Mo_{132} ≈ 3 and $C°$= 3mmol/L. Right: Experimental (circles) and calculated variations (solid lines) of the self-diffusion coefficient of the alkylammonium series $H_{(4-x)}NMe_x^+$ ion (D) with concentration in $\{Mo_{132}\}$ ($C°$). ^{1}H DOSY experiments have been carried out at a fixed ratio AA /$\{Mo_{132}\}$ ≈ 3 using $(NH_4)_{52}\{Mo_{132}\}$ salt.

- **Determination of the binding constant of the guanidinum cation.**

In 2003, Muller *et al*. reported the X-ray structure of $\{Mo_{132}\}$ where its 20 pores are plugged by guanidinium cations interacting with the oxygen atoms of the $\{Mo_9O_9\}$ pores through hydrogen bonding.[3] Since then, these results have never been supported by quantitative analysis in solution justifying efficient plugging process with $HGua^+$. Thus, we were interested to quantify this interaction to support the structural study of Muller et *al.*[3] As guanidinium cation do not constitute an ^{1}H NMR probe, we applied the ion competition method which consist to study the influence of the $HGua^+$ cations on the interaction between $\{Mo_{132}\}$ and NMe_4^+ ions (K_s = 1500). We prepared the $(GuaH)_{42}\{Mo_{132}\}$ salt through two successive precipitation from the ammonium salt as precursor $(NH_4)_{42}[Mo_{132}O_{372}(CH_3COO)_{30}(H_2O)_{72}]•300H_2O•10NH_4CH_3COO$. Characterization of the solid by IR, TGA and EDX are rather consistent with the formula $(HGua)_{42}[Mo_{132}O_{372}(CH_3COO)_{30}(H_2O)_{72}]•200H_2O$. The ^{1}H DOSY NMR experiments were carried out in the presence of 3 equivalents of NMe_4^+ by varying $C°$ in $(GuaH)_{42}\{Mo_{132}\}$. The experimental data shown in Figure 13 have been calculated using K_s = 1550 and K_y = 400.

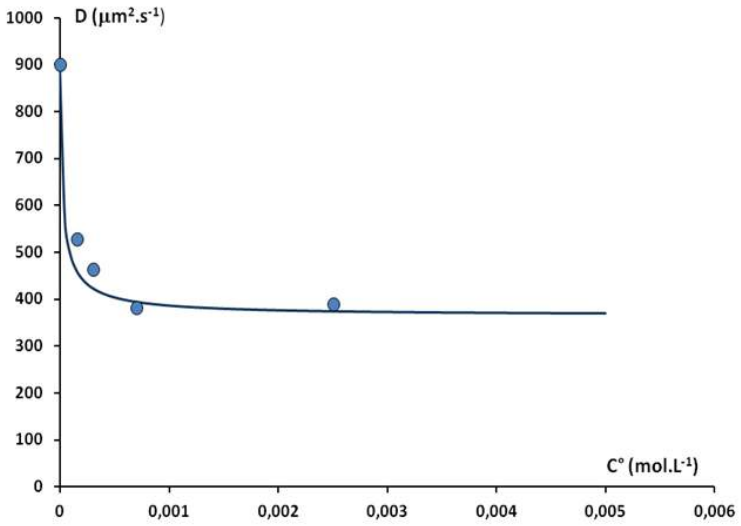

Figure 13: Experimental (circles) and calculated variations (solid lines) of the self-diffusion coefficient of the alkylammonium series NMe_4^+ ion (*D*) with concentration in $(GuaH)_{42}\{Mo_{132}\}$(*C*°). ^1H DOSY experiments have been carried out at a fixed ratio NMe_4^+ /$\{Mo_{132}\}$ ≈ 3.

Surprisingly, we observed that the association between the $\{Mo_9O_9\}$ pores with $HGua^+$ cations is characterized by moderate binding constant K_s = 400. Such a value appear similar to that found with NH_4^+ (K_s = 370) and significantly lower than that obtained with NMe_4^+ ions. Still here, the apolar character of the ions could be one of the factor which govern the host-guest stability.

Table 3: Stability constant of alkali, alkyl-ammonium, guadininium and imidazolium complexes of the multi-receptor Keplerate ions at 25 °*C* in D_2O.

Ion	NMe_4^+	$HNMe_3^+$	$H_2NMe_2^+$	H_3NMe^+
Stability constant	1550 ± 200	900 ± 70	750 ± 50	475 ± 40
ion	Me_3NEt^+	Me_3NPr^+	NEt_4^+	$HGua^+$
Stability constant	1800	1600	6500	400
Ion	*N,N'* MethylEthylimidazolium			
Stability constant	5800			

III.3 General Discussion

The relative binding affinities were determined by using the binding model described previously. The obtained results indicate the following order of the stability constants, NEt_4^+ > Me_3NEt^+ > Me_3NPr^+ ≈ NMe_4^+ > $HNMe_3^+$ > $H_2NMe_2^+$ > H_3NMe^+ > $HGua^+$ ≈ NH_4^+ > Na^+ > Li^+; This observed trend unambiguously demonstrate that binding constant is nicely correlated with the size and/or the apolar character of the cations. This correlation exists in diverse, structurally distinct systems ranging from simple crown assemblies to enzymes with complex architectures and suggests that desolvation plays an important and a general role in molecular

recognition.[32] The formation of the host guest assembly appears to be driven by initial desolvation of the guest (but also of the host) leading to the release of a substantial amount of water molecules into the solvent, accompanied with concomitant rearrangement of the hydrogen bonds network in solution. Such desolvation effect is shown in Figure 14

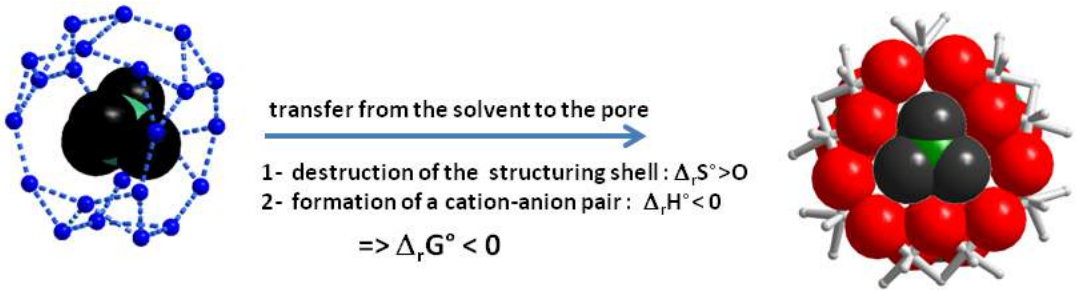

Figure 14: Schematic illustration of the hydrophobic effect

Structural comparison of the $\{Mo_9O_9\}$ pores with some crown-ether macrocycles such as the [27]-crown-O_9 macrocycle prompts us to extend such an analogy to the comparison of their respective binding constants. In the context, *Lehn et al* reported on the ionic recognition properties of some [27]-crown-O_9 derivatives toward a series of ammonium or guanidinium cation.[33] Lehn *et al.* have observed that hexacarboxylate derivative of the [27]-crown-O_9 macrocycle produces stable complexes in aqueous solution for which the NH_4^+ ion gives the most stable complex (Ks = 6000) while the host-guest stability decreases markedly as the number of methyl group increases in the ammonium $H_{(4-x)}NMe_x$ series. Furthermore, Lehn et al. observed that the neutral analogue of the [27]-crown-O_9 macrocycle does not exhibit any significant affinity for the selected guests in aqueous medium and then, the authors concluded that electrostatic interactions between the cationic guest and the anionic host contribute importantly to the stability of the complexes as the main *pull* factor in the inclusion process.

The decrease of the binding constant in the $H_{(4-x)}NMe_x$ series has been attributed by Lehn *et al.* to some steric hindrance between the bulky substituents attached to the macrocycle and the methyl groups of the cation. In the case of $\{Mo_{132}\}$ ion, similar conclusions should be given. The main driving force for the stability of the complexes must arise certainly from electrostatic interactions. However, we did not observed the same trend mentioned by Lehn *et al*. as the methyl group number increases. Surprisingly, the opposite trend is observed specifically using the $\{Mo_{132}\}$ ion. The stability constant increases moderately and continuously from NH_4^+ (K_s = 370) to NMe_4^+ (K_s = 1550). Such an opposite tendency is nicely shown plotting LnK_s versus the number of methyl groups noted n_{Me} (Figure 15).

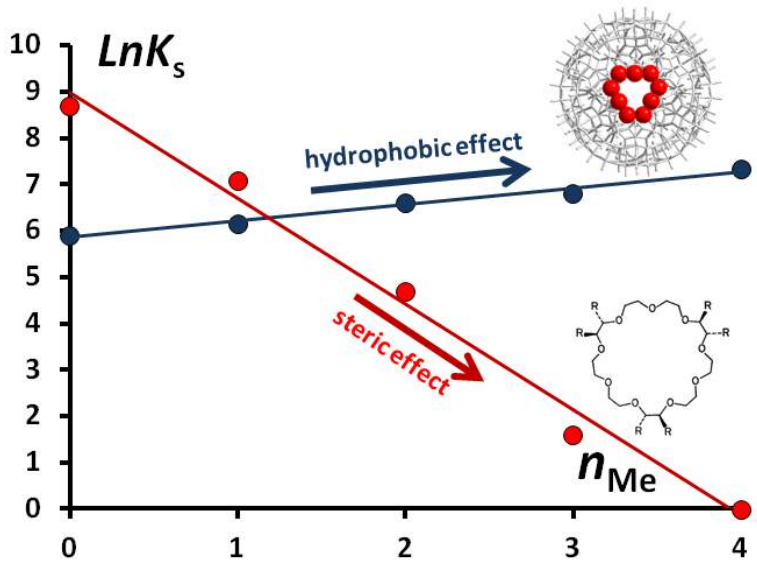

Figure 15: Correlation between Log*K*s and the number of the methyl substituents within the $H_{(4-x)}NMe_x^+$ alkyl-ammonium series obtained with the Keplerate-type ion $\{Mo_{132}\}$ (blue circles) and the hexacarboxylate [27]-crown-O_9 macrocycle (red circles) (data from ref [33].)

Therefore, although electrostatic interaction is the important driving force, our results show that an additional effect contributes to the host-guest stability. This additional contribution, identified as "the hydrophobic effect" constitutes a "pushing factor" for the transfer process from the solvent toward the pore. In few word, this “pushing factor” originates from the polar nature of the solvent i.e. H_2O and can be related to the presence of "high-Gibb’s energy" water molecules surrounded the guest (but also the host). The release of this type of water molecules into the solvent through formation of the host-guest adduct results in a significant decrease of the Gibb’s energy, mainly due to a large entropic gain.

Furthermore, in the periphery of the $\{Mo_9O_9\}$ pores, there is no attached bulky unit which could cause some unfavorable steric effect as in the case for the [27]-crown-O_9 and invoked by Lehn et al. to explain the guest selectivity. In our case, this is precisely the reason why the host-guest stability increases monotonously with the introduction of apolar substituents in the cationic substrate. Such a tendency is comparable in some extend to that found by Raymond *et al.* on the encapsulation of apolar ions into supamolecular tetrahedral $[M_4L_6]^{12-}$ anionic host.[29, 34]

- **Nature of the guest transfer from the solvent to the pore (Hydration structure of the Ammonium cations).**

While the above explanation suggests that guest desolvation is an important determinant in shifting the binding equilibrium, it is practically important to describe and highlight the hydration structure of our considered cations in solution. Such information can be obtained

from previous theoretical studies where the alkyl ammonium ions has been used as ionic model to study hydrophobic behavior in aqueous solution.[35]

a) Ion-water complexes. The structuration of ions in aqueous solution was described by Jorgensen *et al.* owing to *ab initio* Monte-Carlo simulations which were carried out for NH_4^+--H_2O and $CH_3NH_3^+$-H_2O in the three geometries shown below.[35]

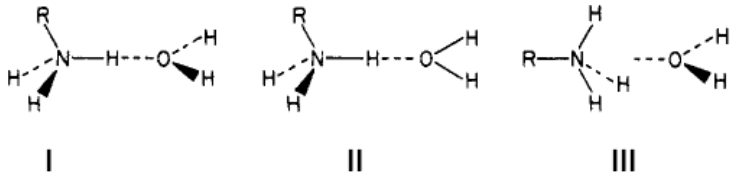

I II III

The obtained results, calculated for both cations showed a stability order I > II > III.

b) Energy Distributions. Ion-water energy distribution shown in Figure 16 gives important information on the nature of ion-water interactions. It should be known that the low energy band in these distributions is attributed to the strongly attractive interactions between the polar ions such as NH_4^+ and $MeNH_3^+$ and the first shell nearest water molecules, while the large peak centered at 0 kcal/mol represents remote water molecules, close in energy to the solvent molecules. The hydrogen bonding for NH_4^+, $CH_3NH_3^+$ is clearly apparent in the bands that spread from around -18 kcal/mol to about -8.9 kcal/mol. However, this feature is fully absent for Me_4N^+, meaning that in such a case, the strongest ion-water interactions are less geometrically specific and involve greater ion-dipole separations.[35]

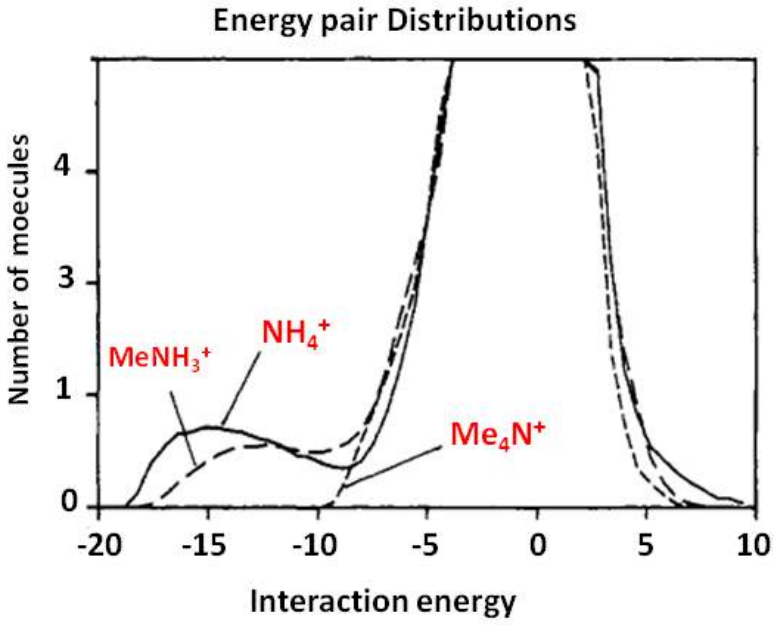

Figure 16: Distributions of individual solute-solvent interaction energies(kcal/mol) for ammonium ions in water. (data from ref.[35])

c) Proximity analysis. Such analyses were carried out by Jorgensen *et al.* to determine the water molecule number that compose the first hydration shell of the TAA cation. The computed hydration numbers of water molecules is given in Table 4 .[35]

Table 4: Computed Primary Hydration Numbers for Ammonium Ions at 25°*C*(data from ref [35])

Primary hydration number		
NH_4^+	$CH_3NH_3^+$	$(CH_3)_4N^+$
5	12.4	31

d) Thermodynamics parameters. Thermodynamics parameters associated to the hydration (or the solvatation) process of ammoniums ions are given in Table 5 from ref.[35] Significantly, the order of computed $\Delta_{sol}H°$ values is consistent with the experimental values and shows the expected reduction in exothermicity with increasing alkylation.

Table 5: Thermodynamic Results (kcal/mol) for Ions in Water at 25°C (data from ref.34)

Ion	$\mathbf{E_{sx}}$	$\mathbf{\Delta E_{ss}}$	$\mathbf{\Delta E_{sol}}$	$\mathbf{\Delta H_{sol}}$ [a]	$\mathbf{\Delta H_{exp}}$ [b]
NH_4^+	-148.6	65	-84	-85	-84
$CH_3NH_3^+$	-137	59	-78	-79	-75
$(CH_3)_4N^+$	-102.4	55	-48	-48	-41

[a] calculated, [b] experimental.

These results of the Monte Carlo simulations provided detailed insights into the hydration shell of the ions. NH_4^+ and $CH_3NH_3^+$ were found to have 5 and 4 water molecules strongly bound in their hydration shell. The hydration of $(CH_3)_4N^+$ is less specific and involves comparatively weak interactions with 31 water molecules in the first hydration shell. This means that the ammonium ion NH_4^+ is a "pure" hydrophilic object, while the NMe_4^+ ion exhibits a strictly "apolar" behavior featured by a weak energy of interaction and by a great number of surrounded water molecules. Other experimental results obtained by neutron diffraction techniques confirms the "apolar" behavior of Me_4N^+ in water.[36] In an expected way, increasing the length of the alkyl chain increases the hydrophobic behavior of the entity, a fact fully supported by experimental evidences and supported by theoretical analysis.[37] So the nice correlation observed in our host-guest system (see Figure 15) between the apolar character of the cationic guest and the associated binding constants are fully supported by the theoretical and experimental investigations about the hydrophobic effect. There are a lot of reviews which documented such an effect.[38] For example, Houk *et al.* have shown that a strong correlation exists between the binding affinity of the substrate and the average surface

area of the guest upon encapsulation for a wide variety of molecular recognition phenomena.[38] Similarly, Gilli and co-workers have suggested that an important driving force for molecular recognition of enzymes in drug-receptor interactions is the rearrangement of the hydrogen bond networks in aqueous solution rather than specific host-guest attractive interactions. [39] Specifically, they propose that the hydrogen bond networks in aqueous solution control the intermolecular association between guest and host. The Gibb's energy related to the host-guest formation refers to an enthalpic (noted $\Delta_r H°$) and an entropic (noted $\Delta_r S°$) contribution. The $\Delta_r H°$ value is primarily assigned to the energetic balance of the broken and formed hydrogen bonds during the reaction, while the observed $\Delta_r S°$ value is mainly due to the rearrangement of solvent. The enthalpic and entropic contributions in solvent hydrogen bond rearrangements are inversely related. These studies provided the initial clues to understand the main factors that are crucial in molecular recognition and the previously described solvent reorganization rationalizes the observed trend in the binding affinities of our host-guest system. The observed relatively low binding constants for NH_4^+ is due to its ability to form strong hydrogen bonds with solvating water molecules, that leads markedly to the decrease of the enthalpy contributions to solvation. On the opposite, the desolvation process requires an enthalpy penalty which must be paid in order to break the hydrogen bonds with surrounding solvent. In this case, unfavorable enthalpic contribution outweighs the entropic forces, thereby prohibiting strong guest complexation. Besides, as the apolar character of the guest increases in the series $NH_4^+ < MeNH_3^+ < Me_2NH_2^+ < Me_3NH^+ < Me_4N^+$, it could be expected that the enthalpic penalty decrease in relationship with the decreasing of the ability of the guest to interact with the solvent through hydrogen bonds. In the same time, the entropic contribution is expected larger. Presumably, upon desolvation of larger guests as in the case of NMe_4^+ or NEt_4^+ ions, a large number of solvated water molecules are released, therefore raising the binding affinity through increasingly favorable solvent rearrangements.

III.3.1 Extension to other POMs systems

Following the same strategy, further experiments were carried out with other POM systems such as $H_4SiW_{12}O_{40}•12H_2O$, $Na_{14}[P_5W_{30}O_{110}]•15H_2O$, and $K_{12}(NMe_4)[(AsW_9O_{33})_3(WO(OH_2))_3(Mo_2O_2S_2(H_2O)_4)]•20H_2O$ with NMe_4^+ as guest. It should be worth noting that the ^1H DOSY NMR study of the binding behavior of the $[Mo_{132}\text{-}Ac_{30}]^{42-}$ constitutes an ideal experimental system, because the self-diffusion coefficient of each component i.e. $D°$ for solvated guest, D^∞ for unplugged host $\{Mo_{132}\}$ and D_{obs} for the host-guest adduct can be determined experimentally. In many case, the studied polyoxometalate

does not contain any ^{1}H NMR probe allowing the measurement of D^∞. Nevertheless, the D^∞ value can be estimated from the Stokes–Einstein equation (Eq.4).

$$D = \frac{K_b T}{6\pi\eta r_h} \quad \text{Eq. 4}$$

Where k_b is the Boltzmann constant, T the temperature (T = 298 K), η the viscosity of the aqueous medium ($\eta \approx 1$ mPa.s) and r_h, the hydrodynamic radius which can be estimated from the crystallographic structure.[28]

Table 6: the hydrodynamic radius (r_h) of the used POM

POM	$r_{h\ (Å)}$	$D^\infty(\mu m^2.s^{-1})$
$H_4SiW_{12}O_{40}$•$12H_2O$	6	364
$Na_{14}[P_5W_{30}O_{110}]$•$15H_20$	10	208
$K_{12}(NMe_4)[(AsW_9O_{33})_3(WO(OH_2))_3(Mo_2O_2S_2(H_2O)_4)]$•$20H_2O$	11.9	190

1. Single pore polyoxometalate as binding model

The mixed salt $NMe_4K_{12}[(\alpha\text{-}AsW_9O_{33})_3(WO(OH_2))_3(Mo_2O_2S_2(H_2O)_4)]$•$20H_2O$ (noted $TMAK_{12}$-**1**) has been obtained as well shaped orange parallepipedic crystals with low yield (10%) by using $[Mo_2O_2S_2(OH_2)_6]^{2+}$ originated from the acidic hydrolysis of the cyclic precursor $K_{1.5}(NMe_4)_{0.5}[I_2Mo_{10}O_{10}S_{10}(OH)_{10}(H_2O)_5].20H_2O$ in the presence of sodium tungstate and the mixed sodium-potassium salt $K_6Na_3AsW_9O_{33}$•$6H_2O$. Surprisingly, despite the very low quantity of introduced NMe_4^+ (as impurities in the thiomolybdate precursor) and the conditions of crystallization which required a very large concentration in potassium chloride (2 mol.L^{-1}), one tetramethylammonium has been found in the structure in the close vicinity of the $\{As_3W_{30}\}$ backbone and located on the opposite face of the $\{Mo_2O_2S_2\}$ core. Actually, the triangular $\{As_3W_{30}\}$ arrangement designs the contour of a small anionic pocket which retains the $\{W_9O_9\}$ formula. This pocket resembles the $\{Mo_9O_9\}$ pores which compose the $\{Mo_{132}\}$ Keplerate ion. The X-ray diffraction analysis revealed that one methyl group of the NMe_4^+ ion plugs the hole, while the three remaining methyl groups are located at the surface of the pore.[27] Such a result suggests that strong interactions between the NMe_4^+ ion and the $\{W_9O_9\}$ pocket exists. In order to determine the binding constant, ^{1}H DOSY experiments were done at different concentration in $TMAK_{12}$-1. In this case, the binding model used to calculate the self-diffusion coefficient considers the competitive contribution of potassium counterions and the NMe_4^+ guests at the $\{W_9O_9\}$ pore. The calculate data fits

nicely with the experimental ones as shown in Figure 17, for the binding *c*onstants *K*s = 20000 and *K*y = 60 (with $Y^+ = K^+$). Such results reflects the strong affinity of the NMe_4^+ ion toward the $\{W_9O_9\}$ pores. It should be worth noting, that the calculations required the self-diffusion value of the POM (corresponding to the trapped NMe_4^+). Such a value has been calculated from Eq. 4 using r_h = 11.9 Å leading to D^{∞}= 190 $\mu m^2.s^{-1}$.

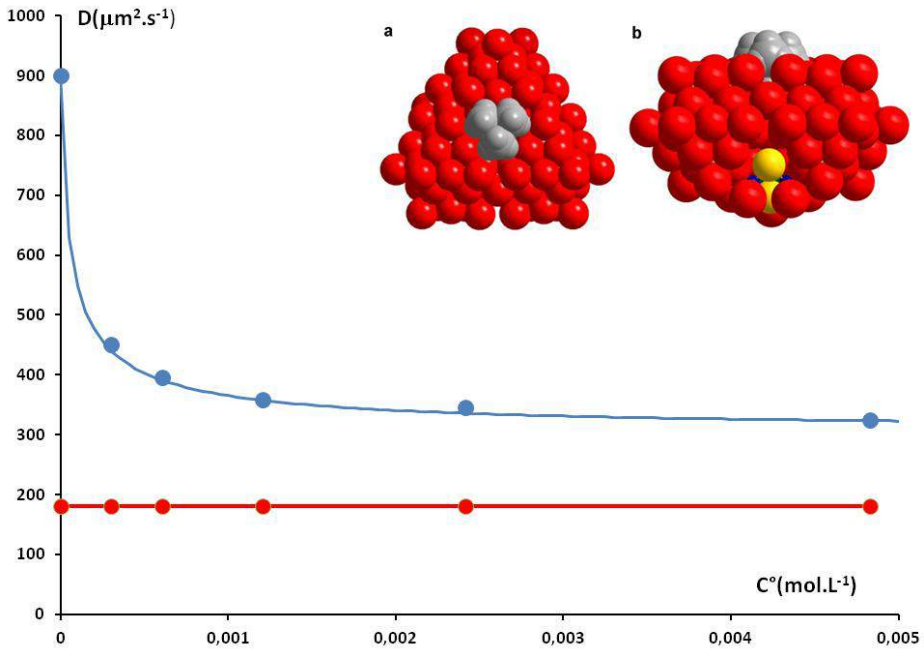

Figure 17: Experimental (blue circles) and calculated variations (blue solid lines) of the self-diffusion coefficient of the NMe_4^+ ion (*D*) with concentration in POM(*C*°); red line correspond to the calculated self-diffusion coefficients of POM using the Stokes-Einstein equation . ^{1}H DOSY experiments have been carried out at a fixed ratio NMe_4^+ /POM ≈ 1. Inset: Space filling representations highlighting the close interactions between the NMe_4^+ cation and the POM; (a) top view showing the location of the NMe_4^+ cation at the centre of the triangular arrangement. (b) side view showing the partial inclusion of the NMe_4^+ within the anionic pocket.

2. Presslyer anion ($Na_{14}[P_5W_{30}O_{110}]$•$15H_20$)

Besides we studied other polyoxometalate systems without apparent pores such as ($Na_{13}[NaP_5W_{30}O_{110}]$•$15H_20$). The self diffusion coefficients were measured at fixed NMe_4^+/POM = 2 and varying the concentration *C*° in POM from 0 to 6 $mmol.L^{-1}$. Surprisingly, large changes with D values were evidenced (Figure 19) showing significant interaction between NMe_4^+ and $[NaP_5W_{30}O_{110}]^{13-}$ even though $\{P_5W_{30}\}$ does not have apparent pores. It should be noted that this slow decrease of the diffusion coefficients cannot be fully explained from a simple binding model. Whatever the assumptions for such a specific case, we were not able to calculate the D_{obs} values over the concentration range to produce a fair agreements between experimental and calculated data. Such a discrepancy could be due to

the lack of any well-defined binding site for the NMe_4^+ ion site that produces no clear host-guest stoichiometry. Looking in the literature, we found that *Cronin et al.* succeeded to crystallize a mixed salt of the $\{P_5W_{30}\}$ ion, which contains tetrabutylammonium.[40] The solid-state structure of this complex is quite informative and provides insights into the origin of the interaction between the hydrophobic NBu_4^+ cation and the $\{P_5W_{30}\}$ ion surface. One NBu_4^+ cations appears located in the close vicinity of the hydrophilic oxygen of the $\{P_5W_{30}\}$ ion showing two butyl arms flattened and sticked over the surface of the $\{P_5W_{30}\}$ ions. Such a structural feature should illustrate the desolvation of the cations and could be viewed as consequence of the hydrophobic effect.

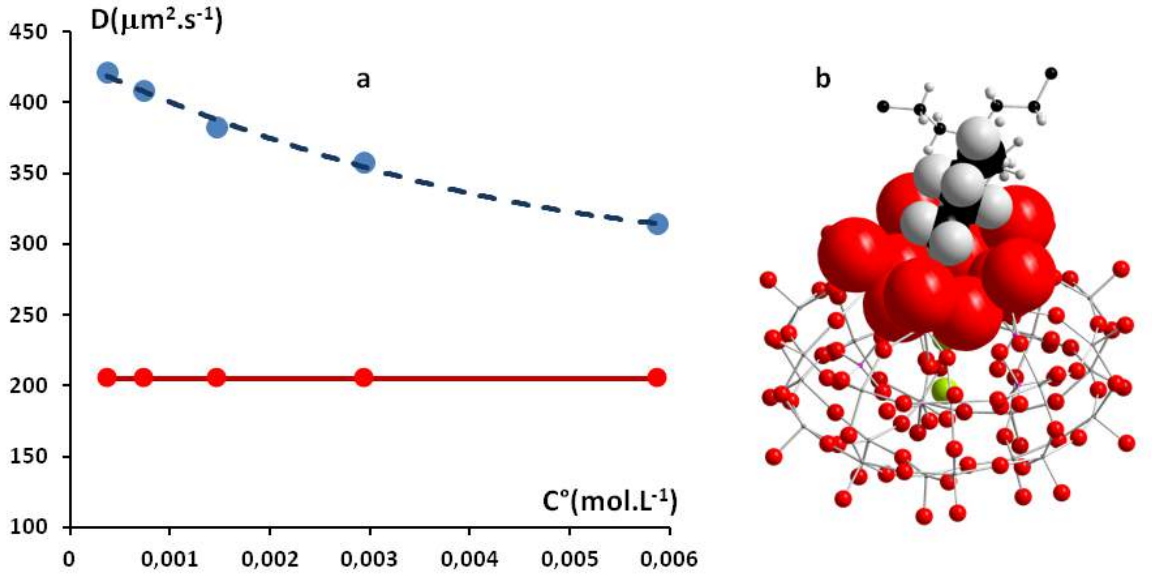

Figure 18: a) Experimental (blue circles) of the self-diffusion coefficient of the NMe_4^+ ion (*D*) with concentration in $\{P_5W_{30}\}^{14-}$ (*C*°) and of $\{\{P_5W_{30}\}^{14-}$ (red line) . ^{1}H DOSY experiments have been carried out at a fixed ratio NMe_4^+ /POM ≈ 2. b) : combined ball and stick and space filling representations showing the tetrabutyl ammonium sticking on the surface of $\{P_5W_{30}\}^{14-}$.

3. Keggin structure ($H_4SiW_{12}O_{40}$•$12H_2O$)

Ending with very basic Keggin anion, introduction of 0.88 equivalents of NMe_4^+ into a solution of $H_4SiW_{12}O_{40}$ lead to no significant decrease of the diffusion coefficients of the NMe_4^+ ions (see Figure 19). This evidences very weak and non-specific interaction between NMe_4^+ and the Keggin anion, as expected. In this case, only weak electrostatic interactions are involved.

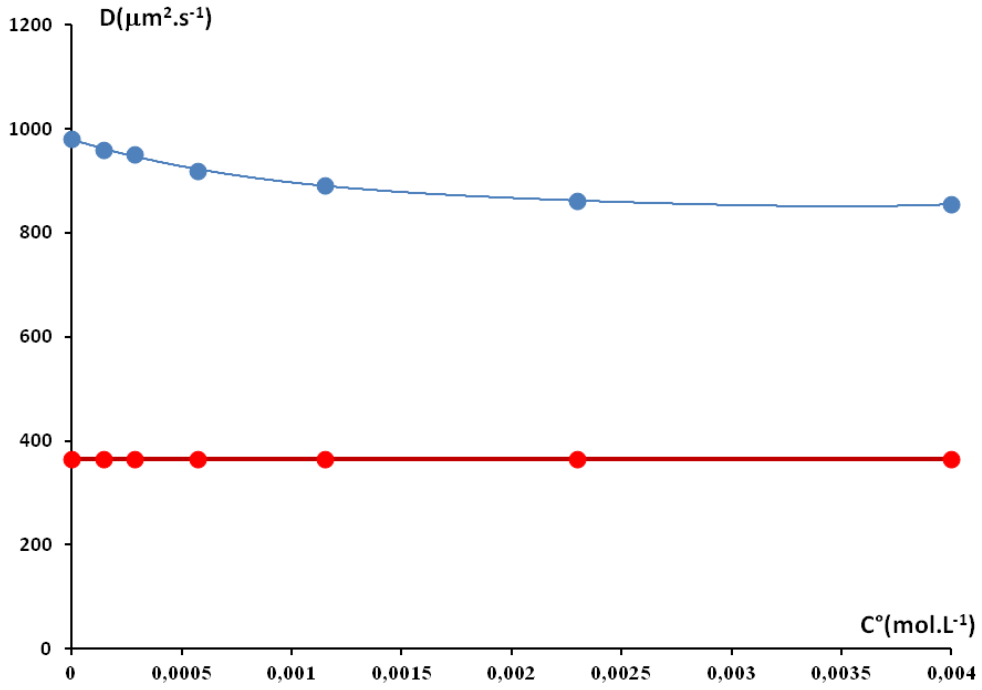

Figure 19: a) Experimental (blue circles) of the self-diffusion coefficient of the NMe_4^+ ion (*D*) with concentration in $\{SiW_{12}\}^{4-}$ (*C*°) and of $\{Si_4W_{12}\}^{4-}$ (red line) . ^{1}H DOSY experiments have been carried out at a fixed ratio NMe_4^+ /POM ≈ 0.88.

III.4 Selective encapsulation of tetramethylammonium cations within the cavity of the Keplerate-type ion compound

The previous section of this chapter was dedicated to the close inspection of interactions between the surface of the Keplerate ion $\{Mo_{132}\}$ and various cations such as Me_4N^+. The experimental condition for such studies required about 3eq of NMe_4^+ and the observed host-guest interaction was based on a fast exchange regime involving solvated and trapped NMe_4^+ ions. Increasing the ratio $Me_4N^+/\{Mo_{132}\}$ and the concentration *C*° of the system (*C*° = 5mmol.L^{-1}) leads to the appearance of two novel weak resonances at 2.9 and 3 ppm (see Figure 20) in addition to the other three resonances attributed to coordinated acetates (0.7-0.9 ppm), solvated acetates (1.9 ppm) and NMe_4^+ cations in fast exchange between the $\{Mo_{132}\}$ surface and the bulk solution (3.0-3.5 ppm). Generally, the presence of upfield resonances is a clear indication of encapsulation according to the typical shielding effect due to the inorganic host. Thus, these two resonances could be assigned to NMe_4^+ ions encapsulated in the $\{Mo_{132}\}$ cavity. It should be noted here that such novel NMR resonances are observed only in the presence of Me_4N^+ ion and were not observed in the recent studies with the sulfurated Keplerate analogue $[Mo_{132}O_{312}S_{60}(H_2O)_{72}(CH_3COO)_{30}]^{42-}$.[8] It should be mentioned also that the presence of other alkylammonium cations including $MeNH_3^+$, $Me_2NH_2^+$, Me_3NH^+, $Me_2NEt_2^+$, Et_4N^+, Me_3NPr^+, and Pr_4N^+ does not provoke the arising of additional upfield

resonances which should be the fingerprint of their encapsulation. This suggests a specific behavior of the NMe_4^+ cations toward the $\{Mo_{132}\}$ capsule. To get more insights about these new resonances, we developed an NMR strategy using one-, two-dimensional correlation methods and variable temperature NMR.

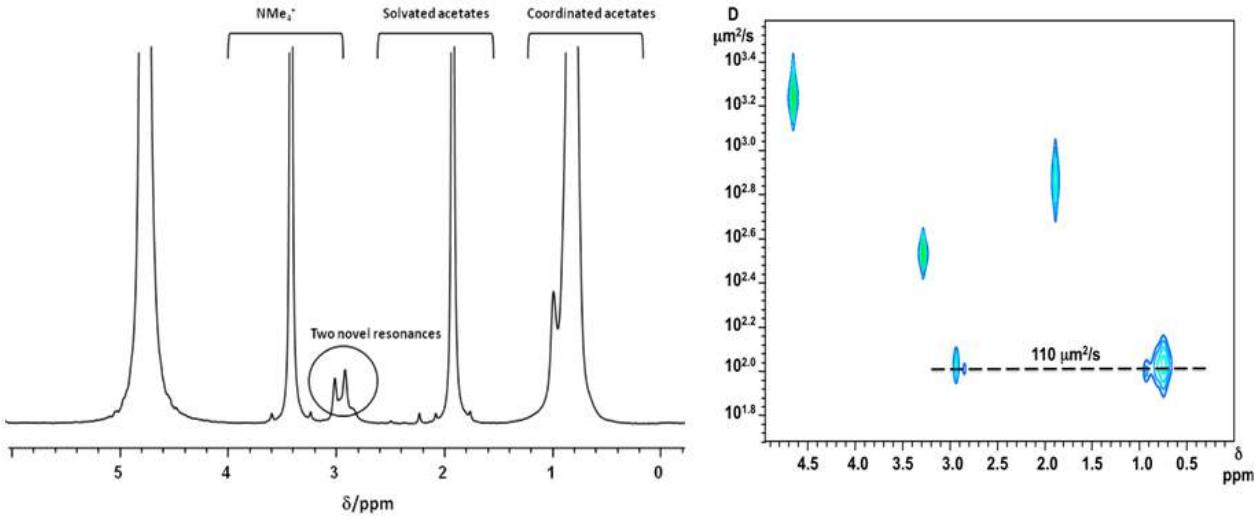

Figure 20: a) ^1H NMR spectra of $NMe_4^+$and $(NH_4)_{52}\{Mo_{132}\}$ in D_2O. b) ^1H 2D DOSY spectrum of $NMe_4^+$and $(NH_4)_{52}\{Mo_{132}\}$ in D_2O. Both with NMe_4^+ /Mo_{132}=3; C= 3mmol/l.

III.4.1 2D 1H DOSY NMR experiment

Evidence that the two new peaks could correspond to species that can be encapsulated within $\{Mo_{132}\}$ comes from 2D ^1H DOSY NMR experiments. ^1H DOSY experiments performed at different concentration in Keplerate aqueous solution containing 3 equivalents of NMe_4^+ ion reveals that coordinated acetates and these two weak resonances at 2.9 and 3 ppm exhibit the same self-diffusion coefficient value (D = 115 $\mu m^2.s^{-1}$) as shown in Figure 20. It should worth noting that such a value corresponds to that of the large Keplerate ion, meaning that 2.9 and 3 ppm species are strongly associated to the capsule. Such a result evidences a new situation for the Me_4N^+ ion in the presence of the $\{Mo_{132}\}$ capsule suggesting their encapsulation. In the new situation, the presence of distinct resonances features a slow exchange regime between the confined and solvated species. In addition, the self-diffusion D_{obs} of these new types of NMe_4^+ were found nearly non-dependent upon the concentration $C°$ in Keplerate with D_{obs} = D_{Mo132}**.** The ^1H NMR (chemical shift and self-diffusion coefficient) of the ^1H NMR spectrum are given for different concentration $C°$ in Table 7.

Table 7. Diffusion coefficients (in $\mu m^2.s^{-1}$) obtained from DOSY as a function of Keplerates concentration ; the ratio NMe_4^+ /{Mo_{132}} is fixed equal to 3.

C° mmol/l	AcOH (free)	AcO (0.75 ppm)	AcO (0.9 ppm)	NMe_4^+ (free)	$NMe4^+$ (2.9 ppm)	NMe_4^+ (3.0 ppm)	water
0.188	863	108	-[a]	450	-[a]	-[a]	1824
0.375	863	111	-[a]	422	-[a]	-[a]	1824
0.75	835	115	-[a]	383	-[a]	-[a]	1765
1.5	835	111	108	370	111	-[a]	1824
3	783	115	108	358	115	115	1765
5	758	111	104	347	108	131	1709

-[a] not or hardly detected.

III.4.2 EXSY and ROESY experiments

Definitive assignment that these new peaks correspond to encapsulated NMe_4^+ within the capsule have been established owing to 2D ^1H-^1H EXSY and ROESY NMR experiments. Importantly, the ^1H EXSY NMR spectrum (mixing time ranging from 50 to 500 ms) of 3 eq of NMe_4^+ and Keplerate ($C°$ = 5 mmol.L^{-1}) in D_2O shows crosspeaks between solvated NMe_4^+ cations (δ = 3.3-3.5 ppm) and the observed peaks at 2.9 and 3.0 ppm. This result confirm the attribution of these two resonances to encapsulated NMe_4^+ species involved within a slow exchange regime with the solvated ones. Furthermore, additional crosspeaks are observed between the resonances of the solvated and coordinated acetates (Figure 21). Such a correlation has been observed in previous studies and correspond also to a slow exchange process involving the inner and outer type of acetates.[41]

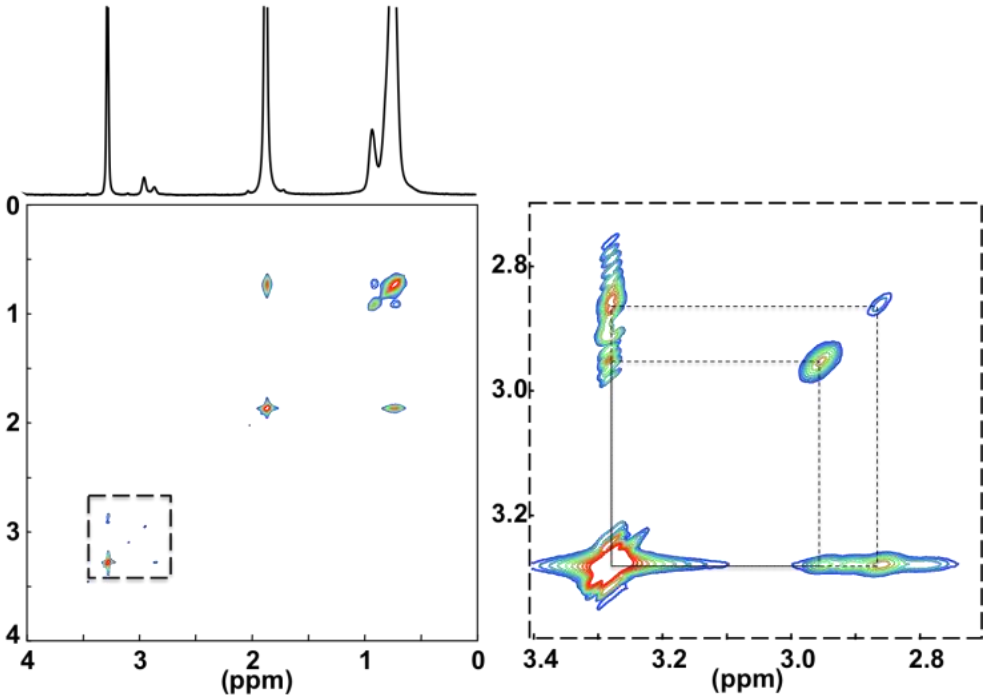

Figure 21. Left: ^1H EXSY NMR spectrum of $(NH_4)_{52}${Mo_{132}} in presence of NMe_4Cl, [{Mo_{132}}] = 5 mmol/l; NMe_4^+/{Mo_{132}} = 3. Right: expansion in the range of the NMe_4^+ resonances (around ca. 3 ppm).

Besides, the ^{1}H EXSY NMR spectrum shows that the crosspeak shared between the 2.9 ppm and the 3.3 ppm resonances is more intense than the other involving the 3 ppm line. Such a qualitative observation indicates that the 2.9 ppm signal should be involved in more efficient exchange process with the solvated ion than the 3.0 ppm other species. It means that the 2.9 ppm species should be located in labile or more accessible site. This differentiation in exchange rate/affinity with the free solvated NMe_4^+ species suggests significant differences in accessibility of these two types of bounded/encapsulated NMe_4^+. Furthermore, no exchange was detected between the two different types of NMe_4^+cations encapsulated within the Keplerate (no crosspeak between the δ = 2.9 and 3.0 ppm resonances), meaning that both sites of the encapsulated NMe_4^+should be nearly independent on the NMR time scale. This feature is in contrast to the scenario of acetate anions, where the two different internal acetate linkers observed at δ = 0.7 and 0.9 ppm are involved in a slow chemical exchange suggesting a typical compartmentalization phenomenon of occluded species into porous nanocapsules such as Keplerates. The lack of correlations between distinct types of encapsulated NMe_4^+ could be consistent with the small quantity of encapsulated NMe_4^+ cations (about 0.5 in average / Mo_{132} in these conditions, see below). In order to explore the NMe_4^+ encapsulated sites location as well as their mutual interactions and spatial proximities, the 2D ^{1}H ROESY experiment, which is based on dipolar interaction, was used.[42] The 2D ^{1}H ROESY spectrum of 5mmol.L^{-1} in Keplerate solution containing 3 eq of NMe_4^+ ions, shown in Figure 22 was acquired at mixing time ranging from 30 to 300 ms in D_2O at room temperature. Based on the ROE experiments, two types of correlations were identified. The on-phase correlations with respect to diagonal signals (blue cross-peaks) which are due to exchange processes in slow regime relative to NMR time scale, and are the same as those observed previously in the EXSY spectrum (Figure 21). The other correlations are anti-phase with respect to diagonal signals (red cross-peaks) which can be seen as a result of dipolar contact between involved species. Such anti-phase correlations are observed between protons of coordinated acetate (0.7-0.8 ppm) and protons of the methyl group of NMe_4^+ located at 2.9 and 3.0 ppm. These observations provide a direct evidence for the close vicinity of these NMe_4^+ species and the inner acetates within the Keplerate capsule. Additionally, no ROESY crosspeaks were found between bounded acetate ions to the pentagonal units (0.9 ppm)[41] and the encapsulated NMe_4^+cations. This also means that both sites are present in proximity to the acetates coordinated to the $\{Mo_2^{V}\}$ linkers.

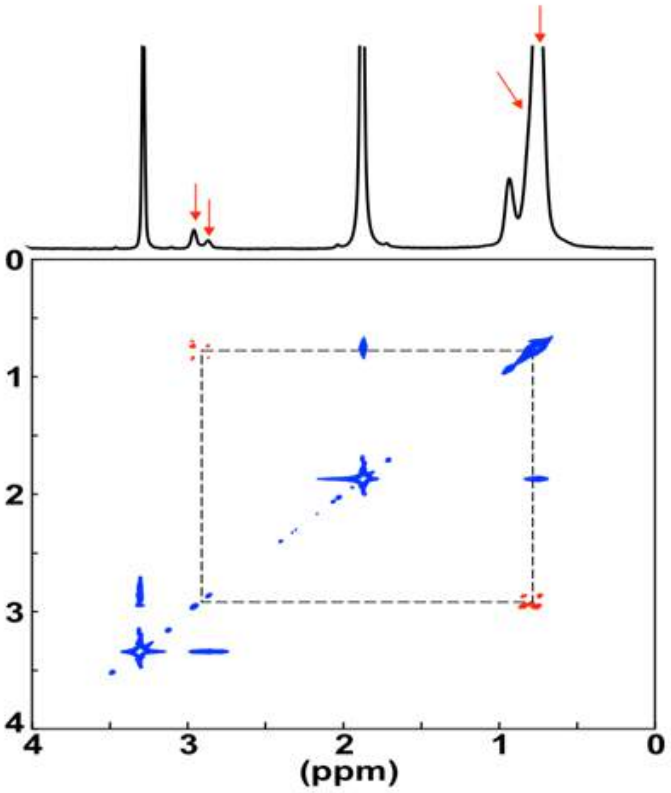

Figure 22. ^{1}H ROESY NMR spectrum of D_2O solution of $(NH_4)_{52}\{Mo_{132}\}$in presence of NMe_4Cl, [$\{Mo_{132}\}$] = 5 mmol/l; $NMe_4/\{Mo_{132}\}$ = 1.5. Negative ROE cross-peaks are shown as red contours, relative to the positive diagonal peaks in blue. The red arrows indicate the peaks involved in the ROESY correlations.

III.4.3 Concentration effect

Recording the ^{1}H NMR spectra of aqueous solution of $\{Mo_{132}\}$ containing 3 eq of NMe_4^+ at different concentration in Keplerate gives also strong arguments that the signals at 2.9 and 3 ppm correspond to two distinct encapsulated NMe_4^+, for which their relative population is concentration dependent. The variable concentration spectra are shown in Figure 23. Here, increasing concentration of the NMe_4^+-Keplerate system provokes the increase of the total number of encapsulated NMe_4^+. As shown in Figure 24**,** the relative intensity of the 2.9 ppm signals tend toward a constant value (about 0.18 NMe_4^+/capsule) while the 3 ppm line increases continuously until 0.28 NMe_4^+/capsule. It should be worth noting that the relative population between both sites is inverted as concentration increase. These results provide more insight into the encapsulation process and can be interpreted as two sites with different affinity for NMe_4^+. As the concentration increases, the site which exhibits the highest affinity should be preferentially occupied. It could correspond to the 2.9 ppm site. When saturation of these sites occurs (observed for 0.17 NMe_4^+/capsule), the population of the second site should increase and even should involve a higher NMe_4^+ number as depicted in Figure 24. The low rate of encapsulated NMe_4^+ (less than 0.5/capsule) is probably due to a competitive process

involving the 42 NH_4^+countercations as previously demonstrated on the pores at the surface of the capsule.

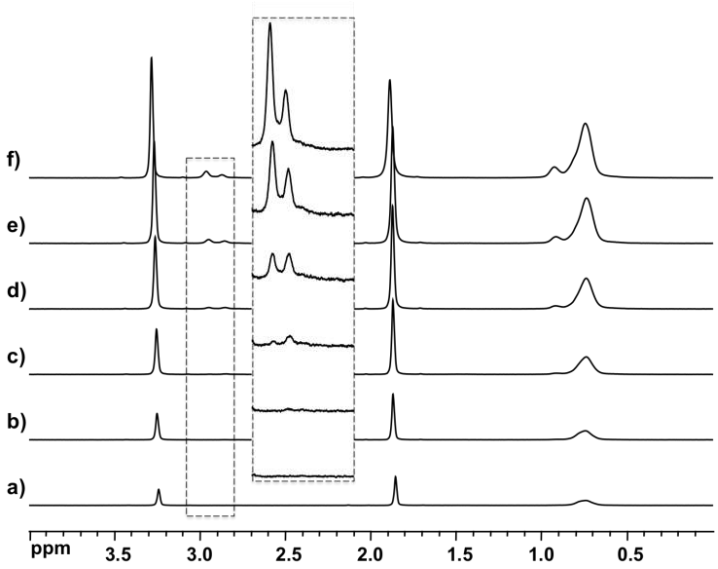

Figure 23. ^{1}H NMR spectra of $(NH_4)_{52}\{Mo_{132}\}$ in presence of NMe_4Cl at fixed $NMe_4^+/\{Mo_{132}\}$ = 3 and variable $\{Mo_{132}\}$ concentrations: a) 0.188, b) 0.375, c) 0.75, d) 1.5, e) 3, and f) 5 mmol/l. The insert highlights the the 3 ppm region.

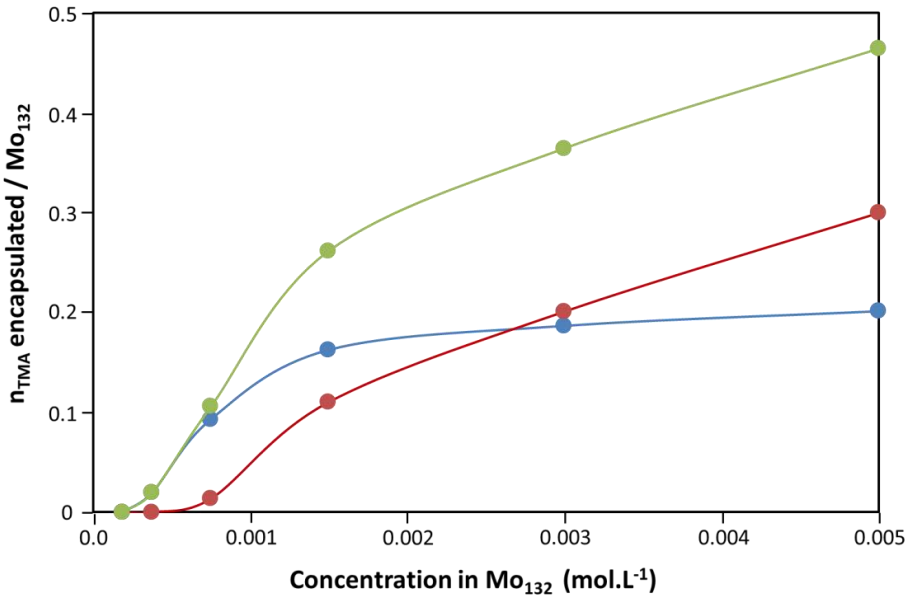

Figure 24: variation of the proportion of the two type of NMe_4^+ with concentration C° in $\{Mo_{132}\}$ (blue = 2.9 ppm species, red = 3.0 ppm species and green = total encapsulated NMe_4^+).

III.4.4 Dependence on $NMe_4^+/\{Mo_{132}\}$ ratio

Additional experiments were conducted to examine the effect of the ratio of NMe_4^+ on the number of encapsulated NMe_4^+ within the capsule. Figure 25 shows the ^{1}H NMR spectra of 5 mmol/L aqueous solution in $\{Mo_{132}\}$ for NMe_4^+ /$\{Mo_{132}\}$ ratio up varying from 1.5 to 9. Above 9 equivalent, further addition of NMe_4^+ provokes the precipitation of the Keplerate.

Conversely to the previous series of experiments, the relative ratio in population between the two types of encapsulated NMe_4^+ identified at 2.9 and 3.0 ppm was found constant, equal to ca. 40:60 respectively whatever the ratio NMe_4^+ /Mo_{132} used. However, the number of encapsulated NMe_4^+ per capsule increases slightly from 0.47 to 1 with the increase of the NMe_4^+ /{Mo_{132}} ratio up to 9 (see Figure 26). With the aim to increase further the number of encapsulated NMe_4^+, we prepared the NMe_4^+ salt of Keplerate which is expected to contain about 42 NMe_4^+ ion/capsule. Unfortunately, the limited solubility of this salt (1.5 mM) did not allow to increase the number encapsulated NMe_4^+.

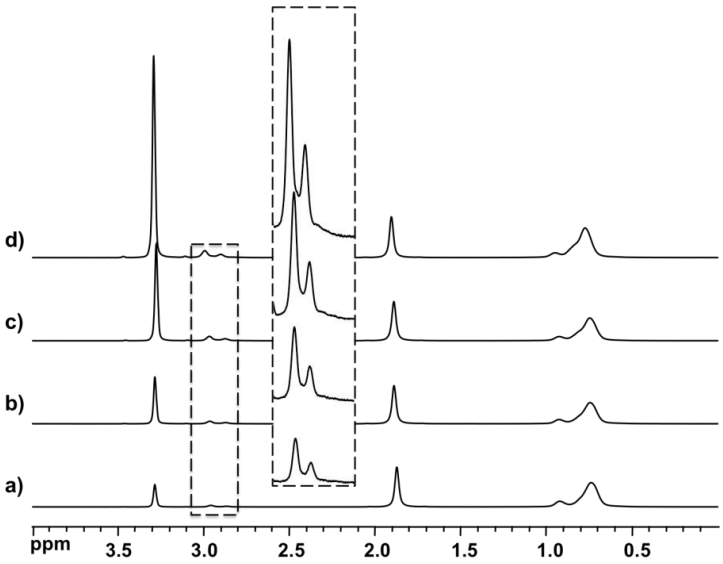

Figure 25. ^1H NMR spectra of D_2O solution of $(NH_4)_{52}${Mo_{132}}in presence of NMe_4Cl at fixed {Mo_{132}} concentration of 5 mmol/l and various NMe_4/{Mo_{132}} ratio: a) 1.5, b) 3, c) 6, and d) 9. In the inset a vertical expansion (x16) is displayed around ca. 3 ppm (a) and variation of encapsulated NMe_4^+ with ratio.

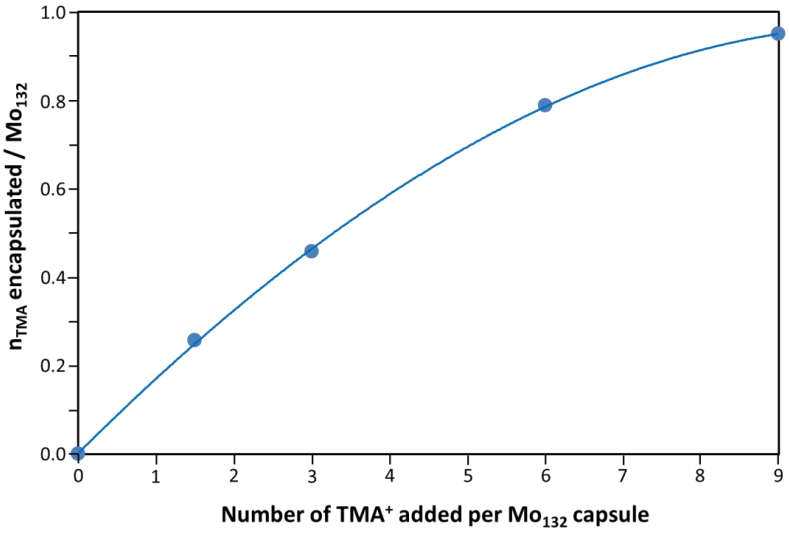

Figure 26: Variation of the number of NMe_4^+ cations encapsulated within the Mo_{132} capsule as a function of the NMe_4^+/{Mo_{132}} ratio.

III.4.5 Effects of the counter cations and the internal ligands

The encapsulation process of NMe_4^+ cations is thought to be controlled by various factors such as thermodynamic equilibriums depending on attractive/repulsive columbic interactions, steric hindrances, hydrophobic effect etc… Keeping in mind that the diameter of the 20 pores of the capsules have similar size of the NMe_4^+ cations, thus encapsulation process is necessarily demanding pores flexibility[43] which in turn probably prohibit kinetically the encapsulation process. Notably, pore flexibility is not the main criteria since from our studies, we know that the smaller cations as $MeNH_3^+$, $Me_2NH_2^+$, or Me_2NH^+ are not able to enter the capsule, while on the basis of very recent DFT calculations carried out by Bo et *al.* presented in the section III.2.7 of this chapter entitled "Molecular dynamics", the capsule cavity tends to encapsulate about a dozen of ammonium cations.

One hypothesis is that the presence of these 12 ammonium cations within the capsule induce unfavorable repulsive electrostatic interaction with NMe_4^+ leading thus to a limitation of their encapsulation as expressed by the competition process. To test this hypothesis, the encapsulation of NMe_4^+ ions was studied using sodium and lithium salts of keplerate. In the same conditions we did not find any significant effect of the nature of the countercations. The maximum number of encapsulated NMe_4^+ remains quite constant at about 0.5/capsule. Thus from these studies there is no clear evidence of the role of the countercations in the encapsulation process of NMe_4^+ cations.

Having successfully mapped the selective encapsulation of NMe_4^+ compared with other alkyl ammonium series and shown the vicinity of the encapsulated NMe_4^+ with the internal acetate ligands, this directly address the question of the importance of the acetates ligands in the encapsulation process. Replacement of the acetate ligands by sulfated ligands results in almost no encapsulation of NMe_4^+ cations , which definitively proves the direct involvement of the acetate ligands in this process. Furthermore, we have recently shown that the number of linked acetates vary significantly between 30 and 22 as function of the concentration of $\{Mo_{132}\}$. Thus to avoid decoordination and to expect the saturation of the 30 coordination sites by acetates, we worked in excess of acetate. In such conditions, the number of encapsulated NMe_4^+ increases until 2.3. As mentioned above, the pure NMe_4^+ salt of Mo_{132} in D_2O at 1.5 mM leads to the encapsulation of one NMe_4^+ cation per capsule. Similar experiment conducted in sodium acetate/ acetic acid (0.25 M / 0.25 M) medium allowed to significantly increase the total encapsulated NMe_4^+ to 2.3, thus supporting the hypothesis that encapsulation of NMe_4^+ is assisted by the internal acetate ligands, probably through ionic and/or hydrophobic interaction between acetate ligands and NMe_4^+. Inside the Keplerate the

acetates ligands define two types of sites shown in Figure 27. Three acetates ligands define a small pocket facing the pore, while facing the pentagonal motif, a larger site is lined by five acetates ligands. In a first assumption, we could tentatively assign the 2.9 and 3.0 ppm signals to these sites. Such an assumption is partially supported by 2D ROESY NMR experiments which demonstrate dipolar contact between encapsulated NMe_4^+ and acetate ligands. The presented results provide a preliminary and qualitative description for the behavior of NMe_4^+ cations in the presence of Keplerate-type ions, which should be confirmed and supported by supplementary experiments.

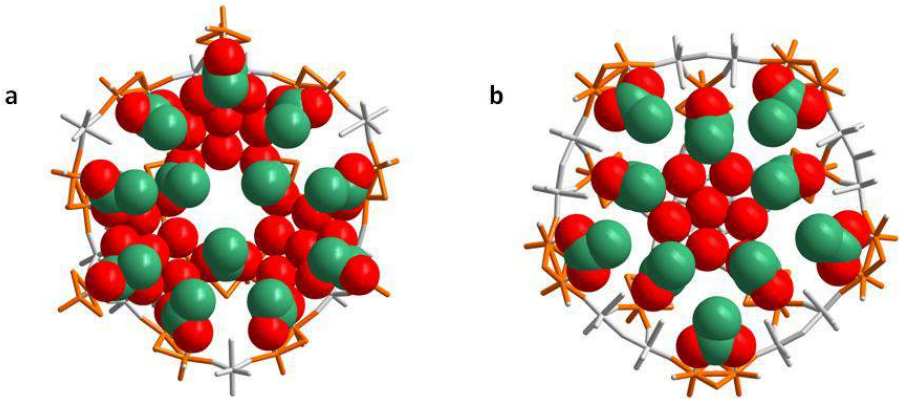

Figure 27: Mixed representation (wire and space filling) highlighting the inner acetate ligands (green and red) defining the two types of sites. a) Three acetates ligands define a small pocket facing the pore. b) five acetates ligands facing the pentagon.

III.4.6 Variable temperature NMR

A variable-temperature ^1H NMR spectroscopy experiment showed that resonances assigned to encapsulated and solvated/plugged NMe_4^+ cations do not coalesce up to 324 K in D_2O (see Figure 28) . This may reflects the remarkable lifetime of NMe_4^+ inside the capsule as well as that the energy barrier is too high to reach coalescences. Such observations have been already observed in case of acetates. In fact, all the signals of encapsulated NMe_4^+ and acetates are broaden, indicating an increase in the rate of internal/external exchange between different types of encapsulated NMe_4^+ and acetates. Inspection of all the resonance reveals a systematic shift for all resonances toward low field.[41]

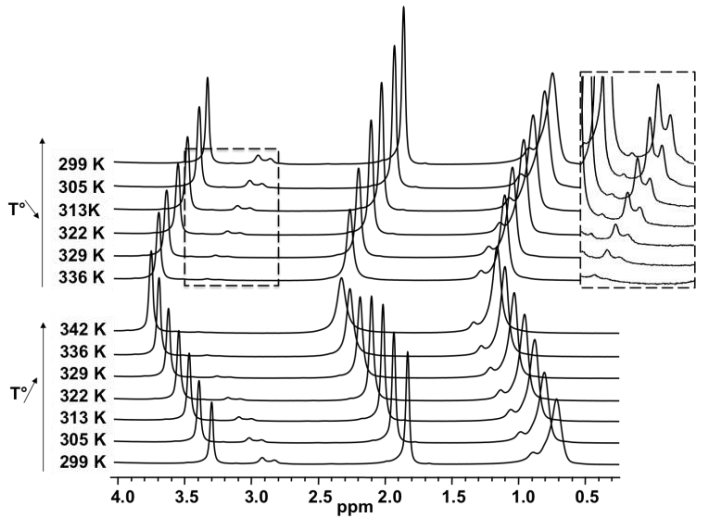

Figure 28. Variable temperature (increase and then decrease) ^{1}H NMR spectra of D_2O solution of$(NH_4)_{52}\{Mo_{132}\}$ in presence of NMe_4Cl: $[\{Mo_{132}\}]$ = 5 mmol/l; TMA/$\{Mo_{132}\}$ = 3. In the inset a vertical expansion (x16) is displayed around ca. 3 ppm.

Concomitantly, the proportion of the encapsulated NMe_4^+ species decreases from 26 % at 299 K to less than 4% after heating at 342 K, indicating that the encapsulation process becomes less favorable at high temperatures probably due to a negative contribution of the enthalpic term $\Delta_rH°$. The reversibility of the phenomena is demonstrated by increasing-decreasing subsequent NMR experiments showing recovery of initial spectrum after temperature change.

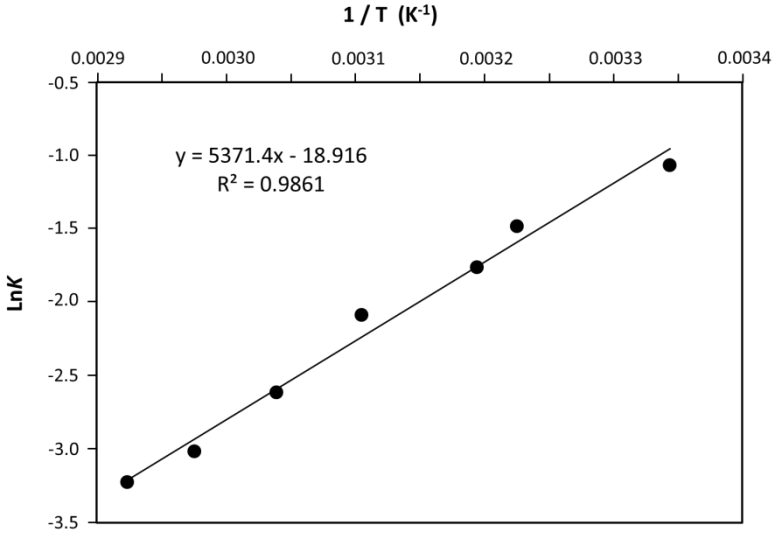

Figure 29: Van't Hoff plot for the equilibrium of NMe_4^+ encapsulation within Keplerate anion.

Even if the encapsulation process of NMe_4^+ inside the Mo_{132} capsule probably involves at least three steps, a first approach of the encapsulation process of the NMe_4^+ cation consists of considering the global encapsulation process, described by the very simple equilibrium $(NMe_4^+)_{outside} = (NMe_4^+)_{inside}$. Determination of the encapsulation equilibrium ($K_{encapsulation}$)

by ^{1}H NMR spectroscopy at different temperature allowed the deriving the thermodynamic parameters of the encapsulation process. Plotting ln*K* versus T^{-1} (see Figure 29) then revealed the enthalpy change $\Delta_r H^\circ$ = -45 ± 1 kJ.mol^{-1} and the entropy change $\Delta_r S$ = -157 ± 5 J.mol^{-1}.K^{-1} for the NMe_4^+ encapsulation. These data show that the encapsulation of NMe_4^+ into $\{Mo_{132}\}$ is enthalpically driven, but disfavored from an entropic point of view. The exothermic encapsulation of NMe_4^+ is probably attributed to attractive coulombic interactions between the cationic guest and the anionic free acetate. However, encapsulation induces a significant entropy decrease understood as loss of degrees of freedom upon internal binding. In such conditions, the encapsulation process involves plugging NMe_4^+ as initial step and therefore does not require any desolvation of the NMe_4^+. In such case, the encapsulation process correspond to a "pure" aggregation resulting in a net decrease of the entropy.

IV. Conclusion

To explore the multi receptor properties of the 20 $\{Mo_9O_9\}$ pores of the spherical keplerate-type $\{Mo_{132}\}$ ion, the ^{1}H DOSY NMR methodology was used to track the interactions between various alkyl ammonium cations and the anionic capsule. The self diffusion coefficients of the cationic guest were found to depend strongly upon the concentration and the nature of the countercations. Quantitative analysis of the obtained data based on two-site diffusion system in fast exchange regime on NMR time scale involving solvated and trapped guest. The full data analysis were based through on a chemical model taking into account ions competition at the 20 independent pores. Such analysis allowed determining the stability constant of the plugging process for the selected guest observed by ^{1}H NMR and for the countercations such NH_4^+ or alkali. Surprisingly, the affinity of the capsule toward a series of cationic guests in aqueous solution increases continuously with the apolar character of the guest as demonstrated by the significant increase of the stability constant from 370 to 6500, for NH_4^+ and NEt_4^+, respectively. Such results evidence that hydrophobic effect may be actually the primary driving force for determining binding affinities which correspond to a pushing factor from the solvent to the POM surface. Furthermore, we showed through pore titration experiment that such a transfer correspond to the selective trapping of NMe_4^+ within the 20 pores.

High level dynamic calculations resulting from collaboration with Bo et *al.* have been carried out in the conjunction of our experimental data. The analysis of the radial distribution functions g(r) reveals that the hydrophilic NH_4^+ and hydrophobic NMe_4^+ ions behave not differently in the close vicinity of the Keplerate cluster. In contrast, the NMe_4^+ ions were

identified as sharp distributions related to different scenario such as a firmly trapped or as a labile and wriggling guest facing the{Mo_9O_9} pores.

Further detailed inspection of the ^{1}H NMR spectrum of NMe_4^+ revealed two novel resonances at 2.9 and 3 ppm appeared which were attributed to encapsulated NMe_4^+. Such behavior was extensively investigated by a combination of ^{1}H NMR methods and various two-dimensional correlation techniques including DOSY, EXSY and ROESY which demonstrate the ability of Keplerate to act as a specific nanoscale recipient for tetramethylammonium cation. By carrying out careful studies on this behavior, we identified at least three situations for the NMe_4^+ in the presence of Keplerate. The guest trapping at the {Mo_9O_9} pores correspond to the primarily situation before encapsulation over two inner sites within the cavity. However, the number of encapsulated NMe_4^+ cations per Keplerate remains less than two probably due to competitive effect of the countercations. Beside, we observed that only NMe_4^+ ions can be encapsulated among the series of the alkyl ammonium $Me_{4-x}NH_x^+$ meaning that all are not yet fully understood. Nevertheless, the global encapsulation process is strongly entropically disfavored as the result of a "net" aggregation reaction. In summary, this study will contribute for a better understanding of the behavior of the Keplerate ions in aqueous solution, a necessary step for the development of innovative and creative supramolecular chemistry. This work demonstrates the fine control of the plugging process can be achieved from the knowledge of the binding constants, crucial for broader implications in supramolecular chemistry for i) a regulated access to the large inner cavity, ii) the functionalization of the surface of the capsule, iii) the development of immobilization strategies of Keplerate-type ions on surfaces or within specific matrices. More broadly, as hydrophobic interactions are affected by various factors such as the presence of specific cationic moieties such like ammonium or guanidinium residues, these results demonstrate that control of the hydrophobic strength is possible, opening the way for fine regulations of the interactions between large polyoxometalates and specific hydrophobic patches of biological substrates such as proteins or DNA.[44-45]

V. References

[1] A. V. Davis, D. Fiedler, G. Seeber, A. Zahl, R. van Eldik, K. N. Raymond, *J. Am. Chem. Soc.* **2006**, *128*, 1324-1333.

[2] R. M. Yeh, J. Xu, G. Seeber, K. N. Raymond, *Inorg. Chem.* **2005**, *44*, 6228-6239.

[3] A. Muller, E. Krickemeyer, H. Bogge, M. Schmidtmann, S. Roy, A. Berkle, *Angew. Chem.-Int. Edit.* **2002**, *41*, 3604-3609.

[4] C. Schaffer, A. M. Todea, H. Bögge, O. A. Petina, D. Rehder, E. T. K. Haupt, A. Müller, *Chem.-Eur. J.* **2011**, *17*, 9634-9639.

[5] S. Kopilevich, A. Gil, M. Garcia-Rates, J. Bonet-Avalos, C. Bo, A. Müller, I. A. Weinstock, *J. Am. Chem. Soc.* **2012**, *134*, 13082-13088.
[6] A. Muller, L. Toma, H. Bogge, C. Schaffer, A. Stammler, *Angew. Chem.-Int. Edit.* **2005**, *44*, 7757-7761.
[7] D. Rehder, E. T. K. Haupt, H. Bögge, A. Müller, *Chemistry – An Asian Journal* **2006**, *1*, 76-81.
[8] A. Rezaeifard, R. Haddad, M. Jafarpour, M. Hakimi, *J. Am. Chem. Soc.* **2013**, *135*, 10036-10039.
[9] A. Müller, S. K. Das, S. Talismanov, S. Roy, E. Beckmann, H. Bögge, M. Schmidtmann, A. Merca, A. Berkle, L. Allouche, Y. Zhou, L. Zhang, *Angewandte Chemie International Edition* **2003**, *42*, 5039-5044.
[10] V. S. Korenev, A. G. Boulay, M. Haouas, F. Bannani, V. P. Fedin, M. N. Sokolov, E. Terazzi, S. Garai, A. Müller, F. Taulelle, J. Marrot, N. Leclerc, S. Floquet, E. Cadot, *Chemistry – A European Journal* **2014**, *20*, 3097-3105.
[11] P. W. Kuchela, C. J. Durrantb, *Journal of Magnetic Resonance* **1999**, *139*, 258-272.
[12] A. R. Waldeck, P. W. Kuchel, A. J. Lennon, B. E. Chapman, *Progress in Nuclear Magnetic Resonance Spectroscopy* **1997**, *30*, 39-68.
[13] A. Einstein, *Ann. Phys* **1906**, *19*, 289 – 306.
[14] M. E. Moseley, Y. Cohen, J. Mintorovitch, L. Chileuitt, H. Shimizu, J. Kucharczyk, M. F. Wendland, P. R. Weinstein, *Magnetic Resonance in Medicine* **1990**, *14*, 330-346.
[15] P. J. Basser, *Nmr in Biomedicine* **1995**, *8*, 333-344.
[16] E. O. Stejskal, J. E. Tanner, *J. Chem. Phys.* **1965**, *42*, 288-292.
[17] J. E. Tanner, *The Journal of Chemical Physics* **1970**, *52*, 2523-2526.
[18] S. J. Gibbs, C. S. Johnson Jr, *Journal of Magnetic Resonance (1969)* **1991**, *93*, 395-402.
[19] B. Levay, *The Journal of Physical Chemistry* **1973**, *77*, 2118-2121.
[20] K. S. Cameron, L. Fielding, *The Journal of Organic Chemistry* **2001**, *66*, 6891-6895.
[21] F. Venema, A. E. Rowan, R. J. M. Nolte, *J. Am. Chem. Soc.* **1996**, *118*, 257-258.
[22] M. Tominaga, K. Suzuki, M. Kawano, T. Kusukawa, T. Ozeki, S. Sakamoto, K. Yamaguchi, M. Fujita, *Angewandte Chemie International Edition* **2004**, *43*, 5621-5625.
[23] P. Shestakova , G. Absillis, F. J. Martin-Martinez, F. De Proft, R. Willem, T. N. Parac-Vogt, *Chemistry – A European Journal* **2014**, *20*, 5258-5270.
[24] A. Müller, E. Krickemeyer, H. Bögge, M. Schmidtmann, F. Peters, *Angew. Chem.-Int. Edit.* **1998**, *37*, 3360-3363.
[25] I. synthesis.
[26] I. Creaser, M. C. Heckel, R. J. Neitz, M. T. Pope, *Inorg. Chem.* **1993**, *32*, 1573-1578.
[27] M.-A. Pilette, J. Marrot, S. Duval, F. Bannani, S. Floquet, F. Sécheresse, E. Cadot, *C. R. Chim.* **2012**, *15*, 124-129.
[28] S. Floquet, S. Brun, J.-F. Lemonnier, M. Henry, M.-A. Delsuc, Y. Prigent, E. Cadot, F. Taulelle, *J. Am. Chem. Soc.* **2009**, *131*, 17254-17259.
[29] M. D. Pluth, B. E. F. Tiedemann, H. van Halbeek, R. Nunlist, K. N. Raymond, *Inorg. Chem.* **2008**, *47*, 1411-1413.
[30] M. Garcia-Ratés, P. Miró, J. M. Poblet, C. Bo, J. B. Avalos, *The Journal of Physical Chemistry B* **2011**, *115*, 5980-5992.
[31] M. Garcia-Ratés, P. Miró, A. Müller, C. Bo, J. B. Avalos, *The Journal of Physical Chemistry C* **2014**, *118*, 5545-5555.
[32] D. H. Leung, R. G. Bergman, K. N. Raymond, *J. Am. Chem. Soc.* **2008**, *130*, 2798-2805.

[33] J. M. Lehn, P. Vierling, R. C. Hayward, *Journal of the Chemical Society, Chemical Communications* **1979**, 296-298.
[34] T. N. Parac, D. L. Caulder, K. N. Raymond, *J. Am. Chem. Soc.* **1998**, *120*, 8003-8004.
[35] W. L. Jorgensen, J. Gao, *The Journal of Physical Chemistry* **1986**, *90*, 2174-2182.
[36] J. Z. Turner, A. K. Soper, J. L. Finney, *The Journal of Chemical Physics* **1995**, *102*, 5438-5443.
[37] A. Yamakata, M. Osawa, *The Journal of Physical Chemistry Letters* **2010**, *1*, 1487-1491.
[38] K. N. Houk, A. G. Leach, S. P. Kim, X. Zhang, *Angewandte Chemie International Edition* **2003**, *42*, 4872-4897.
[39] P. Gilli, V. Ferretti, G. Gilli, P. A. Borea, *The Journal of Physical Chemistry* **1994**, *98*, 1515-1518.
[40] D. Gabb, C. P. Pradeep, T. Boyd, S. G. Mitchell, H. N. Miras, D.-L. Long, L. Cronin, *Polyhedron* **2013**, *52*, 159-164.
[41] A. Grego, A. Müller, I. A. Weinstock, *Angewandte Chemie International Edition* **2013**, *52*, 8358-8362.
[42] A. Grego, A. Muller, I. A. Weinstock, *Angew. Chem.-Int. Edit.* **2013**, *52*, 8358-8362.
[43] A. Ziv, A. Grego, S. Kopilevich, L. Zeiri, P. Miro, C. Bo, A. Müller, I. A. Weinstock, *J. Am. Chem. Soc.* **2009**, *131*, 6380-6382.
[44] S. Garde, *Nature* **2015**, *517*, 277-279.
[45] C. D. Ma, C. Wang, C. Acevedo-Velez, S. H. Gellman, N. L. Abbott, *Nature* **2015**, *517*, 347-350.

Chapter III
Synthesis, Characterization and Application of Surfactant Encapsulated Keplerate Clusters

Chapter III- Synthesis, Characterizations and Applications of Surfactant Encapsulated Keplerate Clusters.

I. Introduction

The overview of giant spherical porous nanocapsule "Keplerate" presented in Chapter I shows that they exhibit unique structural features and easy exchange of the internal ligands/ functionalities, leading to unmatched range of properties that could allow them to be considered as the basis for a new area of nanochemistry and nanomaterials science. This emerging class of molecular materials can display properties in a large panel of domains such as magnetism,[1-2] catalysis [3-4], electric conductivity,[5] non-linear optics [6-7] and are able to serve as nano-reactor for chemical reactions, such as stoichiometric transformations of substrates with unusual selectivity.[8] Several research groups have been interested in this cluster in the context of materials science where many efforts have been done to organize and stabilize such materials. For example, introducing "Keplerate" into suitable matrices as polymers,[9] polyelectrolyte,[10] silica [11] or organic cations [12-15] can enhance further materials stability and the synergistic functionalities of POMs and matrices.

Of particular example, the countercations of $\{Mo_{132}\}$ can be replaced by dioctadecyl-dimethylammonium cations ($DODA^+$) resulting in functional nanodevices.[16] Motivated by this target, *Floquet et al* reported for the first time that wrapping Keplerate-type capsule with $DODA^+$ cations lead to the formation of materials $(DODA)_{36}(NH_4)_6[Mo_{132}O_{372}(CH_3COO)_{30}(H_2O)_{72}] \bullet 75(H_2O)$, $(DODA)_{44}(NH_4)_{14}[Mo_{132}O_{312}S_{60}(SO_4)_{23}(H_2O)_{86}]$ and $(DODA)_{56}(NH_4)_{16}[Mo_{132}O_{312}S_{60}(SO_4)_{30}(H_2O)_{72}]$ exhibiting liquid crystalline properties.[17-18]

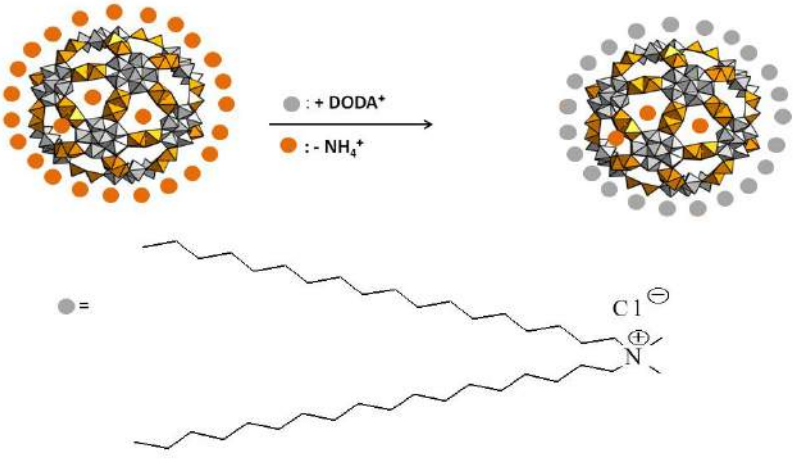

Figure 1: Synthesis of DODA-Keplerate based materials.

After a first order phase transition close to room temperature these materials self-organizes in a hexagonal layered structure with a lamellar periodicity "*h*" ranging from 26.9 Å to 34.6 Å as function of the number of introduced $DODA^+$ cations. Such an organization could appear surprising if we consider the isotropic spherical shape of the cluster and suggest that the alkylammonium heads of the $DODA^+$ cations are not strongly linked to a specific point of the cluster. Therefore the only way to explain this organization is that the $DODA^+$ cations adopt non-uniform distribution around the anionic surface, thus leading to oblate spherical associations within the layers which are partially imbricated when "*h*" value is found less than the size of the "Keplerate" cluster (Figure 2).[18]

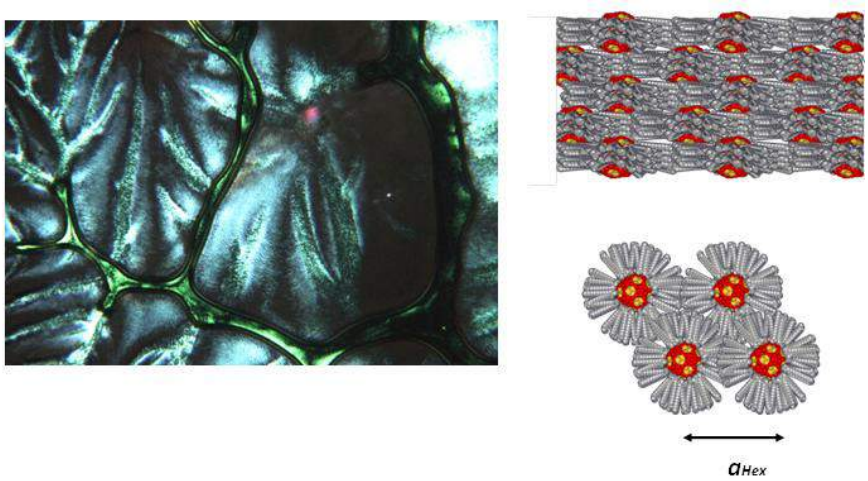

Figure 2: Left: Fluid and birefringent optical texture (TD-POM) for $DODA_{44}$–$Mo_{132}S_{60}$. Right: Top and perpendicular views of the layers in the mesophase. Reproduced from reference [17].

Chapter II provided clear evidence of the strong interaction between $\{Mo_{132}\}$ and of 1-methyl-3-ethylimidazolium cations. Indeed, the binding constant with Keplerate was found to be 5800, much higher than that obtained for tetramethylammonium cations (K= 1500) which can be chemically related to $DODA^+$ cation. Based on this, some questions are to be addressed: Is it possible to build liquid crystal phases with alkylimidazolium cations comprising non-mesogenic unit but simple alkyl chain through encapsulation procedure ? If so, will this stronger interaction provoke uniform liquid crystal materials exhibiting different arrangements like cubic or hexagonal? Finally, can we use these encapsulated Keplerate based materials for diverse properties as ion-trapping properties or incoporate them into silica sol-gel materials?

In this chapter, the main part deals with the synthesis and characterization of imidazolium-based keplerare materials by IR spectra spectroscopy, ^1H NMR, elemental analysis, and

Thermo-Gravimetric Analyses. Then, the stability of materials was assessed by TGA and FT-IR at variable temperature and the liquid crystal properties were studied by polarized optical microscopy (TD-POM), differential scanning calorimetry (DSC) and small angle variable temperature X-ray diffraction (SA-XRD) in collaboration with E. Terazzi (University of Geneva, Switzerland). Preliminary work highlighting the efficient effect of the organic matrix on the interaction and recognition process between the {Mo_{132}} nanocapsule and metallic cations as Zn^{2+} will be also introduced. Finally, we will conclude this chapter by presenting our first attempts to combine the encapsulation method and the sol–gel technique by using terminal hydroxyl cationic surfactant as a bridging unit to obtain a keplerate-based, silica-sol–gel hybrid material.

II. Results and Discussion

II.1 Synthesis of {Mo_{132}}-based materials

The objective of this study was to combine different imidazolium cations shown in the Figure 3 with the Keplerate cluster noted $(NH_4)_{52}\{Mo_{132}\}$, so we synthesized five 1-alkyl-3-methylimidazolium salts with variable alkyl length ranging between 12 and 20, while the dendritic imidazolium salt ($C_{85}H_{145}N_2O_5Br$) (noted dendronBr) was synthesized by E. Terazzi (university of Geneva, Switzerland). The Keplerate-based materials were prepared by mixing aqueous solution of $(NH_4)_{52}\{Mo_{132}\}$ with a large excess (*ca* 170 equivalents per Mo_{132} capsule) of the cations in chloroform in order to replace the maximum of NH_4^+ countercations. After stirring the mixture for about 1 hour, the Keplerate capsule {Mo_{132}} was totally transferred into the chloroform phase, indicating rapid and quantitative transfer. The desired materials were precipitated by addition of ethanol into the chloroform phase and finally filtered, washed with ethanol and dried in air (see Scheme 1 and experimental section). We were also interested to investigate the possibility of tuning the final composition of the material, so we used a mixed salt of C_{12} and C_{20} imidazolium cations with different ratios. The materials were obtained as brown-black soft solids, no longer soluble in water, but soluble in organic solvents such as chloroform, acetonitrile, toluene and even ether, suggesting that the hydrophilic surface of {Mo_{132}} has been effectively modified by the used organic cations. These compounds were characterized by routine techniques such as FT-IR, TGA and EDX which all exhibit the same characteristics. Therefore, in the following, the results of one sample chosen arbitrarily are presented.

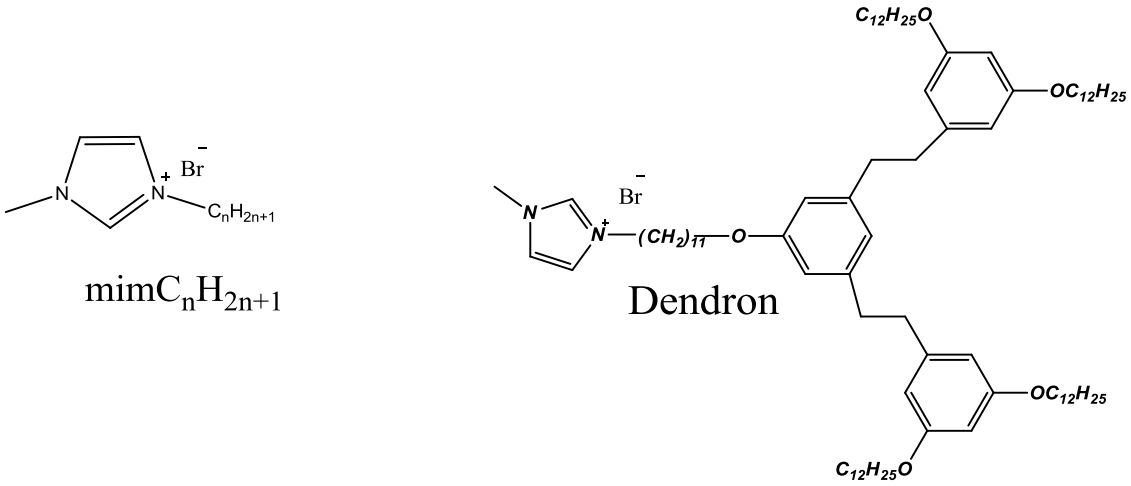

Figure 3: Chemical structure of the used cations

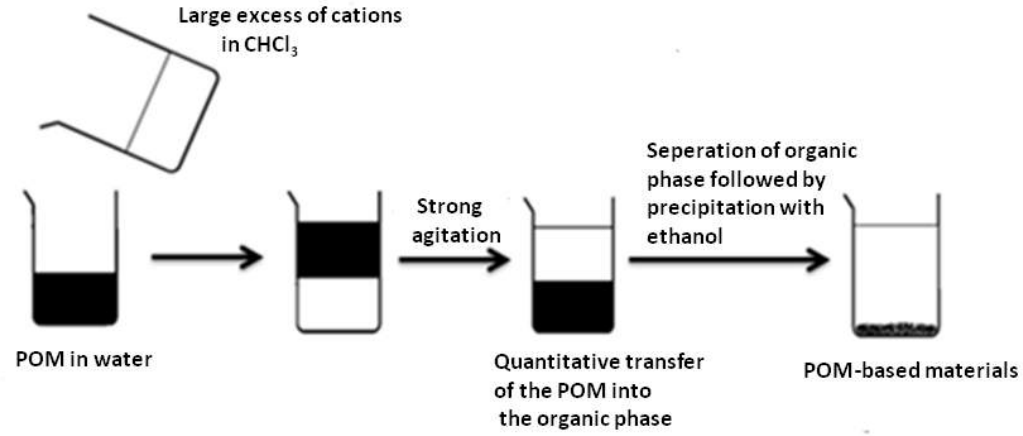

Scheme 1. Synthetic Path for Keplerate-Based Materials

II.2 Characterization of {Mo_{132}}-based materials

II.2.1 FT-IR spectroscopy studies

FT-IR spectra were performed using Diamond ATR technique and an ATR correction was applied. As shown in Figure 4 for the compound **(mimC_{18})$_{37}$-{Mo_{132}}** the comparison with the spectra of the precursors confirm the conservation of the {Mo_{132}} cluster and its association with the organic cation since the IR-spectrum exhibits the characteristic bands of {Mo_{132}}, in agreement with the previously published results.[18] In addition the band at 1403 cm^{-1} attributed to NH_4^+ countercations is still present in the final material indicating that not all NH_4^+ have been replaced by the organic cations.

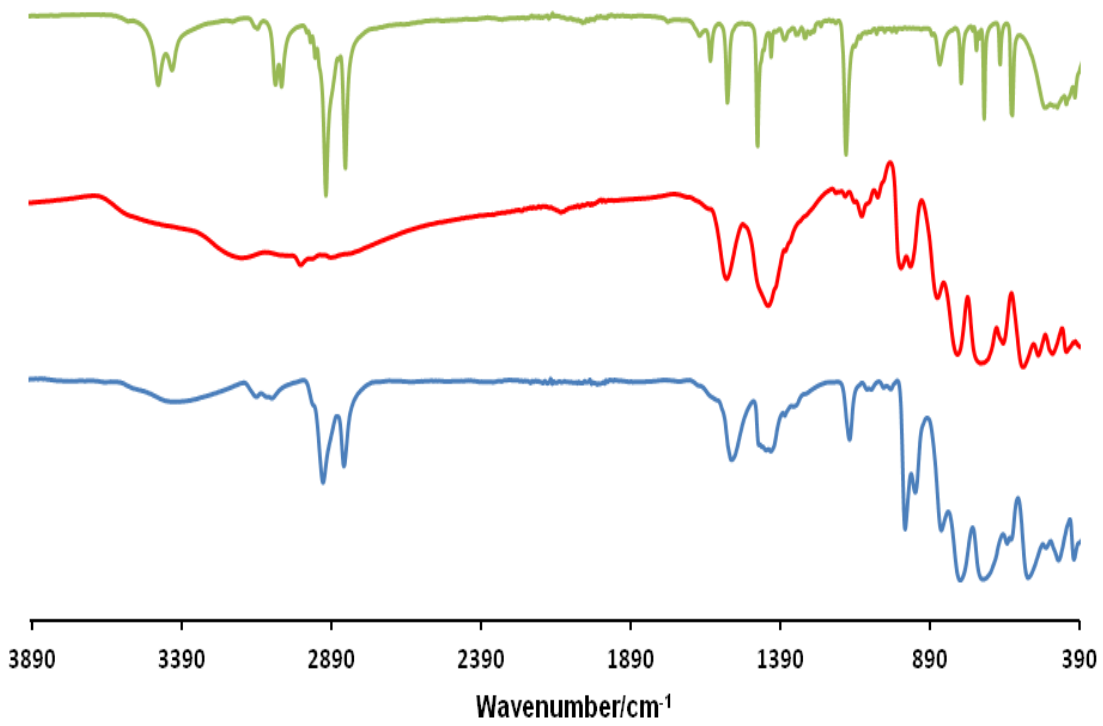

Figure 4: FT-IR spectra of ($mimC_{18}$)Br (green), $(NH_4)_{52}\{Mo_{132}\}$ (red) and **$(mimC_{18})_{37}\{Mo_{132}\}$** (blue)

II.2.2 ^{1}H NMR spectra

As seen in chapter II, the ^{1}H NMR is a good tool for studying interaction between keplerates and organic cations. The ^{1}H NMR spectrum of **$(mimC_{18})_{37}\{Mo_{132}\}$** in $CDCl_3$ depicted in Figure 5 shows that the resonance signals of the N-CH_2 and N-CH_3 protons of imidazolium cations and the protons of the imidazolium rings are considerably broadened and shifted in the final materials as compared to the signals of the pure imidazole salts.

The signal broadening may be explained in terms of the strong association of the imidazolium cations and the keplerate cluster due to electrostatic interaction, which would restrict the mobility of the cations.[19-20] Furthermore it appears difficult to distinguish the NMR lines assigned to the Keplerate capsule, which preclude further accurate investigations.

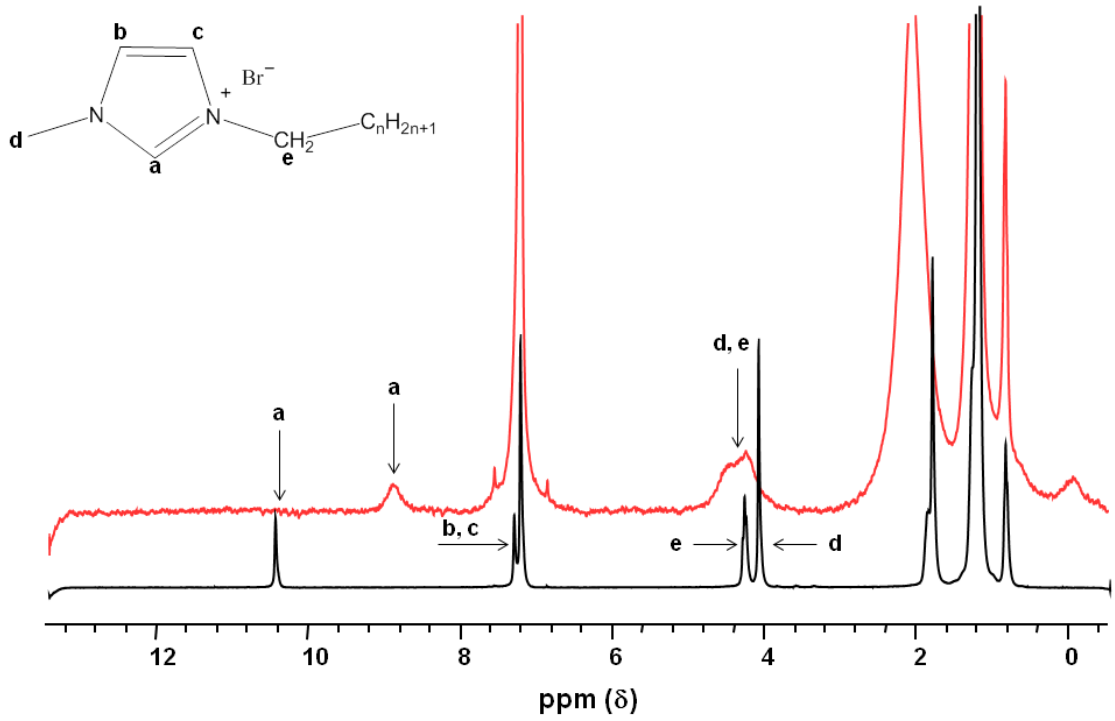

Figure 5: ^{1}H NMR spectra of mimC_{18} (bottom spectrum) and **(mimC_{18})$_{37}${Mo_{132}}** (top spectrum) in $CDCl_3$

II.2.3 Chemical composition

Based on the data of the elemental analyses (C, H, N, Mo), EDX and TGA, the structural formula of the obtained materials is suggested. The results are summarized in the Table 1 and more details are available in the experimental section. First, EDX measurements evidence only the presence of the Mo and reveals the absence of Br which could be due to a residual presence of the starting salt.

The number of acetate ligands within the Mo_{132} capsule is 30 for all synthesized compounds, except for the two compounds with C_{12} and C_{14} alkyl chain length where the number found is 28. The cationic ammonium headgroup can replace the ammonium counterions and combine with {Mo_{132}} through electrostatic interaction. It should be noted, despite the large excess of the used cations, the replacement of the ammonium cations was not complete, in agreement with FT-IR spectra . The number of interacting organic cations with the Keplerate were found between 36 and 41 cations. This is consistent with the previously published results with DODA salts [17-18] and suggests that some NH_4^+ are probably trapped within the {Mo_{132}}, in agreement with DFT calculations performed in Chapter II. Interestingly, it is worth noting that by mixing imidazolium salts bearing C_{12} and C_{20} alkyl chains, a purely statistical distribution is observed in the final compound where the number of each organic cations is controlled with

the introduced ratio. This demonstrates the possibility to tune the final composition of the mixed surfactant encapsulated clusters, a key parameter for the design of functional materials.

The TGA measurements verify exactly the estimated structural formula of these materials. The weight loss of 3.5-8 % between room temperature and 170°C in TGA results under air atmosphere matches the weight content of coordinated and crystallized water molecules and is consistent with the calculated one from the structural formula.

Table 1 : Molecular formulas of the samples from elemental analysis and TGA curves (refer to experimental section for details)

Sample	Estimated molecular formula
$(mimC_{12})_{35}$-$\{Mo_{132}\}$.	$(mimC_{12}H_{25})_{36}(NH_4)_5[Mo_{132}O_{372}(CH_3COO)_{30}(H_2O)_{76}].24H_2O$
$(mimC_{14})_{36}\{Mo_{132}\}$	$(mimC_{14}H_{29})_{38}(NH_4)_4[Mo_{132}O_{372}(CH_3COO)_{30}(H_2O)_{76}].34H_2O$
$(mimC_{16})_{41}\{Mo_{132}\}$	$(mimC_{16}H_{33})_{41}(NH_4)_1[Mo_{132}O_{372}(CH_3COO)_{30}(H_2O)_{72}].38H_2O$
$(mimC_{18})_{37}\{Mo_{132}\}$	$(mimC_{18}H_{37})_{37}(NH_4)_5[Mo_{132}O_{372}(CH_3COO)_{30}(H_2O)_{72}].48H_2O$
$(mimC_{20})_{37}\{Mo_{132}\}$	$(mimC_{20}H_{41})_{37}(NH_4)_5[Mo_{132}O_{372}(CH_3COO)_{30}(H_2O)_{72}].43H_2O$
$(mimC_{12})_{20}(mimC_{20})_{20}\{Mo_{132}\}$.	$(mimC_{12}H_{25})_{20}(mimC_{20}H_{33})_{20}(NH_4)_2[Mo_{132}O_{372}(CH_3COO)_{30}(H_2O)_{72}].38H_2O$
$(mimC_{12})_{33}(mimC_{20})_7\{Mo_{132}\}$.	$(mimC_{12}H_{25})_{33}(mimC_{20}H_{33})_7(NH_4)_2[Mo_{132}O_{372}(CH_3COO)_{30}(H_2O)_{72}].48H_2O$
$(mimC_{12})_8(mimC_{20})_{33}\{Mo_{132}\}$.	$(mimC_{12}H_{25})_8(mimC_{20}H_{33})_{33}(NH_4)[Mo_{132}O_{372}(CH_3COO)_{30}(H_2O)_{72}].38H_2O$
$(Dendron)_{36}\{Mo_{132}\}$.	$(C_{85}H_{145}N_2O_5)_{36}(NH_4)_6[Mo_{132}O_{372}(CH_3COO)_{30}(H_2O)_{72}].58H_2O$

II.2.4 Stability

II.2.4.a TGA under N_2 and O_2

Chemical stability of the Mo_{132}-based materials was assessed by TGA under a mixture of N_2 and O_2 and FT-IR measurements at variable temperature under air or under N_2. As seen in Figure 6, the TGA curve recorded for **$(mimC_{18})_{37}\{Mo_{132}\}$** under oxygen displays several steps. A first step between 20°C and 180°C corresponds to the removal of all the water molecules (hydration and coordination). Furthermore, the TGA traces of all samples show a strong weight loss observed in the temperature range 250-800 °C which are attributed to the decomposition of the cations and the acetate ligands of $\{Mo_{132}\}$ to reach at high temperature a molybdenum oxide. This second step would give a thermal stability at about 250°C for our $\{Mo_{132}\}$ based materials.

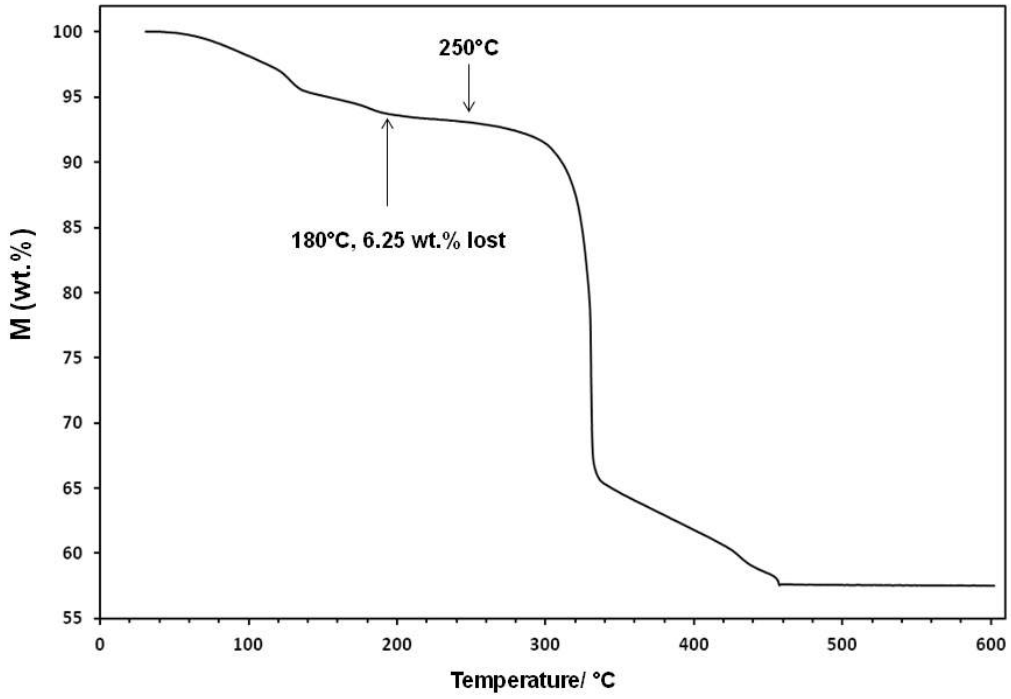

Figure 6: TGA curve of **$(mimC_{18})_{37}\{Mo_{132}\}$** (5°C/minute, under O_2+N_2)

II.2.4.b Variable temperature FT-IR studies

Variable temperature FT-IR studies were performed on the compound **$(mimC_{18})_{37}\{Mo_{132}\}$** arbitrary chosen as a reference compound. The FT-IR spectra were recorded in diffuse reflectance mode on a sample of **$(mimC_{18})_{37}\{Mo_{132}\}$** solid dispersed into a KBr matrix. The experiments were done either under air or under a flow of nitrogen between 20°C and 400°C with a heating/cooling rate of 2°C/minute. Besides, several thermal cycles were conducted with different limits to verify the reversibility of the processes.

The results obtained under air atmosphere are shown in Figure 7 for different temperatures. In these conditions, the disappearance of the bands characteristic of the water molecules around 3400 cm^{-1} and 1640 cm^{-1} below 180°C is in agreement with TGA curve (Figure 6). Interestingly, if we focus on the vibration bands assigned to the keplerate capsules in the 1000-500 cm^{-1} range, no significant modification are observed until ≈ 125°C. In contrast, dramatic changes are observed between 125°C and 200°C, especially for the strong bands located at 855, 727 and 574 cm^{-1}, which almost totally disappear, while the two bands assigned to Mo=O stretching vibration located at 975 and 939 cm^{-1} give only one strong band at 953 cm^{-1} at 190°C. Concomitantly with these strong modifications, the color of the

compound turn to blue and this phenomenon is non-reversible when coming back at room temperature indicating that the keplerate capsule in not stable in air above 125°C.

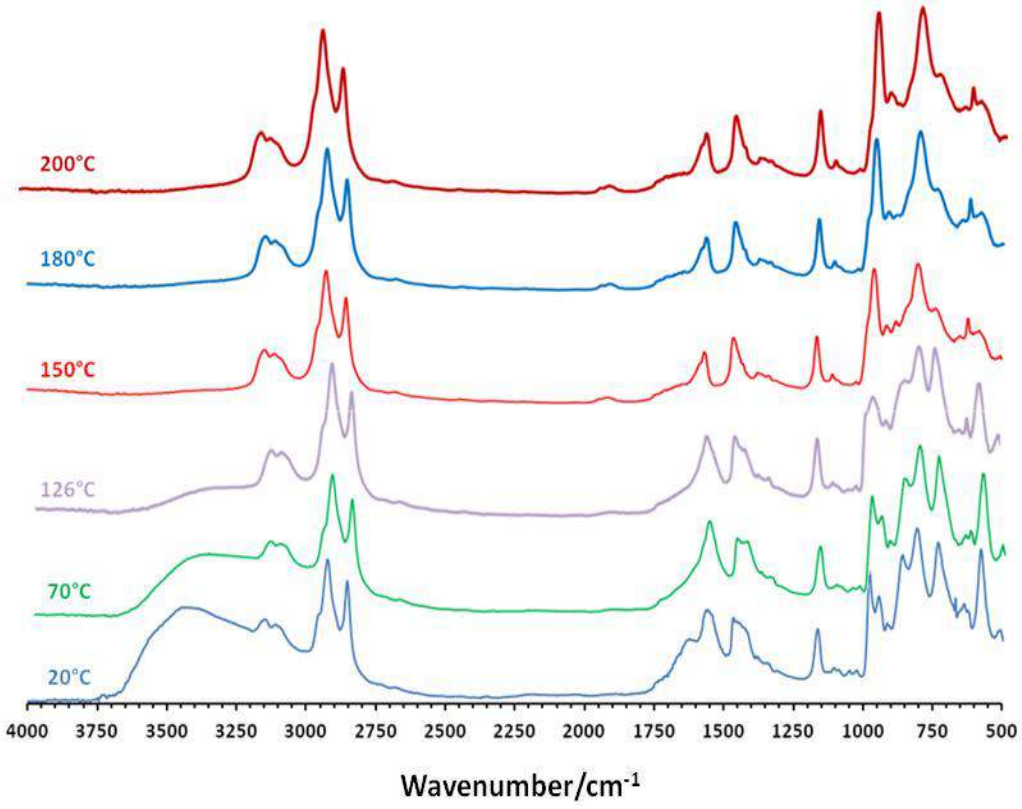

Figure 7: Selected FT-IR spectra recorded at various temperatures for compound **$(mimC_{18})_{37}$-$\{Mo_{132}\}$** in air.

Similar experiments were performed under a flow of nitrogen and the results obtained under nitrogen are shown in Figure 8. In these conditions, the behavior of the product is totally different. The removal of water is observed between 20°C and 180°C, but only small changes of the keplerate skeleton are observed on the FT-IR spectra, in contrast with experiment performed in air. From 20°C to 250°C, the main evolution observed concerns the vibration band at 855 cm^{-1} for which the intensity decreases when temperature increases but this modification is perfectly reversible when coming back at room temperature after rehydration of the material. Finally, heating the compound at temperature higher to 250°C provokes the degradation of the organic cation and the acetate ligands in agreement with TGA data associated to a strong modification of the keplerate which probably transform into a molybdenum oxide which was not identified.

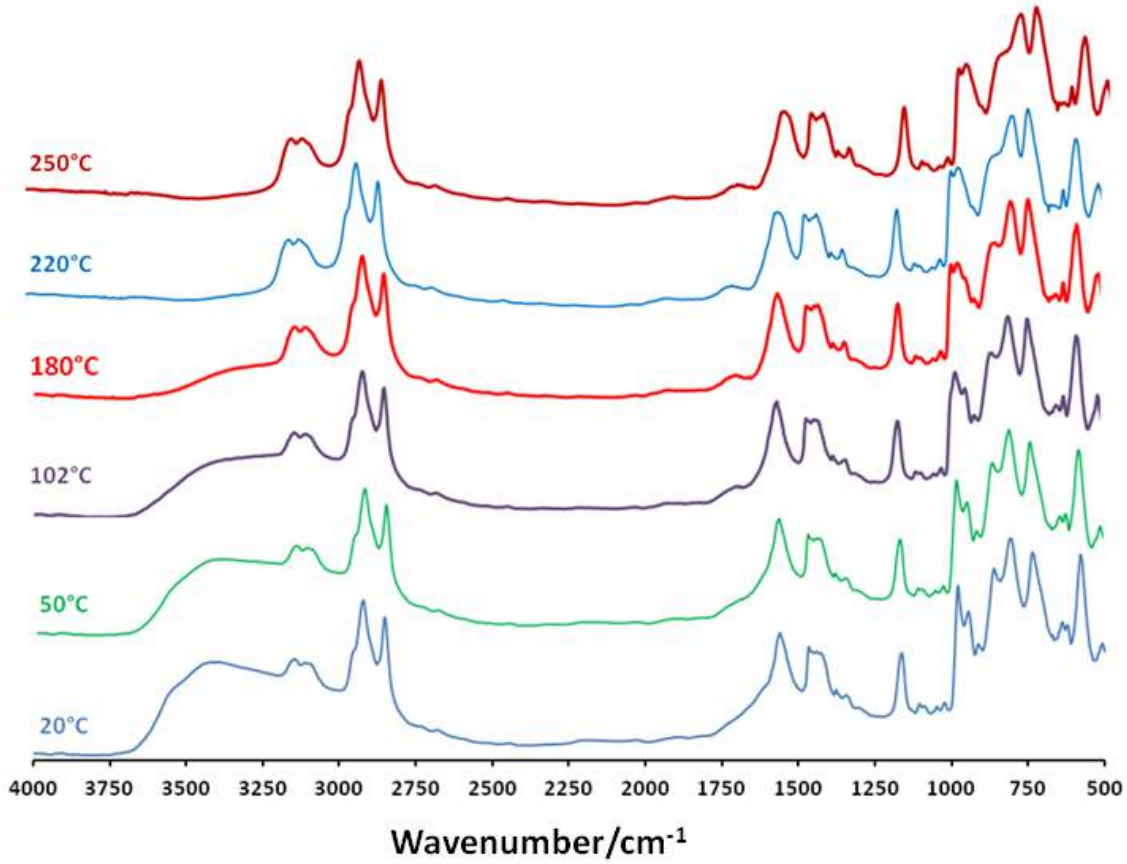

Figure 8: Selected FT-IR spectra recorded at various temperatures for compound **$(mimC_{18})_{37}\{Mo_{132}\}$** under nitrogen.

In summary, whereas TGA curves suggested a good thermal stability of our materials until at least 250°C, the FT-IR spectra recorded in air or under nitrogen reveals that our materials are not stable in air above ≈125°C while the stability is strongly enhanced to 250°C under a nitrogen flow.

II.2.5 Infrared spectroscopic studies at room temperature

Infrared spectroscopy provides highly sensitive and effective probe of molecular structure and dynamics of the alkyl chains.[21] In the high frequency region, the bands around 2920 cm^{-1} and 2850 cm^{-1} are assigned to antisymmetric (d^-) and symmetric (d^+) stretching vibrations of the methylene groups, respectively. These bands are strong indicators of the chain conformation: low wavenumbers (2915-2918 and 2846-2850 cm^{-1}) of the bands are characteristic of highly ordered alkyl chains, while their upward shifts (2924-2928 and 2854-2856 cm^{-1}) indicates the alkyl chain conformation tends toward disorder.[22] The ν_{as} (CH_2) and ν_s (CH_2) frequencies of our compounds lie between the lower and the higher frequencies (2920-2854 cm^{-1}) (Table 2), suggesting the presence of intermediate ordered alkyl chain within the materials, which matches the intermediate order alkyl chain exhibited by the $DODA^+$ salt of $\{Mo_{132}\}$ (2920,

2852 cm^{-1})[18] but in contrast with the highly ordered alkyl chain within the $DODA^+$ salt of $\{Mo_{132}S_{60}\}$ where $\nu_{as}(CH_2)$ and $\nu_s(CH_2)$ frequencies shifted toward low frequencies (2916-2848 cm^{-1}).[17] Furthermore, as the alkyl chains increases, the frequencies decreases and consequently the order increases, such an observation can be due to the increase of the van der Waals interactions in the longer alkyl chains which in turn lead to more ordered alkyl chain arrangement.

Tracking the intensity ratio $I_{vs\ (CH2)}/\ I_{vas\ (CH2)}$ would bring additional information of the alkyl chain arrangement as the conformational order of alkyl chain increases with an increase in this intensity ratio.[23] Plotting $I_{vs\ (CH2)}/\ I_{vas\ (CH2)}$ versus the number of CH_2 and CH_3 groups shows that as the length of the alkyl chain increases, the ratio increases (see Figure 9). This evidences an increase of the conformational order due to increase of the interaction between the alkyl chains as previously indicated. Interestingly, for the two mixed salt compounds **$(mimC_{12})_{20}(mimC_{20})_{20}\{Mo_{132}\}$** and **$(mimC_{12})_{33}(mimC_{20})_{7}\{Mo_{132}\}$**, the ratio appears in good agreement with the other compounds. For example, **$(mimC_{12})_{20}(mimC_{20})_{20}\{Mo_{132}\}$** gives a ratio close to that of **$(mimC_{16})_{41}\{Mo_{132}\}$** which correspond to the average alkyl chain length in this mixed material.

Table 2: antisymmetric and symmetric stretching vibrations of the methylene group of the samples

Samples	$\nu_s\,(CH_2)$	$\nu_{as}\,(CH_2)$	$I_{vs\ (CH2)}/\ I_{vas\ (CH2)}$	Number of CH_2 and CH_3
$(mimC_{12})_{36}\{Mo_{132}\}$	2922	2851	0.66	432
$(mimC_{14})_{36}\{Mo_{132}\}$	2922	2850	0.72	504
$(mimC_{16})_{41}\{Mo_{132}\}$	2923	2853	0.79	656
$(mimC_{18})_{37}\{Mo_{132}\}$	2920	2850	0.81	666
$(mimC_{20})_{37}\{Mo_{132}\}$	2920	2850	0.84	740
$(mimC_{12})_{20}(mimC_{20})_{20}\{Mo_{132}\}$	2922	2851	0.79	640
$(mimC_{12})_{33}(mimC_{20})_{7}\{Mo_{132}\}$	2923	2852	0.74	536
$(mimC_{12})_{8}(mimC_{20})_{33}\{Mo_{132}\}$	2924	2854	0.79	756
$(Dendron)_{36}\{Mo_{132}\}$	2924	2853	0.77	2331
$(DODA)_{36}\{Mo_{132}\}$	2920	2853	0.83	1296

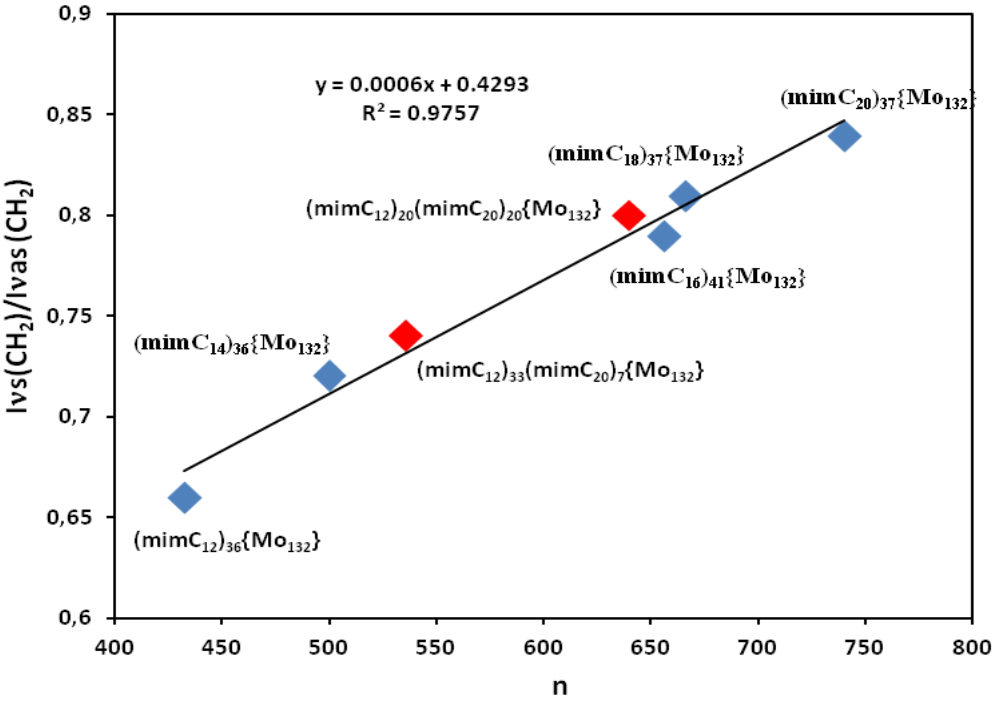

Figure 9: the plot of Ivs(CH_2)/Ivas(CH_2) versus the number of methyl and methylene groups

II.2.6 Liquid Crystal properties

The liquid crystal properties of all the compounds were examined by temperature dependent polarized optical microscopy (TD-POM) between two glass plates, differential scanning calorimetry (DSC) under N_2, and Small Angle X-Ray Diffraction in capillaries in the -40 to 230°C temperature range, in collaboration with Dr Emmanuel Terazzi, Dr Laure Guénée, Ms Kerry Lee Buchwalder and Prof. Claude Piguet from the university of Geneva, Switzerland.

II.2.6.a Polarized Optical Microscopy

Under heating our materials from room temperature to the decomposition temperature, the temperature dependent polarized microscopy revealed the formation of relatively fluid birefringent and homogenous textures characteristic of the liquid cystalline nature for the samples **$(mimC_{12})_{36}\{Mo_{132}\}$**, **$(mimC_{14})_{36}\{Mo_{132}\}$**, **$(mimC_{16})_{41}\{Mo_{132}\}$**, **$(mimC_{18})_{37}\{Mo_{132}\}$**, and **$(mimC_{20})_{37}\{Mo_{132}\}$** in the 100-240°C temperature range as shown in Figure 10. Furthermore, the samples did not show obvious texture due to their decomposition before reaching the isotropic state and consequently it is difficult to identify the type of the mesophase from the TD-POM pictures directly. However, the three mixed compounds, **$(mimC_{12})_{20}(mimC_{20})_{20}\{Mo_{132}\}$**, **$(mimC_{12})_{33}(mimC_{20})_{8}\{Mo_{132}\}$** and

(mimC$_{12}$)$_8$(mimC$_{20}$)$_{33}${Mo$_{132}$} did not show such a texture even at high temperature, indicating the lack of liquid crystal properties for these compounds. Finally in the case of the last compound **(dendron)$_{37}${Mo$_{132}$}**, a birefringent texture was only observed after chemical treatment of the glass plates by sulfochromic acid. Such a treatment induces the formation of defaults on the surface of the glass plates, thus allowing observing non usual liquid crystal phases such as cubic phase.

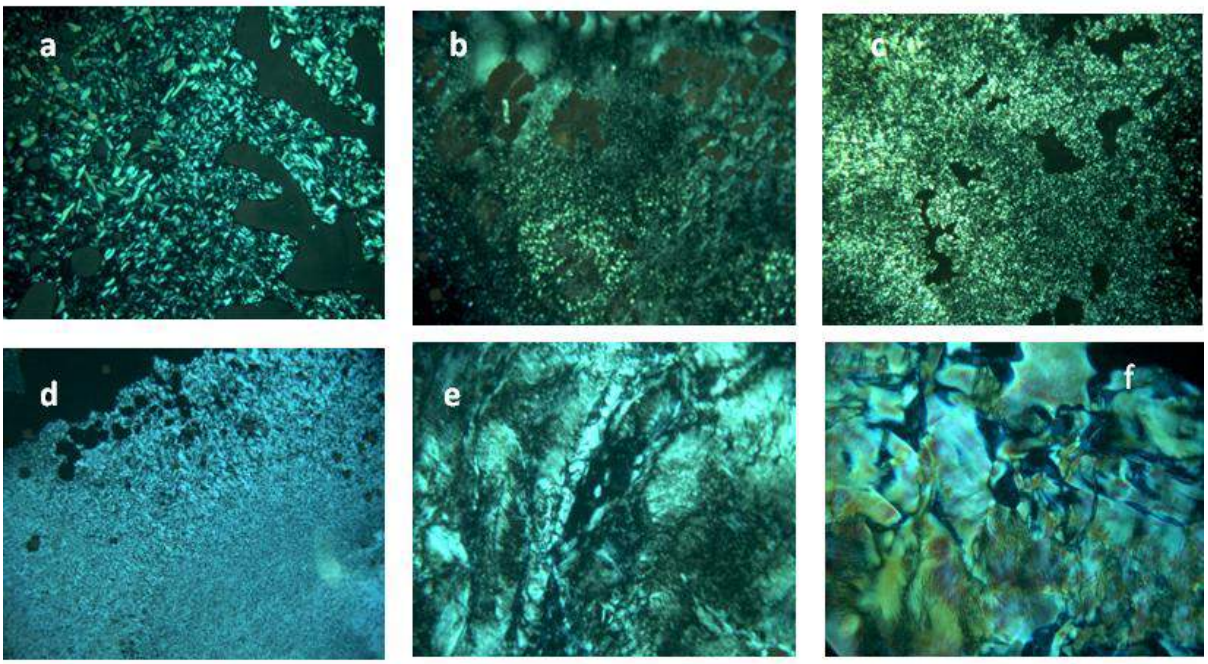

Figure 10: Polarized Optical Microphotgraph of **(mimC$_{12}$)$_{36}${Mo$_{132}$}** at 113°C (a), **(mimC$_{14}$)$_{36}${Mo$_{132}$}** at 220°C (b), **(mimC$_{16}$)$_{41}${Mo$_{132}$}**at 160°C (c), **(mimC$_{18}$)$_{37}${Mo$_{132}$}** at 100°C (d), and **(mimC$_{20}$)$_{37}${Mo$_{132}$}** at 200°C (e) **(dendron)$_{37}${Mo$_{132}$}**at 240°C (f).

II.2.6.b Differential scanning calorimetry (DSC)

The DSC curves of Keplerate based materials were recorded under nitrogen at a scan rate of 5°C/minute between -40°C and 220-260°C depending on the compounds. At least three thermal cycles were achieved, the obtained results of the second thermal cycles are shown in Figure 11 and the thermodynamic parameters are listed in Table 3. Globally, the DSC curves exhibit very broad and often composite first order phase transitions between the solid state and the mesophases, which contrast with the relatively sharp first order phase transitions reported for DODA$^+$ salts of keplerate Mo$_{132}$ and Mo$_{132}$S$_{60}$.[17-18] These results could be consistent with a local molecular or supramolecular mobility unsufficient to allow the development of a network of intermolecular interactions sufficiently regular to obtain a well-developed mesophase and are in agreement with our previous FT-IR observations at room

temperature. In addition, excepted for **(mimC$_{12}$)$_{36}${Mo$_{132}$}**, the phase transition appears reversible for all the other compounds and for some compounds like**(mimC$_{14}$)$_{36}${Mo$_{132}$}** a very broad reversible phase transition is observed.

The average phase transition temperatures, determined in the heating mode, are summarized in Table 3. In short, disregarding the compound **(mimC$_{12}$)$_{36}${Mo$_{132}$}**, the phase transition temperatures increases linearly from +13°C to +46°C with the increase of the alkyl chain length of the imidazolium cation from **(mimC$_{14}$)$_{36}${Mo$_{132}$}**, **(mimC$_{16}$)$_{41}${Mo$_{132}$}**, **(mimC$_{18}$)$_{37}${Mo$_{132}$}**, to **(mimC$_{20}$)$_{37}${Mo$_{132}$}**. These results are significantly different from those obtained with the three previous DODA^{+} salts (+9°C). However, the material obtained with the dendritic cation exhibits a very low phase transition temperature -28°C suggesting another type of arrangement in the liquid crystal phase.

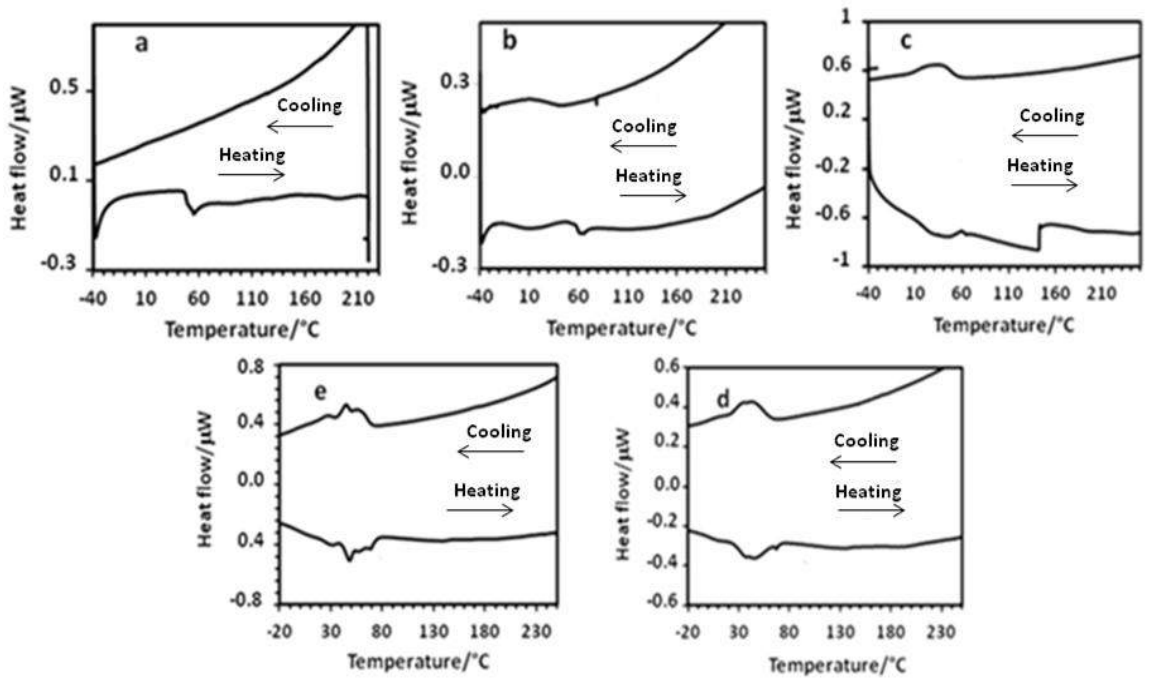

Figure 11: DSC Traces of the second thermal cycle recorded under N_2 (5°C min^{-1}) for **(mimC$_{12}$)$_{36}${Mo$_{132}$}** (a), **(mimC$_{14}$)$_{36}${Mo$_{132}$}** (b), **(mimC$_{16}$)$_{41}${Mo$_{132}$}** (c), **(mimC$_{18}$)$_{37}${Mo$_{132}$}** (d), **(mimC$_{20}$)$_{37}${Mo$_{132}$}** (e) **(Dendron)$_{36}${Mo$_{132}$}**(f).

Table 3: Temperatures, melting enthalpy and entropy changes of the phase transitions between the glassy state and the liquid crystal phases observed for the materials exhibiting liquid crystalline properties. Temperatures are given for the peaks observed by DSC measurements during the second heating process

Compounds	T /°C (Heating mode)	MM g/mol	n(CH_2)	ΔH_m /kJ·mol^{-1}	ΔS_m /J·mol^{-1}·K^{-1}	$\Delta H'_m$ [a] /J·mol^{-1}	$\Delta S'_m$ [a] /J·mol^{-1}K^{-1}
$(mimC_{12})_{36}\{Mo_{132}\}$	+55	30982	396	-4.3	-13	-10.95	-0.03
$(mimC_{14})_{36}\{Mo_{132}\}$	+13	32387	468	-46.3	-162	-99	-0.35
$(mimC_{16})_{41}\{Mo_{132}\}$	+31	34889	615	-204.1	-671	-331.8	-1.1
$(mimC_{18})_{37}\{Mo_{132}\}$	+43	35059	629	-158.5	-501	-252	-0.8
$(mimC_{20})_{37}\{Mo_{132}\}$	+46	36006	703	-163.8	-514	-233	0.73
$(Dendron)_{36}\{Mo_{132}\}$	-28	68743	2177	-442.7	-1807	-202	-0.83
$DODA_{36}\{Mo_{132}\}$[18]	+9	42982	1224	-849.0	-3009	-639	-2.45
$DODA_{44}$–$\{Mo_{132}S_{60}\}$[17]	+9	47838	1548	-1333.0	-4724	-918	-3.25
$DODA_{56}$–$\{Mo_{132}S_{60}\}$[17]	+9	55357	1904	-1649.0	-5848	-866	-3.07
DODACl	+18	586.5	34	-83.1	-278.5	-2445	-8.19

[a] $\Delta Y'm = \Delta Ym /n(CH_2)$ (Y = H, S) where n(CH_2) corresponds to the total number of methylene groups of the alkyl chains born by the cations.

The corresponding melting enthalpy and entropy changes, ΔH_m and ΔS_m, are also given in the Table 3. The direct comparison of these values remains difficult since the number of cations can vary in the series of Mo_{132}-based materials. The weighted $\Delta H'_m$ and $\Delta S'_m$ values correspond to the ratios $\Delta H_m/n(CH_2)$ and $\Delta S_m/n(CH_2)$ respectively, where n(CH_2) is the total number of methylene groups in the compounds, is more convenient. The plot of $-\Delta H'_m$ versus $-\Delta S'_m$, including the previously reported data with DODA salt and DODACl alone, is given in Figure 12. It displays a linear relationship typical for H/S compensation [24] and evidences two sets of points : one corresponding to the imidazolium salts of Mo_{132}, **$(mimC_{12})_{36}\{Mo_{132}\}$**, **$(mimC_{14})_{36}\{Mo_{132}\}$**, **$(mimC_{16})_{41}\{Mo_{132}\}$**, **$(mimC_{18})_{37}\{Mo_{132}\}$**, and **$(mimC_{20})_{37}\{Mo_{132}\}$** and **$(dendron)_{36}\{Mo_{132}\}$** and one corresponding to the $DODA^+$ salts $(DODA)_{36}\{Mo_{132}\}$, $(DODA)_{44}\{Mo_{132}S_{60}\}$ and $(DODA)_{56}\{Mo_{132}\}$ bearing liquid cyrstalline properties,[17-18] whereas DODACl appears clearly different.

For DODACl, the alkyl chains are poorly constrained by the presence of the counter anion Cl^- and the melting of the chains follows the trend expected for simple alkanes.[24] Figure 12 suggests that the alkyl chains of the cations associated to $\{Mo_{132}\}$ are strongly perturbed by the presence of the Keplerate capsule. From a macroscopic point of view, it results in a drastic

lowering of the samples' fluidity. This phenomenon is clearly more pronounced for the series of imidazolium salts than for the three $DODA^+$ salts. Furthermore, as seen in the insert of the Figure 12, the ratio $\Delta H'_m/\Delta S'_m$ appears globally correlated with the alkyl chain length of the imidazolium cation. The magnitude of the ΔH_m / $n$$CH_2$ and ΔS_m / $n$$CH_2$ ratios seems to be strongly and linearly correlated with the average closeness of the -CH_2- with the surface of the anions. In other words, the -CH_2- located closer to the surface are more constrained than those which are more distant. It is as the -CH_2- located in a crown close to the surface were "frozen" and consequently no more available for the melting. In summary, it is the reason why the fluidity of the samples bearing long aliphatic chains is higher.

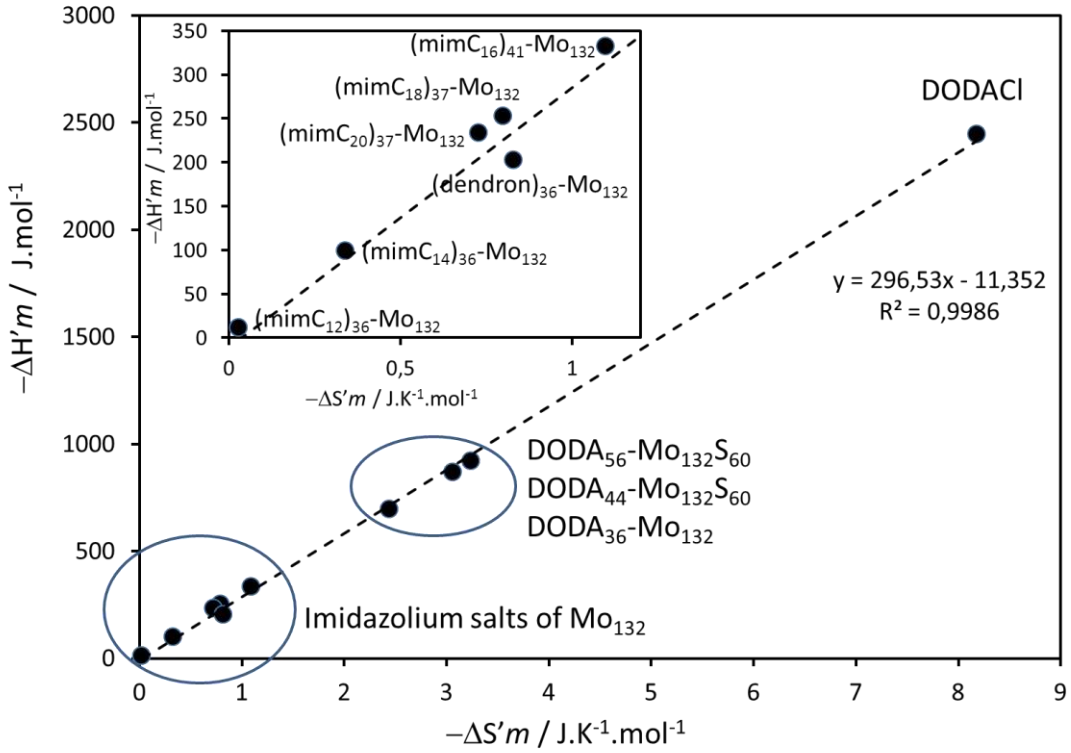

Figure 12: $\Delta H'_m$ versus $\Delta S'_m$ plot

II.2.6.c Temperature dependent Small-Angle X-ray Diffraction (SAXRD)

Small-angle X-ray Diffraction (SA-XRD) experiments (from -40 to 200°C temperature range) were carried out to elucidate the nature of the liquid crystalline phases. Arbitrarily, we have chosen to present the SA-XRD patterns obtained at 200°C, when possible, for two main reasons i) to compare with the previous data at the same temperature,[17-18] ii) at higher temperature the fluidity is relatively high and translated by the presence of sharper lines. The

resulting SA-XRD patterns are depicted in Figure 13, whereas the corresponding data are summarized in Table 4.

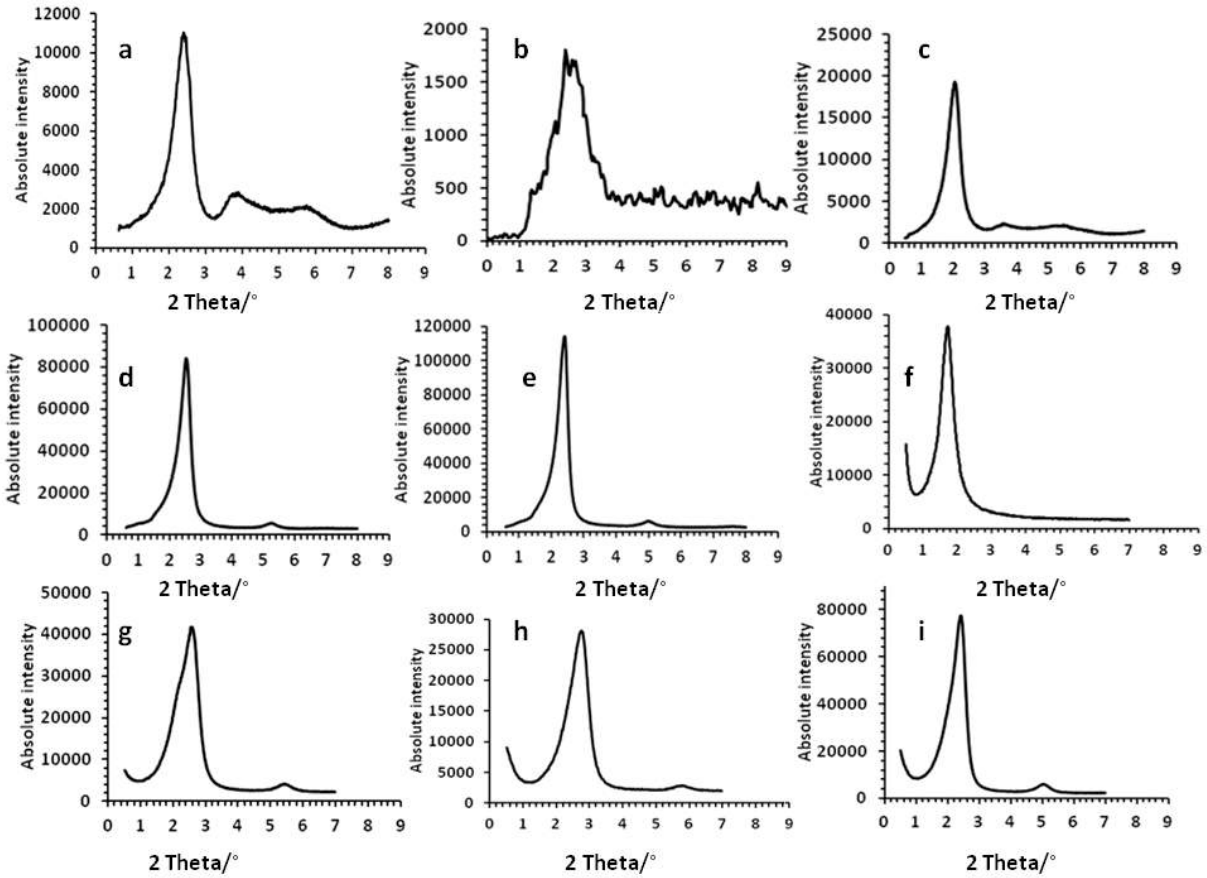

Figure 13: SA-XRD pattern recorded at 200°C for **$(mimC_{12})_{36}\{Mo_{132}\}$** (a), **$(mimC_{14})_{36}\{Mo_{132}\}$** at 190°C (b), **$(mimC_{16})_{41}\{Mo_{132}\}$** (c), **$(mimC_{18})_{37}\{Mo_{132}\}$** (d), **$(mimC_{20})_{37}\{Mo_{132}\}$** (e) **$(Dendron)_{36}\{Mo_{132}\}$** (f). **$(mimC_{12})_{20}(mimC_{20})_{37}\{Mo_{132}\}$** (g), **$(mimC_{12})_{33}(mimC_{20})_{7}\{Mo_{132}\}$** at 140°C (h), **$(mimC_{12})_{8}(mimC_{20})_{33}\{Mo_{132}\}$** (i).

Globally, in contrast with the previous $DODA^+$ salts, which exhibited up to three sharp equidistant reflections indexed as the 001, 002 and 003 Miller indices (00*l*) with a broad and diffuse signal at approximately 4.5 Å associated with the liquid-like molten chains of the $DODA^+$ cations, the imidazolium salts display broader reflections with no signals attributed to the molten chains.

Table 4: Indexation at 200°C during the cooling mode for the reflections detected in the liquid-crystalline phase by SA-XRD.

Compounds	d_{hkl} measured /Å	I /a.u.	indexation	Cell parameters /Å
$(mimC_{12})_{36}\{Mo_{132}\}$	36.90	VS	[c]	
	23.19	MW (broad)	[c]	
	15.45	MW (broad)	[c]	
$(mimC_{14})_{36}\{Mo_{132}\}$[a]	35.57	S	001	h = 35.57
				a_{hex} = 41.79
$(mimC_{16})_{41}\{Mo_{132}\}$	40.71	VS	[c]	
	24.55	MW (broad)	[c]	
	16.52	MW (broad)	[c]	
$(mimC_{18})_{37}\{Mo_{132}\}$	32.78	VS	001	h = 32.78
	16.34	W	002	a_{hex} = 45.29
$(mimC_{20})_{37}\{Mo_{132}\}$	35.34	VS	001	h = 35.34
	17.67	W	002	a_{hex} = 44.21
$(mimC_{12})_{20}(mimC_{20})_{20}\{Mo_{132}\}$	32.91	VS	001	h = 32.91
	16.26	W	002	a_{hex} = 44.98
$(mimC_{12})_{33}(mimC_{20})_{7}\{Mo_{132}\}$[b]	31.34	VS	001	h = 31.34
	15.22	W	002	a_{hex} = 45.23
$(mimC_{12})_{8}(mimC_{20})_{33}\{Mo_{132}\}$	35.30	VS	001	h = 35.30
	17.60	W	002	a_{hex} = 43.42
$(Dendron)_{36}\{Mo_{132}\}$	51.36	VS	[c]	
$DODA_{36}\{Mo_{132}\}$[18]	26.9	VS	001	h = 26.9
	13.3	M	002	a_{hex} = 54.2
	9.1	W	003	
$DODA_{44}$–$\{Mo_{132}S_{60}\}$[17]	34.20	VS	001	h = 34.12
	16.98	M	002	a_{hex} = 51.64
	11.40	W	003	
$DODA_{56}$–$\{Mo_{132}S_{60}\}$ [17]	34.91	VS	001	h = 34.55
	17.09	M	002	a_{hex} = 55.21

[a] measured at 190°C; [b] measured at 140°C; [c] not determined. *I* corresponds to the intensity of the reflections (VS : very strong, S : strong, W : weak, VW : very weak ; br and sh stand for broad and sharp) ; *h* is the lattice parameter of the lamellar phase; a_{Hex} is the local hexagonal organization within the layers calculated with eq. 1.

The three compounds **$(mimC_{14})_{36}$-{Mo_{132}}** **$(mimC_{18})_{37}${Mo_{132}}** and **$(mimC_{20})_{37}${Mo_{132}}** unambiguously display two lines indexed as 001 and 002 reflections which are characteristic of a 1D lamellar ordering, whereas the two compounds **$(mimC_{12})_{36}${Mo_{132}}** and **$(mimC_{16})_{41}${Mo_{132}}** exhibits three lines for which we were not able to give a realistic indexation. Interestingly, the three mixed compounds **$(mimC_{12})_{20}(mimC_{20})_{20}${$Mo_{132}$}, $(mimC_{12})_{33}(mimC_{20})_{7}${$Mo_{132}$}** and **$(mimC_{12})_{8}(mimC_{20})_{33}${$Mo_{132}$}** also display 001 and 002 lines, even though they did exhibit liquid crystalline behaviors as detected by TD-POM and DSC. Such results suggest the propensity for these salts to self-organize in a lamellar fashion even in the solid state. Besides, for the two latter mixed salts, we noticed that increasing temperature above 160°C and 180°C respectively, unidentified additional reflections appears, suggesting either a degradation of the product or a mixture of different compounds in the solid. Finally, the **$(Dendron)_{36}${Mo_{132}}** give an unique reflection at d = 51.36 Å which make any accurate indexation difficult.

Focusing on the major part of our materials, a 1D lamellar ordering is evidenced and the interlayer spacing h can be easily deduced since it correspond to the d_{001} distance. These values are listed in the Table 4 and are found in the range 31.34 to 35.57 Å, in agreement with the values found for the $DODA^+$ salts **$(DODA)_{36}${Mo_{132}}**, **$(DODA)_{44}${$Mo_{132}S_{60}$}** and **$(DODA)_{56}${$Mo_{132}S_{60}$}** for which h was found between 26.90 Å and 34.55 Å.[17,18] As mentioned previously, such a lamellar organization could appear surprising if we consider the spherical shape of the cluster. Nevertheless, as shown by a theoretical study, polyoxometalates even in the absence of charge, tend to form a bidimensional sheet-like structure [11, 15, 18, 25] and previous studies clearly confirm the capability of Mo_{132} to assemble into lamellar aggregates.[15]

The ionic character of this material implies that the positive charges of the cations are necessarily located close to the negatively charged isotropic spherical surface of Mo_{132}. If no external constraint is applied, imidazolium and $DODA^+$ cations should be randomly distributed onto the surface. In the solid or liquid crystalline state, the situation could be different. If a deformation (a deviation from the spherical distribution) is required to minimize the electric multipolar interactions, the system is distorted accordingly. When the starting object is a sphere, an elongation or a compression may occur, thus leading to prolate and oblate spheroids (see Figure 14).

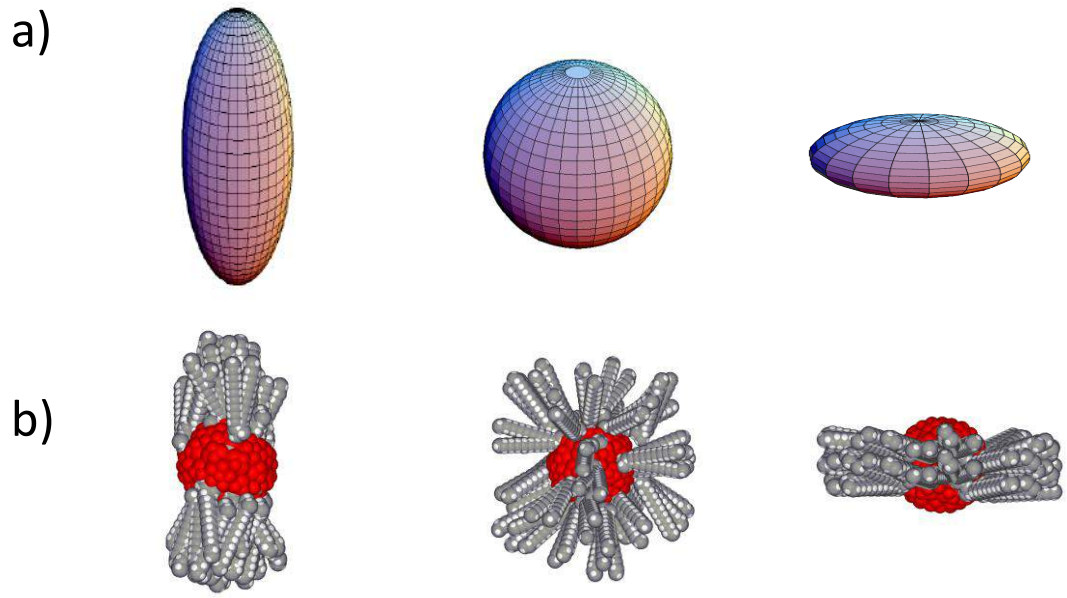

Figure 14: (a) prolate ellipsoid (left), sphere (center), oblate ellipsoid (right); (b) corresponding prolate cluster (left), spherical cluster (center) and oblate cluster (right). Taken from reference [18].

These both anisometric objects have shapes compatible with a lamellar organization. As the central $\{Mo_{132}\}$ core is rigid, the deformation can only originate from the non-uniform distribution of the cations around the Keplerate and several examples of axial deformations of ionic liquid polyoxometalate clusters producing smectic liquid crystalline organizations can be listed.[18]

In all cases, the diameter of the anionic inorganic cores (≈ 30 Å) is of the same order of the lamellar periodicity *h* (31.34 to 35.57Å range), which necessarily implies that the layers of the lamellar phases are composed of oblate clusters (Figure 14b, right). Taking into account a realistic density of d = 1.0 g cm^{-3} in the mesophase[17-18, 26] and assuming that clusters are locally ordered in a compact hexagonal lattice with one cluster per unit cell (Z = 1),[17] we can thus calculate the hexagonal lattice parameter a_{hex} by using the relation (1), where MMc is the molar mass of the cluster, *h* the d_{001} distance and N_{AV}, the Avogadro number.

$$a_{Hex} = \left(\frac{2 \cdot Z \cdot MM_C}{h \cdot d \cdot N_{AV} \cdot 10^{-24} \cdot 3^{1/2}} \right)^{1/2} \qquad (1)$$

Using this relation, a_{hex} are found in the range 41.79 Å to 45.29 Å (see Table 4), which is smaller to that found for DODA salts[17-18] and in perfect agreement with the value reported by Volkmer and Müller [15] for a hexagonal monolayer of $(DODA)_{36}$-Mo_{132} as seen in Figure 15.

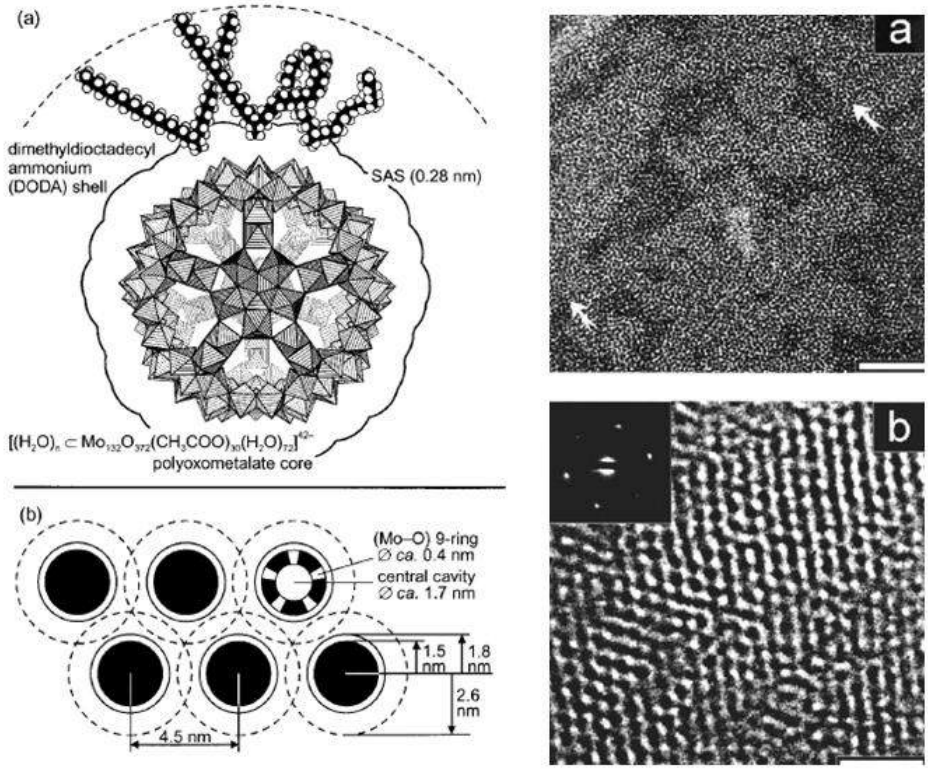

Figure 15: Left: Schematic representation of the $(DODA)_{36}\{Mo_{132}\}$ (a), Schematic representation of a single layer of $(DODA)_{36}\{Mo_{132}\}$ in accordance with TEM data and molecular models. Right: TEM micrograph of a thin film of $(DODA)_{36}\{Mo_{132}\}$(a), TEM micrograph of an ordered region of a thicker film at high magnification. Reproduced from reference [15].

Considering the size of the inorganic cluster (≈ 30 Å) and the size of cations in a linear configuration reported in the Table 5, the a_{hex} distances, which correspond to the distance between two clusters within the layers, [17] necessarily implies that there is folding of the alkyl chains of the cations. Indeed, the hypothesis of linear arrangements of the alkyl chains of the imidazolium cations accompanied by strong interdigitation between the organic cations with the neighboring clusters would lead to a_{hex} distances of at least 50-55 Å. It was the case for the $DODA^+$ salts where a_{hex} distances lies in the range 51.54 to 55.21 Å.[17,18] In contrast to the $DODA^+$ cations for which the two neighboring octadecyl chains probably favor the organization of the cations through Van der Waals interaction, the alkyl chains of the imidazolium cations are probably folded, prohibiting thus the interdigitation with the

neighboring cation and do not favor the organization and consquently delimiting the formation of well-ordered mesophases.

Table 5: Approximative length of the cations in case of linear organization.

Cations	Length /Å
$(mimC_{12})^+$	20
$(mimC_{14})^+$	22.5
$(mimC_{16})^+$	25
$(mimC_{18})^+$	27.5
$(mimC_{20})^+$	30
Dendron$^+$	45

Table 6: Expected dynamic diameters of coated Mo_{132} capsules in comparison with the calculated a_{hex} parameters.

Compounds	Expected dynamic diameter of coated Mo_{132} capsules	a_{hex} / Å
$(mimC_{14})_{36}\{Mo_{132}\}$	75	41.79
$(mimC_{18})_{37}\{Mo_{132}\}$	85	45.29
$(mimC_{20})_{37}\{Mo_{132}\}$	90	44.21
$(mimC_{12})_{20}(mimC_{20})_{20}\{Mo_{132}\}$	≤ 90	44.98
$(mimC_{12})_{33}(mimC_{20})_{7}\{Mo_{132}\}$	≤ 90	45.23
$(mimC_{12})_{8}(mimC_{20})_{33}\{Mo_{132}\}$	≤ 90	43.42

Finally, for the **$(Dendron)_{36}\{Mo_{132}\}$**, the unique reflection presented at d = 51.36 Å difficults the assignment of the mesophase. a_{hex} = 50.7 Å is first calculated by considering the hypothesis of the lamellar organisation. Taking into account, the higher number of alkyl chains, a better organization of the cation is expected and a size of 45 Å seems realistic for this cation. However, the value of calculated a_{hex} is not compatible and thus ruled out the lamellar organization. Finally, keeping in mind that a birefringence appears after chemical treatment of the glass plates, this mesophase could be nematic or cubic but further work is needed to fully understand this system.

In summary, it is possible to generate mesophases by mixing imidazolium cations with keplerate capsules $\{Mo_{132}\}$ but the probable folding of the alkyl chains and the lack of structuring interactions of Van der Waals type between alkyl chains of the cations prevent the formation of fluid and well organized mesophases.

II.3 Keplerate based materials toward promising applications: cation trapping and encapsulation within a silica matrix

II.3.1 Zn^{2+} uptake behavior of Mo_{132} in DODA-Mo_{132} based materials.

As previously reported by Tsunashima and Cronin, the giant cyclic cluster $\{Mo_{154}\}$ surrounded by $DODA^+$ cations exhibit interesting properties such as gas trapping and catalysis while the initial ammonium salt was inactive.[27] In the same sense, the cavity of the Mo_{132} cluster could be used for trapping gas or cations. Preliminary work was conducted in Versailles by Ms Loan Lai during her Master 2 internship by using keplerate capsules functionalized by dicarboxylate ligands such as succinate or glutarate ligand which give one carboxylate function hanging toward the center of the cavity and available for coordinating transition metals (see Figure 16).[28] Some experiments of the cation trapping within the cavity were attempted in aqueous medium. However, the equilibriums which occur between ligand coordinated inside the cavity and free ligands led to the formation of carboxylate complexes of transition metals outside the cavity of the Keplerate. In organic medium, these equilibriums are restricted and consequently preventing the formation of complexes outside the capsule. Thus, we decided in this study to use $DODA^+$ salts of Keplerate compounds, which are soluble in various organic solvent such as $CHCl_3$, toluene or acetonitrile.

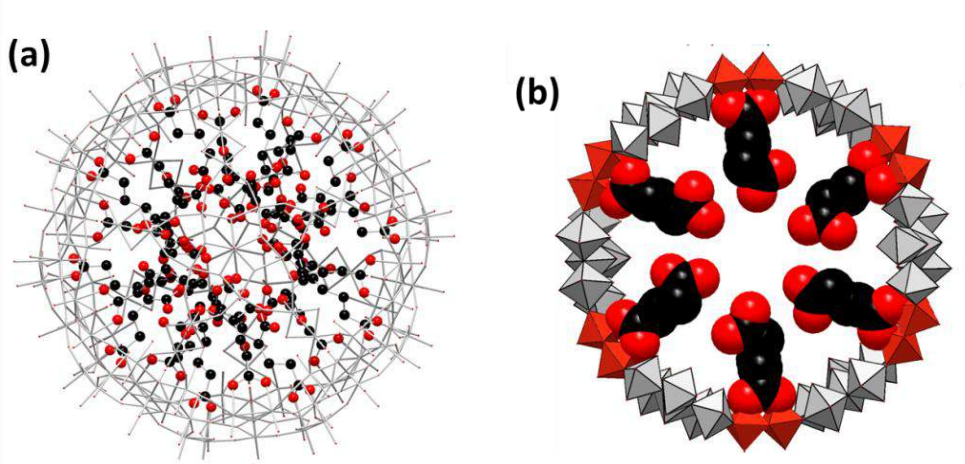

Figure 16: (a) Ball and stick structural representation of the $(H_2NMe_4)_{21}(NH_4)_{16}[Mo_{132}O_{372}(H_2O)_{82}(HGlu)_{25}].65H_2O$ capsule evidencing the embedded glutarate ligands despite their high disorder. (b) Partial structural representation of the inner cavity of the compound showing one possible organization of the ligands inside the cavity.

For this purpose, two $\{Mo_{132}\}$ compounds with different internal ligands as acetate (CH_3COO^-) and succinate ($C_4H_4O_4^{2-}$) were chosen. Their encapsulation by $DODA^+$ cations have been carried out by following the same procedure described above and characterized by

the usual techniques such as elemental analysis, TGA, IR (see experimental section for details) leading to the formulas $(DODA)_{32}(NH_4)_5[Mo_{132}O_{372}(CH_3COO)_{25}(H_2O)_{82}].70H_2O$, noted **$(DODA)_{32}$-$Mo_{132}$** and $(DODA)_{33}(NH_4)_{12}[Mo_{132}O_{372}(HSucc)_{13}(Succ)_{10}(H_2O)_{86}].30H_2O$, noted **$(DODA)_{33}$ Mo_{132}Succ**.

II.3.1.a Zn^{2+} behavior of Mo_{132} in the DODA-encapsulated cluster {Mo_{132}-acetate} and {Mo_{132}-succinate} cluster using flame atomic absorption spectroscopy.

To investigate the trapping of Zn^{2+} ions into encapsulated $\{Mo_{132}\}$ and to show key role of internal ligands in achieving high trapping of Zn^{2+}, we first compared the uptake efficiency of Zn^{2+} on **$(DODA)_{32}$-Mo_{132}** and **$(DODA)_{33}Mo_{132}$Succ** by using flame atomic absorption spectroscopy. In typical experiment, an aqueous solution containing 10 equivalents of $ZnCl_2$ per Mo_{132} capsule were added to a chloroform solution of **$(DODA)_{32}\{Mo_{132}\}$** or **$(DODA)_{33}\{Mo_{132}$Succ$\}$**. After stirring for 20 hours at room temperature, the aqueous phase was separated an analyzed by flame atomic absorption and the quantity of Zn^{2+} trapped in the $\{Mo_{132}\}$ capsule was deduced by the difference with the initial amount of Zn^{2+}. The very preliminary results show that the number of trapped Zn within **$(DODA)_{32}\{Mo_{132}\}$** was 1.6 and that within **$(DODA)_{33}\{Mo_{132}$Succ$\}$** was 2.2. These amounts are very limited but correspond to the extraction of 16% and 22% of the initial quantity of Zn^{2+} in the aqueous phase, which validate this concept. Complementary series of analyses are needed to determine the maximum limit and to extract the associated equilibrium constants.

The best results were obtained with the compound **$(DODA)_{33}Mo_{132}$Succ**, which possesses an available carboxylate ligand. In order to evidence the trapping of Zn^{2+} inside the keplerate capsule, similar experiment was done by mixing an aqueous solution containing a very large excess of $ZnCl_2$ (125 eq. / Mo_{132}) with a chloroform solution of **$(DODA)_{33}Mo_{132}$Succ** to give the target compound containing Zn^{2+}, named as **Mo_{132}SuccZn**, after isolation of the organic phase and precipitation of the compound by addition of ethanol (see experimental section for details). The resulting black solid was characterized by FT-IR, EDX, TGA, elemental analysis (in progress) and MAS NMR.

Based on the data obtained by EDX, TGA, and elemental analysis (C, H, N) the molecular formula of **Mo_{132}SuccZn** was suggested. EDX measurement reveals the presence of 6 Zn

metallic centers per capsule. Elemental analysis show the presence of 23 $DODA^+$ and 7 ammonium cations and the number of succinate ligands was found to be 15. This indicates that the trapping of Zn^{2+} cations results from an exchange of cations to ensure the charge balance. Especially 5 NH_4^+ cations supposed to be trapped within the cavity of the Keplerate capsule are removed and replaced by 6 Zn^{2+} cations, while the number of succinate ligands significantly diminishes from 23 to 15, probably due to steric effects. Thus the overall molecular formula can be written as follow: **$(DODA)_{23}(NH_4)_7[Mo_{132}O_{372}Zn_6(Succ)_{15}(H_2O)_{102}]$**, however the elemental analysis of Zn and Mo are still in progress.

Figure 17 shows the IR of **$(DODA)_{33}Mo_{132}Succ$** and **$(DODA)_{23}Mo_{132}SuccZn$**. First, the bands at 1708 cm^{-1} in **$(DODA)_{33}Mo_{132}Succ$** assigned to vibration of COOH disappeared in **$(DODA)_{23}Mo_{132}SuccZn$** which indicates the full deprotonation of the inner succinates ligands. Regarding the ν_{as}(COO) vibration bands, a new vibration appears as a shoulder at 1580 cm^{-1}, indicating the the appearance of a new type of carboxylate function. Finally, the characteristic absorption band νs(COO) observed at 1467 cm^{-1} in **$(DODA)_{33}Mo_{132}Succ$**, is shifted toward lower frequency by 5 cm^{-1} in **$(DODA)_{23}Mo_{132}SuccZn$** complex. All these observation suggest a metal-coordination through the carbonyl oxygen atoms and thus strongly suggests the coordination of Zn^{2+} cations to the inner carboxylate groups hanging toward the center of the capsule.

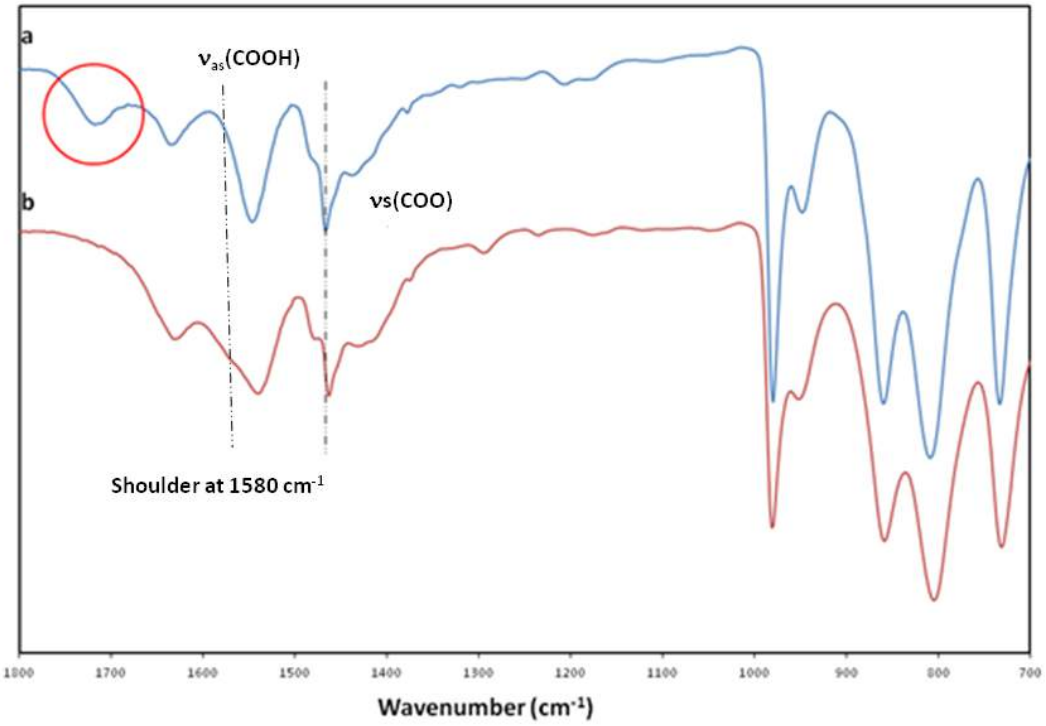

Figure 17: FT-IR spectra of **$(DODA)_{33}Mo_{132}Succ$** (a) and **$(DODA)_{23}Mo_{132}SuccZn$** (b).

II.3.1.b ^{1}H and ^{13}C MAS NMR characterizations

To support the coordination of Zn^{2+} to the inner carboxylate ligands of **$Mo_{132}Succ$**, we used solid-state ^{1}H MAS NMR and ^{13}C MAS NMR spectroscopies enhanced by dynamic nuclear polarization. The ^{1}H MAS NMR spectra of compounds **$(NH_4)_{65}Mo_{132}Succ$**, **$(DODA)_{33}Mo_{132}Succ$** and **$(DODA)_{23}Mo_{132}SuccZn$** are given in the Figure 18. The **$(NH_4)_{65}Mo_{132}Succ$** give a spectrum exhibiting broad lines assigned to ammonium cations at 6.5 ppm, water at 5.4 ppm and inner succinate ligands at 1.2 ppm. The Figure 18b and the Figure 18c show respectively the spectra obtained for **$(DODA)_{33}Mo_{132}Succ$** (b) and **$(DODA)_{23}Mo_{132}SuccZn$** (c). The ^{1}H MAS NMR spectrum is dominated by the signal of the $DODA^{+}$ cations whereas a small amount of NH_4^{+} cation are still present in agreement with the previous characterizations. The signal corresponding to the succinate ligands is unfortunately overlapped by that of $DODA^{+}$ and in these conditions it is difficult to observe any effect upon insertion of Zn^{2+} cation.

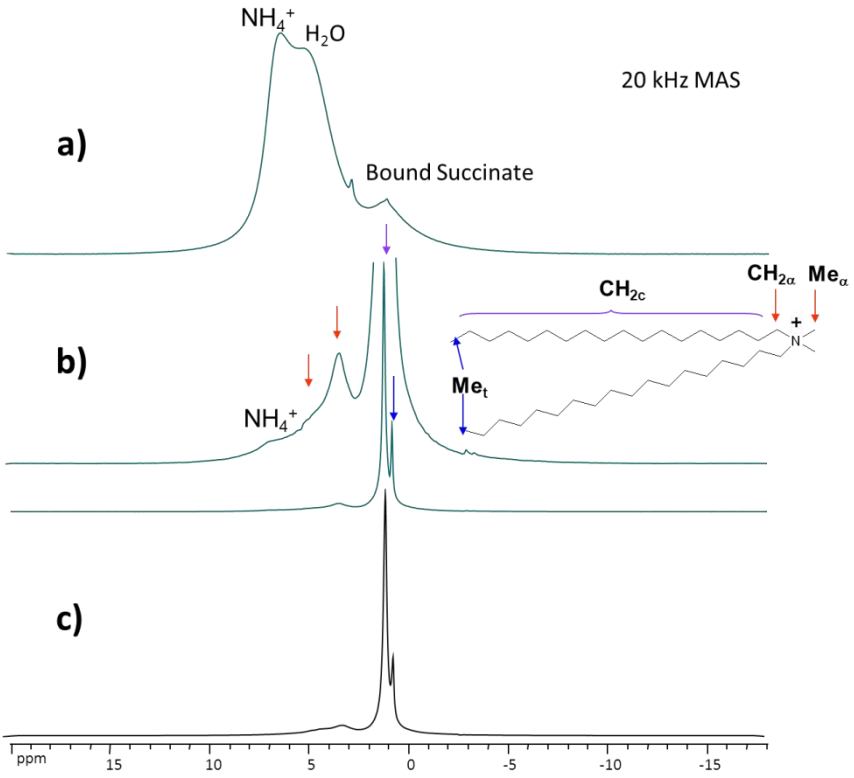

Figure 18: The ^{1}H MAS NMR spectra a) **NH_4-Mo_{132}Succ**; b) **DODAMo_{132}Succ**; c) **DODAMo_{132}Zn**

The DNP-enhanced ^{13}C spectra obtained using ^{1}H-^{13}C cross polarization under magic angle spinning (^{13}C{^{1}H} CPMAS) recorded for compounds **$(NH_4)_{65}Mo_{132}$Succ**, **$(DODA)_{33}Mo_{132}$Succ** and **$(DODA)_{23}Mo_{132}$SuccZn** are shown in Figure 19. The spectrum of **$(NH_4)_{65}Mo_{132}$Succ** shows a broad signal assigned the inner succinate ligands at 30 ppm whereas two other resonances centered at δc ≈ 175 ppm and δc ≈ 182 ppm represents the two carboxylate groups of the encapsulated succinate. In a previous work,[28] we evidenced that two effects are observed for ^{13}C nuclei of the encapsulated ligands within Keplerate capsules in solution: i) a shielding effect due to the encapsulation within the cavity, ii) a deshielding effect due to the coordination on the linker. The first peak at 175 ppm is thus assigned to the uncoordinated carboxylate that is hanging toward the center of the cavity while the second one at 182 ppm is attributed to the carboxylate group coordinated to the inner {Mo^{V}_{2}} linker. The spectrum of **$(DODA)_{33}Mo_{132}$Succ** is similar but the strong resonances of the $DODA^{+}$ cations overlap the signal of the succinate ligands. In the Zn-containing compound **$(DODA)_{23}Mo_{132}$SuccZn**, the ^{13}C peak of the uncoordinated carboxylate disappears and is probably deshielded from 175 ppm to 182 ppm, thus overlapping the signal of the carboxylate function linked the {Mo^{V}_{2}} unit. Such an effect evidences that Zn^{2+} trapped by the compound **$(DODA)_{23}Mo_{132}$SuccZn** are coordinated to the inner succinate ligands, in agreement with the

FT-IR data. Further work is now needed to fully understand this process and determine the parameters involved in this process.

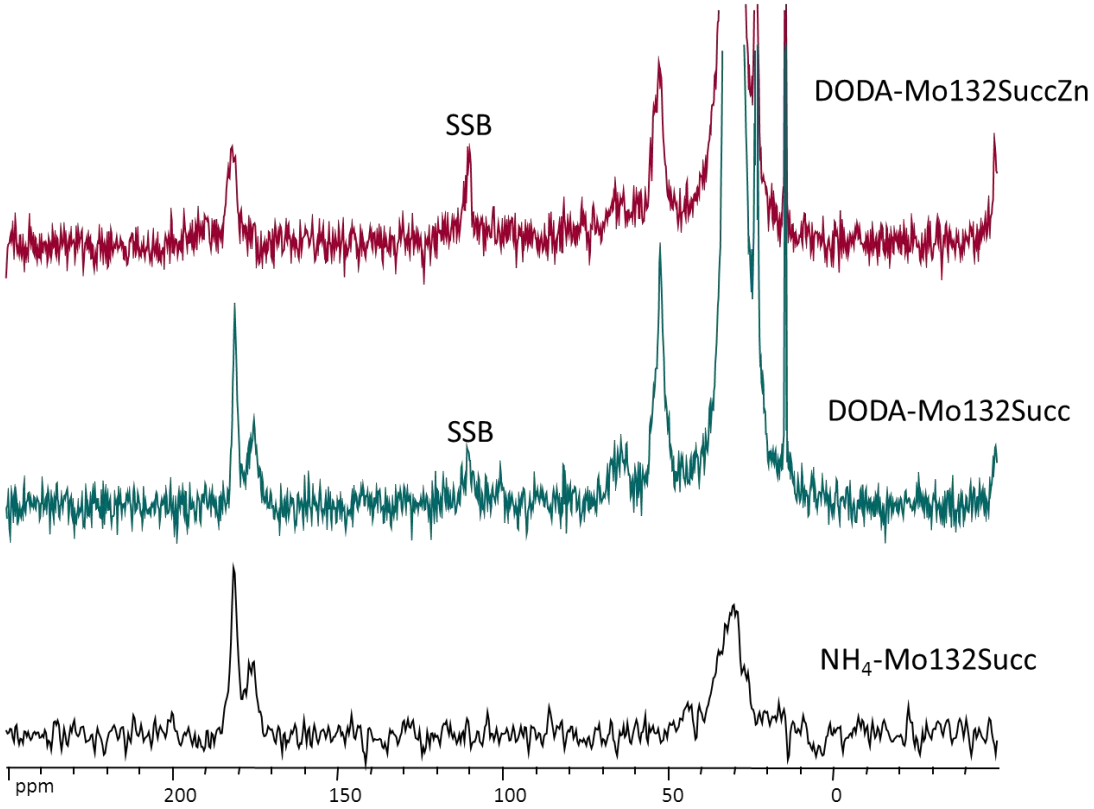

Figure 19: DNP-enhanced $^{13}C\{^{1}H\}$ NMR spectr of **$(NH_4)_{65}Mo_{132}$Succ, $(DODA)_{33}Mo_{132}$Succ and $(DODA)_{23}Mo_{132}$SuccZn.** SSB: Spinning sidebands

II.3.2 Embedding Keplerate cluster within silica matrix

Silica sol–gel is another viable option to organize and assemble POMs into easily processed materials. The intrinsic property of POMs and the easily tuneable properties of silica can be easily combined to get hybrid materials exhibiting interesting properties for optics,[29] catalysis,[30] and so on. Several approaches have been employed to organize POM into silica sol-gel materials i) a physical blending method, in which the POMs are not directly connected to the silica matrix, however this approach is limited as that the POMs can be easily decomposed by the presence of acid;[31] ii) grafting Si–O–R (R = methyl or ethyl) groups onto the reactive sites of specific POMs through a covalent linkage where POM derivatives are then embedded in the silica matrix through the Si–O–Si bond.[32] This strategy cannot be is restricted only to vacant POMs; iii) grafting an alkyl chain on the surface of a mesoporous silica followed by the immobilization of a surfactant encapsulated POM. This strategy has been notably employed by Barboiu by using MCM41 silica and the Keplerate $(DODA)_{40}Mo_{132}$.[11] Finally, Lixin Wu recently developed a new method to organize and assemble POMs into the easily processed silica-gel materials. By employing terminal

hydroxyl-modified cationic surfactants to encapsulate POMs such as the preyssler anion "NaP_5W_{30}", the obtained surfactant-encapsulated POM clusters (SECs) can link to the silica backbones covalently and disperse uniformly in the silica matrix as shown in (Figure 20). [33]

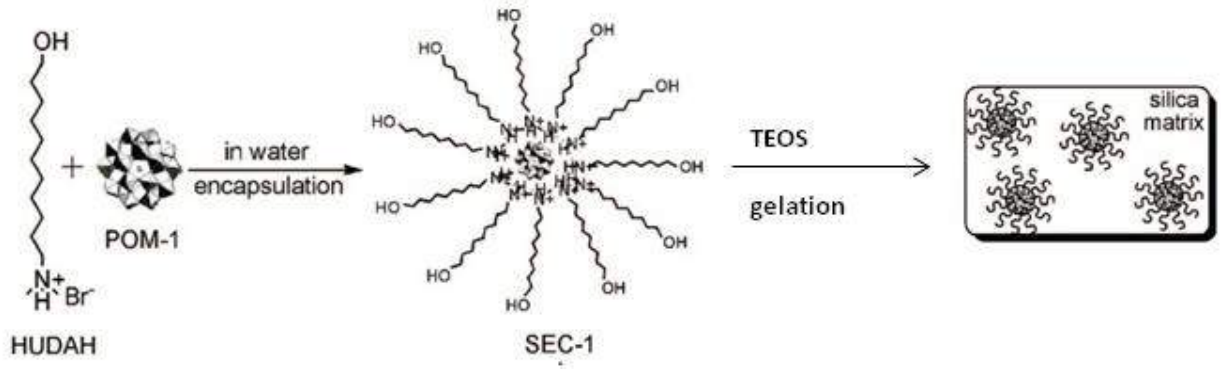

Figure 20: Overall procedure for fabricating POM-based silica hybrid materials [33]

II.3.2.a {Mo$_{132}$}-Silica Hybrid materials.

Introducing {Mo_{132}} into silica matrix will open new perspectives in the material science of this nanocapsule because the new hybrid material would possess the interesting properties of the Keplerate (especially in catalysis), as well as those of the silica, especially the biocompatibility and the low solubility in water. In the light of this potential applications, we attempted to combine the encapsulation method and the sol–gel technique by using (11-hydroxyundecyl) trimethylammonium bromide (HDTA, see Figure 21) as a bridging unit to obtain a stable, {Mo_{132}}-based silica-sol–gel hybrid material. The choice of the surfactant (HDTA) is vital for the construction of this material as each part plays an important role during the process: as shown in Chapter II, the cationic ammonium headgroup will interact with the Keplerate capsule, while the terminal hydroxyl group grafted on the alkyl chain could be covalently involved in the silica backbones through condensation of the silica precursor with the alcohol sites.[33]

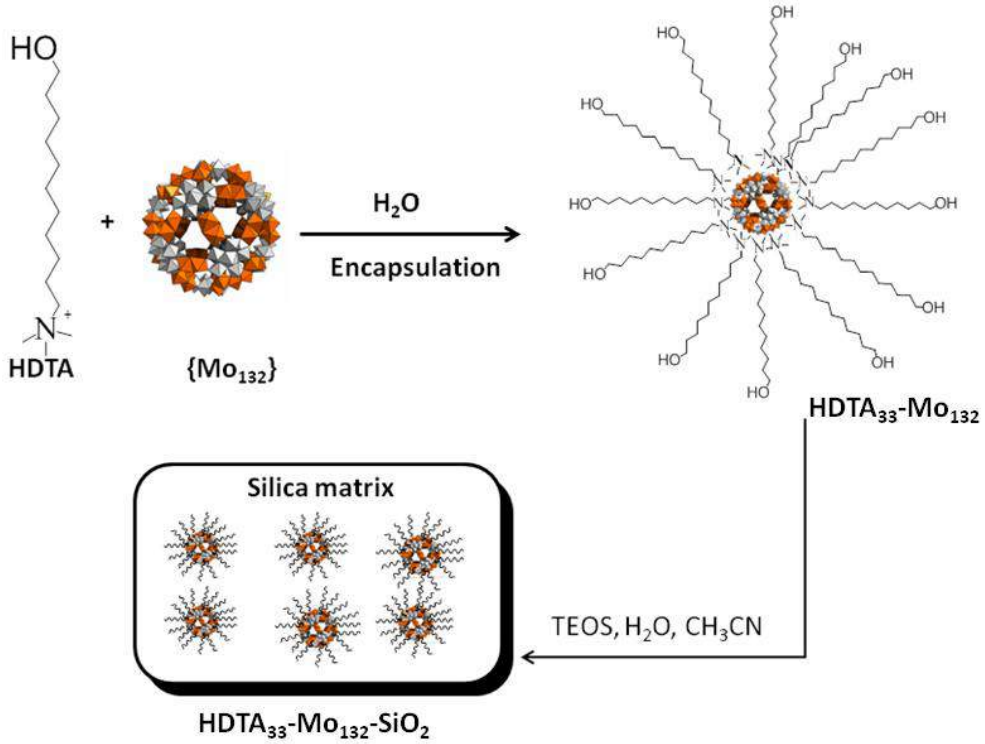

Figure 21: Schematic illustrating the overall procedures for the preparation of **$HDTA_{35}$-Mo_{132}-SiO_2**, including surfactant encapsulation (not all cations are drawn for clarity) and sol–gel formation.

As shown in Figure 21, the synthesis of $\{Mo_{132}\}$-Silica Hybrid materials is made up of two steps. The first step consists of encapsulation of $\{Mo_{132}\}$ by the cations $HDTA^+$ through direct precipitation in water (see experimental section) to yield **$HDTA_{33}$-Mo_{132}**. The usual characterizations techniques confirm the success of encapsulation step. The FT- IR spectrum exhibits the characteristic band of both keplerate and the $HDTA^+$ cation. Elemental analysis and TGA allowed the estimation of the final molecular formula of **$HDTA_{33}$-Mo_{132}** as follows $(HDTA)_{33}(NH_4)_3[Mo_{132}O_{372}(CH_3COO)_{24}(H_2O)_{72}].70H_2O$. The compound **$HDTA_{33}$-$Mo_{132}$** is soluble in mixed solvent containing acetonitrile and water due to the presence of the hyroxyl group on its surface but poorly soluble in water.

In a second step, the compound **$HDTA_{33}$-Mo_{132}** was added to the sol-gel precursor tetraethylorthosilicate (TEOS) in the mixed solvent (19.5 ml acetonitrile and 0.5 ml water). Based on the work of Wu, [33] two reactions are expected: hydrolysis of TEOS and the nucleophilic substitution of an ethoxy group by the hydroxyl group of the $HDTA^+$ cation for giving a silica backbones involving covalently the $HDTA^+$. Such a strategy allows keeping the**{Mo_{132}}** clusters dispersed in the silica matrix and yield the hybrid material **$HDTA_{35}$-Mo_{132}-SiO_2**, for which the formula was established by EDX and elemental analysis (C, H, N

only while Mo and Si are in progress). Interestingly, the formula **HDTA$_{35}$-Mo$_{132}$-SiO$_2$** shows the final negative charge of {Mo_{132}} has been increased concomitantly with the number of cations $HDTA^+$ and NH_4^+, since the number of acetate ligands was found 30 instead of 24 in the precursor compound **HDTA$_{33}$-Mo$_{132}$**. This result which could be explained by the presence of equilibriums between solvated acetate ligands and coordinated one in solution and must be confirmed on the basis of the full elemental analysis including Si and Mo percentages. Finally, it should be noted that nature of solvent and order of added precursors play an important role in the homogeneity of the final product. For example, blending the **HDTA$_{33}$-Mo$_{132}$** and the sol-gel precursor in mixed ethanol/water solution, or addition of TEOS to **HDTA$_{33}$-Mo$_{132}$** lead to isolation of heterogeneous solid powders (colorless solid containing some brown spots), which were not fully characterized.

II.3.2.b Characterization of the hybrid material HDTA$_{35}$-Mo$_{132}$-SiO$_2$.

The FT-IR spectrum of **HDTA$_{35}$-Mo$_{132}$-SiO$_2$** (Figure 22) shows the FT-IR bands of both (HDTA) surfactant and {Mo_{132}} thus confirming the existence of the assembly **HDTA$_{35}$-Mo$_{132}$** in the silica matrix. The presence of intense and broad stretching vibrations at 1070 cm^1 (ν Si-O-Si) and bending vibration at 440 cm^{-1} ν(Si-O-Si) indicates the formation of the silica network, the shoulder at 1150 cm^{-1} is attributed by Shroden and Wu to the vibration ν(Si-O-C) and evidences the condensation between TEOS and the hydroxyl group on the surface of **HDTA$_{35}$-Mo$_{132}$**.[32-33] The IR results thus suggest that the structural integrity of the Keplerate has been preserved and the clusters are chemically bound to the silica materials. Based on FT-IR data our first hypothesis is that **HDTA$_{33}$-Mo$_{132}$** may be grafted covalently onto the silica matrix.

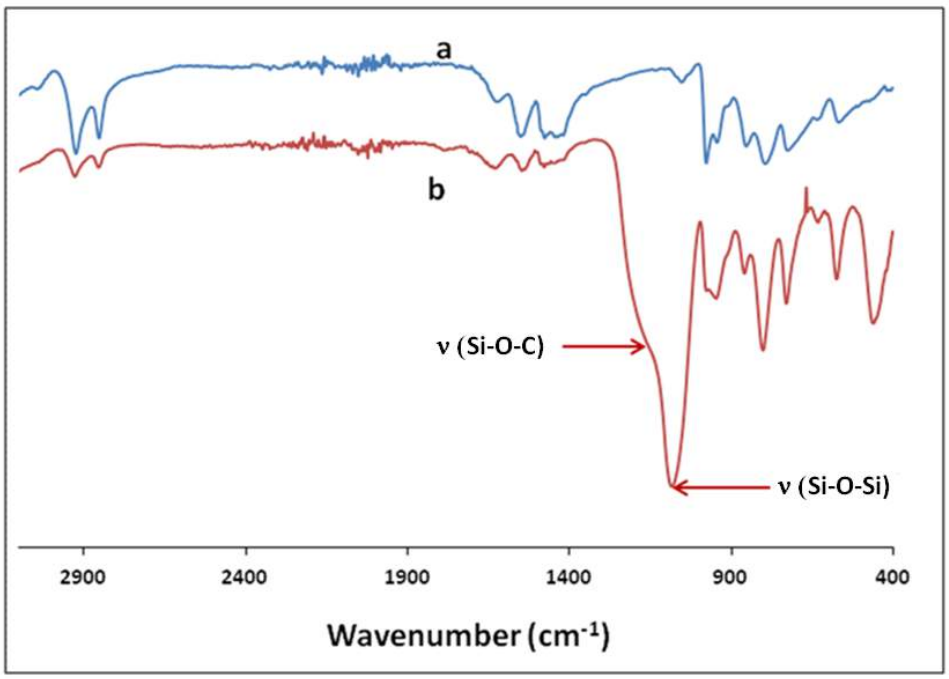

Figure 22: IR spectra of **HDTA$_{33}$-Mo$_{132}$** (a) **HDTA$_{35}$-Mo$_{132}$-SiO$_2$** (b)

II.3.2.c Solid state NMR characterization

^{1}H MAS NMR and ^{13}C{^{1}H} CPMAS NMR.

Information about the integrity of the organic species can be provided by ^{1}H MAS and ^{13}C{^{1}H} CPMAS NMR (Figure 23 and Figure 24). ^{1}H MAS NMR spectrum gives broad lines which are difficult to confidently be assigned. In contrast, the ^{13}C{^{1}H} CPMAS NMR spectrum displays well resolved resonances. The spectrum is dominated by the lines expected for the ($HDTA^{+}$) surfactant molecules present in the material **HDTA$_{35}$-Mo$_{132}$-SiO$_2$**. These NMR signals are assigned to the Alkyl carbon atoms of surfactant between 25 and 30 ppm, while the trimethylammonium polar head is observed at 55 ppm (CH_3) and 67 ppm (N-CH_2). Besides, regarding the good resolution of the spectrum, we can tentatively rule out the hypothesis of a distribution of different types of $HDTA^{+}$ cations in the solid and suggest the hypothesis of an unique favored configuration of the cations in the material. The peak at 180 ppm is assigned to the coordinated acetate to the inner {Mo^{V}_{2}} linker of the Keplerate capsule (Figure 24), whereas the signal expected for the methyl groups of the acetate ligands is expected around 30 ppm and probably overlapped by the signals of the alkyl chain of $HDTA^{+}$.

Finally, no solvent trace such as CH_3CN is detected in this spectrum, which demonstrates the presence of both Mo_{132} and $HDTA^+$ moieties.

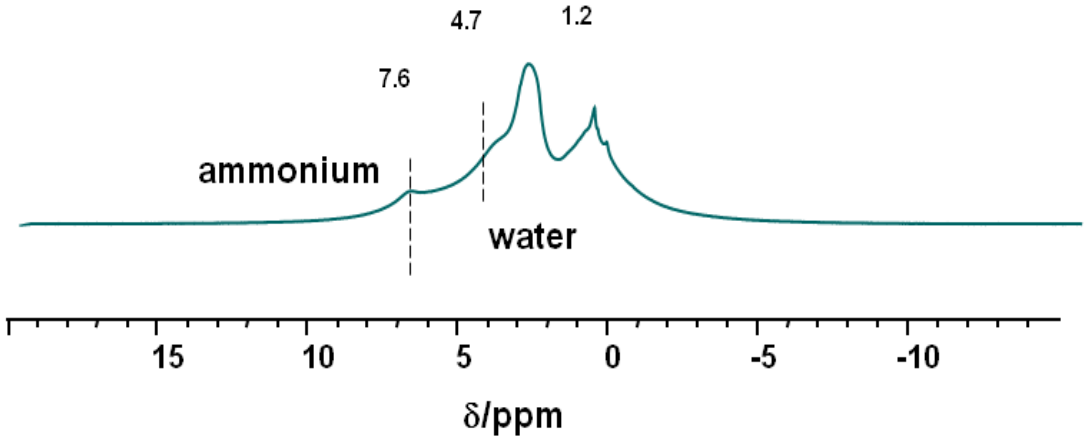

Figure 23: ^{1}H MAS NMR spectrum of **HDTA$_{35}$-Mo$_{132}$-SiO$_2$**.

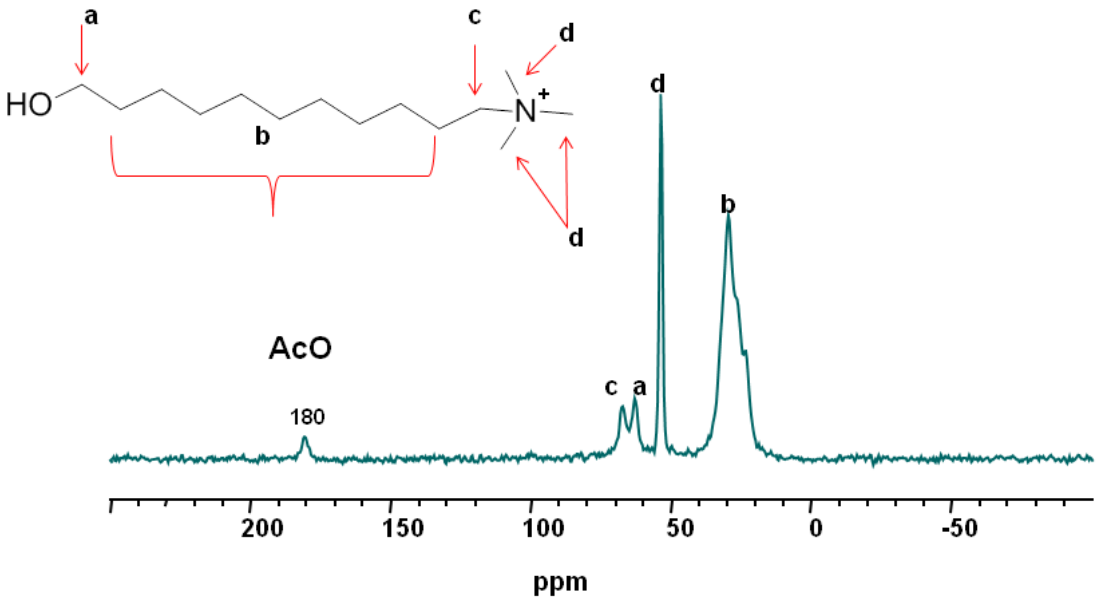

Figure 24: $^{13}C\{^1H\}$ CPMAS NMR spectra of **HDTA$_{35}$-Mo$_{132}$-SiO$_2$**

^{29}Si MAS NMR.

To confirm the incorporation and connection of the **HDTA$_{33}$-Mo$_{132}$** with the silica framework, the hybrid material **HDTA$_{35}$-Mo$_{132}$-SiO$_2$** was analyzed by the solid-state ^{29}Si MAS NMR, which informs about the environment of silicon atoms and consequently about the degree of condensation of silica network. Figure 25 shows the ^{29}Si MAS NMR spectra of **HDTA$_{35}$-Mo$_{132}$-SiO$_2$** obtained at a frequency of 99.35 MHz in CPMAS and in hpdec MAS modes. For

both spectra, three resonances at about -108, -98, and -88 ppm, corresponding respectively to Q^4 (Si-$(OSi)_4$), Q^3 (Si-$(OSi)_3(OH)$) and Q^2 (Si-$(OSi)_2(OH)_2$) units are observed. The CPMAS mode allows increasing the sensibility of the Si nuclei by polarization transfer from the protons and allows acquiring rapidly a spectrum with a good signal/noise ratio. However, by using this technique the signals of Q^2 and Q^3 Si nuclei are favored in comparison to that of Q^4, which preclude a quantitative analysis. This analysis can be obtained by decomposition of the spectrum obtained in hpdec MAS mode by using DMfit software. This decomposition gives the proportion of each $Q^n = (O)_{4-n}Si(OSi)_n$ type species which were 49% for Q^4, 43% for Q^3 and 8% for Q^2. The presence of Q^2 and Q^3 in the ^{29}Si NMR is indicative of the surface silanol groups and incomplete condensation of the silica frameworks.

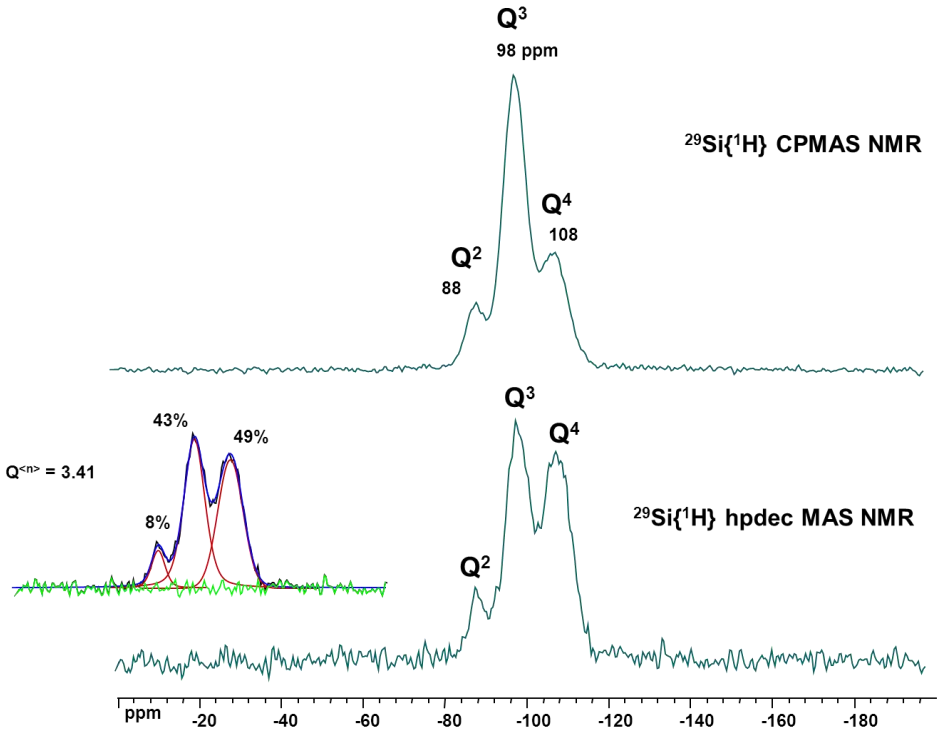

Figure 25: ^1H -decoupled ^{29}Si MAS NMR spectra of **$HDTA_{35}$-Mo_{132}-SiO_2**

Finally, the **$^{29}Si\{^1H\}$ Hetcor MAS** NMR experiment performed on **$HDTA_{35}$-Mo_{132}-SiO_2** (Figure 26) shows a strong correlation of the Q^3 silicon atoms and a signal around 6.5 ppm and a much smaller correlation between Q^4 Si atoms and a ^1H signal at 5 ppm. The ^1H MAS NMR spectrum being very broad, it is difficult to clearly identify the groups which are involved in these correlations. The ^1H signal at 6.5 ppm contains a contribution of the NH_4^+ cations and could also contain a contribution of the alcoholic groups of the $HDTA^+$ cation. Indeed these signals are expected in the 4-5 ppm but can be deshielded when involved in H-

Bond with the silanols groups Si-OH. At this stage, a correlation between ^{29}Si and ^{13}C is needed to clearly identify the groups of the HDTA+ cations which interact with the Q^3 Si atoms of the matrix.

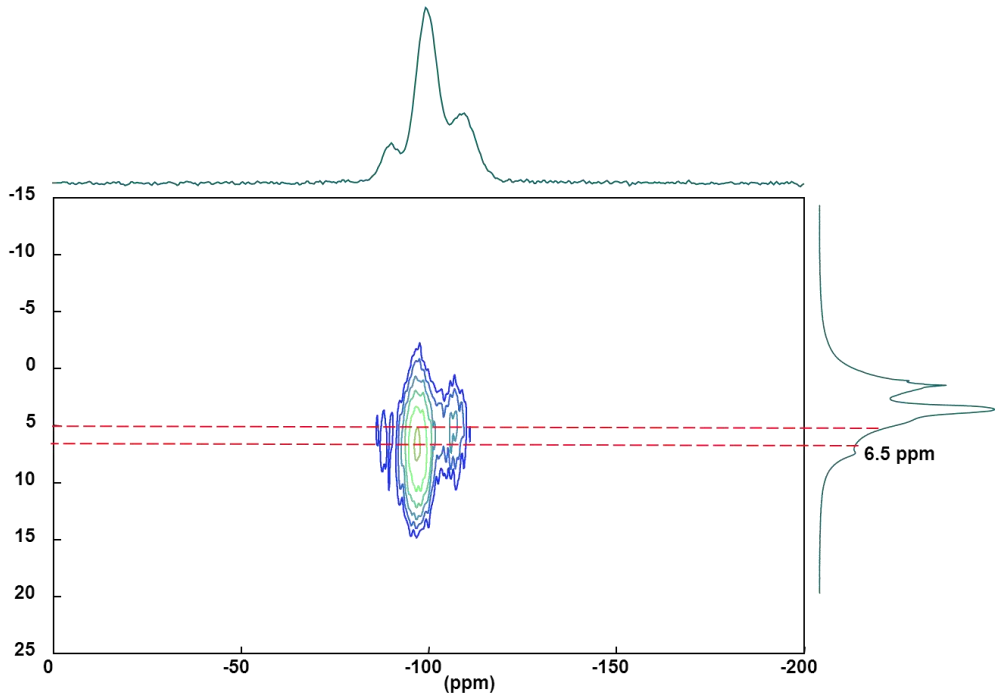

Figure 26: $^{29}Si\{^{1}H\}$ Hetcor MAS NMR spectrum of **$HDTA_{35}$-Mo_{132}-SiO_2**

In summary, for this part, it is possible to form a silica matrix around a Keplerate compound surrounded by ammonium cation bearing final alcoholic functions. On the basis of the FT-IR and MAS NMR experiments, the obtained materials contain all the starting components but the exact organization of these components is still not well established. On the basis of the FT-IR spectra and the work of Lixin Wu, the cation would be covalently engaged in the silica matrix. This hypothesis suggest that the Si-O-R^+ bond is stable against hydrolysis, which could be surprising. In contrast, the MAS NMR in the solid state suggest that the cations are present as one main form and the strong correlation evidenced between a Q^3 Si atom and ^{1}H signal probably due to cation interacting with the silica matrix through H-bonds of the type $(SiO)_3Si\text{-}OH\cdots OH\text{-}R^+$, which could result from the hydrolysis of Si-O-R^+ bond. Further MAS NMR experiments are currently in progress to definitely establish the organization within this material prior to the elaboration of new materials based on other keplerate compound containing transition metals such as Fe, Cr or V and open promising perspectives in the field of catalysis.

III. Conclusion

On the basis of the interactions observed in solution between the Keplerate cluster Mo_{132} and alkylammoniums or imidazoliums cations, the aim of this chapter was to exploit these interactions to build organized materials such as liquid crystals or to incorporate Keplerate in extended matrices such as silica.

For this purpose, we exchanged the ammonium counterions of the Keplerate cluster $\{Mo_{132}\}$ with a series of imidazoliums cations with different alkyl chain length to prepare Keplerate-based materials. The latter were characterized by many techniques and studied for their liquid crystalline properties and their organization in the solid state. The routine characterization techniques allowed establishing the composition of the materials and determine their thermal stability in different experimental conditions, thus revealing that these materials are stable in air till only 126°C, while under N_2 are stable till 250°C at least.

Liquid crystal properties of Keplerate-based materials were investigated in collaboration with Dr E. Terazzi (University of Geneva, Switzerland) using Polarized optical Microscopy, DSC and small-angle X-ray diffraction. The major part of the synthesized materials exhibit liquid crystalline phase. However, DSC show very broad phase transitions between the solid and the mesophase which could be explained by insufficient supramolecular mobility to develop network of intermolecular interaction. The organization of the materials was probed by small angle-X ray diffraction which reveal that three of the compounds, namely **$(mimC_{14})_{36}\{Mo_{132}\}$**, **$(mimC_{18})_{37}\{Mo_{132}\}$** and **$(mimC_{20})_{37}\{Mo_{132}\}$**, exhibit a lamellar ordering, while for the other we were not able to assign the type of ordering. The interlayer spacing values *h* were determined for the lamellar phases and are consistent with the non-uniform distribution of the imidazolium cations around the spherical clusters $\{Mo_{132}\}$. Finally calculation of the hexagonal lattice parameter a_{hex} implies the folding of the alkyl chains which lead to not well organized mesophases, in contrast to previously published work on the $DODA^+$ salts of keplerates.

The future work of this part will mainly concern the full understanding the nature of the organization of our compounds especially for the compound **$(Dendron)_{36}\{Mo_{132}\}$**, which could give a cubic mesophase, a phase rarely observed in this domain.

The hydrophobic surface of the surfactant encapsulated Keplerate materials increase their solubility in organic solvent and thus extend their scope of application. In this chapter, we present very preliminary results concerning metal trapping within the DODA-$\{Mo_{132}\}$ cavity.

We evidenced that it is possible to trap transitions metals within the cavity of Keplerate compound by transfer from aqueous to organic phase, while it was not possible in aqueous phase only. The choice of the internal ligand undoubtly plays an important role and the number and the nature of the organic cation could also have an importance since they can more or less block the access to the pores and are exchanged in order to balance the charge. Further work in now needed to precisely quantify the maximum amount of Zn^{2+} or other transition metals we can trap, to compare the properties of different keplerate compounds and to identify the possible role of the organic cations in this process.

Finally, in the last part, we used a sol-gel approach to prepare Keplerate-based silica materials by using a trimethylalkylammonium cations bearing an hydroxo group at its end and tetraethoxysilane TEOS in acetonitrile/water medium. This material was characterized by FT-IR, TGA, EA and solid state NMR and two hypotheses are made about the organization within the solid: a cation covalently involved within the silica matrix or a cation interacting by H-Bonds with silanol groups at the surface of the silica and some additional experiments are needed to definitely determine the organization of this material, which could be promising in catalysis, especially if we consider the flexibility of the sol-gel materials.

IV. Experimental Section

IV.1 Physical methods

Fourier transformed infrared (FT-IR) spectra. Fourier Transformed Infrared (FT-IR) spectra were recorded on a 6700 FT-IR Nicolet spectrophotometer, using diamond ATR technique. The spectra were recorded on undiluted samples and ATR correction was applied. **The variable temperature FT-IR spectra** were recorded on an IRTF Nicolet iS10 spectrometer in diffuse reflectance mode by using high temperature diffuse reflectance environmental chamber. The background was recorded using dry KBr at 150°C and the samples were diluted into a KBr matrix (about 10% of compound) before heating. The FT-IR spectra were recorded in the 20–500°C temperature range under air with a heating rate of 2°C min^{-1}. **Elemental analyses** were performed by the service central d'analyses du CNRS, Vernaison, France and by the service d'analyses du CNRS, ICSN, Gif sur Yvette, France. **Water content** was determined by thermal gravimetric (TGA) analysis with a Seiko TG/DTA 320 thermogravimetric balance (5°C min^{-1}, under air). **Nuclear magnetic resonance (NMR)**. Solution 1H NMR measurements were performed on a Bruker Avance 300 instrument operating at 300 MHz in 5 mm o.d. tubes. Chemical shifts were referenced to TMS.

Differential scanning calorimetry (DSC). DSC traces were obtained with a Mettler Toledo DSC1 Star Systems differential scanning calorimeter from 3 to 5 mg samples (5°C min^{-1}, under N_2). Several thermal cycles were performed between 40 °C and 220°C, the first one allowing the removal of water and the organization of the solid, the following cycles explored the reproducibility and the thermal stability of the materials in this temperature range.

Temperature dependent polarized optical microscopy (TD-POM). Temperature dependent polarized optical microscopy (TD-POM) characterizations of the optical textures of the mesophases were performed with a Leitz Orthoplan Pol polarizing microscope with a Leitz LL 20°/0.40 polarizing objective and equipped with a Linkam THMS 600 variable temperature stage.

IV.2 Synthesis of{Mo_{132}}-based materials for liquid crystalline properties

Compounds $(NH_4)_{42}[Mo_{132}O_{372}(CH_3COO)_{30}(H_2O)_{72}].300H_2O.ca.10CH_3COONH_4$ noted $(NH_4)_{52}\{Mo_{132}\}$ and $(NH_4)_{72}[Mo_{132}O_{372}(H_2O)_{72}(SO_4)_{30}].\sim200H_2O$ noted $(NH_4)_{72}\{Mo_{132}$-sulfate$\}$ were prepared as described by Müller et al.[26-27]. Dimethyldioctadecylammonium

chloride (DODACl) were purchased from Aldrich or Acros chemicals and "Dendron"Br was supplied from University of Geneva, Switzerland (Dr. Emmanuel Terrazi).

IV.2.1 Synthesis of 1-methyl-3-alkylimidazolium bromides, mimCnBr (n = 12, 14, 16, 18, 20).

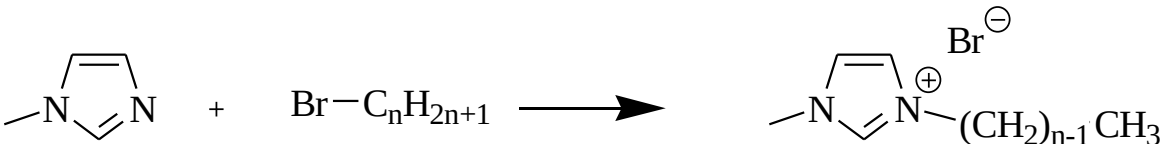

10^{-2} mole of 1-methyl imidazole and 1.2 10^{-2} mole of $C_nH_{2n+1}Br$ were dissolved in acetonitrile (5 mL for n = 12-16, 15 mL for n = 18, 20). The resulting solution was refluxed for 24 hrs. After, it was cooled down in an ice bath; a precipitate appeared. The latter was isolated by filtration and washed with diethyl ether. The mimC_nBr salts were characterized by FT-IR and ^{1}H NMR in $CDCl_3$.

mimC_{12}Br. IR/cm^{-1}, (ATR diamond, ATR correction applied): 3475 (ms), 3427 (ms), 3082 (s), 3062 (s), 2950 (m), 2915 (vs), 2870 (mw), 2850 (s), 1668 (w), 1627 (m), 1572 (s), 1472 (s), 1426 (mw), 1382 (w), 1177 (vs), 861 (ms), 791 (s), 741 (w), 716 (ms), 662 (m), 622 (s), 503 (s), 472 (s), 444 (s), 419 (s), 400 (s). ^{1}H NMR (δ / ppm / CDCl3): 10.44 (s., 1H), 7.41 (s. br., 1H), 7.30 (s. br., 1H), 4.32 (t., 2H), 4.13 (s., 3H), 2.13 (m, 2H), 1.92 (m, 2H), 1.35-1.20 (m, 16H), 0.88 (t., 3H).

mimC_{14}Br. IR/cm^{-1}, (ATR diamond, ATR correction applied): 2954 (m), 2920 (vs), 2870 (m), 2851 (s), 1639 (mw), 1467 (m), 1135 (m), 1078 (m), 1022 (w), 939 (s), 879 (m), 792 (s), 723 (s). 1H NMR (δ / ppm / CDCl3): 10.52 (s., 1H), 7.39 (s. br., 1H), 7.28 (s. br., 1H), 4.32 (t., 2H), 4.13 (s., 3H), 1.92 (m, 2H), 1.85 (m, 2H), 1.35-1.20 (m, 20H), 0.88 (t., 3H).

mimC_{16}Br. IR/cm^{-1}, (ATR diamond, ATR correction applied): 2954 (m), 2920 (vs), 2870 (m), 2851 (s), 1639 (mw), 1467 (m), 1135 (m), 1078 (m), 1022 (w), 939 (s), 879 (m), 792 (s), 723 (s). 1H NMR (δ / ppm / CDCl3): 10.60 (s., 1H), 7.35 (s. br., 1H), 7.25 (s. br., 1H), 4.32 (t., 2H), 4.14 (s., 3H), 1.92 (m, 2H), 1.83 (s. br., 2H), 1.35-1.20 (m, 24H), 0.88 (t., 3H).

mimC_{18}Br. IR/cm^{-1}, (ATR diamond, ATR correction applied): 2954 (m), 2920 (vs), 2870 (m), 2851 (s), 1639 (mw), 1467 (m), 1135 (m), 1078 (m), 1022 (w), 939 (s), 879 (m), 792 (s),

723 (s). 1H NMR (δ / ppm / CDCl3): 10.57 (s., 1H), 7.33 (s. br., 1H), 7.26 (s. br., 1H), 4.32 (t., 2H), 4.14 (s., 3H), 1.92 (m, 2H), 1.76 (s. br., 2H), 1.35-1.20 (m, 28H), 0.88 (t., 3H).

mimC_{20}Br. IR/cm^{-1}, (ATR diamond, ATR correction applied): 2954 (m), 2920 (vs), 2870 (m), 2851 (s), 1639 (mw), 1467 (m), 1135 (m), 1078 (m), 1022 (w), 939 (s), 879 (m), 792 (s), 723 (s). 1H NMR (δ / ppm / CDCl3): 10.62 (s., 1H), 7.25 (s. br., 1H), 7.22 (s. br., 1H), 4.33 (t., 2H), 4.14 (s., 3H), 1.93 (t, 2H), 1. (s. br., 2H), 1.35-1.20 (m, 32H), 0.89 (t., 3H).

IV.2.2 General preparation of keplerate-based materials.

The Keplerate based materials was prepared as follows: $(NH_4)_{52}\{Mo_{132}\}$(300 mg, 0.01 mmol) was dissolved in 30 ml of water and then a chloroform solution containing the organic cations (≈ 168 equivalents / Mo_{132}, 1.72 mmol). The mixture was stirred for 1 hour, where the keplerate was totally transferred into the organic phase as indicated by the colorless aqueous phase. The organic phase was then separated and the target materials were precipitated from the organic phase by addition of an excess of ethanol, isolated by filtration, washed with ethanol, dried in air and characterized by FT-IR, EDX, Elemental Analyses, TGA and ^{1}H NMR.

$(mimC_{12}H_{25})_{36}(NH_4)_5[Mo_{132}O_{372}(CH_3COO)_{30}(H_2O)_{72}].24H_2O$, $(mimC_{12})_{35}$-Mo_{132}. It was prepared using $mimC_{12}Br$ (582 mg, 1.76 mmol). Yield 200 mg, 63 %. IR/cm^{-1} : 2922 (vs) , 2852 (s), 1553 (s), 1442 (m), 1163 (m), 975 (vs), 940 (s), 855(s) 801 (vs), 727 (s), 635 (m), 573 (s). Elemental analysis calcd (%) for $(mimC_{12}H_{25})_{35}(NH_4)_5[Mo_{132}O_{372}(CH_3COO)_{28}(H_2O)_{72}].24H_2O$ (M = 30961 g.mol^{-1}) C 23.90; H, 4.52; N, 3.39; Mo, 40.90. Found C, 24.30; H, 4.45; N, 3.39; Mo, 39.28. EDX only evidenced Mo and shows no traces of Br which could be due to an excess of the starting salt. Thermogravimetric analysis (TGA) suggests a mass loss of 6 % from room temperature to 188°C corresponding to crystallization and coordinated water molecules (calcd: 5.8%).

$(mimC_{14}H_{29})_{38}(NH_4)_4[Mo_{132}O_{372}(CH_3COO)_{30}(H_2O)_{72}].38H_2O$, $(mimC_{14})_{36}$-Mo_{132}. It was prepared using $mimC_{14}Br$ (634 mg, 1.76 mmol). Yield 269 mg, 80 %. IR/cm^{-1} : 2920 (m) , 2850 (m), 1547 (m), 1440 (m), 1161 (m), 974 (vs), 939 (s), 789 (vs), 711 (vs), 563 (vs), 410 (vs). Elemental analysis calcd (%) for $(mimC_{14}H_{29})_{36}(NH_4)_4[Mo_{132}O_{372}(CH_3COO)_{28}(H_2O)_{72}].38H_2O$ (M = 32387g.mol^{-1}) C 26.11; H, 4.92; N, 3.28; Mo, 39.1. Found C, 26.22 ; H, 4.90; N, 3.30; Mo, 39.28. EDX only evidenced Mo and shows no traces of Br which could be due to an excess of the starting salt.

Thermogravimetric analysis (TGA) suggests a mass loss of 5.4 % from room temperature to 135°C corresponding to crystallization and coordinated water molecules (calcd: 5.7%).

$(mimC_{16}H_{33})_{41}(NH_4)_1[Mo_{132}O_{372}(CH_3COO)_{30}(H_2O)_{72}].38H_2O$, $(mimC_{16})$-$\{Mo_{132}\}$. It was prepared using $mimC_{16}Br$ (683 mg, 1.76 mmol). Yield 350 mg, quantitative yield. IR/cm^{-1} : 3451 (m), 2923 (s) , 2853 (m), 1560 (m), 1466 (m), 1164 (m), 976 (vs), 941 (m), 807 (vs), 729 (vs), 577 (s), 415 (vs). Elemental analysis calcd (%) for $(mimC_{16}H_{29})_{40}(NH_4)_3[Mo_{132}O_{372}(CH_3COO)_{30}(H_2O)_{72}].48H_2O$ (M = 34889.2g.mol^{-1}) C 29.61; H, 5.62; N, 3.25; Mo, 36.33. Found C, 29.60 ; H, 5.48; N, 3.39; Mo, 36.3. EDX only evidenced Mo and shows no traces of Br which could be due to an excess of the starting salt. Thermogravimetric analysis (TGA) suggests a mass loss of 6.4 % from room temperature to 150°C corresponding to crystallization and coordinated water molecules (calcd: 6.2%).

$(mimC_{18}H_{37})_{37}(NH_4)_5[Mo_{132}O_{372}(CH_3COO)_{30}(H_2O)_{72}].48H_2O$, $(mimC_{18})_{37}$-Mo_{132}. It was prepared using $mimC_{18}Br$ (732 mg, 1.76 mmol). Yield 355 mg, 96 %. IR/cm^{-1} : , 2919 (s) , 2849 (m), 1555 (m), 1424 (m), 1161 (m), 975 (s), 941 (s), 854 (s), 791 (vs), 713 (vs), 565 (vs), 411 (vs). Elemental analysis calcd (%) for $(mimC_{18}H_{29})_{40}(NH_4)_3[Mo_{132}O_{372}(CH_3COO)_{30}(H_2O)_{72}].48H_2O$ (M = 35058.68 g.mol^{-1}) C 29.88; H, 5.57; N, 3.11; Mo, 36.28 Found C, 29.94 ; H, 5.58; N, 3.15; Mo, 36.13. EDX only evidenced Mo and shows no traces of Br which could be due to an excess of the starting salt. Thermogravimetric analysis (TGA) suggests a mass loss of 6.25 % from room temperature to 188°C corresponding to crystallization and coordinated water molecules (calcd: 6.16%).

$(mimC_{20}H_{41})_{37}(NH_4)_5[Mo_{132}O_{372}(CH_3COO)_{30}(H_2O)_{72}].43H_2O$, $(mimC_{20})_{37}$-Mo_{132}. It was prepared using $mimC_{20}Br$ (780 mg, 1.76 mmol). Yield 0.35 mg, 92 %. IR/cm^{-1} : 2919 (s) , 2850 (s), 1541 (m), 1443 (m), 1162 (m), 973 (s), 938 (s), 854 (s), 792 (vs), 632 (vs), 565 (vs), 411 (vs). Elemental analysis calcd (%) for $(mimC_{20}H_{41})_{37}(NH_4)_5[Mo_{132}O_{372}(CH_3COO)_{30}(H_2O)_{72}]. 43H_2O$ (M = 36006.57g.mol^{-1}) C 31.62; H, 5,81; N, 3.07; Mo, 35.17. Found C, 31.36 ; H, 5.51; N, 3.07; Mo, 35.12. EDX only evidenced Mo and shows no traces of Br which could be due to an excess of the starting salt. Thermogravimetric analysis (TGA) suggests a mass loss of 5.5 % from room temperature to 160°C corresponding to crystallization and coordinated water molecules (calcd: 5.7%).

$(mimC_{12}H_{25})_{20}(mimC_{20}H_{33})_{20}(NH_4)_2[Mo_{132}O_{372}(CH_3COO)_{30}(H_2O)_{72}].38H_2O$, $(mimC_{12})_{20}$-$(mimC_{20})_{20}$-Mo_{132}. It was prepared using $mimC_{20}Br$ (390 mg, 0.882 mmol) and $mimC_{12}Br$ (290 mg, 0.882 mmol). Yield 100 mg, 28%. IR/cm^{-1} : 2920 (vs) , 2849 (s), 1557 (m), 1442

(m), 1162 (m), 972 (vs), 940 (s), 854 (s), 798 (vs), 570 (s), 412 (s). Elemental analysis calcd (%) for ($mimC_{12}H_{25})_{20}$ ($mimC_{20}H_{33})_{20}(NH_4)_2[Mo_{132}O_{372}(CH_3COO)_{30}(H_2O)_{72}].38H_2O$ (M = 34709.05 g.mol^{-1}) C 29.75; H, 5.45; N, 3.30. Found C, 29.70 ; H, 5.63; N, 3.25. EDX atomic ratios calculated for ($mimC_{12}$)($mimC_{20}$)-{Mo_{132}} shows no Br or traces. Thermogravimetric analysis (TGA) suggests a mass loss of 5.7 % from room temperature to 170°C corresponding to crystallization and coordinated water molecules (calcd: 5.7%) and % org 42.5% (cald 40.6%)

$(mimC_{12}H_{25})_{33}(mimC_{20}H_{33})_7(NH_4)_2[Mo_{132}O_{372}(CH_3COO)_{30}(H_2O)_{72}].48H_2O$, $(mimC_{12})_{33}(mimC_{20})_7$-$Mo_{132}$. It was prepared using $mimC_{12}Br$ (462 mg, 1.41 mmol) and $mimC_{20}Br$ (156 mg, 0.34 mmol). Yield 120 mg, 34.3%. IR/cm^{-1}. 2922 (vs) , 2851 (s), 1557 (s), 1444 (m), 1163 (m), 973 (vs), 941 (s), 855 (s), 799 (s), 724 (vs), 570 (vs), 412 (vs). Elemental analysis calcd (%) for $(mimC_{12}H_{25})_{33}(mimC_{20}H_{33})_7(NH_4)_2[Mo_{132}O_{372}(CH_3COO)_{30}(H_2O)_{72}].38H_2O$ (M = 33430.45 g.mol^{-1}) C 27.16; H, 5.09; N, 3.43. Found C, 27.30 ; H, 5.01; N, 3.14. EDX only evidenced Mo and shows no traces of Br which could be due to an excess of the starting salt. Thermogravimetric analysis (TGA) suggests a mass loss of 6.6 % from room temperature to 170°C corresponding to crystallization and coordinated water molecules (calcd: 6.4%) and % org: 37.4 (calcd 37.4%)

$(mimC_{12}H_{25})_8(mimC_{20}H_{33})_{33}(NH_4)_1[Mo_{132}O_{372}(CH_3COO)_{30}(H_2O)_{72}].38H_2O$, $(mimC_{12})_8(mimC_{20})_{33}$-$Mo_{132}$. It was prepared using $mimC_{12}Br$ (120 mg, 0.35 mmol) and $mimC_{20}Br$ (620 mg, 1.4 mmol). Yield 110 mg, 30.5 %. IR/cm^{-1} : 2923 (vs) , 2852 (s), 1559 (s), 1465 (m), 1163 (s), 976 (vs), 941 (vs), 859 (vs), 732 (vs), 576 (s), 412 (vs). Elemental analysis calcd (%) for $(mimC_{12}H_{25})_8(mimC_{20}H_{33})_{33}(NH_4)_2[Mo_{132}O_{372}(CH_3COO)_{30}(H_2O)_{72}].38H_2O$ (M= 34709.05 g.mol^{-1}) C 32.17; H, 5.87; N, 3.17. Found C, 32.11; H, 5.71; N, 3.24. EDX atomic ratios calculated for ($mimC_{12}$)($mimC_{20}$)-{Mo_{132}} shows no Br or traces. Thermogravimetric analysis (TGA) suggests a mass loss of 5.7 % from room temperature to 170°C corresponding to crystallization and coordinated water molecules (calcd: 5.7%) and org 46.8% (calc 49%)

$(C_{85}H_{145}N_2O_5)_{36}(NH_4)_6[Mo_{132}O_{372}(CH_3COO)_{30}(H_2O)_{72}].58H_2O$, (Dendron)$_{36}$-$Mo_{132}$. It was prepared using "Dendron"Br (300 mg, 0.221 mmol). Yield 243 mg, 33.75 %. IR/cm^{-1} : 2924 (vs) , 2853 (s), 1597 (m), 1464 (m), 1162 (m), 979 (vs), 944 (vs), 861 (s), 731 (vs), 570 (s), 412 (vs). Elemental analysis calcd (%) for $(C_{85}H_{145}N_2O_5)_{36}(NH_4)_6[Mo_{132}O_{372}(CH_3COO)_{30}(H_2O)_{72}].58H_2O$ (M =68742.5 g.mol^{-1}) C 54.60; H, 8.20; N, 1.58; Mo 18.4. Found C, 54.45 ; H, 8.25; N, 1.60; Mo 18.1. EDX only evidenced Mo and shows no traces of Br which could

be due to an excess of the starting salt. Thermogravimetric analysis (TGA) suggests a mass loss of 3.5 % from room temperature to 140°C corresponding to crystallization and coordinated water molecules (calcd: 3.4 %).

IV.3 Zn^{2+} uptake behavior of Mo_{132} in DODA-Mo_{132} based materials.

$(DODA)_{32}(NH_4)_5[Mo_{132}O_{372}(CH_3COO)_{25}(H_2O)_{82}].70H_2O$, noted $(DODA)_{32}\{Mo_{132}\}$. It was prepared using $DODA^+$ cations (300 mg, 0.5 mmol). Yield 170 mg, 85%, IR/cm^{-1}: 2921(s), 2851(s), 1635(m), 1558(m), 1467(m), 981(s), 946(m), 861(s), 808(s), 732(s), 635(m), 577(s), 471(m). Elemental analysis calcd (%) for $(C_{38}H_{80}N)_{32}(NH_4)_5[Mo_{132}O_{372}(CH_3COO)_{25}\ H_2O)_{82}].\ 70H_2O$ (M =39480.8 $g.mol^{-1}$) C 37.18; H, 7.21; N, 1.29. Found C, 37.31 ; H, 7.25; N, 1.11. Thermogravimetric analysis (TGA) suggests a mass loss of 5.6 % from room temperature to 150°C corresponding to crystallization and coordinated water molecules (calcd: 5.2 %).

$(NH_4)_{65}[Mo_{132}O_{372}(HSucc)_7(Succ)_{23}(H_2O)_{72}].170H_2O$, noted $(NH_4)_{65}\{Mo_{132}Succ\}$.

A large excess of succinic acid (1.53 g, 13 mmol, 300 eq.) was added under stirring to a 40 mL aqueous solution of $(NH_4)_{72}\{Mo_{132}$-sulfate$\}$ (1.2 g; 4.3 10^{-5} mol). The pH was adjusted to 4 with an aqueous solution of ammoniac at 2%. After two hours, the dark brown solution was kept to slowly evaporate in air for several days. Large hexagonal black crystals were obtained when the solution was almost totally evaporated. The crystals were isolated by filtration and washed with ethanol and diethyether. Yield 0.85 g, 72%. FT-IR/cm^{-1}, (Diamond ATR): 1710(w), 1618(m), 1545(vs), 1425(vs, br.), 959(s), 935(s), 843(s), 785(vs), 723(s), 669(m), 571(ms). Elemental analysis calcd (%) for $(NH_4)_{65}[Mo_{132}O_{372}(HC_4H_4O_4)_7\ (C_4H_4O_4)_{23}\ (H_2O)_{72}].170H_2O$ (M = 27692 g mol^{-1}): C 5.21; H 3.18; N 3.29; Mo 45.82; found: C 5.10; H 3.28; N 3.53; Mo 45.86. EDX: Only Mo can be analyzed and no traces of sulfates.

$(DODA)_{33}(NH_4)_{12}[Mo_{132}O_{372}(HSucc)_{13}(Succ)_{10}(H_2O)_{86}].30H_2O$. noted $(DODA)_{33}\{Mo_{132}Succ\}$: It was prepared following the same phase transfer procedure described above using $(NH_4)_{65}$-Mo_{132}Succ (300 mg, 1.08.10^{-2} mmol) in 30 mL water and $DODA^+$ cations (300 mg, 0.5 mmol) in 30 mL chloroform. Yield 150 mg, 0.75%, IR/cm^{-1}: 2919(s), 2850(s), 1710(w), 1618(m), 1545(vs), 1425(vs, br.), 959(s), 935(s), 843(s), 785(vs), 723(s), 669(m), 571(ms). Elemental analysis calcd (%) for $(C_{38}H_{80}N)_{33}(NH_4)_{12}[Mo_{132}O_{372}(HC_4H_4O_4)_{13}(C_4H_4O_4)_{10}(H_2O)_{82}].70H_2O$ (M = 41789.73 $g.mol^{-1}$) C, 38.69; H, 7.30; N, 1.51. Found C, 38.52 ; H, 7.52; N, 1.37. Thermogravimetric analysis

(TGA) suggests a mass loss of 4.1 % from room temperature to 150°C corresponding to crystallization and coordinated water molecules (calcd: 4.0 %).

$(DODA)_{23}(NH_4)_7[Mo_{132}O_{372}Zn_6(Succ)_{15}(H_2O)_{102}]$. noted $(DODA)_{23}Zn_6Mo_{132}Succ$: 500 mg of $(DODA)_{33}Mo_{132}Succ$ ($1.2\ 10^{-2}$ mmol) was dissolved in 30 mL of chloroform . An aqueous solution (10ml of deionized water) containing 206 mg of $ZnCl_2 \bullet 2H_2O$ (1.5 mmol) was added to the above solution under stirring. The solution was stirred at room temperature for 20 hours then the organic phase was separated and precipitated with ethanol to get $(DODA)_{33}Zn_6\{Mo_{132}\text{-succ}\}$ which was washed with diethyl ether and dried under air. IR (cm^{-1}): 2919(s), 2850(s), 1540(m), 1462(m), 977(s), 852(s), 790(vs), 717(vs), 632(s), 566(vs),411(vs). Elemental analysis calcd (%) for $(DODA)_{23}(NH_4)_7[Mo_{132}O_{372}Zn_6(Succ)_{15}(H_2O)_{102}]$ (M= 35387 $g.mol^{-1}$) C, 31.70; H, 6.07; N, 1.19; Mo 35.79; Zn 1.11. Found C, 31.69; H, 5.90; N, 0.97, Mo and Zn (in progress). EDX atomic ratios calculated for $DODA)_{33}Zn_6$ $\{Mo_{132}\text{-succ}\}$: Mo/Zn = 22 (found = 22). Thermogravimetric analysis (TGA) suggests a mass loss of 5.2 % from room temperature to 120°C corresponding to crystallization and coordinated water molecules (calcd: 5.2 %). % Org 42.5% (calc 41.1)

Flame atomic absorption experiment: In a typical experiment, 16 mg of $(DODA)_{33}$ $Mo_{132}Succ$ was dissolved in 10 mL of Chloroform. An DI aqueous solution (5 mL) containing a certain amount of $ZnCl_2 \bullet 2H_2O$ ranging between 10 and 200 equivalents was added to the above solution under stirring. The emulsion was stirred at room temperature for 20 hour. Then the aqueous solution was dilluted 100 times and analyzed by FAA.

IV.4 Preparation of $\{Mo_{132}\}$-Silica Hybrid materials.

Preparation of (11-hydroxyundecyl)trimethylammonium bromide (HDTA)

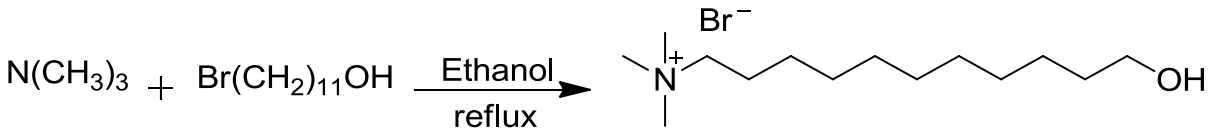

Trimethylamine $N(CH_3)_3$ (4 mL, 28 mmol) and $Br(CH_2)_{11}OH$ (1 g, 4 mmol) were dissolved in 50 mL of ethanol and the initial molar ratio of $N(CH_3)_3$ to $Br(CH_2)_{11}OH$ was controlled at 7:1. The reaction mixture was heated at reflux with stirring for 24h and then cooled to room temperature. After that, ethanol was evaporated and the product was precipitated by addition

of ether, followed by filtration (Yield: 90 %). ^{1}H NMR ($CDCl_3$): 1.28 (m, 14H), 1.47 (m, 2H), 1.56 (m, 2H), 2.25 (s, 6H), 2.28 (t, 2H), 3.64 (t, 2H).

Preparation $(C_{14}H_{32}ON)_{33}(NH_4)_3[Mo_{132}O_{372}(CH_3COO)_{24}(H_2O)_{84}].58H_2O$, noted $(HDTA)_{33}\{Mo_{132}\}$.

The compound $(HDTA)_{33}\{Mo_{132}\}$ was prepared as follows: a solution of $(NH_4)_{52}\{Mo_{132}$-acetate$\}$ (600 mg, 0.02 mmol, 11 ml of water) was added drop by drop to a water solution containing an excess of HDTA in water (0.28 mg , 20 mL), provoking the formation of a black precipitate. After stirring for 1 hr, the resulting precipitate was filtered and washed with diethyl ether (390 mg, 65%). IR (cm^{-1}): 2922 (vs), 2850 (s), 1549 (m), 1475 (m), 976 (s), 794 (vs), 725 (s), 586 (vs). The final formula was estimated based on elemental analysis and TGA. Elemental analysis (calcd %) $(C_{14}H_{32}ON)_{33}(NH_4)_3[Mo_{132}O_{372}(CH_3COO)_{24}(H_2O)_{84}].58H_2O$ (M =30104.8 $g.mol^{-1}$) C 20.35; H, 4.71 ; N, 1.67.Found C, 20.40 ; H, 4.71; N, 1.67. Thermogravimetric analysis (TGA) suggests a mass loss of 8.0 % from room temperature to 170°C corresponding to crystallization and coordinated water molecules (calcd: 8.4 %).

Preparation of $(HDTA)_{33}\{Mo_{132}$-acetate$\}$-1 silica hybrid materials.

0.1 g of $(HDTA)_{33}\{Mo_{132}$-acetate$\}$ was dissolved in 19.5 mL acetonitrile and 0.5 mL of water. When it was completely dissolved, it was then added drop by drop to 0.5 g of TEOS. The precipitation occurs after 4 days, the obtained precipitate was filtered washed with ethanol. 375 mg, Yield 75%. IR (cm^{-1}): 2925 (m), 2850 (w), 1627(w), 1550 (w), 1477(w), 1070 (vs), 943 (s), 801(s) ,794 (s), 725 (s), 459 (s). Elemental analysis (calcd %) $(SiO_2)_{450}(C_{14}H_{32}ON)_{35}(NH_4)_7[Mo_{132}O_{372}(CH_3COO)_{30}(H_2O)_{72}].160H_2O$ (M =59761 $g.mol^{-1}$) C 11.05; H 2.86 ; N 0.98; Si 21.14; Mo 21.19. Found C 11.06; H 3.08; N 1.05, Si and Mo in progress. Thermogravimetric analysis (TGA) suggests a mass loss of 7 % from room temperature to 150°C corresponding to crystallization and coordinated water molecules (calcd: 6.9 %). EDX atomic ratios calculated for: Si/Mo = 3.45 (3.7%).

V. References

[1] P. Kogerler, B. Tsukerblat, A. Muller, *Dalton Trans.* **2010**, *39*, 21-36.
[2] B. Botar, P. Kogerler, A. Muller, R. Garcia-Serres, C. L. Hill, *Chem. Commun.* **2005**, 5621-5623.
[3] A. Rezaeifard, R. Haddad, M. Jafarpour, M. Hakimi, *J. Am. Chem. Soc.* **2013**, *135*, 10036-10039.
[4] S. Kopilevich, A. Gil, M. Garcia-Rates, J. Bonet-Avalos, C. Bo, A. Müller, I. A. Weinstock, *J. Am. Chem. Soc.* **2012**, *134*, 13082-13088.
[5] A. A. Ostroushko, K. V. Grzhegorzhevskii, *Russ. J. Phys. Chem. A* **2014**, *88*, 1008-1011.
[6] Y. S. Zhou, Z. H. Shi, L. J. Zhang, S. ul Hassan, N. N. Qu, *Appl. Phys. A-Mater. Sci. Process.* **2013**, *113*, 563-568.
[7] L. J. Zhang, Z. H. Shi, L. H. Zhang, Y. S. Zhou, S. ul Hassan, *Mater. Lett.* **2012**, *86*, 62-64.
[8] C. Besson, S. Schmitz, K. M. Capella, S. Kopilevich, I. A. Weinstock, P. Kögerler, *Dalton Trans.* **2012**, *41*, 9852-9854.
[9] Q. Zhang, L. P. He, H. Wang, C. Zhang, W. S. Liu, W. F. Bu, *Chem. Commun.* **2012**, *48*, 7067-7069.
[10] F. Caruso, D. G. Kurth, D. Volkmer, M. J. Koop, A. Muller, *Langmuir* **1998**, *14*, 3462-3465.
[11] A. Cazacu, S. Mihai, G. Nasr, E. Mahon, A. van der Lee, A. Meffre, M. Barbiou, *Inorg. Chim. Acta* **2010**, *363*, 4214-4219.
[12] D. G. Kurth, D. Volkmer, M. Ruttorf, B. Richter, A. Muller, *Chem. Mat.* **2000**, *12*, 2829-+.
[13] D. G. Kurth, P. Lehmann, D. Volkmer, A. Muller, D. Schwahn, *J. Chem. Soc.-Dalton Trans.* **2000**, 3989-3998.
[14] D. G. Kurth, P. Lehmann, D. Volkmer, H. Colfen, M. J. Koop, A. Muller, A. Du Chesne, *Chem.-Eur. J.* **2000**, *6*, 385-393.
[15] D. Volkmer, A. Du Chesne, D. G. Kurth, H. Schnablegger, P. Lehmann, M. J. Koop, A. Muller, *J. Am. Chem. Soc.* **2000**, *122*, 1995-1998.
[16] M. Clemente-Leon, T. Ito, H. Yashiro, T. Yamase, *Chem. Mat.* **2007**, *19*, 2589-2594.
[17] S. Floquet, E. Terazzi, V. S. Korenev, A. Hijazi, L. Guenee, E. Cadot, *Liq. Cryst.* **2014**, *41*, 1000-1007.
[18] S. Floquet, E. Terazzi, A. Hijazi, L. Guenee, C. Piguet, E. Cadot, *New J. Chem.* **2012**, *36*, 865-868.
[19] W. Bu, H. Li, H. Sun, S. Yin, L. Wu, *J. Am. Chem. Soc.* **2005**, *127*, 8016-8017.
[20] W. Li, W. Bu, H. Li, L. Wu, M. Li, *Chem. Commun.* **2005**, 3785-3787.
[21] H. L. Casal, D. G. Cameron, H. H. Mantsch, *The Journal of Physical Chemistry* **1985**, *89*, 5557-5565.
[22] R. A. MacPhail, H. L. Strauss, R. G. Snyder, C. A. Elliger, *The Journal of Physical Chemistry* **1984**, *88*, 334-341.
[23] N. Nakashima, N. Yamada, T. Kunitake, *The Journal of Physical Chemistry* **1986**, *90*, 3374-3377.
[24] T. Dutronc, E. Terazzi, L. Guenee, K. L. Buchwalder, A. Spoerri, D. Emery, J. Mareda, S. Floquet, C. Piguet, *Chem.-Eur. J.* **2013**, *19*, 8447-8456.
[25] E. Mani, J. Groenewold, W. K. Kegel, *Inorg. Chim. Acta* **2010**, *363*, 4295-4298.
[26] R. Deschenaux, B. Donnio, D. Guillon, *New J. Chem.* **2007**, *31*, 1064-1073.

[27] S.-i. Noro, R. Tsunashima, Y. Kamiya, K. Uemura, H. Kita, L. Cronin, T. Akutagawa, T. Nakamura, *Angewandte Chemie International Edition* **2009**, *48*, 8703-8706.
[28] T. L. Lai, M. Awada, S. Floquet, C. R. Marchal, N. Watfa, J. Marrot, M. Haouas, F. Taulelle, E. Cadot., *Chemistry - A European Journal* **2015**, submitted.
[29] V. C. Costa, M. J. Lochhead, K. L. Bray, *Chem. Mat.* **1996**, *8*, 783-790.
[30] G. Budroni, A. Corma, *Angewandte Chemie International Edition* **2006**, *45*, 3328-3331.
[31] S. Polarz, B. Smarsly, C. Goltner, M. Antonietti, *Adv. Mater.* , **2000**, *12*, 1503-1507.
[32] R. C. Schroden, C. F. Blanford, B. J. Melde, B. J. S. Johnson, A. Stein, *Chem. Mat.* **2001**, *13*, 1074-1081.
[33] W. Qi, H. L. Li, L. X. Wu, *J. Phys. Chem. B* **2008**, *112*, 8257-8263.

Chapter IV
Synthesis, Characterizaiton and Tuning of the Liquid Crystal Properties of Ionic Materials based on Cyclic Polyoxothiometetalate $[\{Mo_4O_4S_4(H_2O)_3(OH)_2\}_2(P_8W_{48}O_{184})]^{36-}$

Chapter IV- Synthesis, Characterization and Tuning of the Liquid Crystal Properties of Ionic Materials based on Cyclic Polyoxothiometalate $[\{Mo_4O_4S_4(H_2O)_3(OH)_2\}_2(P_8W_{48}O_{184})]^{36-}$

I. Introduction

The Chapter III showed the possibility to build Keperate-based liquid crystals by electrostatic combination of a Keplerate cluster with imidazolium cations, however, the folding of the alkyl chains probably prevents the formation of fluid and highly ordered mesophases. Such results prompted us to extend our investigation toward other highly charged polyoxometalate systems exhibiting anisotropic shape in an attempt to force the cations to interact together through van der waals interactions and consequently improve the organization. The cyclic superlacunary anionic POM, $[H_7P_8W_{48}O_{184}]^{33-}$ (P_8W_{48}) [1] represents an attractive system. It possesses a large anionic pocket of about 1 nm in diameter, which is able to include various transition metals, a key step for the elaboration of efficient materials for magnetic, luminescent, catalytic or electrocatalytic properties.[2-3] Consequently this system offers the possibility to design multifunctional materials by association with appropriate organic cations. Additionally, this macrocyclic system could offer promising properties towards the sequestration of various substrates or for catalysis as highlighted by Noro, Cronin and Nakamura with the encapsulation of the gigantic ring-shape cluster $[Mo_{154}(NO)_{14}O_{448}H_{14}(H_2O)_{70}]^{28-}$ with $DODA^+$ cations.[4-5]

The used precursor $Na_{25}Li[K_2\{Mo_4O_4S_4(H_2O)_3(OH)_2\}_2(P_8W_{48}O_{184})]^{36-}$, noted **NaK-1**, corresponds to a $\{P_8W_{48}\}$ macrocyclic ring capped on both sides by two cationic molybdenum clusters $[Mo_4O_4S_4(H_2O)_3(OH)_2]^{2+}$. On each side, the $[Mo_4O_4S_4(H_2O)_3(OH)_2]^{2+}$ hemicycles may occupy two equivalent positions, which gives a mixture of two positional isomers characterized by their relative orientation: parallel (noted *para*, not depicted) or perpendicular (noted *perp*, depicted in Figure 1).[6] In this study, the precursor **1** mainly contains the *perp* isomer and the proportion of the two isomers is not further considered.

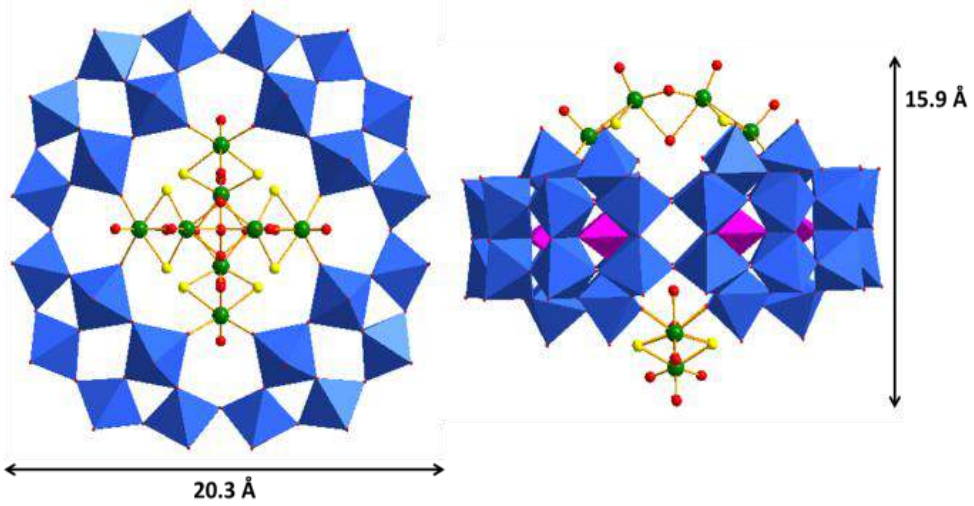

Figure 1: Top and side structural views of the perpendicular isomer of **1** in polyhedral and ball-and-stick representation. The $\{P_8W_{48}\}$ moiety is depicted in blue and pink polyhedra, molybdenum in green, sulfur in yellow and oxygen in red. Reproduced from reference [6].

In this chapter, we report the preparation, the characterizations in the solid state and the properties of POM-based ionic liquid crystal materials obtained by the electrostatic combination of a ring-shape polyoxothiometalate $[\{Mo_4O_4S_4(H_2O)_3(OH)_2\}_2(P_8W_{48}O_{184})]^{36-}$ (Figure 1) [6] with various organic cations depicted in Scheme 1. These latter correspond to simple tetralkylammoniums and imidazolium salts, which are commercially available or easily prepared, thus offering the possibility to prepare these materials on a large scale.

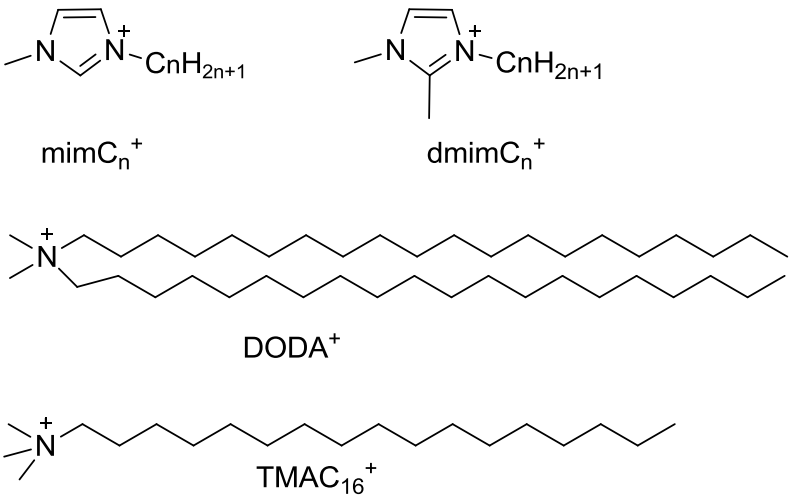

Scheme 1: Cations used in this study

II. Results and Discussion

II.1 Syntheses and Characterization of the POM-based materials

The POM-based materials are prepared by mixing a 1 M LiCl aqueous solution of **NaK-1** with a $CHCl_3$ solution containing a large excess of organic cations (144 equivelants/ POM

unit). Due to the red color of the precursor, the transfer of the anionic cluster **1** from the aqueous phase into the organic phase is easily monitored. It occurs rapidly and quantitatively, and the target materials are selectively precipitated with a good yield by addition of ethanol into the chloroform phase. Finally, the obtained materials are characterized by FT-IR, TGA, EDX and elemental analysis.

The FT-IR spectra were recorded at room temperature (Figure 2 and Figures A4.1-A4.8, Appendix) and some selected stretching vibrations are gathered in the Table 2. Firstly, as exemplified with the compound **$(mimC_{18})_{24}$-1**, the FT-IR spectrum displays the vibration modes of the organic cations associated with the initial cluster **1**, which confirms the integrity of the anionic cluster during the experimental procedure.

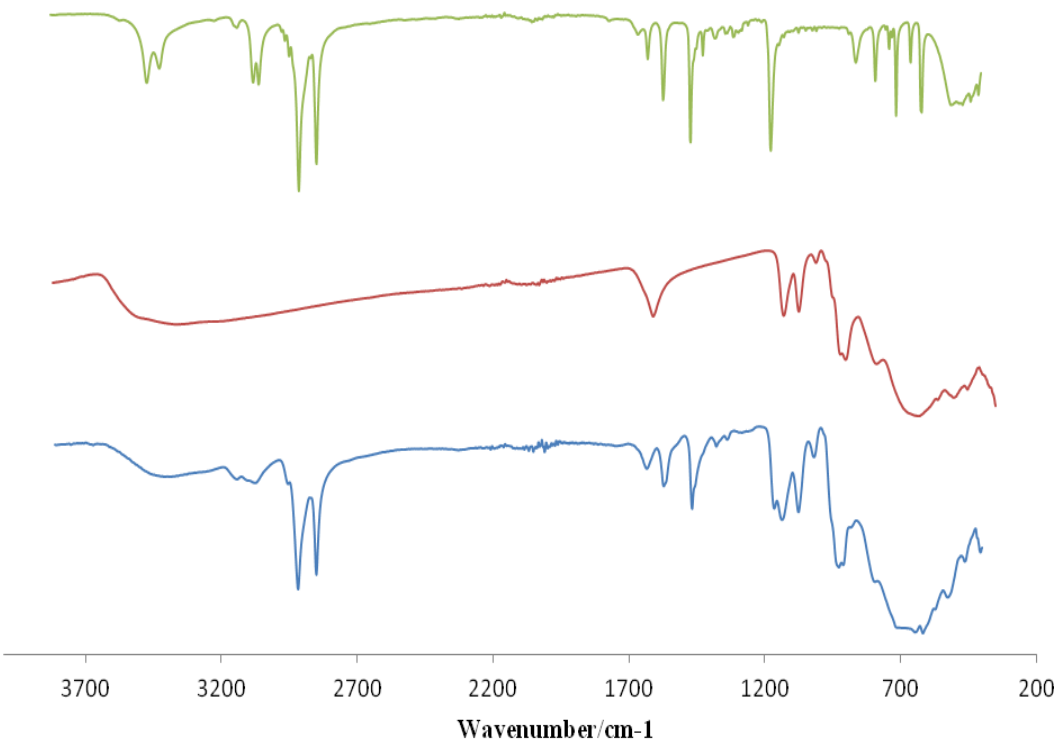

Figure 2: . FT-IR spectra of $mimC_{18}Br$ (green), **NaK-1** (red) and **$(mimC_{18})_{24}$-1** (blue)

II.1.1 Chemical composition

EDX, elemental analysis and TGA unambiguously enable establishing the formula of the POM-based materials. Interestingly, even if a large excess of organic cations is used, the replacement of the alkali cations is not complete. Indeed, the number of organic cations interacting with the anionic cluster **1** are found in the 18-26 range, and the residual anionic charges are balanced by protons and residual alkali cations. All the obtained results are summarized in Table 1.

The trapping of potassium cations inside the cavity of P_8W_{48} derivatives is commonly observed in the literature. [1, 7-10] The precursor compound $Na_{25}Li[K_2\{Mo_4O_4S_4(OH)_2(H_2O)_3\}_2(H_8P_8W_{48}O_{184})]\cdot 125H_2O$ contains two potassium cations which are strongly coordinated inside the P_8W_{48} ring. The presence of two potassium cations is found for all materials in this study, which demonstrates their efficient embedding within the cluster **1**. EDX and elemental analysis reveal the presence of 1 to 3 sodium cations and 3 to 6 lithium cations, which also suggest a good affinity of these alkali cations for the cavity of the P_8W_{48} cluster. Finally, 3 to 8 protons are bound to the P_8W_{48} moiety because the pH of the aqueous phase is maintained between 3 and 4.5. To summarize, the cavity of the cluster is filled with alkali cations whereas protons are likely localized at the surface P_8W_{48} cluster. The general formula of the POM based materials can be written as $[K_2Na_xLi_y\{Mo_4O_4S_4(OH)_2(H_2O)_3\}_2(H_zP_8W_{48}O_{184})]^{(34-x-y-z)-}$ (with $1 \leq x \leq 3$, $3 \leq y \leq 6$ and $3 \leq z \leq 8$) together with 18 to 26 organic cations.

Interestingly, when $dmimC_n^+$ (n = 12 and 16) cations are used, the number of cations is significantly lower than that observed in analogous materials incorporating the $mimC_{12}^+$ and $mimC_{16}^+$ cations. This result suggests that (i) the number of organic cations can be modulated by changing the size and the steric hindrance of the imidazolium part of the organic cations and (ii) the organic cations are probably not randomly distributed around the inorganic cluster. It can also suggest that the imidazolium cationic heads are probably closely located which is considered as a key parameter for forcing van der waals interaction between them.

Table 1: Molecular formula of the samples from elemental analysis and TGA curves (refer to experimental section for details)

Sample	Estimated molecular formula
$DODA_{19}$-1	$(DODA)_{19}[K_2Na_2Li_5\{Mo_4O_4S_4(OH)_2(H_2O)_3\}_2(H_8P_8W_{48}O_{184})]$. 10 H_2O
$(TMAC_{16})_{18}$-1	$(NMe_3C_{16}H_{33})_{18}[K_2Na_2Li_6\{Mo_4O_4S_4(OH)_2(H_2O)_3\}_2(H_8P_8W_{48}O_{184})]$. $30H_2O$
$(mimC_{12})_{25}$-1	$(mimC_{12}H_{25})_{25}[K_2NaLi_4\{Mo_4O_4S_4(OH)_2(H_2O)_3\}_2(H_4P_8W_{48}O_{184})]$. $20H_2O$
$(mimC_{14})_{26}$-1	$(mimC_{14}H_{29})_{26}[K_2Na_2Li_3\{Mo_4O_4S_4(OH)_2(H_2O)_3\}_2(H_3P_8W_{48}O_{184})]$. $35H_2O$
$(mimC_{16})_{23}$-1	$(mimC_{16}H_{33})_{23}[K_2Na_3Li_3\{Mo_4O_4S_4(OH)_2(H_2O)_3\}_2(H_5P_8W_{48}O_{184})]$. $40H_2O$
$(mimC_{18})_{24}$-1	$(mimC_{18}H_{37})_{24}[K_2NaLi_3\{Mo_4O_4S_4(OH)_2(H_2O)_3\}_2(H_6P_8W_{48}O_{184})]$. $25H_2O$
$(mimC_{20})_{24}$-1	$(mimC_{20}H_{41})_{24}[K_2NaLi_3\{Mo_4O_4S_4(OH)_2(H_2O)_3\}_2(H_6P_8W_{48}O_{184})]$. $15H_2O$
$(dmimC_{12})_{18}$-1	$(dmimC_{12}H_{25})_{18}[K_2Na_3Li_5\{Mo_4O_4S_4(OH)_2(H_2O)_3\}_2(H_8P_8W_{48}O_{184})]$. $15H_2O$
$(dmimC_{16})_{20}$-1	$(dmimC_{16}H_{33})_{20}[K_2Na_2Li_4\{Mo_4O_4S_4(OH)_2(H_2O)_3\}_2(H_8P_8W_{48}O_{184})]$. $20H_2O$

II.1.2 Thermal stability

Finally, the amount of water content and the thermal stability of the POM-based materials are assessed by TGA and by variable–temperature FT-IR experiments (see Figures A4.9-A4.19, Appendix). For all materials, a weight loss of 16-46 water molecules per POM-organic assembly occurs in the 25-180°C range in agreement with the molecular formula. The decomposition temperatures under an oxygen atmosphere vary as a function of the organic cation from 205 to 235°C. Higher decomposition temperatures are found under air or under nitrogen. The FT-IR spectra recorded in air in the 20-300°C temperature range for **$DODA_{19}$-1**, **$(mimC_{16})_{23}$-1** and **$(mimC_{18})_{24}$-1** (see Figure 3 and Figures A4.9-A4.10, Appendix) confirm the removal of water molecules in the 20-180°C range, and suggest that the degradation of the materials occurs at temperature above 250°C and demonstrate their stability in air (Figure 3) contrary to the Keplerate-based materials which are modified above 126°C in air as already shown in chapter III.

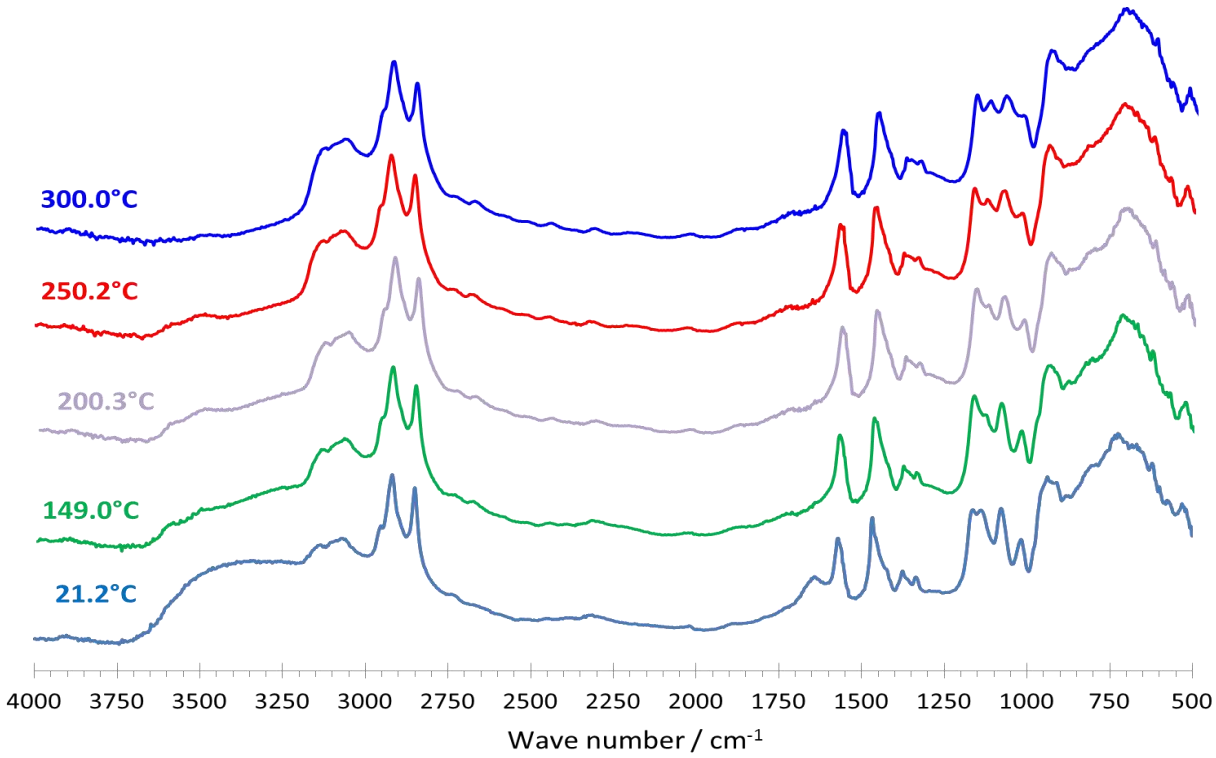

Figure 3: Selected FT-IR spectra recorded at various temperatures for compound **$(mimC_{18})_{24}$-1** in air.

II.2 FT-IR spectroscopies studies

As seen in the previous chapter, the antisymmetric ($\nu_{as}(CH_2)$) and symmetric ($\nu_s(CH_2)$) stretching vibrations of the methylene groups represents a powerful tool for investigating the

organization and dynamics of alkyl chains.[11-12] On the basis of the data reported in Table 2, the alkyl chains of the organic cations found in the compounds **$DODA_{19}$-1, $(mimC_{14})_{26}$-1, $(mimC_{16})_{23}$-1, $(mimC_{18})_{24}$-1, $(mimC_{20})_{24}$-1** appear highly ordered, which was not the case of Keplerate-based materials. However, the compounds **$(TMAC_{16})_{18}$-1, $(dmimC_{12})_{18}$-1, $(dmimC_{16})_{20}$-1** seem to be poorly ordered. These data must be correlated to the possible induction of liquid crystal properties for the former compounds whereas the latter does not exhibit any liquid crystal properties (*vide infra*). In the case of **$(mimC_{12})_{25}$-1**, the IR vibration frequencies are intermediate, which suggest this compound to be probably at the boundary between a liquid crystal and a solid. In addition, the intensity ratio $I(\nu_s(CH_2))/I(\nu_{as}(CH_2))$ can also be used as an indicator of the alkyl chain arrangement.[12-13] The intensity of this ratio increases when the conformational order of the alkyl chain increases. Indeed, as shown in Table 2, mainly two different ranges of values are found for our materials: a "low" ratio in the 0.69-0.74 range for the compounds **$(TMAC_{16})_{18}$-1, $(dmimC_{12})_{18}$-1** and **$(dmimC_{16})_{20}$-1** and a "high" ratio in the 0.81-0.85 range for the compounds **$DODA_{19}$-1, $(mimC_{14})_{26}$-1, $(mimC_{16})_{23}$-1, $(mimC_{18})_{24}$-1, $(mimC_{20})_{24}$-1**, whereas the **$(mimC_{12})_{25}$-1** exhibits an intermediate value.

The analysis of the position and the intensities of $\nu_{as}(CH_2)$ and $\nu_s(CH_2)$ thus appears as a tool for estimating the potentialities of these materials as liquid crystals. Considering the materials prepared with $mimC_n^+$ cations (n = 12-20), a longer alkyl chain leads to van der Waals interactions between the chains and thus better organizations.

Finally, in the low frequency region, the absorption bands are mostly composed of the scissoring, wagging, twisting and rocking modes of the CH_2 groups together with the vibration modes of the POM. The vibration bands in the 1483-1466 cm^{-1} are assigned to the -CH_2- scissoring bending modes, which can be used to diagnose alkyl chains packing. Indeed, a single narrow peak at 1473 cm^{-1} is attributed to triclinic subcell packing of alkyl chains, while a single narrow band at 1467 cm^{-1} is typical of a hexagonal subcell.[11-12] The FT-IR spectra of our POM-based materials reveal a narrow peak at 1466-1467 cm^{-1}, which is consistent with the tendency of the alkyl chains to give a hexagonal packing arrangement.

Table 2: Selected IR vibration bands.

Compounds	ν_{as} (CH_3)	ν_{as} (CH_2)	ν_s (CH_3)	ν_s (CH_2)	$I(\nu_s CH_2)/I(\nu_{as} CH_2)$
$DODA_{19}$-1	2954	2921	2870	2851	0.81
$(TMAC_{16})_{18}$-1	2955	2924	2871	2853	0.70
$(mimC_{12})_{25}$-1	2954	2923	2870	2852	0.76
$(mimC_{14})_{26}$-1	2955	2920	2871	2851	0.84
$(mimC_{16})_{23}$-1	2954	2919	2871	2850	0.84
$(mimC_{18})_{24}$-1	2953	2920	2871	2851	0.83
$(mimC_{20})_{24}$-1	2953	2920	2870	2851	0.85
$(dmimC_{12})_{18}$-1	2953	2925	2871	2853	0.69
$(dmimC_{16})_{20}$-1	2954	2924	2871	2853	0.74

II.3 NMR Studies

^1H and ^{31}P NMR studies in solution were performed for the selected compounds **$DODA_{19}$-1**, **$(TMAC_{16})_{18}$-1**, and **$(mimC_{18})_{24}$-1** in $CDCl_3$. The recorded ^{31}P NMR spectra did not exhibit any significant signal which results from an extreme line broadening of the signals while the ^1H NMR spectrum exhibit very broad lines. This behavior could be due to the reduced molecular tumbling in the POM-cation assemblies (see Figure 4). In these conditons NMR studies are poorly informative.

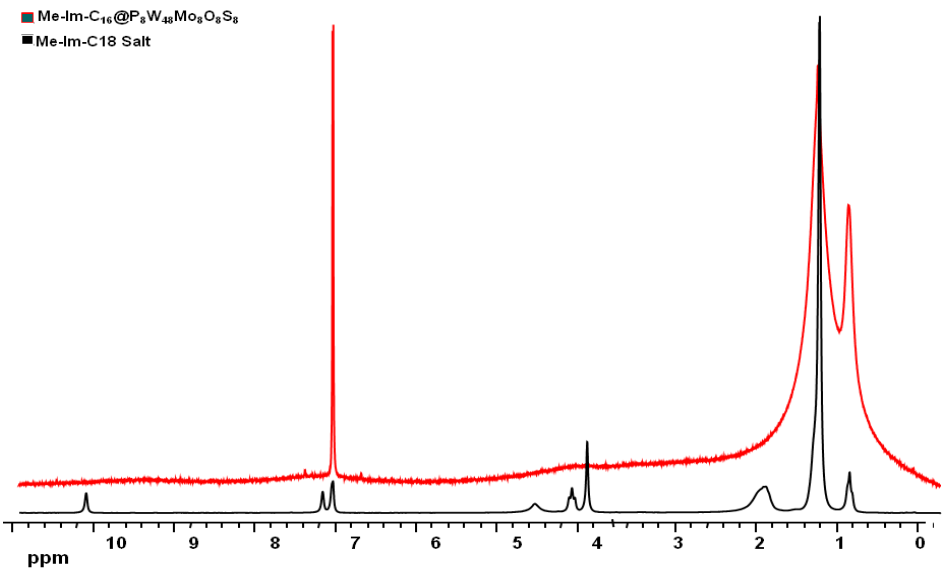

Figure 4: ^1H NMR spectra of $mimC_{18}Br$ (black) and **$(mimC_{18})_{24}$-1** (red) in $CDCl_3$.

Solid state NMR

Solid state NMR remains underused in the domain of polyoxometalate chemistry although it represents a powerful characterization technique in materials science. This technique was previously used to investigate local structures, interactions between species and some dynamic aspects occurring within the hybrid POM-organic cation assemblies.[14] ^{1}H and ^{13}C NMR are pertinent for probing the organic moiety while ^{31}P NMR is used to investigate the POM part.

Three compounds were considered as representative samples: **$(TMAC_{16})_{18}$-1, $DODA_{19}$-1**, and **$(mimC_{18})_{24}$-1**. The ^{1}H NMR spectra of the precursor **NaK-1**, **$(TMAC_{16})_{18}$-1, $DODA_{19}$-1**, **$(mimC_{18})_{24}$-1**, and of the corresponding salts $TMAC_{16}Cl$, DODACl, and $(mimC_{18})Br$ are shown in Figure 5 to Figure 8 . The ^{1}H NMR spectrum of **NaK-1** (Figure 5a) exhibits a main resonance at 4.4 ppm with a shoulder at 3.3 ppm (≈2%) due to water molecules present outside and inside the POM cavity, respectively. In contrast, these NMR signals appear minor in the ^{1}H NMR spectra of **$(TMAC_{16})_{18}$-1, $DODA_{19}$-1** and **$(mimC_{18})_{24}$-1** (Figure 5c, Figure 6b and Figure 8b respectively) in agreement with the presence of organic cations with dominant signals. The ^{1}H NMR spectrum of **$TMAC_{16}Cl$** (Figure 5b) consists of two broad resonances at 0.8 and 3.2 ppm corresponding to the protons of the aliphatic chain together with the methyl and methylene groups located close to the ammonium head.

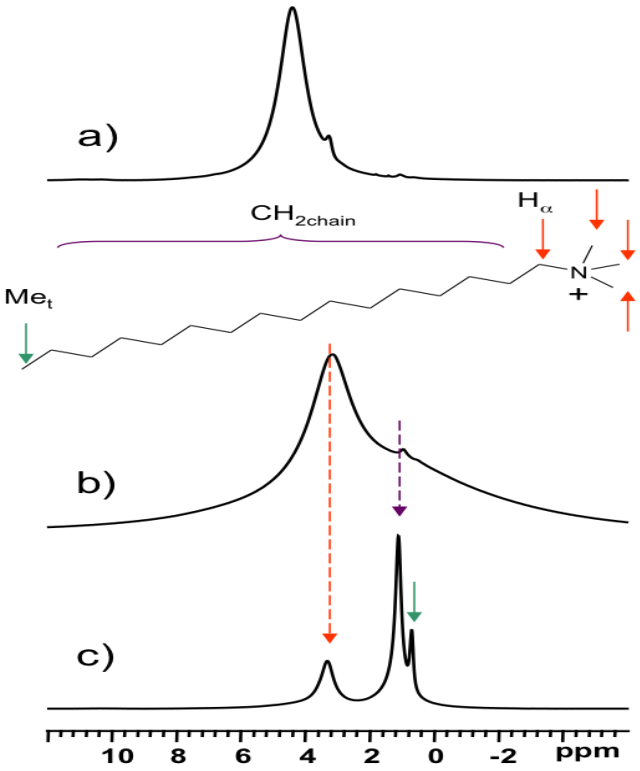

Figure 5: 500.13 MHz ^{1}H NMR spectra at 20 kHz MAS of **NaK-1** (a) trimethylhexadecylammonium chloride **($TMAC_{16}Cl$)** (b) and **$(TMAC_{16})_{18}$-1** (c). Arrows indicate the assignments of the NMR lines.

The ^{1}H NMR spectrum of the bromide salt **mimC_{18}Br** (Figure 6a) suffers from severe line broadening due to strong H-H dipolar interactions. In contrast, the ^{1}H MAS NMR spectra of their corresponding POM-based materials, **(TMAC_{16})$_{18}$-1** (Figure 5c and Figure A4.21 in the Appendix) and **(mimC_{18})$_{24}$-1** (Figure 6b) exhibit much narrower signals. For **(TMAC_{16})$_{18}$-1** the NMR spectrum displays three resonances at 0.7, 1.1, and 3.3 ppm due to end-chain methyl group, chain methylene protons, and methylene and methyl groups of the tetraalkylammonium head. For **(mimC_{18})$_{24}$-1,** five resonances assigned to end-chain methyl, chain methylene, *N*-CH_3/*N*-CH_2 and aromatic resonances can be distinguished at 0.7, 1.1, 4.3, and 7.6 and 9.2 ppm, respectively. This assignment is supported by ^{13}C{^{1}H} ^{2}D correlation experiments (Figure 7 and A4.24). The narrowing of the signals for **(TMAC_{16})$_{18}$-1,** and **(mimC_{18})$_{24}$-1** indicates a much lower H-H dipolar interaction (in comparison with the starting salts). This could be the consequence of a lower density of chain-chain stacking organization in the POM-based materials, which favors chains mobility and increases intermolecular H-H distances.

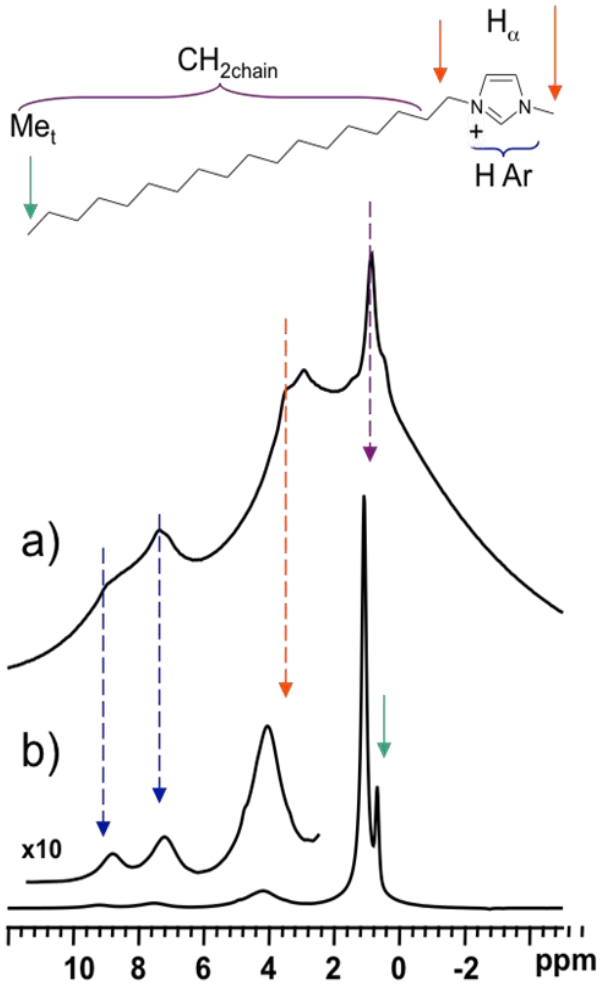

Figure 6: 500.13 MHz ^{1}H NMR spectra at 20 kHz MAS of mimC_{18}Br (a) and **(mimC_{18})$_{24}$-1** (b). Arrows indicate the assignments of the NMR lines.

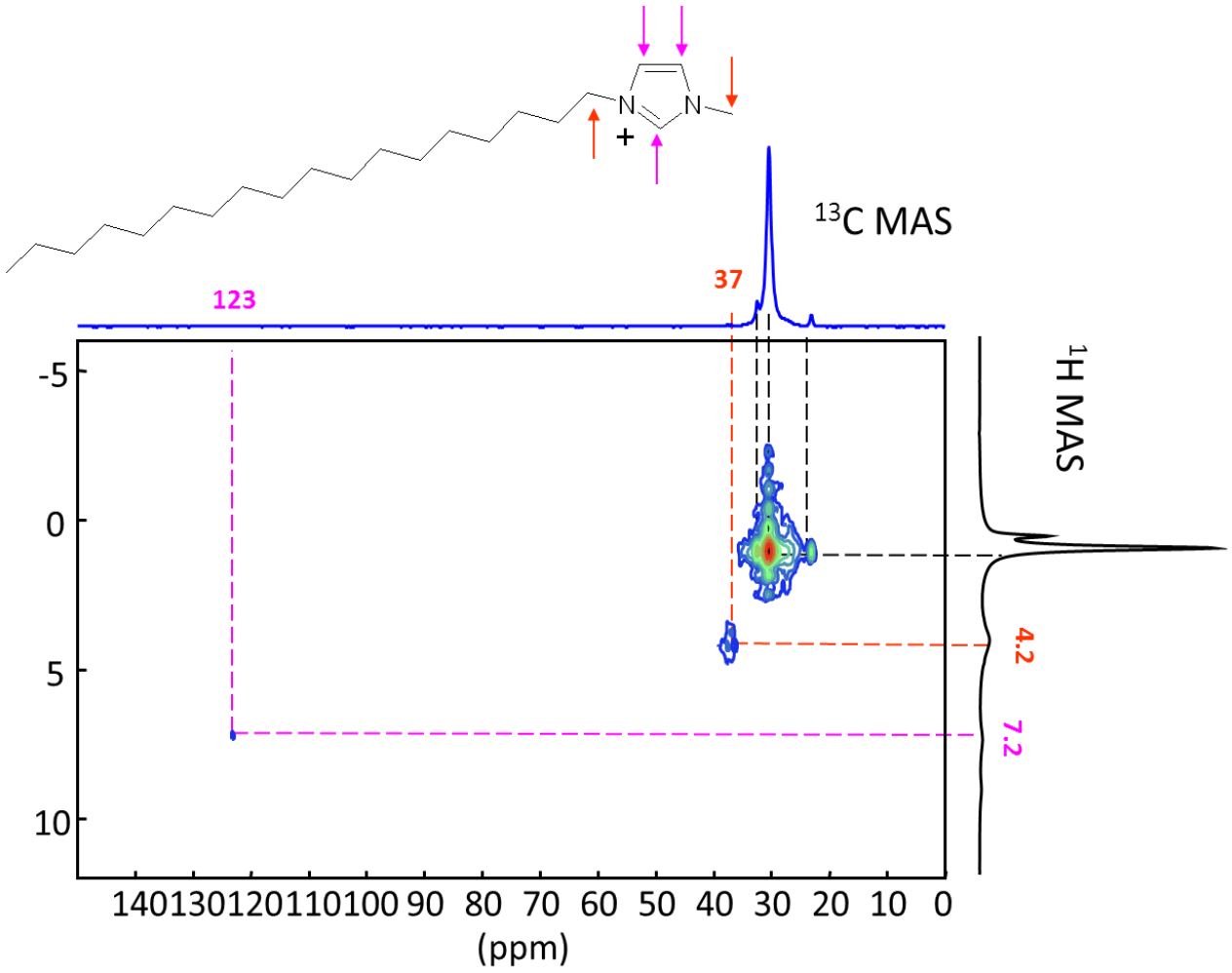

Figure 7: $^{13}C\{^{1}H\}$ HETCOR MAS NMR spectrum of **$(mimC_{18})_{24}$-1**.

The reverse situation is observed for **$DODA_{19}$-1**, where the ^{1}H NMR trace shows higher resolution in the chloride salt (Figure 8). We conclude that the H-H dipolar interaction should be weaker in **DODACl** than in **$DODA_{19}$-1**. The dynamic motions of organic chains in **$DODA_{19}$-1** should be restricted to some extent, and not fast enough to completely average out these interactions. One can therefore deduce that the organic cations are well organized around the POM with a stacking of the aliphatic chains and/or accompanied by strong interdigitation with some neighboring $DODA^{+}$ cations.

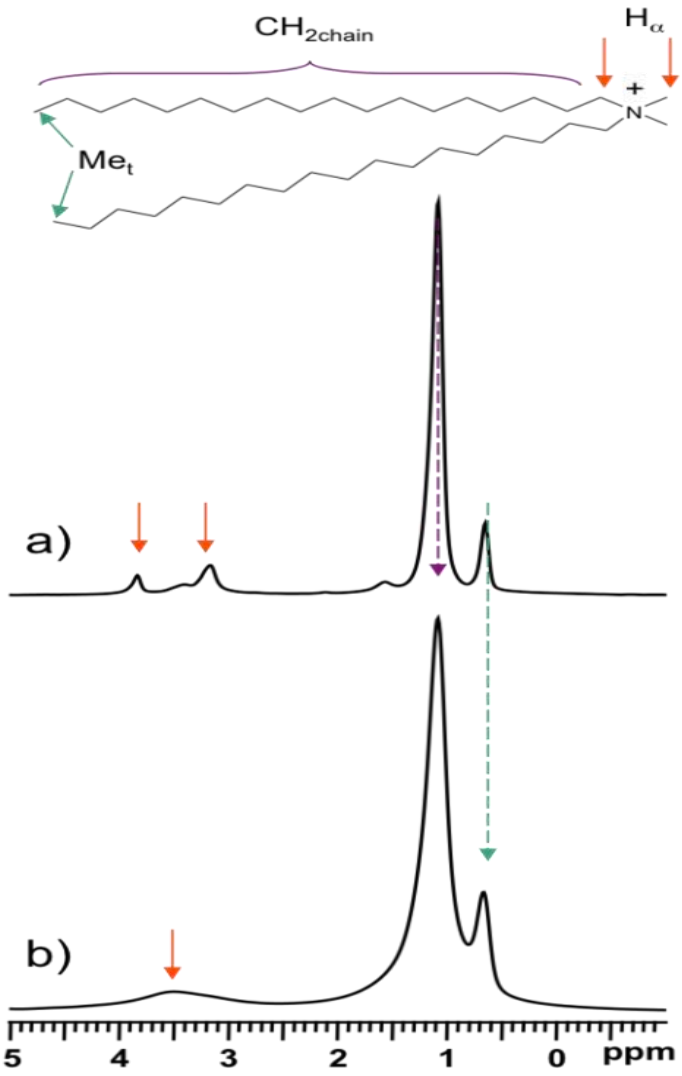

Figure 8: 500.13 MHz ^{1}H NMR spectra at 20 kHz MAS of DODACl (a) and **DODA$_{19}$-1** (b). Arrows indicate the assignments of the NMR lines.

The ^{13}C{^{1}H} CPMAS spectra of **(TMAC$_{16}$)$_{18}$-1** and **DODA$_{19}$-1** (A4.23 and A4.24, in Appendix) reveal a narrowing of the NMR lines compared with their halide salts, while the ^{13}C{^{1}H} CPMAS spectrum of **(mimC$_{18}$)$_{24}$-1** (Figure 9) showed an opposite trend because the resonances are much broader compared with the starting bromide salt. This is consistent with some local disorder in **(mimC$_{18}$)$_{24}$-1**, which produces variable chemical environment around the organic cations. Such a disorder could be explained by the low density of chain-chain staking in the solid state favoring some dynamic motion of these organic chains.

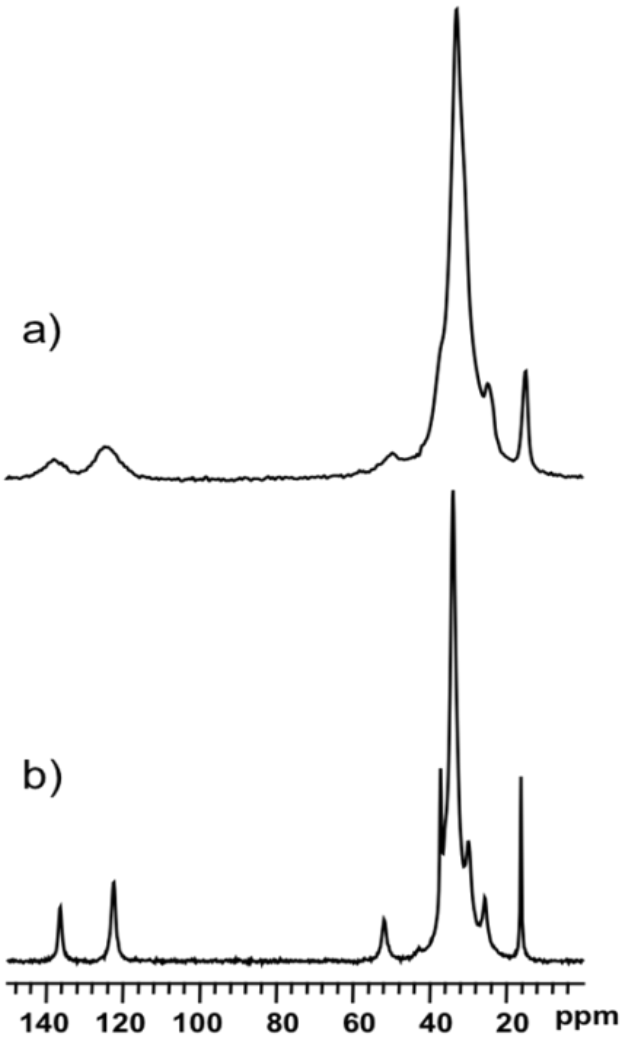

Figure 9: 125.76 MHz $^{13}C\{^{1}H\}$ CP NMR spectra at 10 kHz MAS of **$(mimC_{18})_{24}$-1** (a) and **$mimC_{18}Br$** (b).

Figure 10 and Figure 11 show the $^{31}P\{^{1}H\}$ MAS spectra of **NaK-1**, **$(TMAC_{16})_{18}$-1**, **$(mimC_{18})_{24}$-1** and **$DODA_{19}$-1** at 81.01 and 202.45 MHz respectively. The precursor **NaK-1** is characterized by a unique resonance at -8.3 ppm consistent with the NMR spectrum recorded in solution (Figure A4.26c, Appendix) and characteristic for the presence of the perpendicular isomer as the major species (Figure 10 and Figure 11). [6] The spectra of **$(TMAC_{16})_{18}$-1**, **$(mimC_{18})_{24}$-1** and **$DODA_{19}$-1** are comparable to that of the precursor at 81.01 MHz. At higher frequency the spectrum of **$(TMAC_{16})_{18}$-1** shows an asymmetric resonance with a maxima at -7.0 ppm, and a shoulder at -5.5 ppm, while spectra of **$(mimC_{18})_{24}$-1** and **$DODA_{19}$-1** exhibit two main ensembles of composite signals located at ca. -6 to -7 and ca. -9 ppm. In previous studies, we evidenced that the chemical shift of ^{31}P nuclei of this cluster strongly depended on the nature of the cations trapped within the cavity (see Figure A4.26, Appendix).[6] Based on this, the existence of slightly different environments for the ^{31}P nuclei could be explained by a random distribution of K^+, Na^+ and Li^+ cations within the cavity of the polyoxometalate. This

distribution of different sites within the cavity would be at the origin of the multicomponent resonances visible in the ^{31}P NMR spectra at 202.45 MHz. In summary, these spectra are consistent with the integrity of the polyoxometalate moiety in the materials.

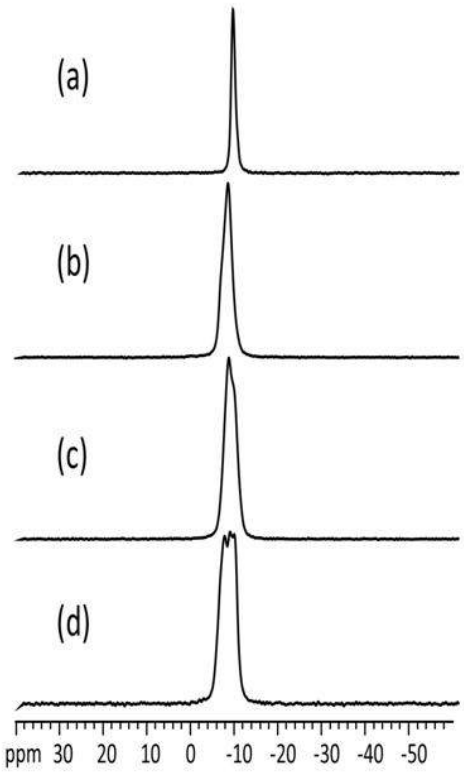

Figure 10: 81.01 MHz $^{31}P\{^{1}H\}$ CP NMR spectra at 20 kHz MAS of **NaK-1 (a),** $(TMAC_{16})_{18}$-1**(b),** $(mimC_{18})_{24}$-1 (c), and $DODA_{19}$-1 (d)

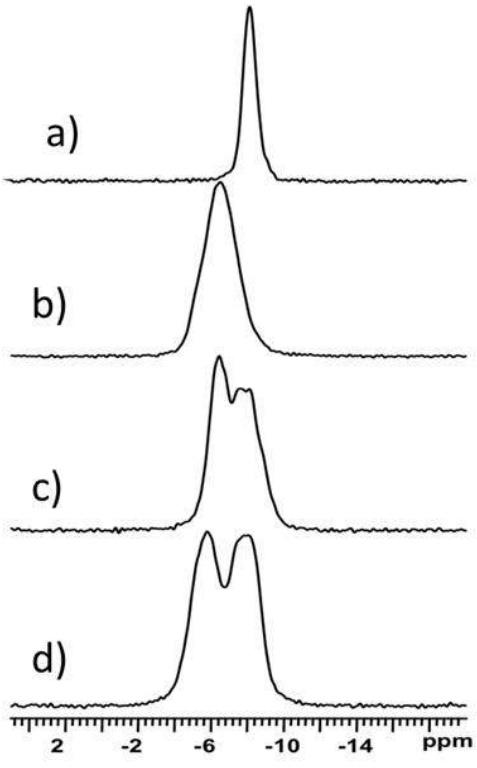

Figure 11: 202.45 MHz $^{31}P\{^{1}H\}$ CP NMR spectra at 20 kHz MAS of **NaK-1** (a), **$(TMAC_{16})_{18}$-1**(b), **$(mimC_{18})_{24}$-1 (c), and $DODA_{19}$-1 (d)**

Finally, the $^{31}P\{^{1}H\}$ ^{2}D HETCOR experiments performed on **$(TMAC_{16})_{18}$-1** , **$(mimC_{18})_{24}$-1** and **$DODA_{19}$-1** (Figure 12) unambiguously evidence specific interactions between the inorganic cluster and the organic cation since a correlation between the ^{31}P nuclei of the cluster and some protons of the organic cations is observed. The major contribution to the ^{1}H to ^{31}P CP transfer arises from the methyl protons of tetraalkylammonium head for **$(TMAC_{16})_{18}$-1**, from the methyl and methylene groups attached to nitrogen atoms of the imidazolium ring for **$(mimC_{18})_{24}$-1**, and from the methyl and methylene groups bound to the ammonium head of $DODA^{+}$ cations for **$DODA_{19}$-1**. These results demonstrate that the polar group of the organic cation interacts with the POM. Wu *et al*. evidenced such an interaction using ^{1}H NMR in solution [12, 15-16] and our results indicate that this information can be obtained in the solid state by MAS NMR.

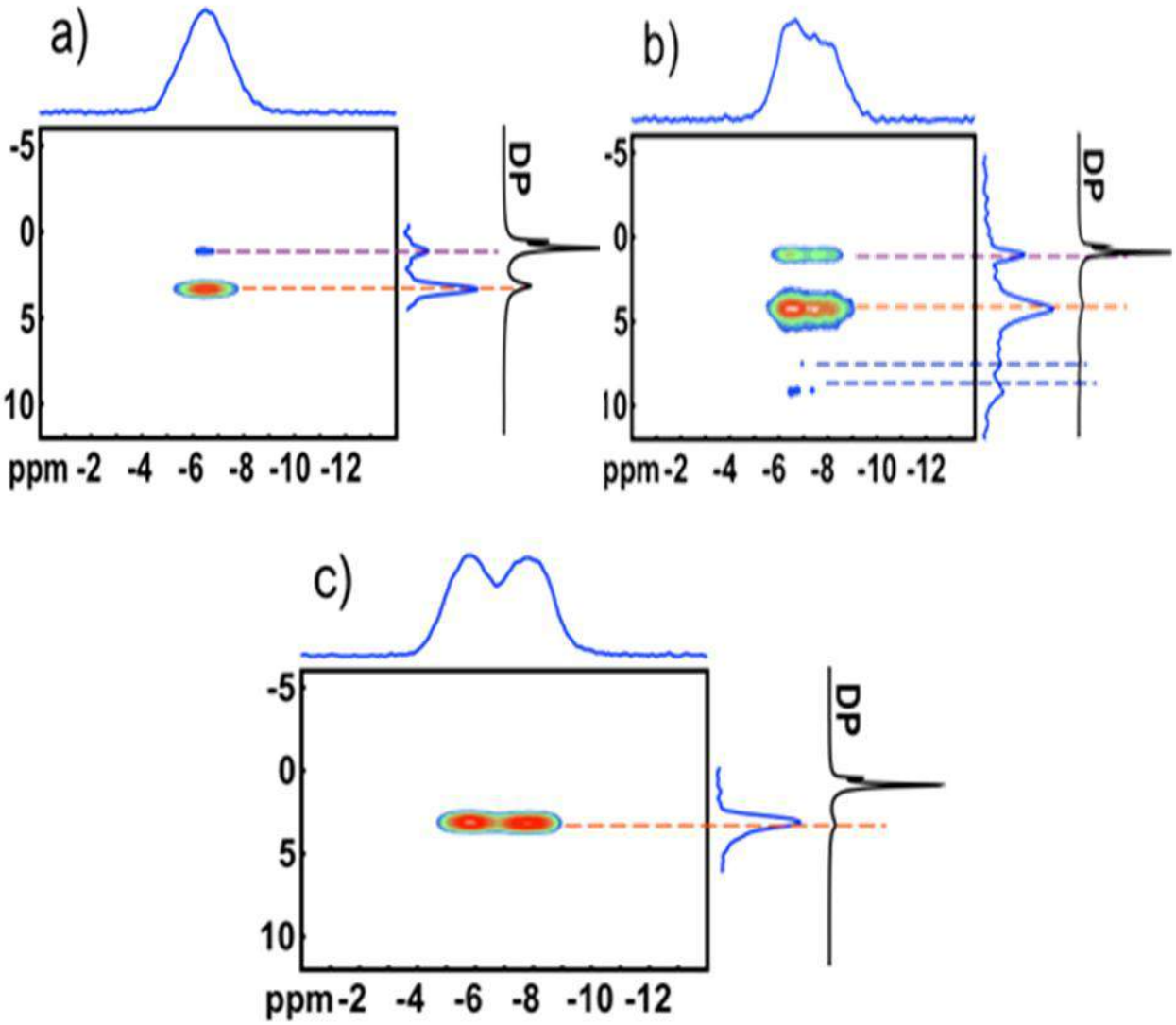

Figure 12: $^{31}P\{^{1}H\}$ Hetcor CPMAS NMR spectra of compounds **$(TMAC_{16})_{18}$-1** (a), **$(mimC_{18})_{24}$-1** (b), and **$DODA_{19}$-1** (c). Projections along ^{1}H and ^{31}P dimensions are shown as well as ^{1}H direct polarization (DP) spectra for comparison purpose.

II.4 Liquid Crystal Properties

The liquid crystal properties of our compounds were studied by Polarized Optical Microscopy, DSC and SA-XRD during their second heating and cooling process after a first thermal cycle which ensures (i) the removal of water molecules and (ii) the organization of the materials in collaboration with Dr Emmanuel Terazzi, in the university of Geneva, Switzerland.

II.4.1.a Polarized Opical Microscopy

Mesomorphism in the **$DODA_{19}$-1, $(mimC_{12})_{25}$-1 $(mimC_{14})_{26}$-1, $(mimC_{16})_{23}$-1, $(mimC_{18})_{24}$-1,** and **$(mimC_{20})_{24}$-1** materials has been detected by temperature dependent polarized optical

microscopy (TD-POM), which revealed the formation of birefringent and homogeneous textures suggesting the liquid-crystalline nature of the samples (Figure 13). Note that, excepted for **$DODA_{19}$-1,** the fluidity of the compounds **$(mimC_n)_x$-1** is very low and necessitates the use of high temperature to get polarized optical micrograph of good quality. Additionally, in the series of compounds **$(mimC_n)_x$-1**, we note that the fluidity of the sample is related to the length of the alkyl chain. However, the three compounds **$(TMAC_{16})_{18}$-1, $(dmimC_{12})_{18}$-1, $(dmimC_{16})_{20}$-1** did not reveal any liquid crystalline behaviour, thus evidencing the influence of the cationic head on the organization of the materials especially on the arrangments of the organic cations around the POM. Unfortunately, the lack of typical texture due to the decomposition of the cluster before reaching the isotropic state precludes an unambiguous phase assignment by TD-POM.

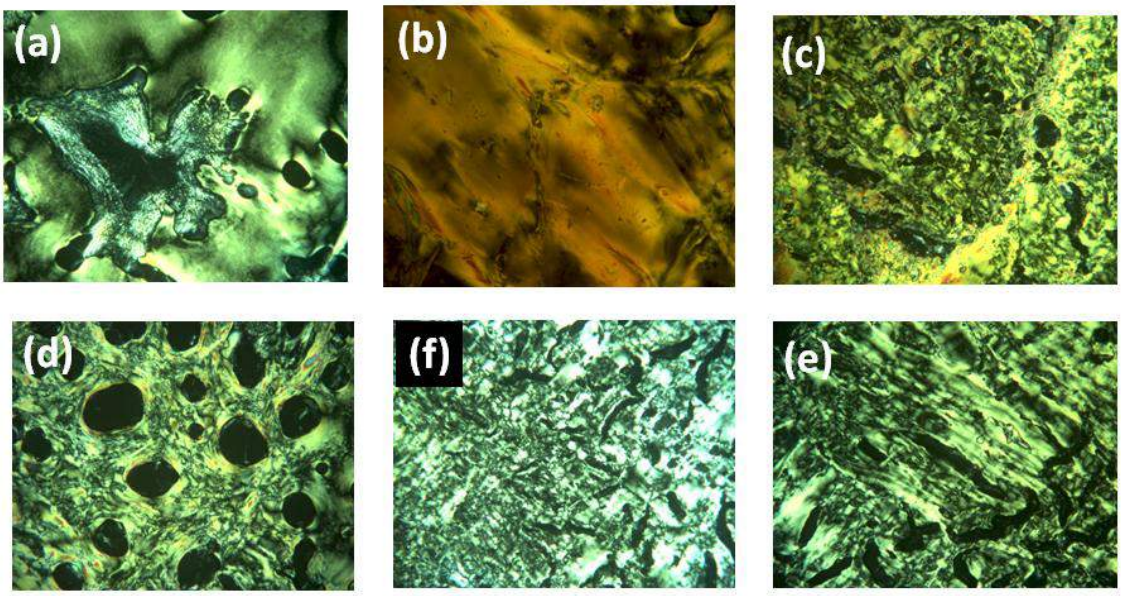

Figure 13: Polarized Optical Microphotograph of **$DODA_{19}$-1** at 203°C (a), **$(mimC_{12})_{25}$-1** at 240°C (b), **$(mimC_{14})_{26}$-1** at 240°C (c), **$(mimC_{16})_{23}$-1** at 240°C (d), **$(mimC_{18})_{24}$-1** at 240°C (e) and **$(mimC_{20})_{24}$-1** at 240°C (f).

II.4.1.b Differential scanning calorimetry (DSC)

The DSC curves of Keplerate based materials were recorded under nitrogen at a scan rate of 5°C/minute between -40°C and 220-250°C. In this case and contrary to Keplerate-based materials, the DSC curves exhibit clear sharp first order phase transitions attributed to the transition from solid state to mesophases (Figure 14) in the -3.5°C to +46.2°C temperature range (Table 3) and before the decomposition temperature. It is noteworthy that no first-order phase transition could be observed for $(mimC_{12})_{25}$-1. The corresponding melting enthalpy and melting entropy changes, $\Delta H'_m$ and $\Delta S'_m$ respectively (ratios $\Delta H_m/n(CH_2)$ and $\Delta S_m/n(CH_2)$

respectively) are given in Table 3 . Similarly to the Keplerate series, the plot of $-\Delta H'_m$ versus $-\Delta S'_m$ (Figure 10) displays a linear relationship typical for *H/S* compensation [17] and evidences two sets of points for the materials of this study: $DODA_{19}$-1, $(mimC_{18})_{24}$-1, and $(mimC_{20})_{24}$-1 on one hand and $(mimC_{14})_{26}$-1 and $(mimC_{16})_{23}$-1 on the other hand, whereas DODACl is clearly different as previously mentioned in chapter III. For the three compounds $DODA_{19}$-1, $(mimC_{18})_{24}$-1, and $(mimC_{20})_{24}$-1, the ratios ΔH_m /nCH_2 and ΔS_m / nCH_2 are very similar. Taking DODACl as a reference for a "free" alkyl chain, Figure 15 suggests that the alkyl chains are strongly perturbed by the presence of the bulky P_8W_{48} moieties which results in a drastic lowering of the fluidity of the samples (the fluidity is qualitatively determined by TD-POM). This phenomenon is more pronounced for the two last compounds, $(mimC_{16})_{23}$-1, and $(mimC_{14})_{26}$-1, which could be better described as soft crystals than as liquid crystals.

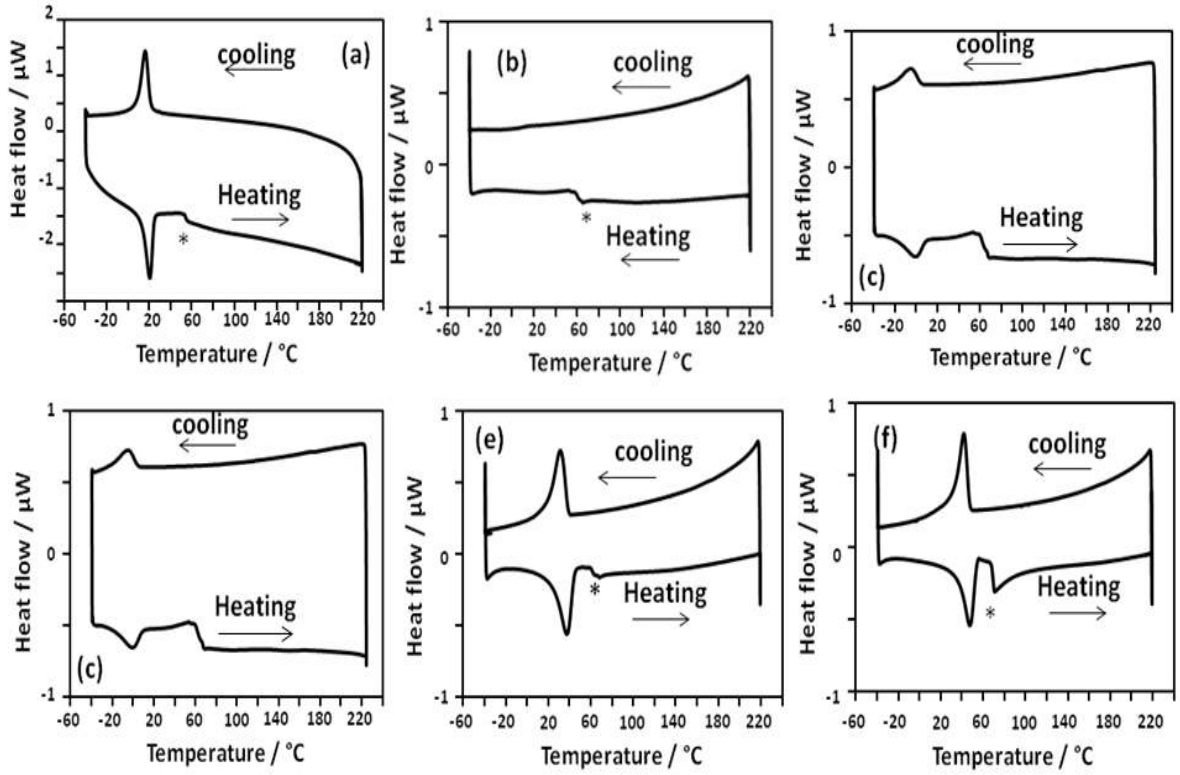

Figure 14: DSC Traces of the second thermal cycle recorded under N_2 (5°C/min) for **$DODA_{19}$-1** (a), **$(mimC_{12})_{25}$-1** (b), **$(mimC_{14})_{26}$-1** (c), **$(mimC_{16})_{23}$-1** (d), **$(mimC_{18})_{24}$-1** (e) and **$(mimC_{20})_{24}$-1** (f). * indicates an unidentified process which has been observed for all samples between 55 and 70°C during the heating mode. This process does not correspond to a modification of the supramolecular organization and might be attributed to an internal structural change within the cluster cores.

Table 3: Temperatures, melting enthalpy and entropy changes of the phase transitions between the glassy state and the lamellar smectic A phase observed for the materials exhibiting liquid crystalline properties. Temperatures are given for the peaks observed by DSC measurements during the second heating process

Cluster	T /°C (Heating mode)	$-\Delta H_m$ /kJ·mol^{-1}	$-\Delta S_m$ /J·mol^{-1}·K^{-1}	$-\Delta H'_m$ [a] /kJ·mol^{-1}	$-\Delta S'_m$ [a] /J·mol^{-1}K^{-1}
$DODA_{19}$-1	+19.7	499.0	1704.1	772.5	2.64
$(mimC_{14})_{26}$-1	-3.0	106.7	395.1	315.8	1.17
$(mimC_{16})_{23}$-1	-3.5	127.0	471.0	368.2	1.37
$(mimC_{18})_{24}$-1	+37.7	330.8	1067.6	813.4	2.62
$(mimC_{20})_{24}$-1	+46.2	375.9	1177.1	823.4	2.58
DODACl	+18.0	83.1	278.5	2445.4	8.19

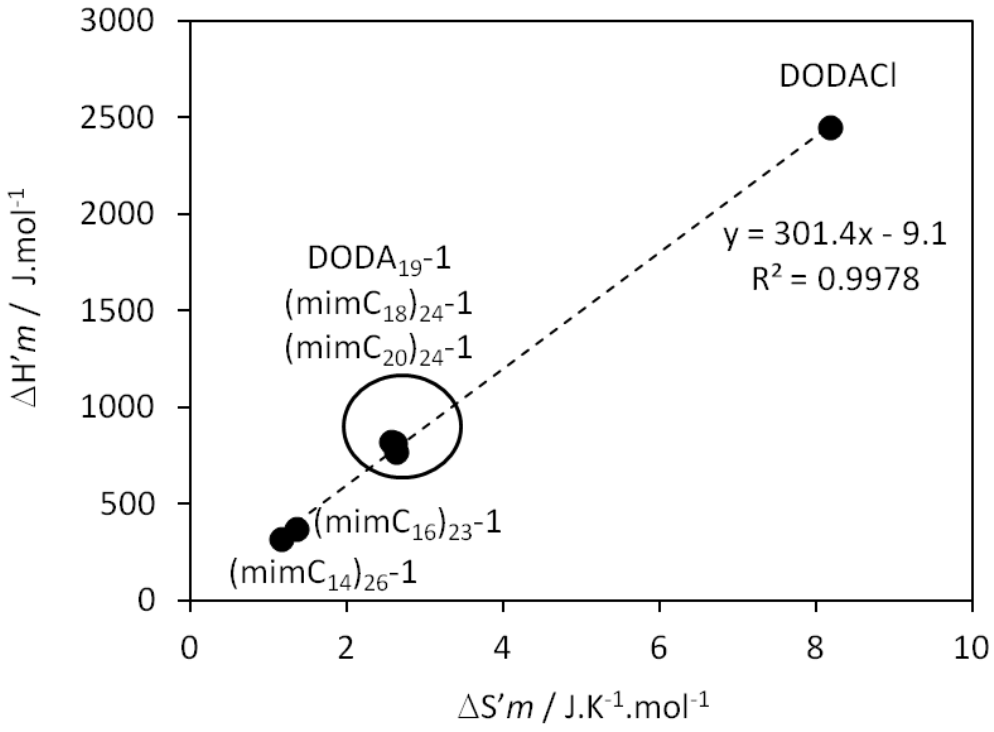

Figure 15: . $\Delta H'_m$ versus $\Delta S'_m$ plot.

II.4.1.c Temperature dependent Small-Angle X-ray Diffraction (SA-XRD)

Temperature dependent Small-Angle X-ray Diffraction (SA-XRD) experiments (-40°C to 200°C) were carried out to probe the organization of the liquid crystalline phases. For all compounds, the presence of two, and sometimes three, equidistant reflections in the 1:2 (1:2:3) ratio (indexed as (00*l*) = (001), (002) and (003)) were detected in the low angle domain (Figure 16 ,Table 4 , Tables A4.1-A4.6 in the Appendix) characteristic for a 1D lamellar ordering as already stated. The sharpness of the reflections indicates that they correspond to long range organizations in contrast to {Mo_{132}} materials for which broad lines were obtained. In addition to the (00*l*) reflections, a weak reflection called *h*' is found at $d_{hkl} \approx$ 22 Å for at least four of our compounds. This additional reflection is compatible with partial 3D structuration, a result in line with the low fluidity of these compounds.[18-20] The presence of a broad and diffuse reflection at approximately 4.5 Å associated with the liquid-like molten chains is not observed for our materials, in agreement with the high viscosity of our mesophases. Finally, the absence of any reflection corresponding to intercluster distances implies that clusters are not well organized within the layers. Consequently the liquid crystalline phases behave like a smectic A phase (SmA).

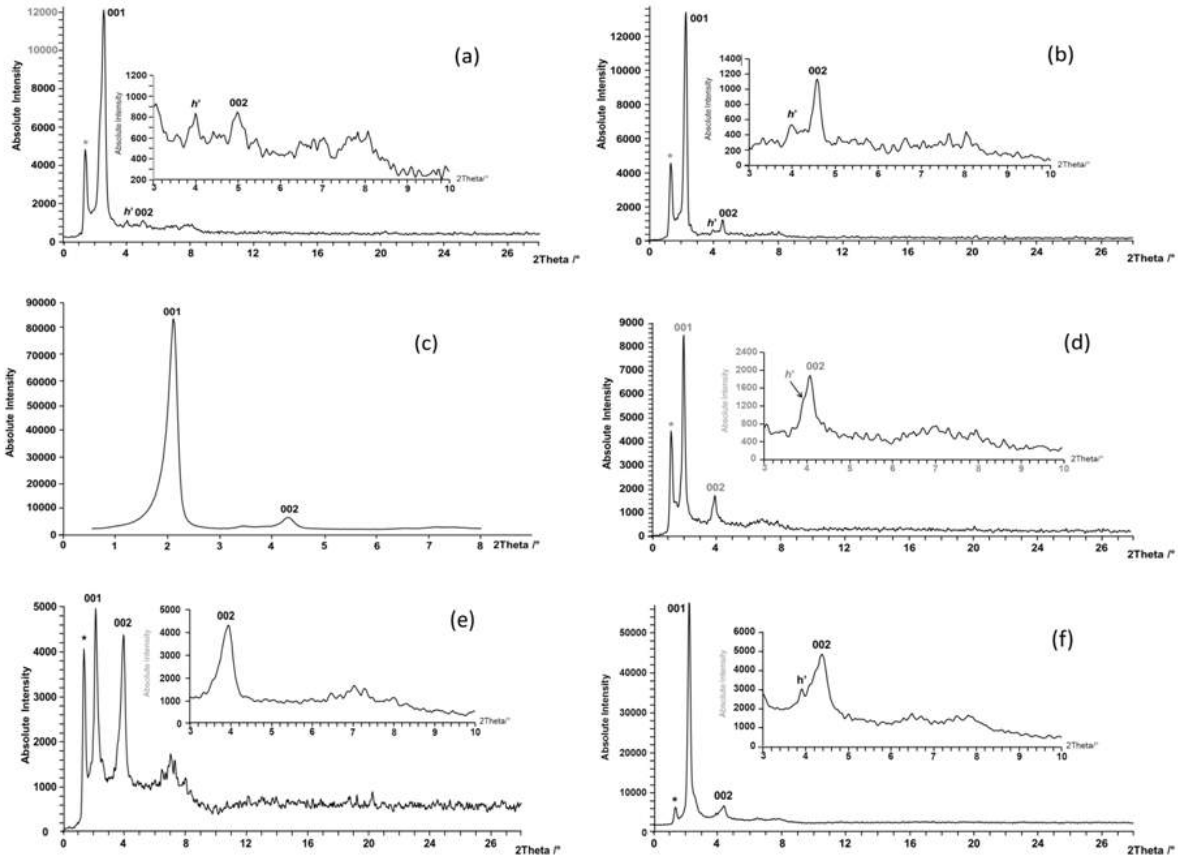

Figure 16: SA-XRD pattern recorded at 200°C for compounds **$(mimC_{12})_{25}$-1 (a), $(mimC_{14})_{26}$-1 (b), $(mimC_{16})_{23}$-1 (c), $(mimC_{18})_{24}$-1 (d), $(mimC_{20})_{24}$-1 (e) and $DODA_{19}$-1(f)**

Table 4: Indexation at 200°C during the cooling mode for the reflections detected in the liquid-crystalline phase by SA-XRD. Full data are given in the supporting information.

Compounds	$d_{hkl\ (mes)}$ /Å	*I* /a.u.	*00l*	$d_{hkl\ (calc\ )}$ /Å	
$DODA_{19}$-1	40.25	VS(Sh)	001	40.33	*h* = 40.33 Å
	22.54	S(Sh)			*h'*=22.54 Å
	20.20	S(Sh)	002	20.16	a_{Hex} = 33.68 Å
	13.5	W(Br)			
	11.4	W(Br)			
$(mimC_{12})_{25}$-1	35.01	VS(Sh)	001	35.15	*h* = 35.15 Å
	22.15	W(Sh)			*h'* = 22.15 Å
	17.64	S(Sh)	002	17.57	a_{Hex} = 32.75 Å
	13	W(Br)			
	11	W(Br)			
$(mimC_{14})_{26}$-1	38.39	VS(Sh)	001	38.44	*h* = 38.14 Å
	22.19	W(Sh)			*h'* = 22.19 Å
	19.24	S(Sh)	002	19.22	a_{Hex} = 32.10 Å
	13	W(Br)			
	11	W(Br)			
$(mimC_{16})_{23}$-1	41.09	VS(Sh)	001	40.96	*h* = 40.96 Å
	21.98	-			*h'* = 21.98 Å
	20.41	S(Sh)	002	20.48	a_{Hex} = 30.97 Å
	12	W(Br)			
$(mimC_{18})_{24}$-1	43.28	VS(Sh)	001	43.28	*h* = 43.28 Å
	22.37	W(Sh)			*h'* = 22.37 Å
	21.63	S(Sh)	002	21.64	a_{Hex} = 30.81 Å
	12	W(Br)			
$(mimC_{20})_{24}$-1	45.10	S(Sh)	001	45.03	*h* = 45.03 Å
	22.48	S(Sh)	002	22.52	a_{Hex} = 30.68 Å
	12	W(Br)			

$d_{hkl(mes)}$ and $d_{hkl(calc)}$ are the measured and calculated diffraction spacing ; *h* is the lattice parameter of the lamellar phase ; *I* corresponds to the intensity of the reflections (VS : very strong, S : strong, W : weak, VW : very weak ; br and sh stand for broad and sharp) ; *h* and $d_{hkl(calc)}$ are respectively calculated according the formula : $h = 1/2 (d_{001(exp)} + 2d_{002\ (exp)})$ and $d_{hkl(calc)} = h/l$; a_{Hex} is the local hexagonal organization within the layers calculated with eq. 1. The reflection corresponding to the molten aliphatic chains (usually ~ 4.5Å) is too broad to be measured.

The lattice parameters *h* are deduced from the (00*l*) lines and are found almost constant in the 40-200°C temperature range (Table 4, Figure 17 and Tables A4.1-A5.6 in the Appendix). This parameter depends on the nature of the organic cations associated with the polyoxometalate. Focusing on the $mimC_n^+$ salts, the plot of the *h* parameters as a function of the alkyl chain length (Figure 17b) exhibits a linear relationship with an increase of the *h* parameter by ca 2.6 Å for successive $mimC_n^+$ and $mimC_{n+2}^+$ salts. This increment is compatible with the distance increase induced by the introduction of two methylene group within an alkyl chain. This result demonstrates i) that it is possible to easily tune the interlamellar spacing of such a huge inorganic cluster by simply playing with the alkyl chain length of the associated organic cations and ii) that the interdigitation of the organic cations belonging to two opposite clusters remains necessarily unchanged (it is a full interdigitation), thus leading to a linear expansion of the *h* parameter with the increasing of the alkyl chains length.

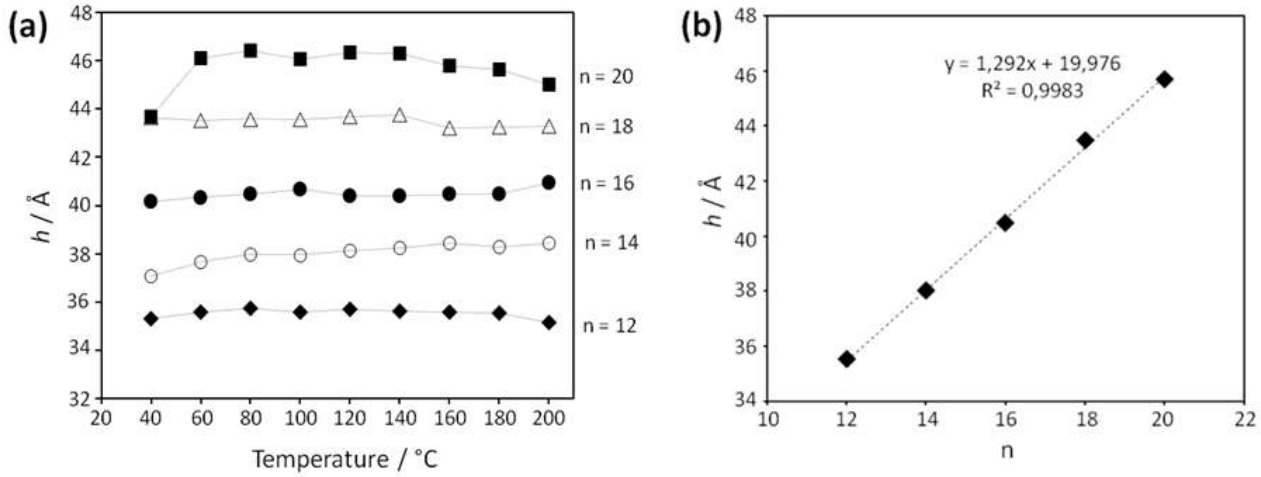

Figure 17: (a) Variation of the structural parameter *h* as a function of temperature for compounds $(mimC_n)_x$-1 (n = 12, 14, 16, 18, 20). (b) Variation of the averaged value of h (in the 20-200°C temperature range) as a function of alkyl chain length *n*.

The hexagonal lattice parameters a_{Hex} which correspond to the average inter-cluster distances was calculated as previously described in chapter III where we based on the following equation:

$$a_{Hex} = \left(\frac{2 \cdot Z \cdot MM_C}{h \cdot d \cdot N_{AV} \cdot 10^{-24} \cdot 3^{1/2}} \right)^{1/2} \qquad \textbf{(eq.1)}$$

(where N_{AV} is the Avogadro's number, MM_C the molecular weight of the cluster in g.mol^{-1}, d = 1 g.cm^{-1}, $Z = 1$ and *h* the lamellar periodicity measured by SA-XRD).

The obtained data are gathered in Table 4. The a_{Hex} parameter is minimum for **mimC$_{20}$)$_{24}$-1** (a_{Hex} = 30.68 Å) and maximum for **DODA$_{19}$-1** (a_{Hex} = 33.89 Å) in the liquid crystalline phase at 200°C.

The compounds of this study result from the ionic assemblies of $DODA^+$ or $mimC_n^+$ organic cations with the ellipsoidal polyoxometalate anion **1** (diameter ≈ 20.3 Å, thickness ≈ 15.9 Å). As evidenced by solid state NMR, the positive charges of the cations are located close to the negatively charged tungstate groups of the toroidal surface of the P_8W_{48} moiety. They are however not mechanically linked to a specific point of the cluster core. Considering that the values of a_{Hex} do not vary significantly with the nature of the cation, we can rule out the possibility of having the cations aligned along the longer axis as depicted in Figure 13a and previously reported for $(DODA)_{24}Li[Cu_{20}Cl(OH)_{24}P_8W_{48}O_{184}]\cdot 18H_2O$ in the solid state.[21]
The consideration of a diameter of *ca* 20 Å with a length of 22 Å for the $DODA^+$ cation, confirms that this hypothesis is not realistic. The only way to make these objects compatible with the values of $30.68 \leq a_{Hex} \leq 33.89$ Á requires that the anchoring sites of the cations are

located on the surface of the negatively charged inorganic clusters, whilst the alkyl chains are spread perpendicular to the polyoxometalate macrocycle (Figure 18b). A related organization is supposed to occur for **$(mimC_n)_x$-1,** whereas the cations in **$(dmimC_n)_x$-1** and **$(TMAC_{16})_{18}$-1** do not display a similar orientation of cations around the POM either due to stronger interactions between the cation and the POM anion or due to sterical contraints between cations which limit the van der waals contact between the alkyl chains. The inorganic cluster shown in the Figure 18b are packed in the solid state to give the hexagonal lamellar arrangement depicted in Figure 18c and Figure 18d. The associated lattice parameters *h* depend on the alkyl chain length and they are controlled by the thickness of the inorganic cluster (15 Á) and the partial interdigitation of the alkyl chains of the cations. This organization reminds that proposed for Langmuir-Blodgett film obtained for $(DODA)_{24}Li[Cu_{20}Cl(OH)_{24}P_8W_{48}O_{184}]\cdot 18H_2O$.[21] In summary, the ionic associations between the anisotropic POM **1** and organic cations such as $DODA^+$ and a $mimC_n^+$ give lamellar organization, in which the layers are composed of the inorganic clusters and the interlayer spacing is filled by the alkyl chains of the cations.

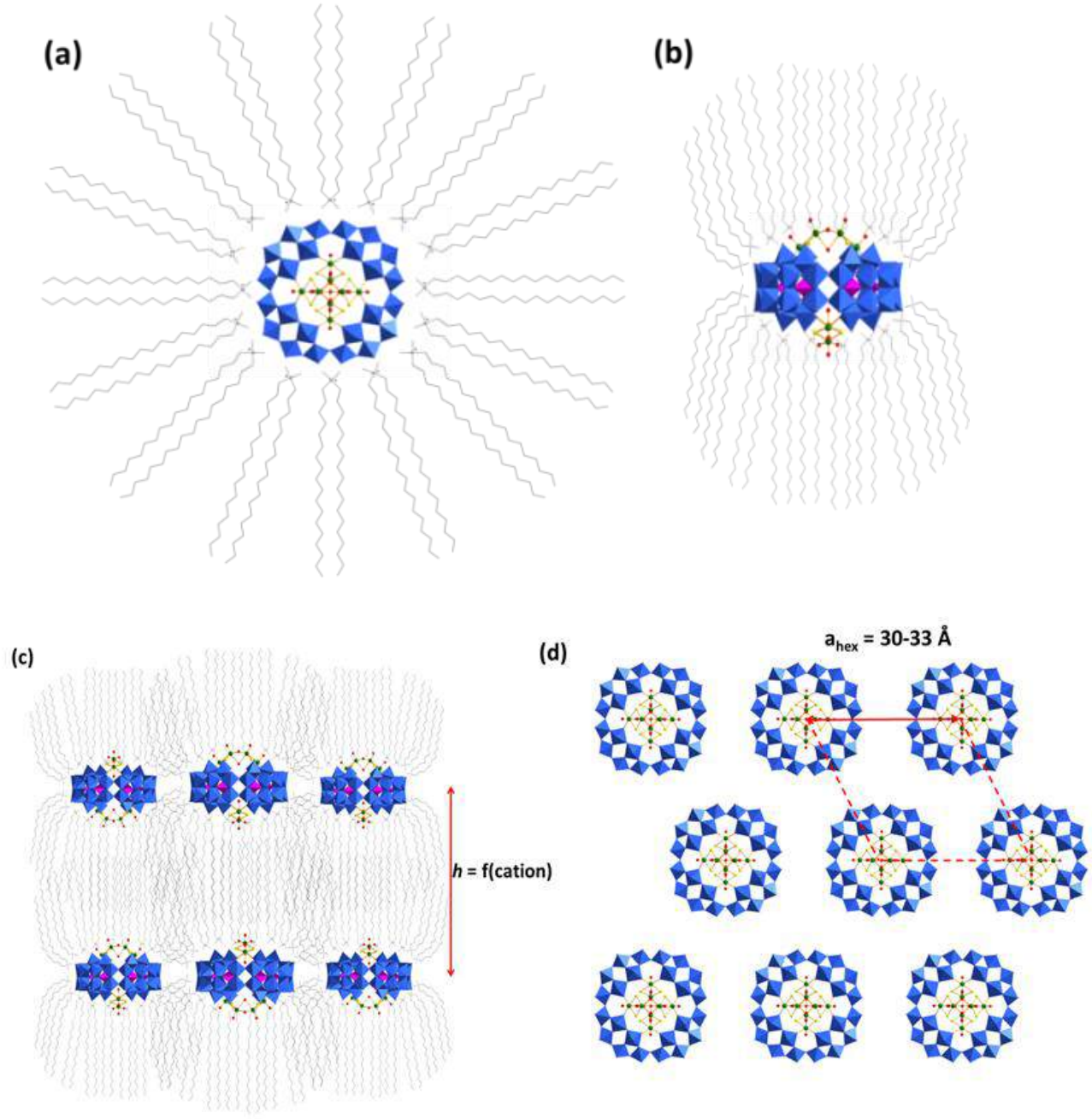

Figure 18: Schematic representation of the hypothetical organizations of organic cations around the polyanion **1** (a,b); side and top views of the lamellar organisation of ionic liquid crystal phases of materials based of the polyanion **1** (c and d). The *perp* isomer of **1** is mainly taken into account but different position of this isomer should be considered. For the top view, the organic cations are omitted for clarity.

III. Conclusion

In an attempt to improve the organization of mesophases obtained by electrostatic combination of a POM cluster with organic cation, we replaced the isotropic Keplerate cluster by the cyclic superlacunary anionic POM, $Na_{25}Li[K_2\{Mo_4O_4S_4(OH)_2(H_2O)_3\}_2(H_8P_8W_{48}O_{184})]\cdot 125H_2O$ noted **1**. For this purpose, we prepared a series of new compounds using various organic cations such as $DODA^+$, $TMAC_{16}^+$, $mimC_n^+$ (n = 12-20) and $dmimC_n^+$

(*n* = 12 and 16). The materials were characterized in the solid state by the usual techniques as FT-IR which suggest the integrity of the anionic cluster during the experimental procedure and the Molecular formula was estimated using EA, EDX and TGA. Generally, the number of replaced organic cations does not exceed 26 and are found in the range 18-26. The residual charge was completed by potassium, sodium and lithium cations demonstrating the good affinity of these alkali ions with the P_8W_{48} cavity. Significantly lower number of organic cations were found in the case of $dmimC_n^+$ (n = 12 and 16) cations , this suggest that the number of cations can be modulated by changing the nature of the imidazolium ring of the organic cations and that the cations are very close to each other. In addition, TGA and FT-IR at variable temperature confirm the stability of the materials up to 250°C in air.

The multinuclear solid state NMR revealed to be a powerful technique for the characterization of these materials and (i) allowed evidencing the strong contacts between the POM and the organic cations and (ii) provided some support for the intermolecular H-H dipolar contacts induced by the interdigitation of the alkyl chains of the cations. For $DODA^+$ and $mimC_n^+$ salts of **1**.

Polarized Optical Microscopy, DSC studies revealed ionic liquid crystalline phases even if the fluidity of the $mimC_n^+$ salts is low.

Contrary to the Keplerate-based materials, these materials formed highly and well organized mesophase as probed by Small-Angle X-Ray diffraction studies. The presence of Miller indices (00*l*) indicates that the materials exhibit 1D lamellar organization in which the layers are composed of the inorganic clusters and the interlayer spacing is filled by the alkyl chains of the cations. Finally, the absence of any reflection corresponding to intercluster distances implies that clusters are not organized within the layers. Consequently the liquid crystalline phases behave like smectic A phase (SmA).

Finally, the crystallographic parameters were determined and demonstrated that the inter-lamellar spacing could be finely controlled upon changing the length of the alkyl chain, a very interesting result if we consider the huge size of the inorganic cluster **1** and the simple nature of the cations.

These results demonstrate that the strategy which consists by associating highly charged anisotropic polyoxometalate clusters with very simple organic cations bearing only alkyl chains with variable size can be efficient for providing fine tuneable liquid crystal phases. Such a strategy allows envisioning the easy preparation of multifunctional materials at a gram

scale and the main perspectives for this work aim now at designing materials combining magnetic, optical or trapping properties with liquid crystal behavior.

IV. Experimental part

Physical method

Fourier Transformed Infrared (FT-IR) spectra were recorded on a 6700 FT-IR Nicolet spectrophotometer, using diamond ATR technique. The spectra were recorded on undiluted samples and ATR correction was applied. The variable temperature FT-IR spectra were recorded on an IRTF Nicolet iS10 spectrometrer in Diffuse Reflectance mode by using High temperature Diffuse Reflectance Environmental Chamber. The background was recorded using dry KBr at 150°C and the samples were diluted into a KBr matrix (about 10% of compound) before heating. The FT-IR spectra were recorded in the 20-300°C temperature range under air with a heating rate of 2°C/min. **Elemental analyses** were performed by the service central d'analyses du CNRS, Vernaison, France and by the service d'analyses du CNRS, ICSN, Gif sur Yvette, France. **Water content** was determined by thermal gravimetric (TGA) analysis with a Seiko TG/DTA 320 thermogravimetric balance (5°C min^{-1}, under O_2). **Energy-dispersive X-ray spectroscopy (EDX)** measurements were performed on a JEOL JSM 5800LV apparatus.

Nuclear Magnetic Resonance (NMR). Solution ^{1}H NMR measurements were performed on a Bruker Avance 300 instrument operating at 300 MHz in 5 mm o.d. tubes. Chemical shifts were referenced to TMS. Solid-state NMR spectra were measured at room temperature under magic angle spinning (MAS) condition. The NMR spectra were obtained on a Bruker Avance-500 spectrometer equipped with a MAS accessory operating at 500.125, 125.761, and 202.452 MHz for ^{1}H, ^{13}C and ^{31}P. Zirconium oxide cylindrical-type rotors (3.2-mm outer diameter) were used. ^{1}H NMR spectra were recorded with single 90° pulse (3.8 μs) at spinning rate of about 20 kHz. The spectral width and data points were 10 kHz and 1 k respectively. The spectra were obtained after 8 transients at a repetition time of ca. 30 s. $^{31}P\{^{1}H\}$ and $^{13}C\{^{1}H\}$ CPMAS NMR spectra were recorded with typical rf field in X channel (^{13}C or ^{31}P) of ca. 90 kHz, high power decoupling during acquisition (26 ms) of ca. 50-60 kHz, and contact time of 1-2 ms. 2D ^{1}H->^{31}P MAS heteronuclear correlation (HETCOR) experiments were performed using CP transfer. The chemical shifts were calibrated relative to

a 85% H_3PO_4 solution (set to δ = 0 ppm) for ^{31}P, and adamantane (set to δ = 1.74 ppm in ^{1}H and 38.48 ppm in ^{13}C with respect to TMS) for ^{1}H and ^{13}C as external standards. The experimental errors on the chemical shifts were estimated to be ± 0.4 ppm.

Differential Scanning Calorimetry (DSC). DSC traces were obtained with a Mettler Toledo DSC1 Star Systems differential scanning calorimeter from 3 to 5 mg samples (5°C min^{-1}, under N_2). Several thermal cycles were performed between -40°C and 220°C, the first one allowing the removal of water and the relaxation of the solid, the following cycles explored the reproducibility and the thermal stability of the materials in this temperature range.

Temperature dependent polarized optical microscopy (TD-POM) characterizations of the optical textures of the mesophases were performed with a Leitz Orthoplan Pol polarizing microscope with a Leitz LL 20×/0.40 polarizing objective and equipped with a Linkam THMS 600 variable temperature stage.

Small angle X-ray diffraction (SA-XRD). The crude powder was filled in Lindemann capillaries of 0.8 mm diameter. Diffraction patterns were measured with a STOE transmission powder diffractometer system STADI P using a focused monochromatic Cu-$K_{\alpha 1}$ beam obtained from a curved Germanium monochromator (Johann-type) and collected on a curved image plate position-sensitive detector (IP-PSD). A calibration with silicon and copper laurate standards, for high and low angle domains, respectively, was preliminarily performed. Sample capillaries were placed in the high-temperature furnace for measurements in the range of desired temperatures (from -40 up to 240°C) within 0.05 °C. Periodicities up to 50 Å could be measured. The exposure times were of 15 min. For compound **$(mimC_{16})_{23}$-1**, X-ray diffraction experiments were performed on an Empyrean (PANalytical) diffractometer in capillary mode, with a focusing X-ray mirror for Cu radiation and a PIXcel3D area detector.

Syntheses

The precursor $Na_{25}Li[K_2\{Mo_4O_4S_4(OH)_2(H_2O)_3\}_2(H_8P_8W_{48}O_{184})]$ $.125H_2O$, noted **NaK-1**, was prepared according to the literature and characterized by standard methods.[6] Trimethylhexadecylammonium chloride and dimethyldioctadecylammonium chloride were purchased from Aldrich or Acros chemicals.

Synthesis of 1-methyl-3-alkylimidazolium bromides, $mimC_nBr$ (n = 12, 14, 16, 18, 20). 10^{-2} mole of 1-methyl imidazole and 1.2 10^{-2} mole of $C_nH_{2n+1}Br$ were dissolved in acetonitrile (5 mL for n = 12-16, 15 mL for n = 18, 20). The resulting solution was refluxed for 24 hrs.

After, cooling in an ice bath; a precipitate appeared. The latter was isolated by filtration and washed with diethyl ether. The mimC_nBr salts were characterized by FT-IR and ^{1}H NMR in $CDCl_3$ (see experimental section of Chapter III).

Synthesis of 1,2-dimethyl-3-alkylimidazolium bromides, dmimC_nBr (n = 12, 16). The same procedure was used except that 10^{-2} mole of 1,2-dimethylimidazole was used. The dmimC_nBr salts were characterized by FT-IR and ^{1}H NMR in $CDCl_3$ (see Supporting Information).

Synthesis of POM-based materials

The POM-based materials presented in this study were prepared by phase transfer of the anionic cluster **1** from aqueous LiCl 1 M solution into chloroform. 300 mg of the precursor **NaK-1** (0.018 mmol) were solubilised in aqueous LiCl 1 M solution (30 mL). The resulting red solution was then added to a chloroform solution containing a large excess of the organic cation (150 equivalents / **NaK-1**, 2.7 mmol). After vigorous stirring for one hour, the cluster **1** was totally transferred into the organic phase, which was separated from the colourless aqueous phase. Addition of ethanol into the organic phase induced the formation of a red-orange solid, which was isolated by filtration, washed with ethanol and dried in air.

$(DODA)_{19}[K_2Na_2Li_5\{Mo_4O_4S_4(OH)_2(H_2O)_3\}_2(H_8P_8W_{48}O_{184})]$. 10 H_2O, $DODA_{19}$-1, was prepared by using 1.56 g of dimethyldioctadecylammonium chloride DODACl (2.68 mmol). Yield 421 mg, 94%. IR/cm^{-1}: 2954 (m), 2920 (vs), 2870 (m), 2851 (s), 1639 (mw), 1467 (m), 1135 (m), 1078 (m), 1022 (w), 939 (s), 879 (m), 792 (s), 723 (s). Elemental analysis calcd (%) for $(DODA)_{19}[K_2Na_2Li_5H_8P_8W_{48}O_{184}Mo_8O_8S_8(OH)_4(H_2O)_6].10H_2O$ (M = 24143.3 g.mol^{-1}) Li 0.14; Na 0.19; K 0.32; C 35.92; H 6.52; N 1.10; S 1.06. Found: Li 0.12; Na 0.16; K 0.21; C 35.82; H 6.36; N 1.29; S 0.95. EDX atomic ratios calculated for $(DODA)_{19}[K_2Na_2Li_5H_8P_8W_{48}O_{184}Mo_8O_8S_8(OH)_4(H_2O)_6].10H_2O$ (found): Mo/S = 1 (1.10); W/Mo = 6 (5.87); W/P = 6 (6.05); Na/K = 1 (1.15). TGA: A weight loss of 1.1% between *RT* and 150 °C corresponding to crystallization and coordinated water molecules (cald: 1.2%).

$(NMe_3C_{16}H_{33})_{18}[K_2Na_2Li_6\{Mo_4O_4S_4(OH)_2(H_2O)_3\}_2(H_8P_8W_{48}O_{184})]$. 30$H_2O$, **$(TMAC_{16})_{18}$-1,** was prepared by using 860 mg of trimethylhexadecylammonium chloride (2.68 mmol). Yield 295 mg, 85%. IR/cm^{-1}: 2954 (m), 2924 (vs), 2871 (m), 2853 (s), 1636 (mw), 1487 (m), 1474 (m), 1469 (m), 1130 (ms), 1076 (m), 1022 (w), 941 (s), 879 (m, sh.), 794 (s), 722 (s). Elemental analysis calcd (%) for $(N(Me)_3C_{16})_{18}[K_2Na_2Li_6H_8P_8W_{48}O_{184}Mo_8O_8S_8(OH)_4(H_2O)_6].30H_2O$ (M = 19180.4 g.mol^{-1}) Li 0.22; Na

0.23; C 21.42; H 4.41; N 1.31; S 1.34. Found: Li 0.24; Na 0.13; C 21.20; H 4.36; N 1.09; S 1.20. EDX atomic ratios calculated for $(N(Me)_3C_{16})_{18}[K_2Na_2Li_6H_8P_8W_{48}O_{184}Mo_8O_8S_8(OH)_4(H_2O)_6].30H_2O$ (found): Mo/S = 1 (1.15); W/Mo = 6 (6.22); W/P = 6 (5.82); Na/K = 1 (1.06). TGA: A weight loss of 3.1% between *RT* and 180 °C corresponding to crystallization and coordinated water molecules (cald: 3.4%).

$(mimC_{12}H_{25})_{25}[K_2NaLi_4\{Mo_4O_4S_4(OH)_2(H_2O)_3\}_2(H_4P_8W_{48}O_{184})].\ 20H_2O$,$(mimC_{12})_{25}$-1 was prepared by using $mimC_{12}Br$ (890 mg, 2.68 mmol). Yield 341 mg, 95%. IR/cm^{-1}: 3144 (m), 3101 (m), 3080 (m), 2956 (m), 2925 (vs), 2870 (m), 2854 (s), 1631 (mw), 1571 (m), 1466 (m), 1166 (m), 1131 (m), 1077 (m), 1021 (w), 941 (s), 887 (m), 818 (s), 744 (vs). Elemental analysis calcd (%) for $(mimC_{12}H_{25})_{25}[K_2NaLi_4H_4P_8W_{48}O_{184}Mo_8O_8S_8(OH)_4(H_2O)_6].20H_2O$ (M = 20123.3 g.mol^{-1}) Li 0.14; Na 0.12; C 24.09; H 4.12; N 3.51; S 1.29. Found: Li 0.14; Na 0.11; C 23.87; H 4.18; N 3.48; S 1.27. EDX atomic ratios calculated for $(mimC_{12}H_{25})_{25}[K_2NaLi_4H_4P_8W_{48}O_{184}Mo_8O_8S_8(OH)_4(H_2O)_6].20H_2O$ (found): Mo/S = 1 (0.91); W/Mo = 6 (5.85); W/P = 6 (6.34); Na/K = 0.50 (0.79). TGA: A weight loss of 2.3 % between *RT* and 180°C corresponding to crystallization and coordinated water molecules (cald: 2.3 %).

$(mimC_{14}H_{29})_{26}[K_2Na_2Li_3\{Mo_4O_4S_4(OH)_2(H_2O)_3\}_2(H_3P_8W_{48}O_{184})].\ 35H_2O$,$(mimC_{14})_{26}$-1, was prepared by using aqueous LiCl 1 M solution and $mimC_{14}Br$ (960 mg, 2.68 mmol). Yield 220 mg, 59%. IR/cm^{-1}: 3144 (m), 3091 (m), 3074 (m), 2955 (m), 2920 (vs), 2871 (m), 2851 (s), 1636 (mw), 1572 (m), 1467 (m), 1168 (m), 1130 (m), 1077 (m), 1020 (w), 936 (s), 882 (mw), 802 (s), 733 (vs). Elemental analysis calcd (%) for $(mimC_{14}H_{29})_{26}[K_2Na_2Li_3H_3P_8W_{48}O_{184}Mo_8O_8S_8(OH)_4(H_2O)_6].35H_2O$ (M = 21389.4 g.mol^{-1}) Li 0.10; Na 0.22; C 26.28; H 4.70; N 3.40; S 1.20. Found: Li 0.22; Na 0.35; C 26.57; H 4.53; N 3.58; S 1.12. EDX atomic ratios calculated for $(mimC_{14}H_{29})_{26}[K_2Na_2Li_3H_3P_8W_{48}O_{184}Mo_8O_8S_8(OH)_4(H_2O)_6].35H_2O$ (found): Mo/S = 1 (1.09); W/Mo = 6 (6.07); W/P = 6 (6.02); Na/K = 1 (1.28). TGA: A weight loss of 3.4 % between *RT* and 170°C corresponding to crystallization and coordinated water molecules (cald: 3.5 %).

$(mimC_{16}H_{33})_{23}[K_2Na_3Li_3\{Mo_4O_4S_4(OH)_2(H_2O)_3\}_2(H_5P_8W_{48}O_{184})].\ 40H_2O$,$(mimC_{16})_{23}$-1, was prepared by using $mimC_{16}Br$ (1.038 g, 2.68 mmol). Yield 218 mg, 59%. IR/cm^{-1}: 3144 (m), 3102 (m), 3075 (m), 2955 (m), 2922 (vs), 2871 (m), 2852 (s), 1637 (mw), 1571 (m), 1467 (m), 1166 (m), 1136 (m), 1078 (m), 1016 (w), 932 (s), 880 (mw), 799 (s), 721 (vs). Elemental analysis calcd (%) for $(mimC_{16}H_{33})_{23}[K_2Na_3Li_3H_5P_8W_{48}O_{184}Mo_8O_8S_8(OH)_4$

$(H_2O)_6$].40H_2O (M = 21311.2 g.mol^{-1}) C 25.93; H 4.72; N 3.02; S 1.20. Found: C 26.09; H 4.62; N 3.18; S 1.33. EDX atomic ratios calculated for ($mimC_{16}H_{33})_{23}[K_2Na_3Li_3H_5P_8W_{48}O_{184}Mo_8O_8S_8$ $(OH)_4(H_2O)_6$].40H_2O (found): Mo/S = 1 (1.02); W/Mo = 6 (5.73); W/P = 6 (5.58); Na/K = 1.5 (1.65). TGA: A weight loss of 4.1 % between *RT* and 170°C corresponding to crystallization and coordinated water molecules (cald: 3.9 %).

($mimC_{18}H_{37})_{24}[K_2NaLi_3\{Mo_4O_4S_4(OH)_2(H_2O)_3\}_2(H_6P_8W_{48}O_{184})]$. 25$H_2O$, ($mimC_{18})_{24}$-1, was prepared by using $mimC_{18}Br$ (1.113 g, 2.68 mmol). Yield 385 mg, 98%. IR/cm^{-1}: 3142 (m), 3100 (m), 3078 (m), 2953 (m), 2920 (vs), 2871 (m), 2851 (s), 1635 (w), 1573 (m), 1468 (m), 1166 (m), 1141 (m), 1077 (m), 1017 (w), 938 (s), 882 (mw), 802 (s), 741 (vs). Elemental analysis calcd (%) for ($mimC_{18}H_{37})_{24}[K_2NaLi_3$ $H_6P_8W_{48}O_{184}Mo_8O_8S_8(OH)_4(H_2O)_6$].25$H_2O$ (M = 21976.9 g.mol^{-1}) Li 0.09; Na 0.10; C 28.86; H 5.06; N 3.06; S 1.17. Found: Li 0.09; Na 0.08; C 29.05; H 5.22; N 3.06; S 1.13. EDX atomic ratios calculated for ($mimC_{18}H_{37})_{24}[K_2NaLi_3H_6P_8W_{48}O_{184}Mo_8O_8S_8$ $(OH)_4(H_2O)_6$].25H_2O (found): Mo/S = 1 (1.03); W/Mo = 6 (6.16); W/P = 6 (5.74); Na/K = 0.5 (0.42). TGA: A weight loss of 2.6% between *RT* and 180 °C corresponding to crystallization and coordinated water molecules (cald: 2.5%).

($mimC_{20}H_{41})_{24}[K_2NaLi_3\{Mo_4O_4S_4(OH)_2(H_2O)_3\}_2(H_6P_8W_{48}O_{184})]$. 15$H_2O$, ($mimC_{20})_{24}$-1, was prepared by using $mimC_{20}Br$ (1.189 g, 2.68 mmol). Yield 212 mg, 52%. IR/cm^{-1}: 3146 (m), 3103 (m), 3077 (m), 2953 (m), 2920 (vs), 2870 (m), 2851 (s), 1639 (mw), 1572 (m), 1468 (m), 1166 (m), 1138 (m), 1078 (m), 1016 (w), 935 (s), 881 (mw), 800 (s), 720 (vs). Elemental analysis calcd (%) for ($mimC_{20}H_{41})_{24}[K_2NaLi_3H_6P_8W_{48}O_{184}Mo_8O_8S_8(OH)_4(H_2O)_6$].15$H_2O$ (M = 22470.0 g.mol^{-1}) C 30.79; H 5.29; N 2.99; S 1.14. Found: C 30.53; H 5.17; N 2.91; S 1.14. EDX atomic ratios calculated for ($mimC_{20}H_{41})_{24}[K_2NaLi_3H_6P_8W_{48}$ $O_{184}Mo_8O_8S_8(OH)_4(H_2O)_6$].15$H_2O$ (found): Mo/S = 1 (1.12); W/Mo = 6 (5.98); W/P = 6 (6.15); Na/K = 0.50 (0.44). TGA: A weight loss of 1.9% between *RT* and 150 °C corresponding to crystallization and coordinated water molecules (cald: 1.7%).

($dmimC_{12}H_{25})_{18}[K_2Na_3Li_5\{Mo_4O_4S_4(OH)_2(H_2O)_3\}_2(H_8P_8W_{48}O_{184})]$. 15$H_2O$, ($dmimC_{12})_{18}$-1, was prepared by using $dmimC_{12}Br$ (930 mg, 2.68 mmol). Yield 180 mg, 55%. IR/cm^{-1}: 2953 (m), 2925 (vs), 2871 (m), 2853 (s), 1637 (mw), 1588 (w), 1537 (w), 1467 (m), 1240 (w), 1128 (m), 1078 (m), 1016 (w), 932 (s), 880 (mw), 799 (s), 719 (vs). Elemental analysis calcd

(%) for $(dmimC_{12}H_{25})_{18}$ $[K_2Na_3Li_5H_8P_8W_{48}O_{184}Mo_8O_8S_8(OH)_4(H_2O)_6].15H_2O$ (M = 18582.6 $g.mol^{-1}$) Li 0.19; Na 0.37; C 19.78; H 3.51; N 2.71; S 1.38. Found: Li 0.22; Na 0.45; C 19.84; H 3.65; N 2.82; S 1.25. EDX atomic ratios calculated for $(dmimC_{12}H_{25})_{18}[K_2Na_3Li_5H_8P_8W_{48}O_{184}$ $Mo_8O_8S_8(OH)_4(H_2O)_6].15H_2O$ (found): Mo/S = 1 (1.12); W/Mo = 6 (5.75); W/P = 6 (7.10); Na/K = 1.5 (0.90). TGA: A weight loss of 2.1% between *RT* and 180 °C corresponding to crystallization and coordinated water molecules (cald: 2.0%).

$(dmimC_{16}H_{33})_{20}[K_2Na_2Li_4\{Mo_4O_4S_4(OH)_2(H_2O)_3\}_2(H_8P_8W_{48}O_{184})].$ $20H_2O$, $(dmimC_{16})_{20}$-1, was prepared by using $dmimC_{16}Br$ (1.080 g, 2.68 mmol). Yield 348 mg, 91%. IR/cm^{-1}: 3144 (m), 2956 (m), 2924 (vs), 2872 (m), 2853 (s), 1639 (mw), 1589 (w), 1539 (w), 1466 (m), 1377 (w), 1241 (w), 1142 (m), 1080 (m), 1016 (w), 937 (s), 884 (mw), 808 (s), 721 (vs). Elemental analysis calcd (%) for $(dmimC_{16}H_{33})_{20}[K_2Na_2Li_4H_8P_8W_{48}O_{184}Mo_8O_8S_8(OH)_4(H_2O)_6].20H_2O$ (M = 20316.0 $g.mol^{-1}$) Li 0.14; Na 0.23; C 24.83; H 4.48; N 2.76; S 1.26. Found: Li 0.11; Na 0.27; C 24.82; H 4.62; N 2.79; S 1.19. EDX atomic ratios calculated for $(dmimC_{16}H_{33})_{20}$ $[K_2Na_2Li_4H_8P_8W_{48}O_{184}Mo_8O_8S_8(OH)_4(H_2O)_6].20H_2O$ (found): Mo/S = 1 (1.07); W/Mo = 6 (5.73); W/P = 6 (5.94); Na/K = 1 (0.98). TGA: A weight loss of 2.5% in the *RT*-180°C range corresponding to crystallization and coordinated water molecules (cald: 2.3%).

V. References

[1] R. Contant, A. Teze, *Inorg. Chem.* **1985**, *24*, 4610-4614.

[2] S. S. Mal, B. S. Bassil, M. Ibrahim, S. Nellutla, J. van Tol, N. S. Dalal, J. A. Fernandez, X. Lopez, J. M. Poblet, R. N. Biboum, B. Keita, U. Kortz, *Inorg. Chem.* **2009**, *48*, 11636-11645.

[3] S. S. Mal, M. H. Dickman, U. Kortz, A. M. Todea, A. Merca, H. Bogge, T. Glaser, A. Muller, S. Nellutla, N. Kaur, J. van Tol, N. S. Dalal, B. Keita, L. Nadjo, *Chem.-Eur. J.* **2008**, *14*, 1186-1195.

[4] S. Noro, R. Tsunashima, Y. Kamiya, K. Uemura, H. Kita, L. Cronin, T. Akutagawa, T. Nakamura, *Angew. Chem.-Int. Edit.* **2009**, *48*, 8703-8706.

[5] T. Akutagawa, R. Jin, R. Tunashima, S. Noro, L. Cronin, T. Nakamura, *Langmuir* **2008**, *24*, 231-238.

[6] V. S. Korenev, S. Floquet, J. Marrot, M. Haouas, I. M. Mbomekalle, F. Taulelle, M. N. Sokolov, V. P. Fedin, E. Cadot, *Inorg. Chem.* **2012**, *51*, 2349-2358.

[7] M. Zimmermann, N. Belai, R. J. Butcher, M. T. Pope, E. V. Chubarova, M. H. Dickman, U. Kortz, *Inorg. Chem.* **2007**, *46*, 1737-1740.

[8] S. S. Mal, N. H. Nsouli, M. H. Dickman, U. Kortz, *Dalton Trans.* **2007**, 2627-2630.

[9] F. L. Sousa, H. Bogge, A. Merca, P. Gouzerh, R. Thouvenot, A. Muller, *Chem. Commun.* **2009**, 7491-7493.

[10] A. Muller, M. T. Pope, A. M. Todea, H. Bogge, J. van Slageren, M. Dressel, P. Gouzerh, R. Thouvenot, B. Tsukerblat, A. Bell, *Angew. Chem.-Int. Edit.* **2007**, *46*, 4477-4480.
[11] Y. X. Jiang, S. X. Liu, J. Zhang, L. X. Wu, *Dalton Trans.* **2013**, *42*, 7643-7650.
[12] S. Y. Yin, H. Sun, Y. Yan, W. Li, L. X. Wu, *J. Phys. Chem. B* **2009**, *113*, 2355-2364.
[13] Y. Jiang, S. Liu, J. Zhang, L. Wu, *Dalton Trans.* **2013**, *42*, 7643-7650.
[14] H. El Moll, J. C. Kemmegne-Mbouguen, M. Haouas, F. Taulelle, J. Marrot, E. Cadot, P. Mialane, S. Floquet, A. Dolbecq, *Dalton Trans.* **2012**, *41*, 9955-9963.
[15] X. K. Lin, W. Li, J. Zhang, H. Sun, Y. Yan, L. X. Wu, *Langmuir* **2010**, *26*, 13201-13209.
[16] S. Y. Yin, W. Li, J. F. Wang, L. X. Wu, *J. Phys. Chem. B* **2008**, *112*, 3983-3988.
[17] T. Dutronc, E. Terazzi, L. Guenee, K. L. Buchwalder, A. Spoerri, D. Emery, J. Mareda, S. Floquet, C. Piguet, *Chem.-Eur. J.* **2013**, *19*, 8447-8456.
[18] R.Deschenaux, B. Donnio, D. Guillon, *New J. Chem.* **2007**, *31*, 1064-1073.
[19] S. Floquet, E. Terazzi, V. S. Korenev, A. Hijazi, L. Guenee, E. Cadot, *Liq. Cryst.* **2014**, *41*, 1000-1007.
[20] S. Floquet, E. Terazzi, A. Hijazi, L. Guenee, C. Piguet, E. Cadot, *New J. Chem.* **2012**, *36*, 865-868.
[21] Y. Y. Bao, L. H. Bi, L. X. Wu, S. S. Mal, U. Kortz, *Langmuir* **2009**, *25*, 13000-13006.

Appendix

Chapter II Appendix
Hydrophobic Effect as a Driving Force For Host-Guest Chemistry of a Multi-receptor Keplerate type-Capsule

I. ^{1}H NMR data

Table A2.1. ^{1}H NMR parameters (chemical shifts and self-diffusion coefficients) of S-Y_{52}{Mo_{132}} mixtures in aqueous solution at 3.10^{-3} mol.$L^{-1.}$

				Chemical shift (ppm)			Self-diffusion coefficient ($\mu m^2.s^{-1}$)		
Y^+	S^+	S^+/Y_{52}{Mo_{132}}	Cation S^+	SCl	Free acetate	Coordinated acetate	D_{obs}	$D°$	D^{∞}
Li^+	NMe_4^+	3.2	3.39	3.12	1.85	0.74	193	900	115
Na^+	NMe_4^+	2.7	3.33	3.12	1.86	0.75	230	900	114
$GuaH^+$	NMe_4^+	2.8	3.24	3.12	1.88	0.73	370	900	118
NH_4^+	NMe_4^+	2.96	3.25	3.12	1.85	0.78	357	900	118
	$HNMe_3^+$	2.75	2.97	2.834	1.90	0.75	530	1049	113
	$H_2NMe_2^+$	2.8	2.82	2.522	1.90	0.75	555	1100	115
	H_3NMe^+	3.3	2.64	2.508	1.89	0.75	730	1200	112
	$EtNMe_3^+$	3.1	3.545(2H) 3.275(9H) 1.497 (3H)	3.328 3.030 1.308	1.88	0.75	324	880	114
	NEt_4^+	3,4	3.474(8H) 1.452(9H)		1.89	0.75	170	665	117
	Me-Et-imi	3.3	4,501 (2H) 4,105 (3H) 1.591 (3H)		1.85	0.74	190	808	112

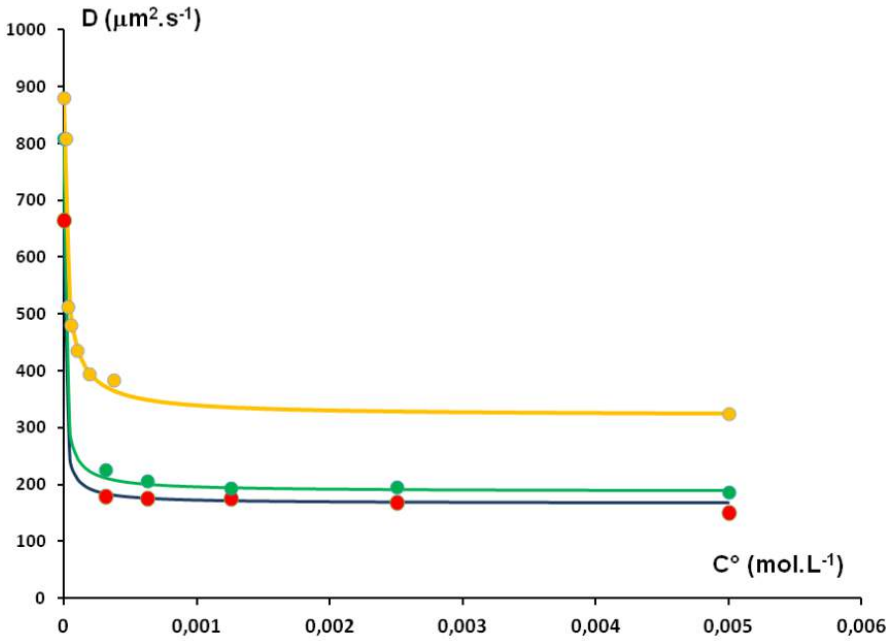

Figure A2.1. Experimental (circles) and calculated variations (solid lines) of the self-diffusion coefficient (*D*) of the cationic substrate S^+ with S = tetraéthylammonium (NEt_4^+,red) or methyl-ethyl-imidazolium(green) or trimethylethylammonium ($EtNMe_3^+$, yellow) ions with concentration in {Mo_{132}} (*C*°). ^{1}H DOSY experiments have been carried out at a fixed ratio S^+ /{Mo_{132}} ≈ 3 using $(NH_4)_{52}${Mo_{132}} as Keplerate salts.

II. Analytical treatment of the ^{1}H NMR data. Calculation of the D_{calc} values from chemical model.

II.1 Pore titration experiment

The concentration $C°$ in $Li_{52}\{Mo_{132}\}$ was fixed at $C° = 1.2\ 10^{-3}$ mol.L^{-1} and the equivalent number in NMe_4^+ varied from 0 to 50. In this case, no approximation can be considered. Based on the following equations:

$$K_Y = \frac{[PY]}{[P][Y]} \rightarrow [PY] = [P][Y].K_Y \ (17) \qquad \text{and } K_S = \frac{[PS]}{[P][S]} \rightarrow [PS]\ [P][S].K_S \ (18)$$

$$nC° = [S] + [PS] \rightarrow nC° = [S] + [P][S].K_S \quad [S] = \frac{nC°}{([P].K_S+1)} \quad (19)$$

$$52C° = [Y] + [PY] \rightarrow 52C° = [Y] + [P][Y].K_Y \quad [Y] = \frac{52C°}{([P].K_y+1)} \quad (20)$$

sub eq. (17) , (18) , (19) and (20) in eq. (6)

$$20C° = [P] + [PS] + [PY]$$

$$20C° = [P] + [P]K_S.\frac{nC°}{([P].K_S+1)} + [P]K_Y.\frac{52C°}{([P].K_y+1)} \quad (21)$$

solving this equation give rise to the following cubic equation :

$$a''[P]^3 + b''[P]^2 + c''[P] + d'' = 0 \quad (22)$$

with :

$$a'' = K_sK_y$$

$$b'' = 20C°K_sK_y - K_s - K_y - nC°K_sK_y - 52C°K_sK_y$$

$$c'' = 20C°K_s + 20C°K_y - nC°K_s - 52C°K_y - 1$$

$$d'' = 20C°$$

This cubic equation has to be solved in several steps. First we define variable 'f ' , 'g' and 'h'

$$f = \frac{\left(\frac{3c''}{a''}\right) - \left(\frac{b''^2}{a''^2}\right)}{3} \ ; \qquad g = \frac{\left(\frac{2b''^3}{a''^3}\right) - \left(\frac{9b''c''}{a''^2}\right) + (27\frac{d''}{a''})}{27} \qquad ; \quad h = \frac{g^2}{4} + \frac{f^3}{27}$$

Since h $\leq$ 0 , *all three roots are real and we will proceed as follows*:

$$i = ((g^2\ /4) - h)^{\frac{1}{2}} \qquad ; \quad j = (i)^{\frac{1}{3}} \qquad ; \quad k = arc\ cosine\ (-\left(\frac{g}{2i}\right)$$

$$L = j * -1 \qquad ; \quad M = cosine\ \left(\frac{k}{3}\right) \quad ; \quad N = \sqrt{3} * \sin\left(\frac{k}{3}\right) \quad ; \quad p = (\frac{b''}{3\ a''})$$

The three real roots are calculated as follows:

$x_1 = 2j * M - p$ $\quad x_2 = L * (M + N) + p$ $\quad x_3 = L * (M - N) + p$

only the positive one has been retained. The concentration *[P], [S] and [PS]* are then calculated using equation (7) and (5):

$[S] = \frac{nC^\circ}{1+K_s[P]}$ and $[SP] = nC^\circ - [S]$

Finally, the fraction x and D_{calc} are obtained from equation (15) and (16), respectively. The ratios of plugged pores/capsule correspond to : *n*.(1-x).

II.2 Single Pore POM model

The binding model is similar to that used for the determination of the binding constant with the $\{Mo_{132}\}$ Keplerate ion. Nevetheless, such a model has been slightly adapted for the single pore system, which contains one binding site, one NMe_4^+ ion and twelve potassium ion in competition.

the host-guest process can be expressed simply by equations (23) and (24).

P + Y ⇌ P-Y (2)

P + S ⇌ P-S (3)

$K_Y = \frac{[PY]}{[P][Y]}$ (4)and $K_S = \frac{[PS]}{[P][S]}$ (5)

With P corresponding to the single $\{W_9O_9\}$ pore.

The following equations (25), (26) and (27) correspond to the conservation equations in P, S and Y, respectively.

$C^\circ = [P] + [PS] + [PY]$ (25)

$C^\circ = [S] + [PS]$ (26)

$12C^\circ = [Y] + [PY]$ (27)

In such conditions , the presence of only one pore and whatever the concentration *C*°, the amount of bound substrate PY remains weak and the concentration $[PY]$ can be neglected with respect to the $[Y]$.

From equation (25), (23) and (24)

$C^\circ = [PS] + Ky[Y][P] + \frac{[SP]}{SKs} \longrightarrow C^\circ = [PS] + Ky[12C^\circ]\frac{[SP]}{SKs} + \frac{[SP]}{SKs}$ $\quad X\ SKs$

$C^\circ[S]Ks = [PS][S]Ks + Ky[12C^\circ + 1]\,[PS]$ $\quad with\ [S] = C^\circ - [PS]$

the quadratic equation is then established :

$Ks[PY]^2 - [2C^\circ Ks + 12C^\circ Ky + 1][PS] + C^{\circ 2}Ks = 0$

and the suitable positive square root [PS] as a function of K_y and K_s is established .The fraction x of the free substrate is given by equation (28) :

$$x = \frac{[S]}{[S]+[SP]} \quad (28)$$

allowing to the calculate self-diffusion coefficient $D_{calc.}$

$$D_{calc} = xD^0 + (1-x)D^{\infty} \quad (16)$$

Chapter III Appendix

Synthesis, Characterizations and Applications of Surfactant Encapsulated Keplerate Clusters.

I. FT-IR Characterizaiton

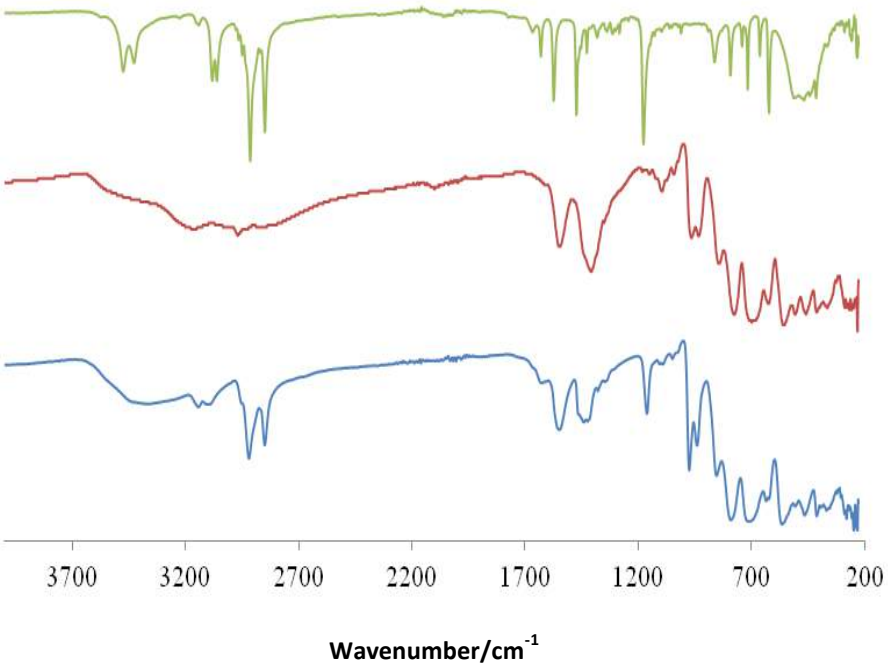

Figure A3.1. FT-IR spectra of($mimC_{14}Br$)(green),$(NH_4)_{52}\{Mo_{132}\}$ (red) and $(mimC_{14})_{36}$-$\{Mo_{132}\}$(blue)

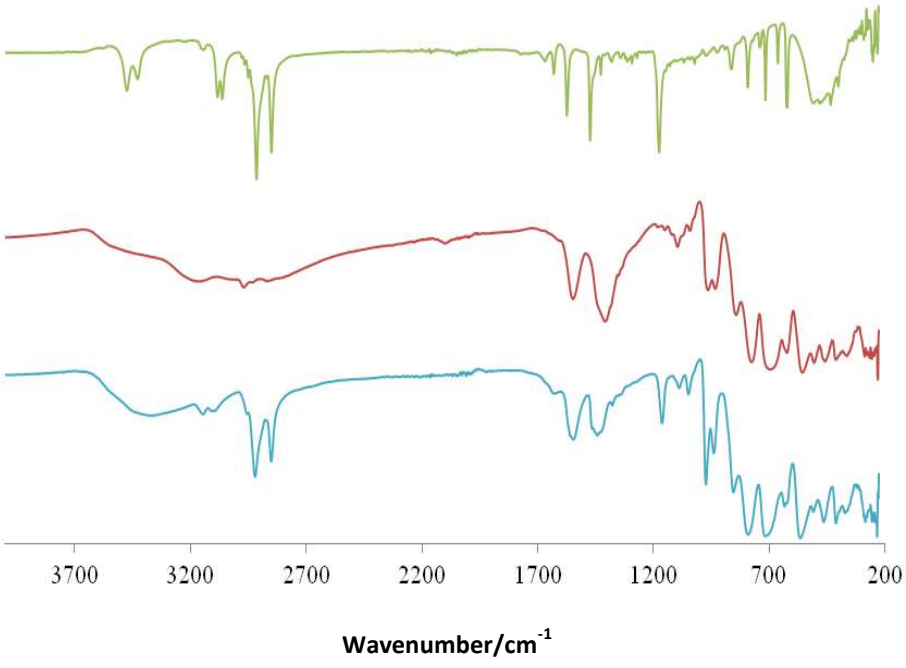

Figure A3.2. FT-IR spectra of($mimC_{16}Br$)(green),$(NH_4)_{52}\{Mo_{132}\}$ (red) and $(mimC_{16})_{41}$-$\{Mo_{132}\}$(blue)

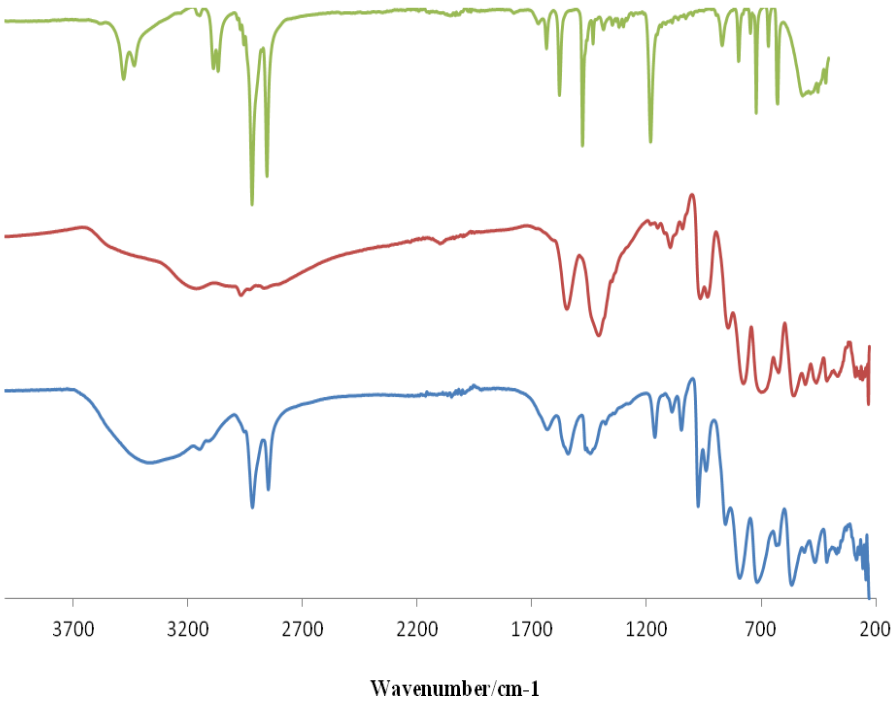

Figure A3.3. FT-IR spectra of($mimC_{20}Br$)(green),$(NH_4)_{52}\{Mo_{132}\}$ (red) and $(mimC_{20})_{37}$-$\{Mo_{132}\}$(blue)

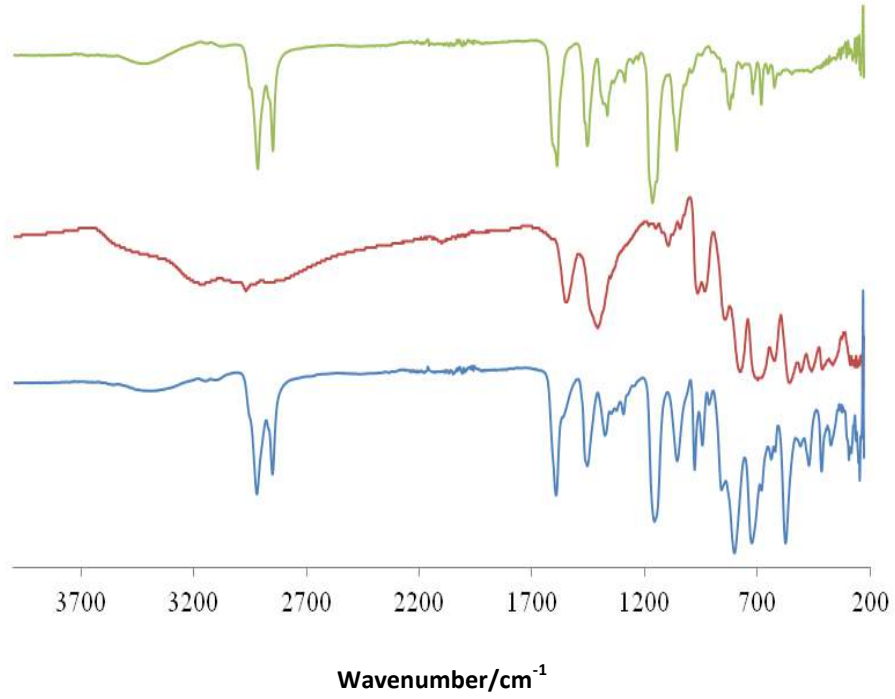

Figure A3.4. FT-IR spectra of(Dendron)(green),$(NH_4)_{52}\{Mo_{132}\}$ (red) and $(Dendron)_{37}$-$\{Mo_{132}\}$(blue)

II. TGA Curves

Water content and thermal stability were determined by thermal gravimetric analysis with a Seiko TG/DTA 320 thermogravimetric balance (5°C min^{-1}, **under O_2**).

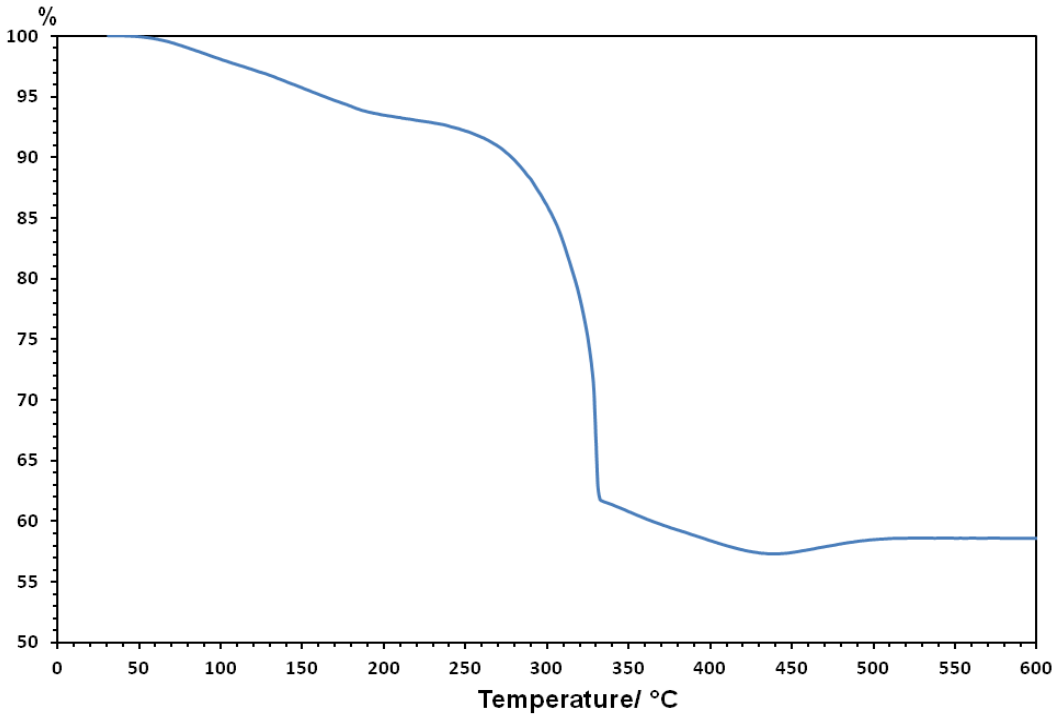

Figure A3.5. TGA curve of $(mimC_{12})_{36}\{Mo_{132}\}$under air.

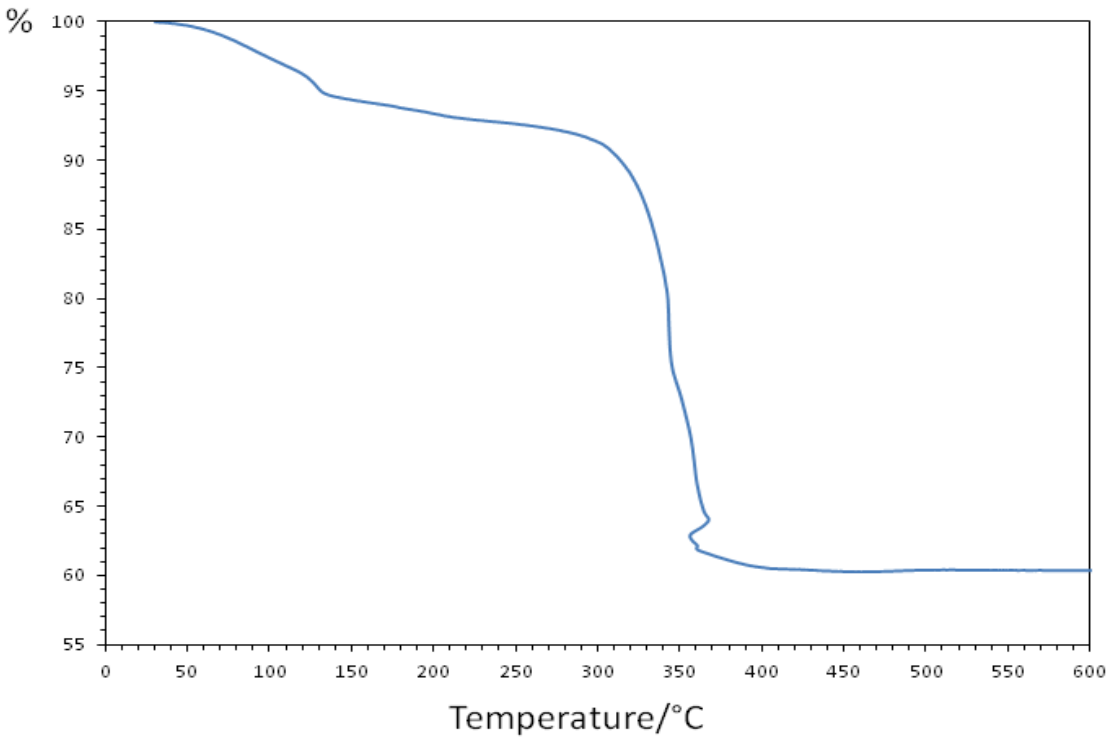

Figure A3.6. TGA curve of $(mimC_{14})_{36}\{Mo_{132}\}$under air.

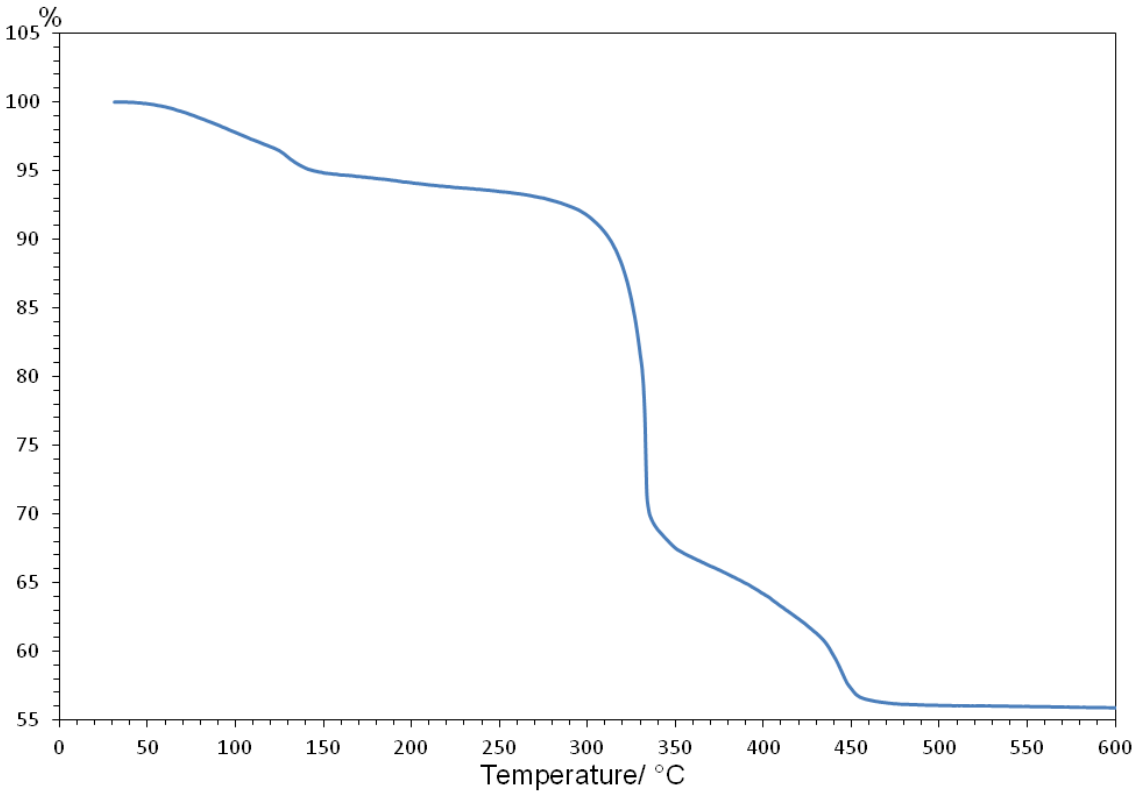

Figure A3.7. TGA curve of $(mimC_{20})_{37}\{Mo_{132}\}$under air.

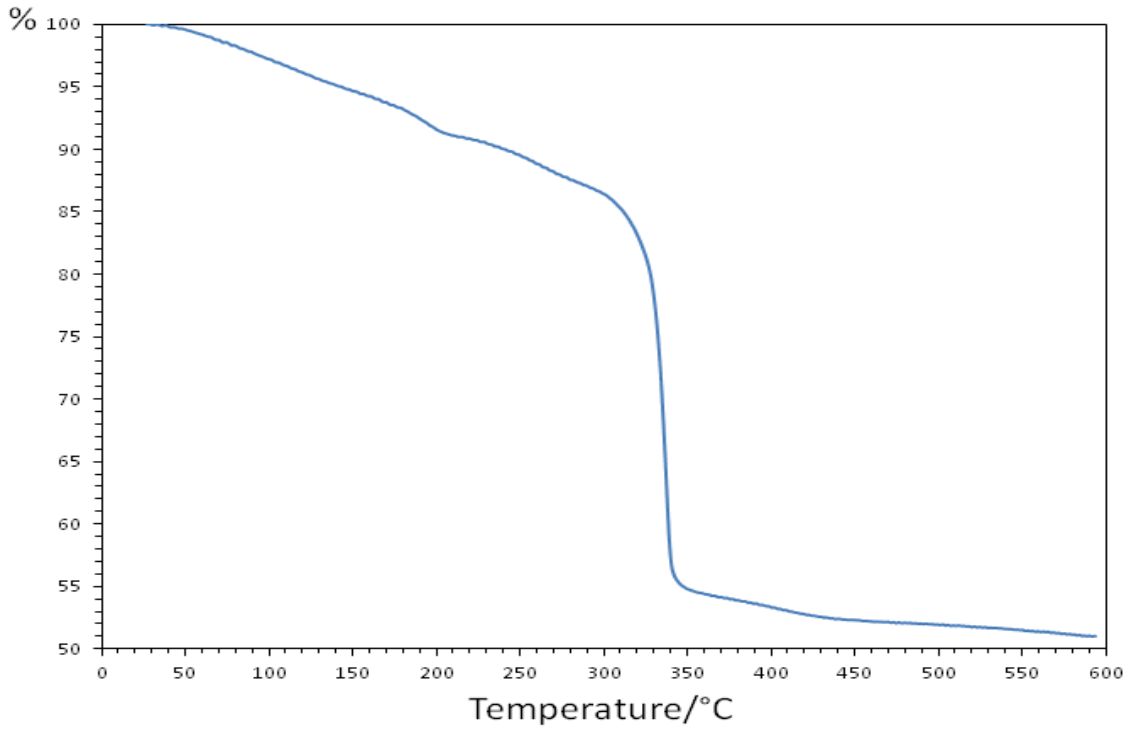

Figure A3.8. TGA curve of $(mimC_{12})_{20}(mimC_{20})_{20}\{Mo_{132}\}$under air.

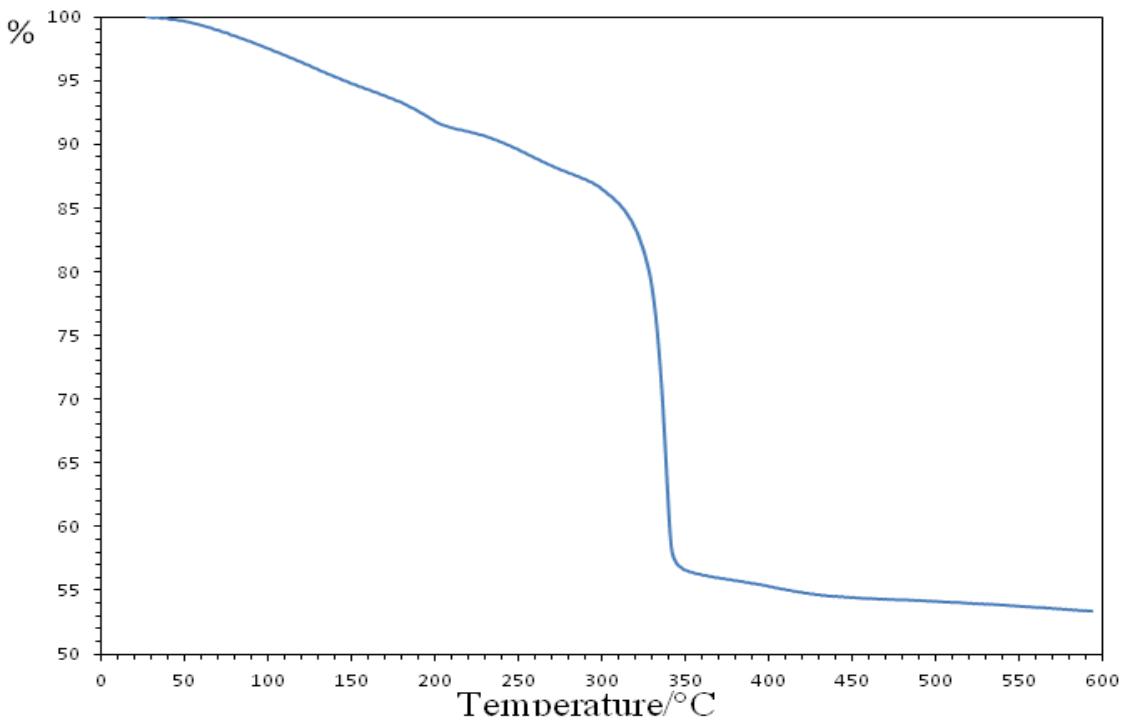

Figure A3.9. TGA curve of $(mimC_{12})_{33}(mimC_{20})_{7}\{Mo_{132}\}$under air.

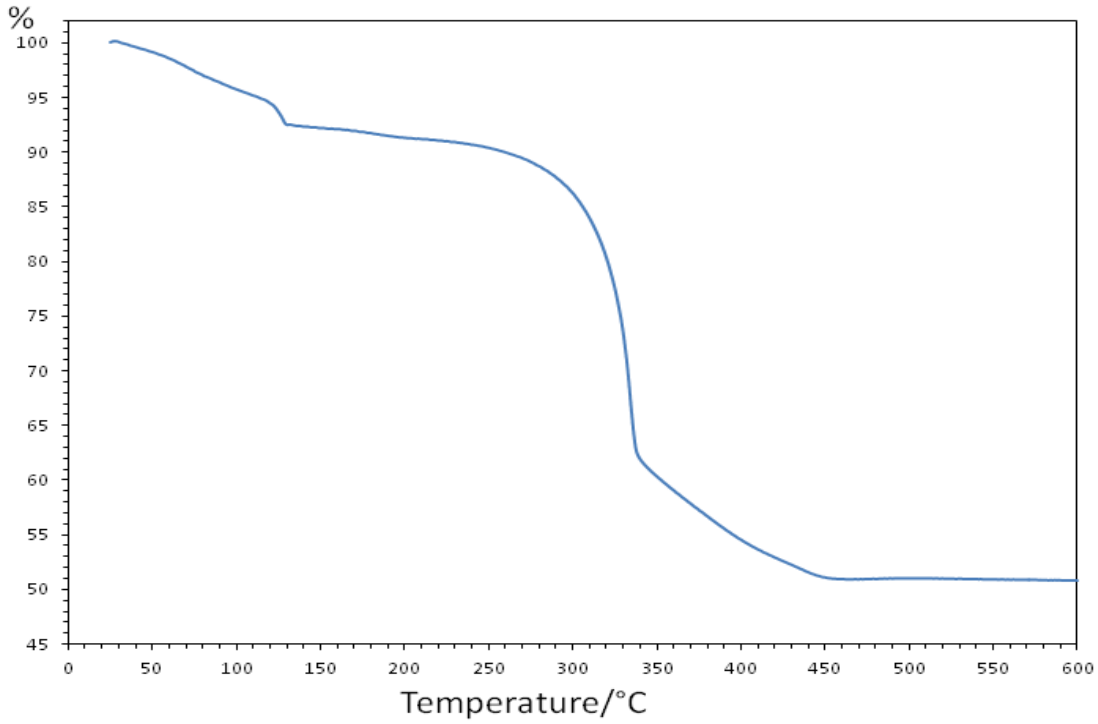

Figure A3.10. TGA curve of $(mimC_{12})_{8}(mimC_{20})_{33}\{Mo_{132}\}$under air.

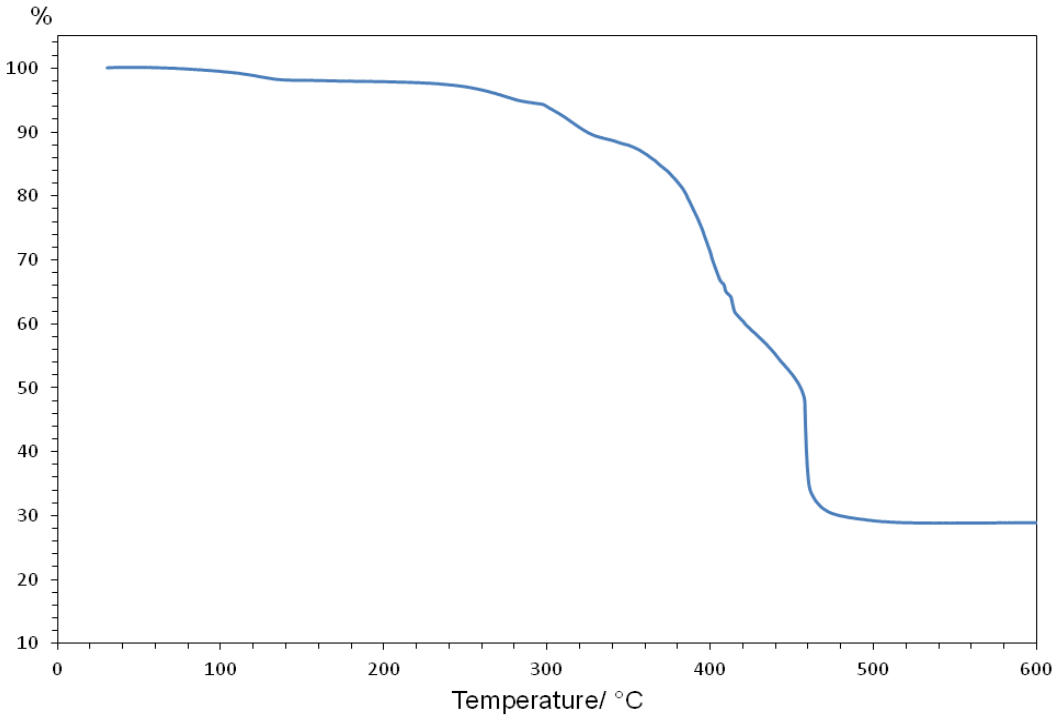

Figure A3.11. TGA curve of $(Dendron)_{36}\{Mo_{132}\}$ under air.

III. DSC curves

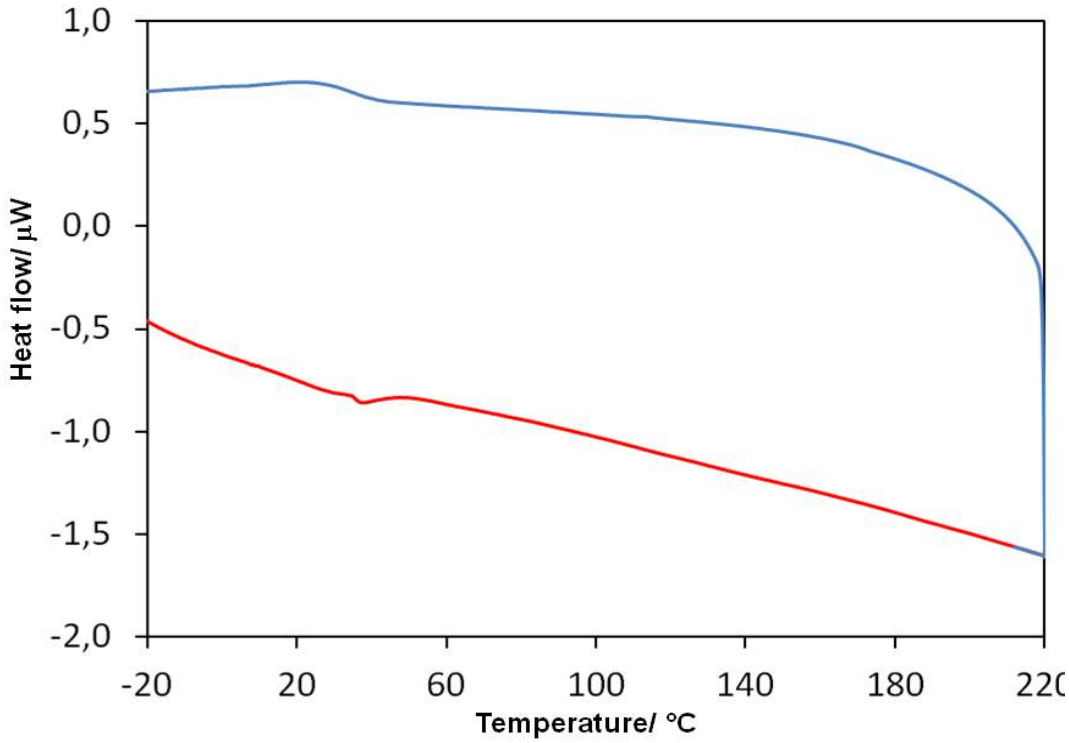

Figure A3.11. DSC Traces of the second thermal cycle recorded under N_2 for $(mimC_{12})_{20}(mimC_{20})_{20}\{Mo_{132}$; second heating cycle (red), second cooling cycle (blue).

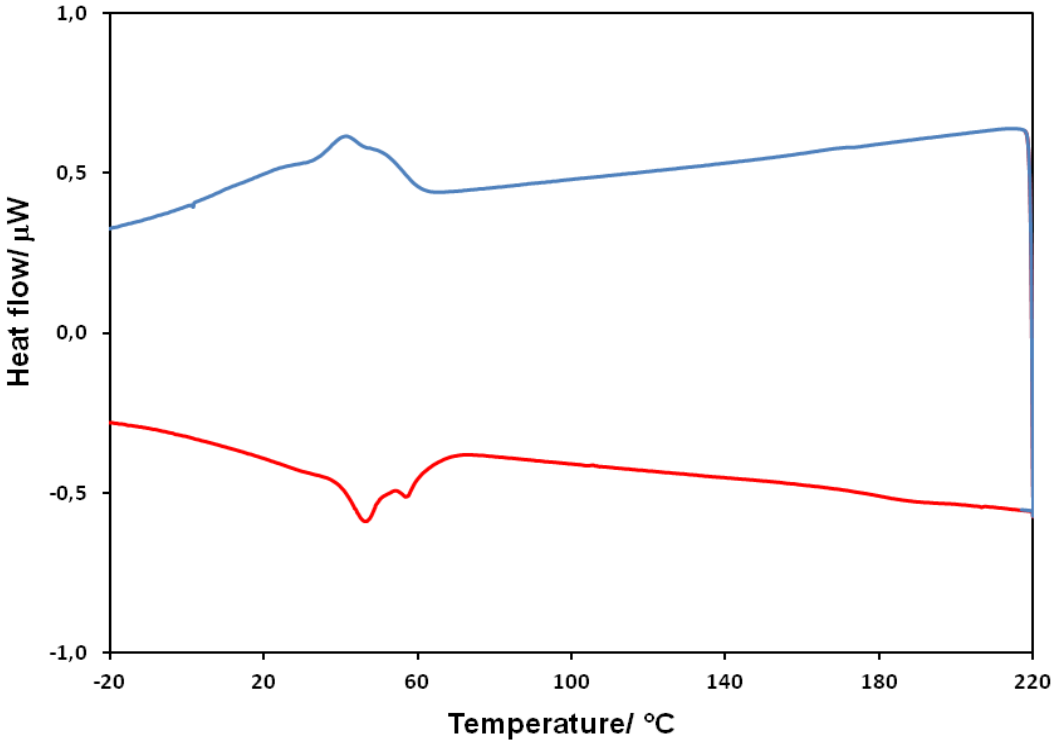

Figure A3.12. DSC Traces of the second thermal cycle recorded under N_2 for $(mimC_{12})_8(mimC_{20})_{33}\{Mo_{132}$; second heating cycle (red), second cooling cycle (blue).

Chapter IV Appendix

Synthesis, characterization, and tuning of the liquid crystal properties of ionic materials based on the cyclic polyoxothiometalate[$\{Mo_4O_4S_4(H_2O)_3(OH)_2\}_2(P_8W_{48}O_{184})]^{36-}$.

I. FT-IR Characterization

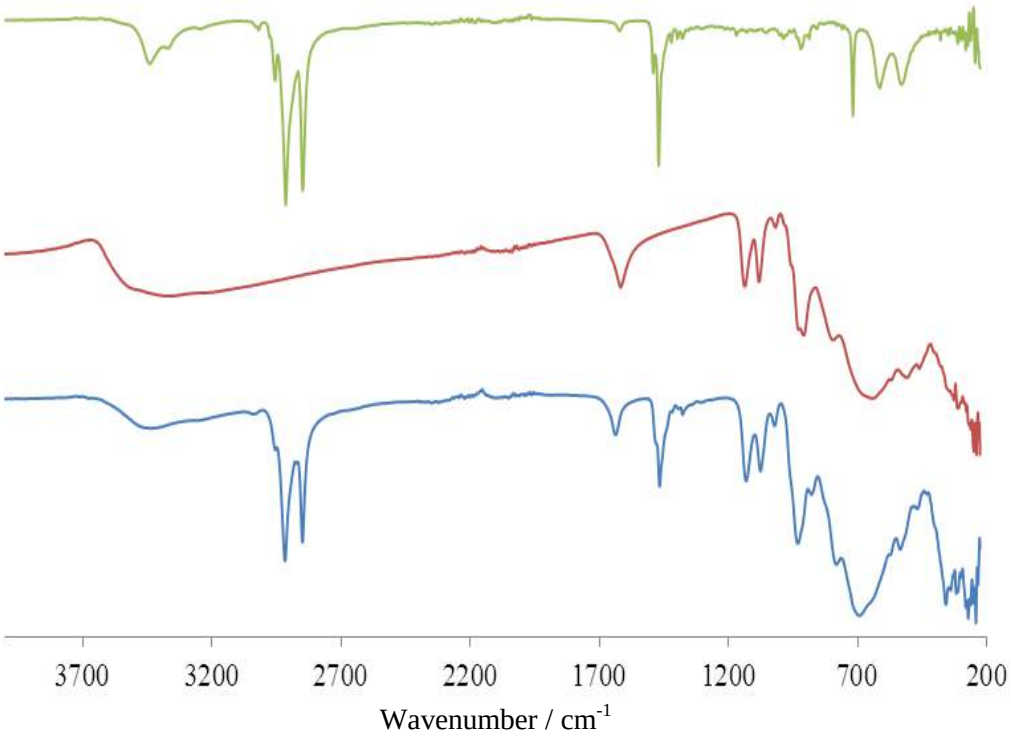

Figure A4.1. FT-IR spectra of DODACl (green), **NaK-1** (red) and **$DODA_{19}$-1** (blue)

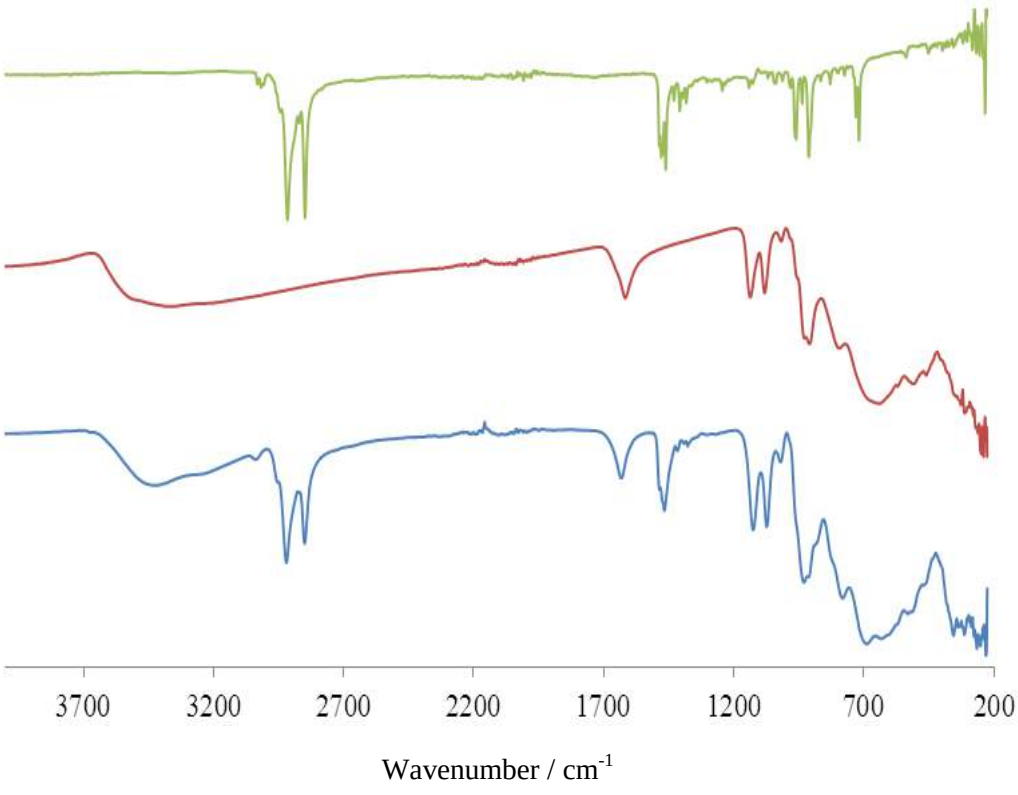

Figure A4.2. FT-IR spectra of $TMAC_{16}Cl$(green), **NaK-1** (red) and **$(TMAC_{16})_{18}$-1 (blue)**

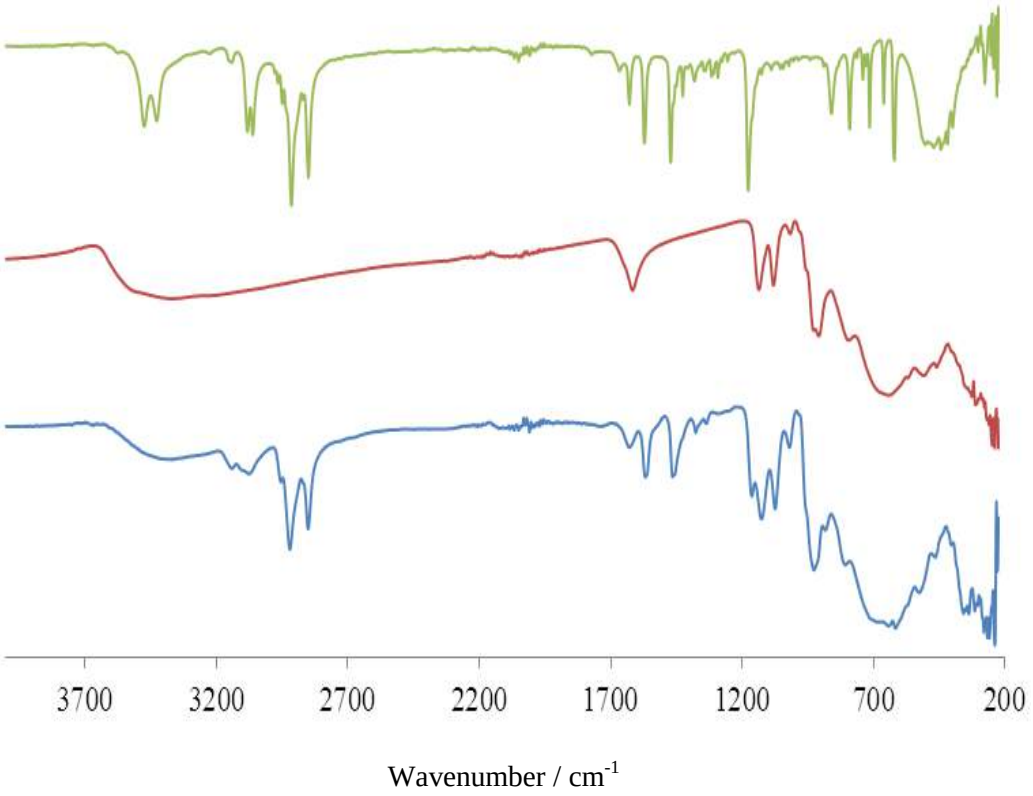

Figure A4.3. FT-IR spectra of $mimC_{12}Br$ (green), **NaK-1** (red) and **$(mimC_{12})_{25}$-1** (blue)

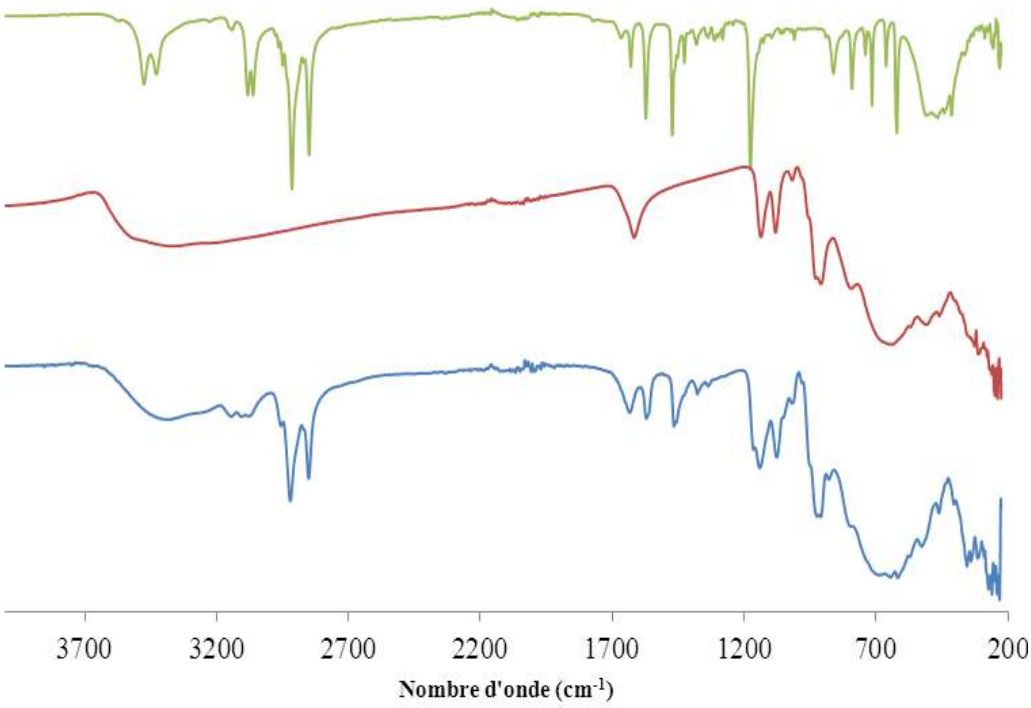

Figure A4.4. FT-IR spectra of $mimC_{14}Br$ (green), **NaK-1** (red) and **$(mimC_{14})_{26}$-1** (blue)

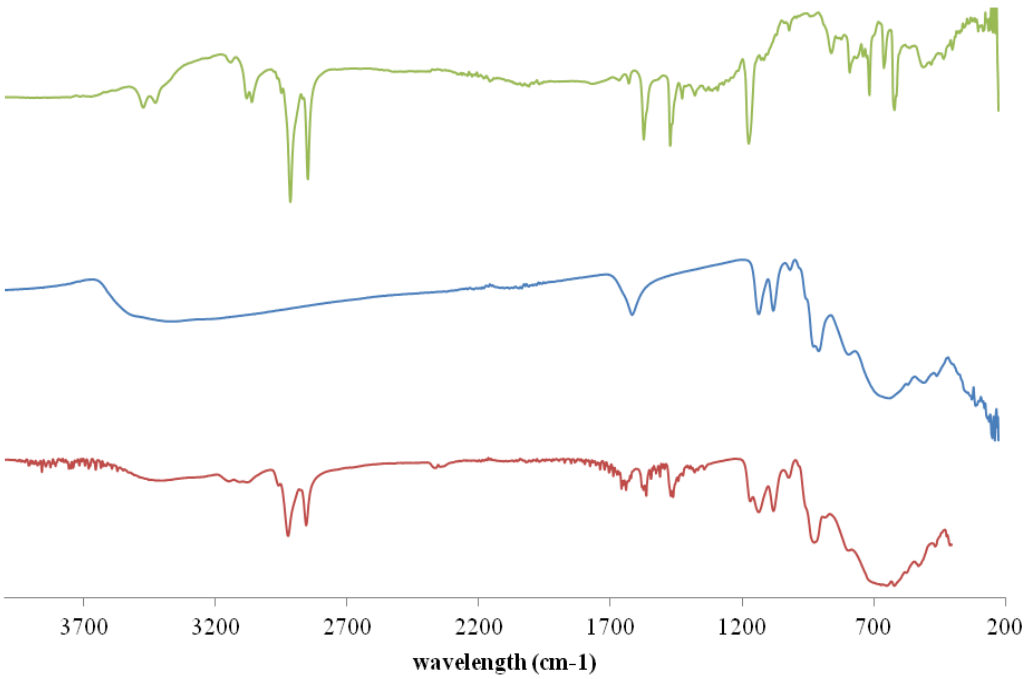

Figure A4.5. FT-IR spectra of mimC_{16}Br (green), **NaK-1** (red) and **(mimC_{16})$_{23}$-1** (blue)

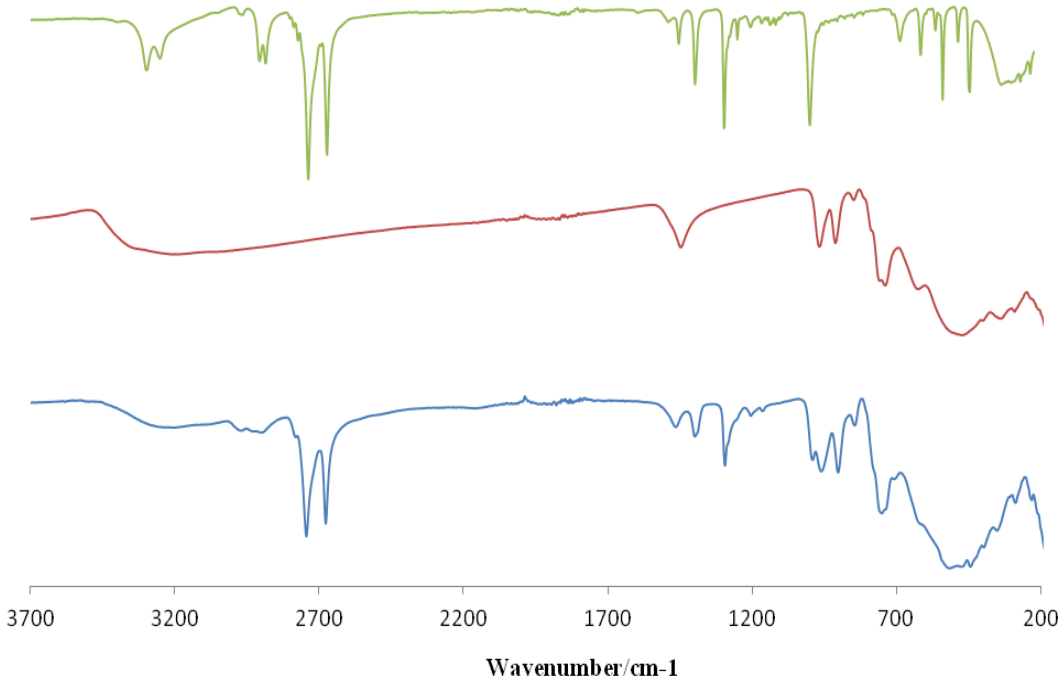

Figure A4.6. FT-IR spectra of mimC_{20}Br (green), **NaK-1** (red) and **(mimC_{20})$_{24}$-1** (blue)

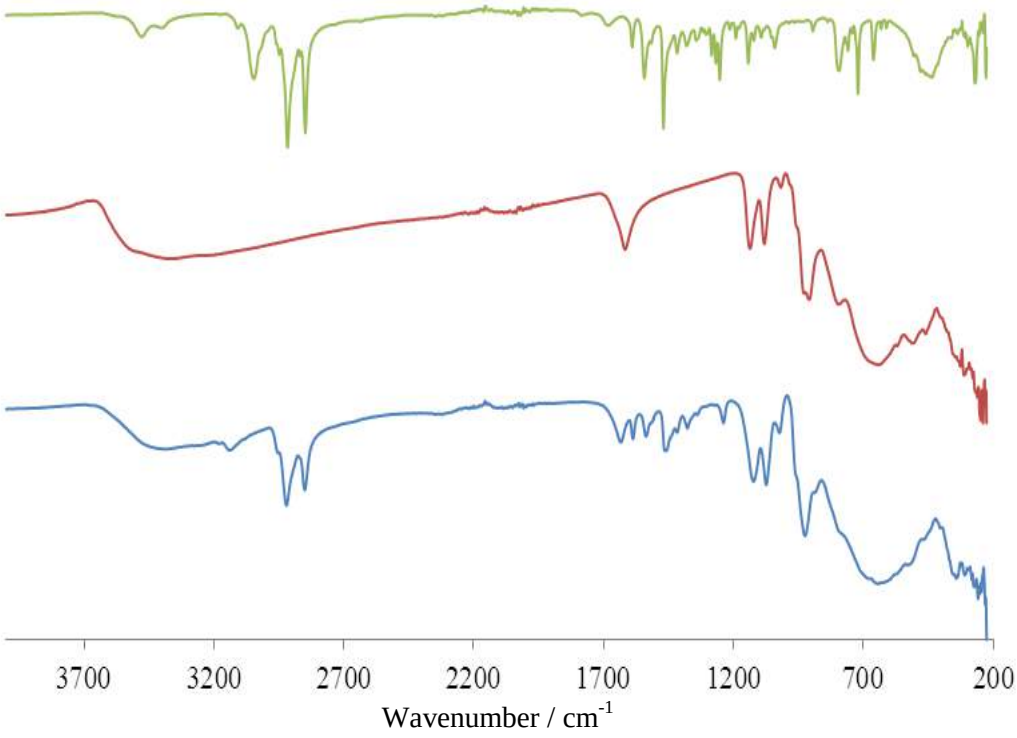

Figure A4.7. FT-IR spectra of dmimC_{12}Br (green), **NaK-1** (red) and **(dmimC_{12})$_{18}$-1** (blue)

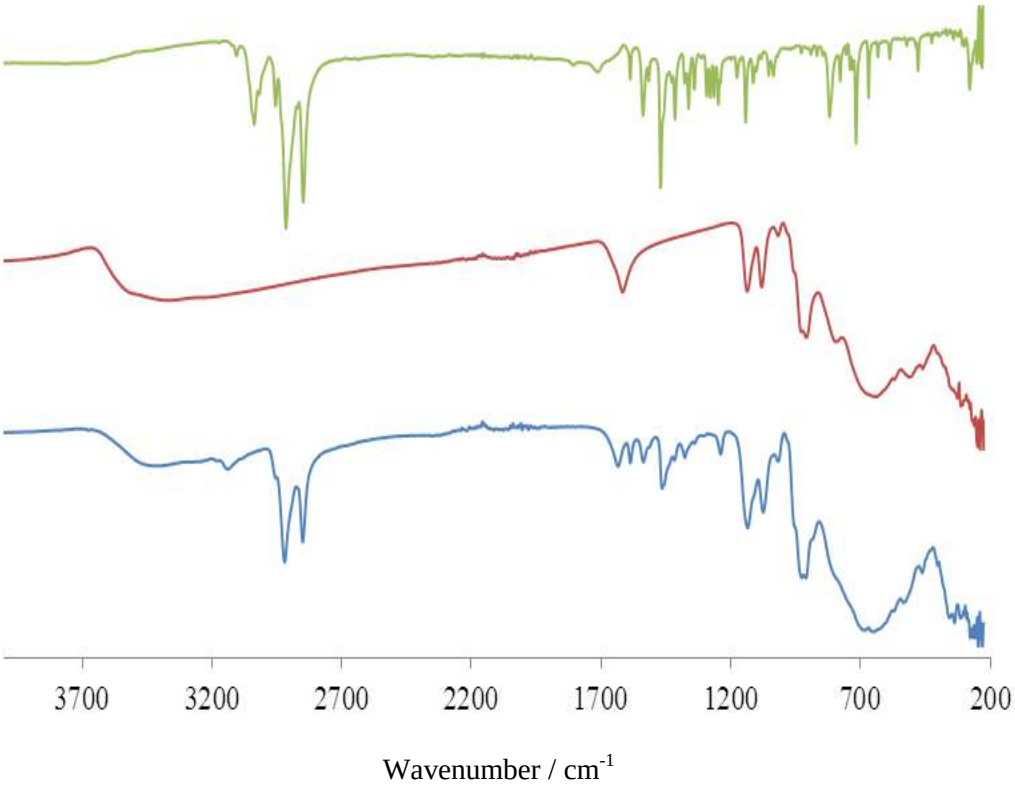

Figure A4.8. FT-IR spectra of dmimC_{16}Br (green), **NaK-1** (red) and **(dmimC_{16})$_{20}$-1** (blue)

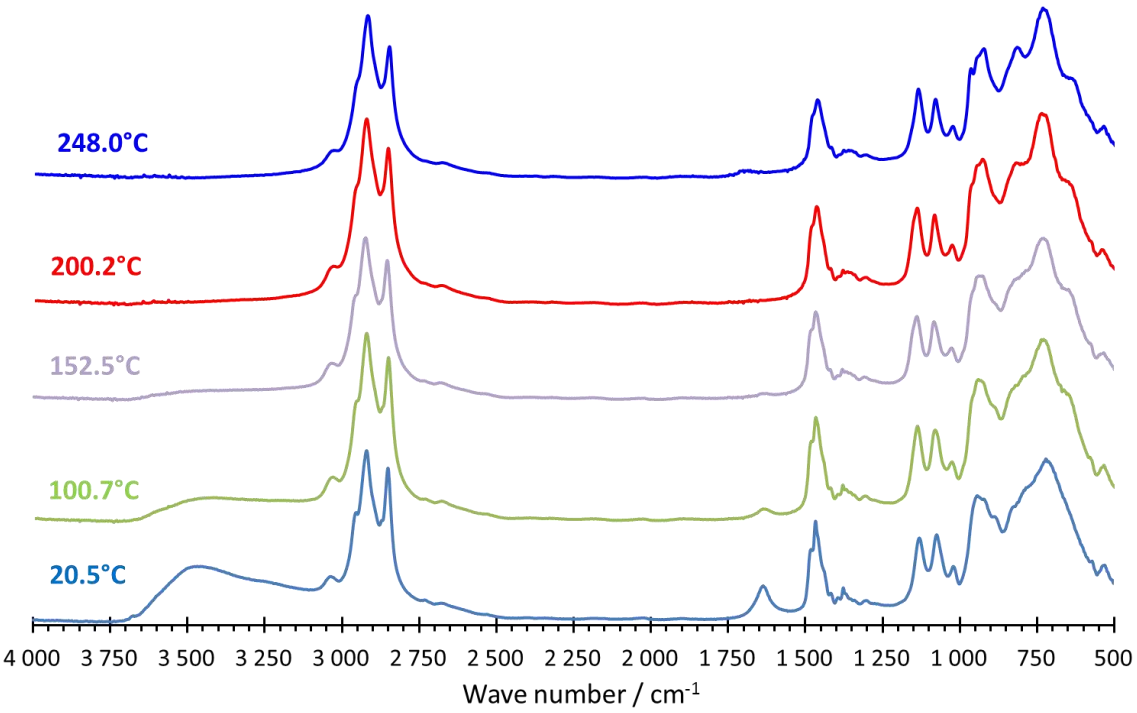

Figure A4.9. Selected FT-IR spectra recorded at various temperatures for compound **$DODA_{19}$-1** in air.

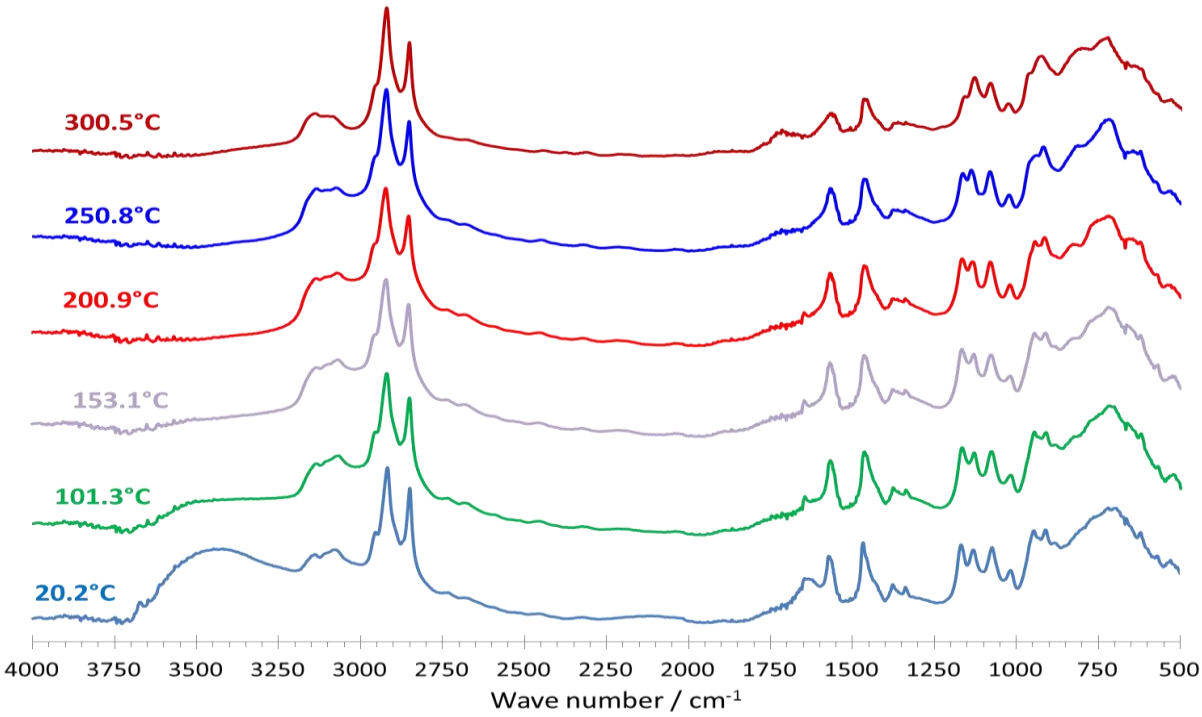

Figure A4.10 Selected FT-IR spectra recorded at various temperatures for compound **$(mimC_{16})_{23}$-1** in air.

II. TGA

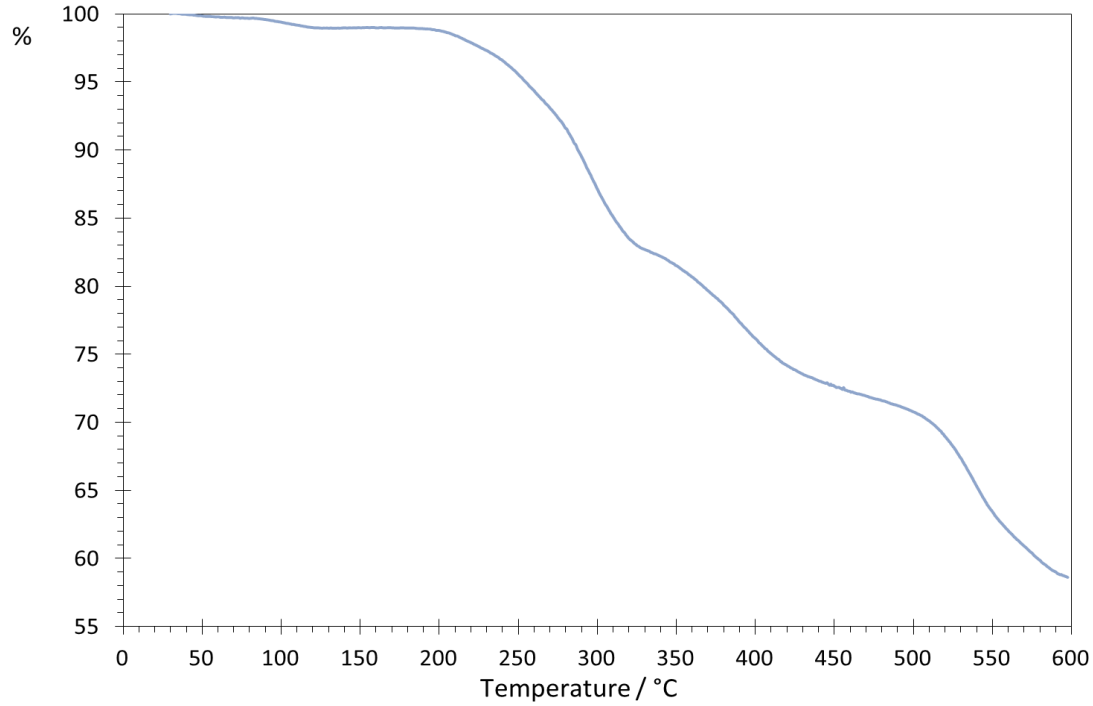

Figure A4.11. TGA curve of **$DODA_{19}$-1** under O_2.

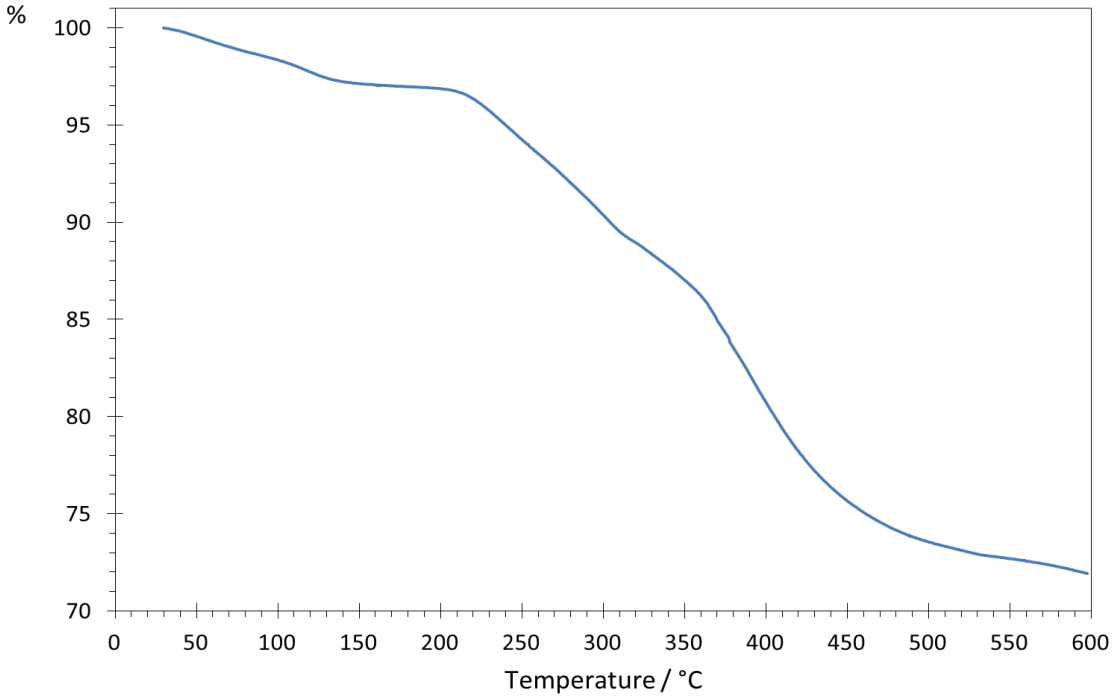

Figure A4.12. TGA curve of **$(TMAC_{16})_{18}$-1** under O_2.

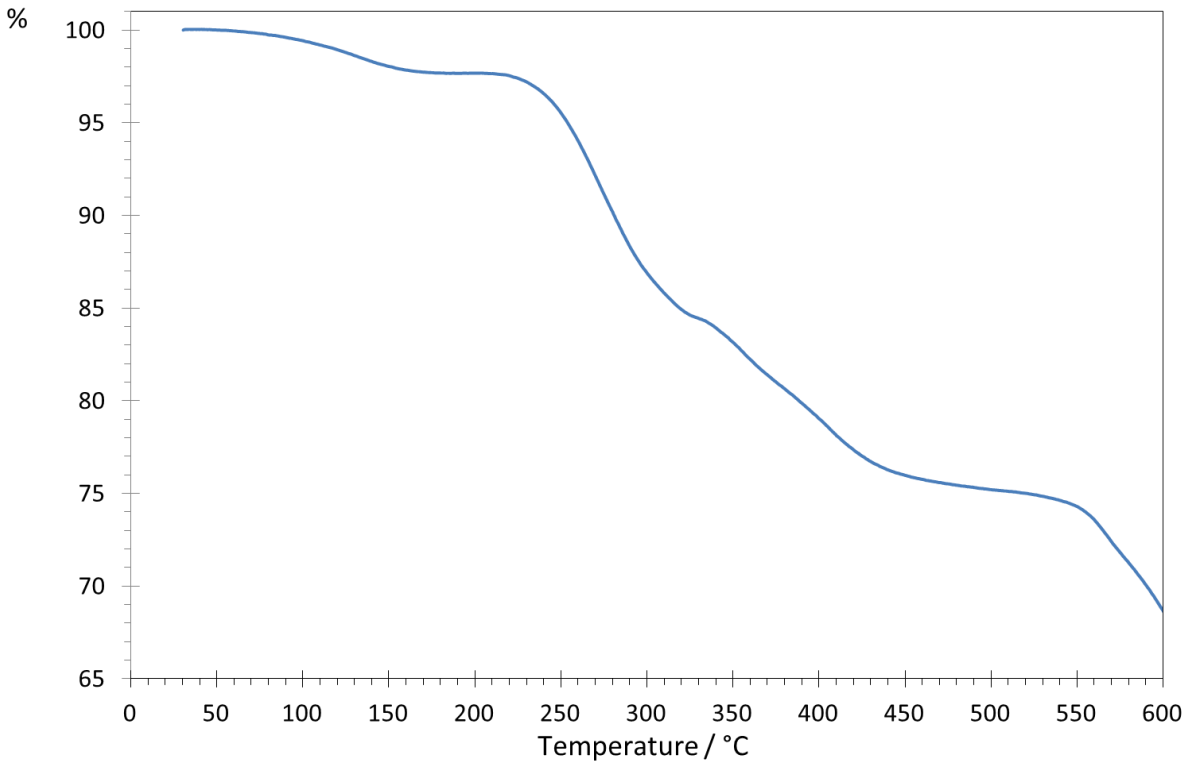

Figure A4.13. TGA curve of **(mimC$_{12}$)$_{25}$-1** under O_2.

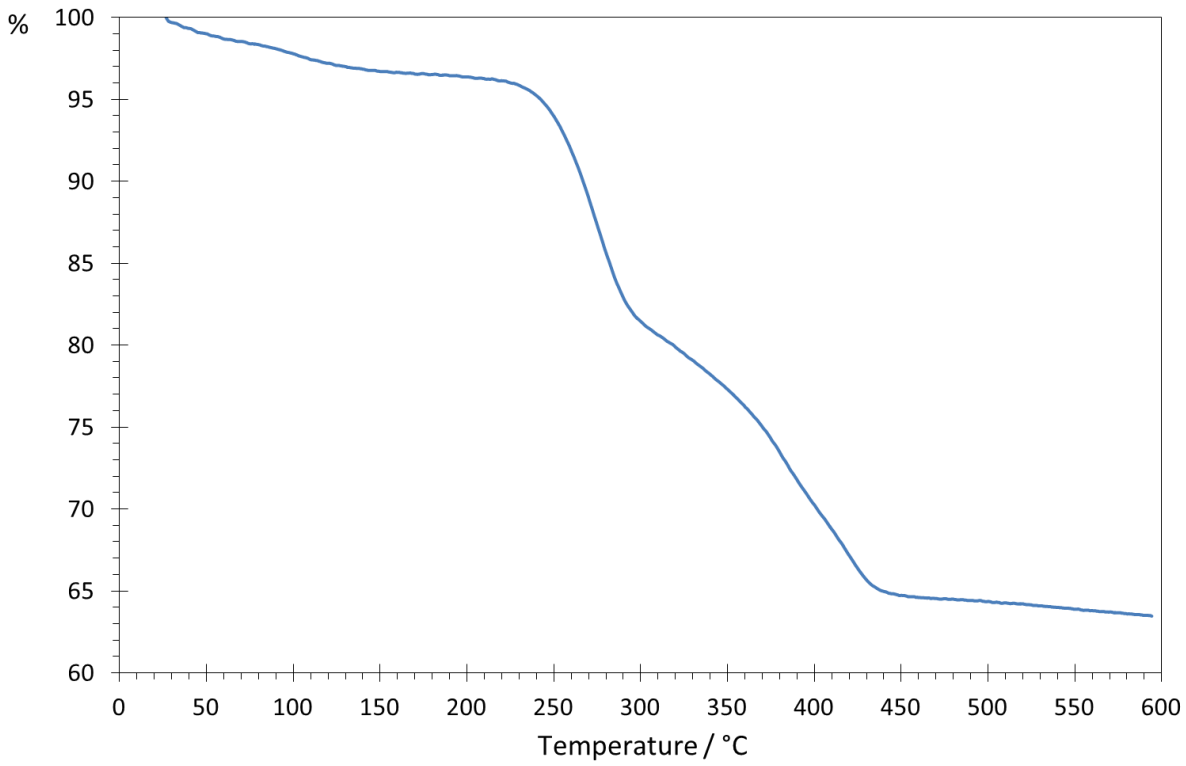

Figure A4.14. TGA curve of **(mimC$_{14}$)$_{26}$-1** under O_2.

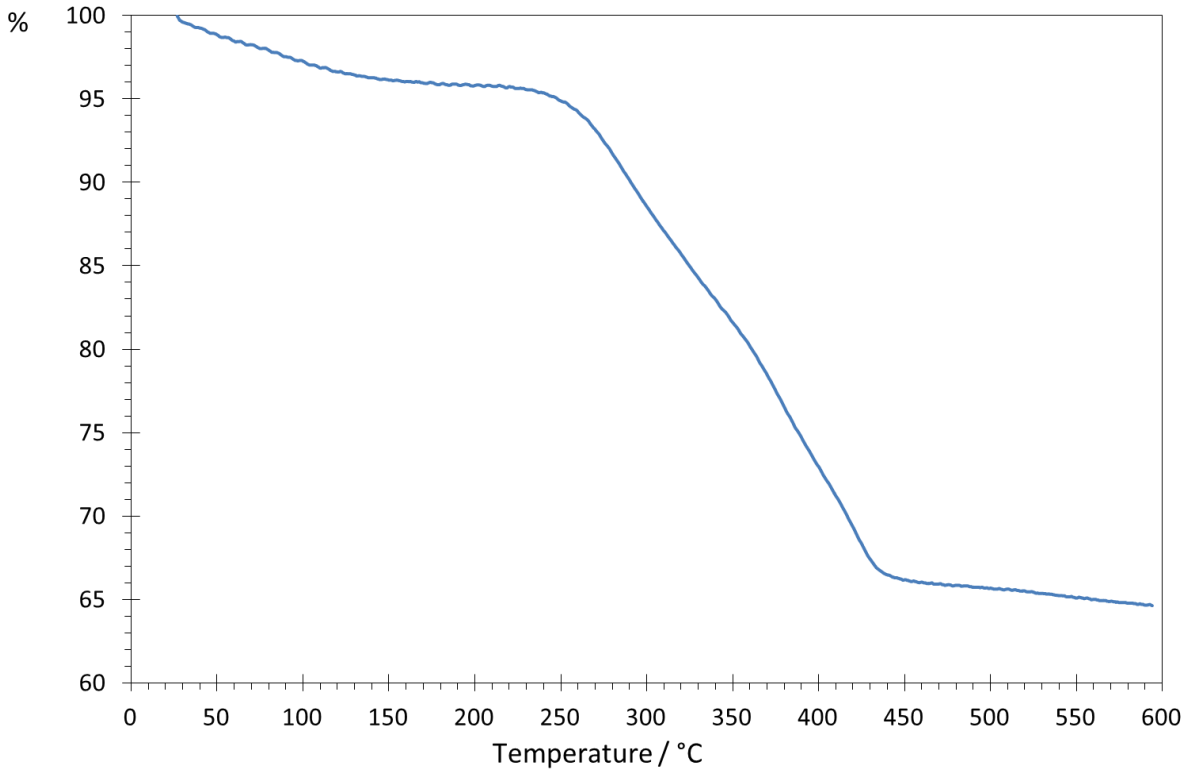

Figure A4.15. TGA curve of **$(mimC_{16})_{23}$-1** under O_2**.**

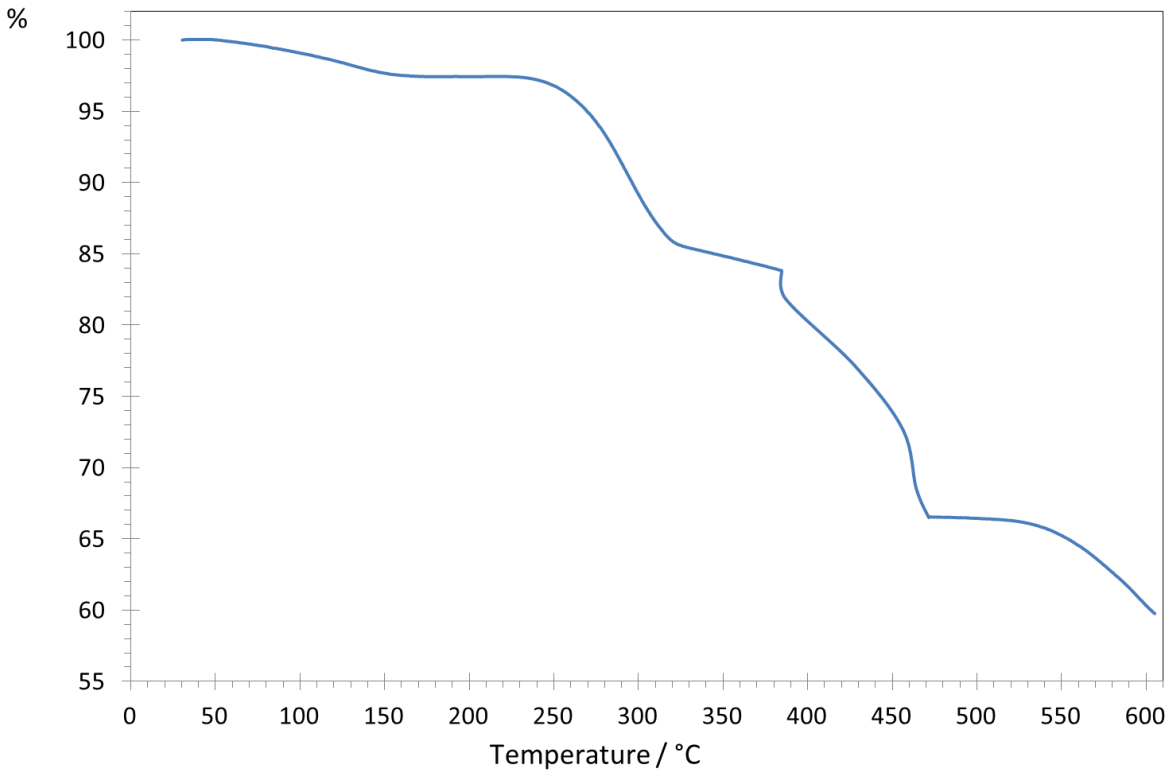

Figure A.4.16. TGA curve of **$(mimC_{18})_{24}$-1** under O_2**.**

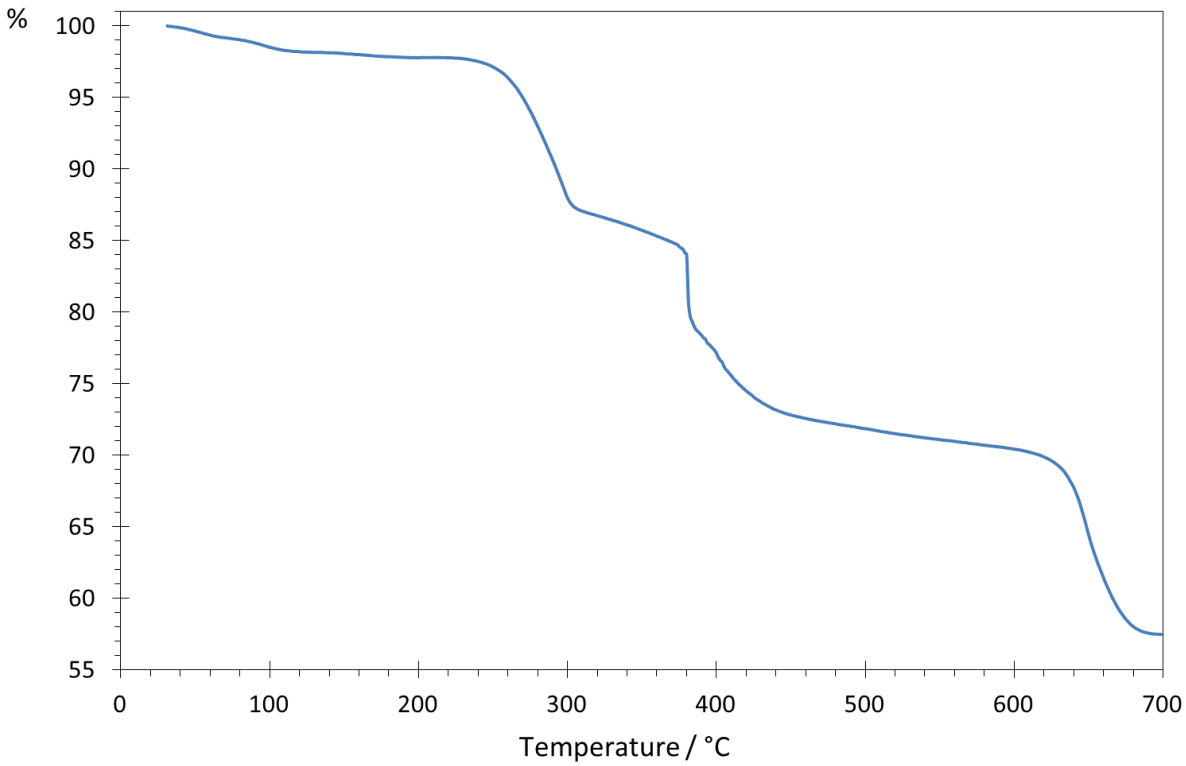

Figure A4.17. TGA curve of **(mimC_{20})$_{24}$-1** under O_2.

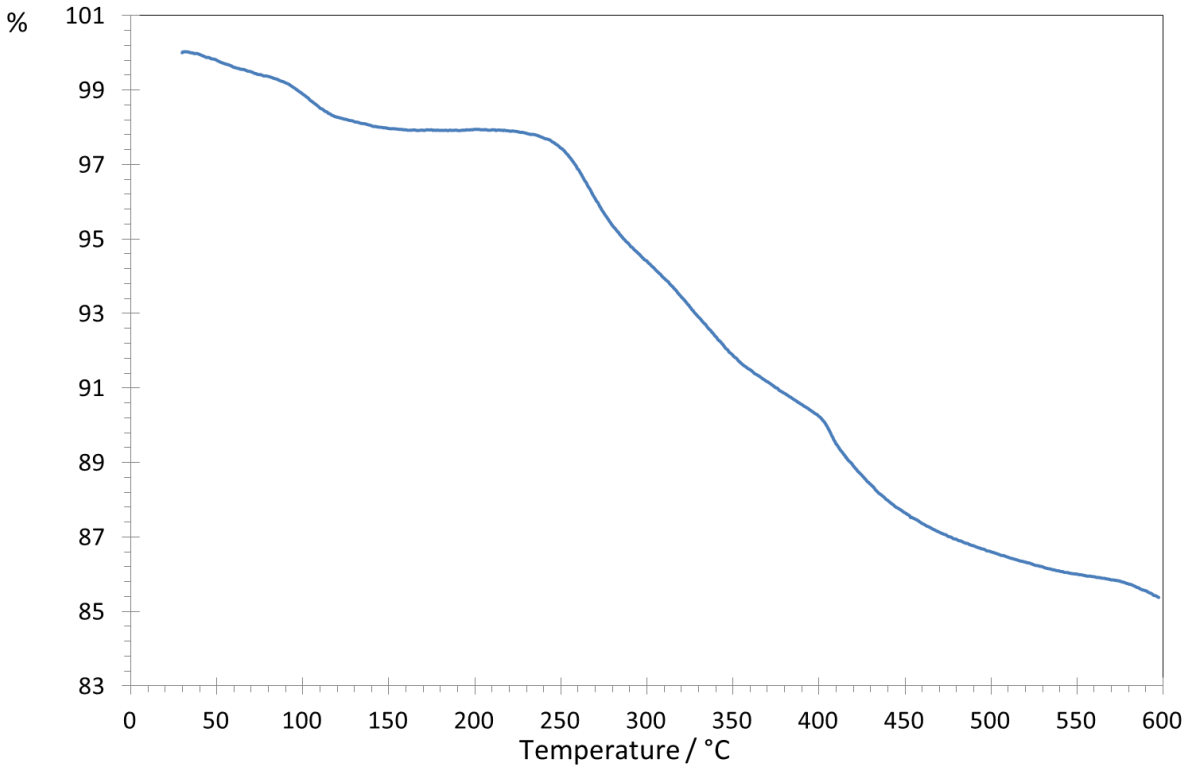

Figure A4.18. TGA curve of (dmimC_{12})$_{18}$-1 under O_2.

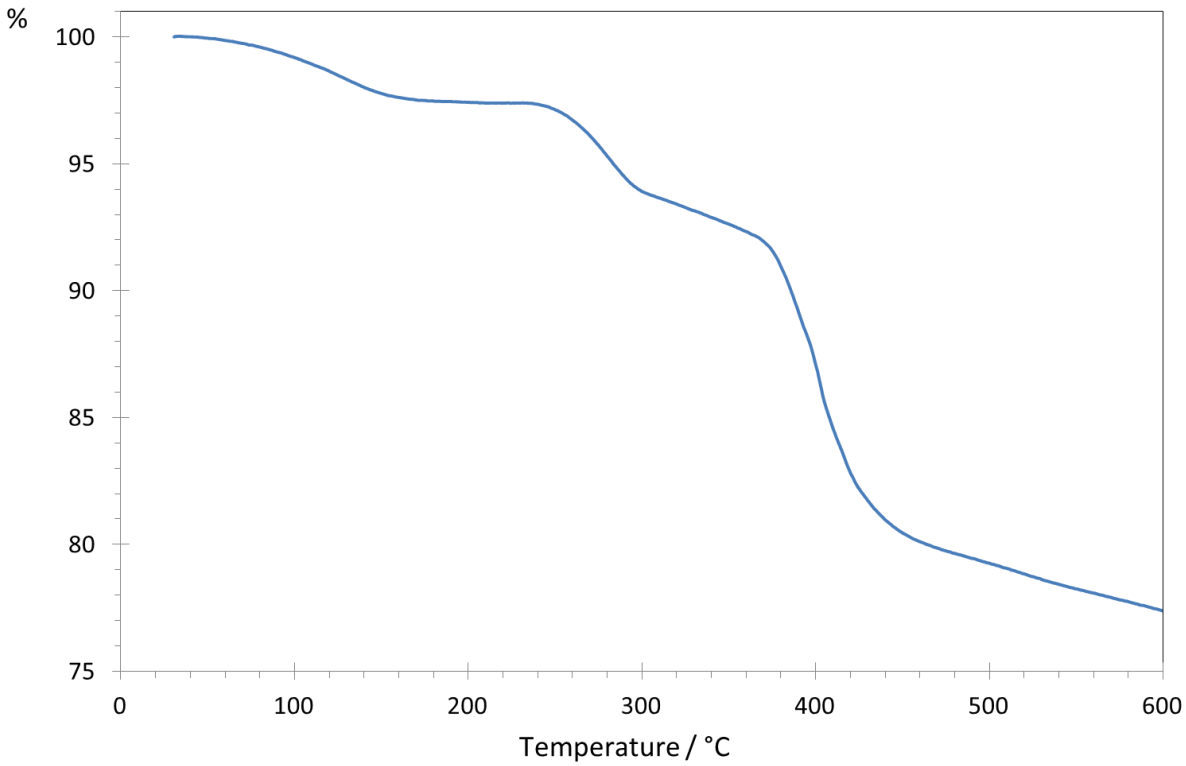

Figure A4.19. TGA curve of $(dmimC_{16})_{20}$-1 under O_2**.**

III. ^{1}H NMR studies in solution

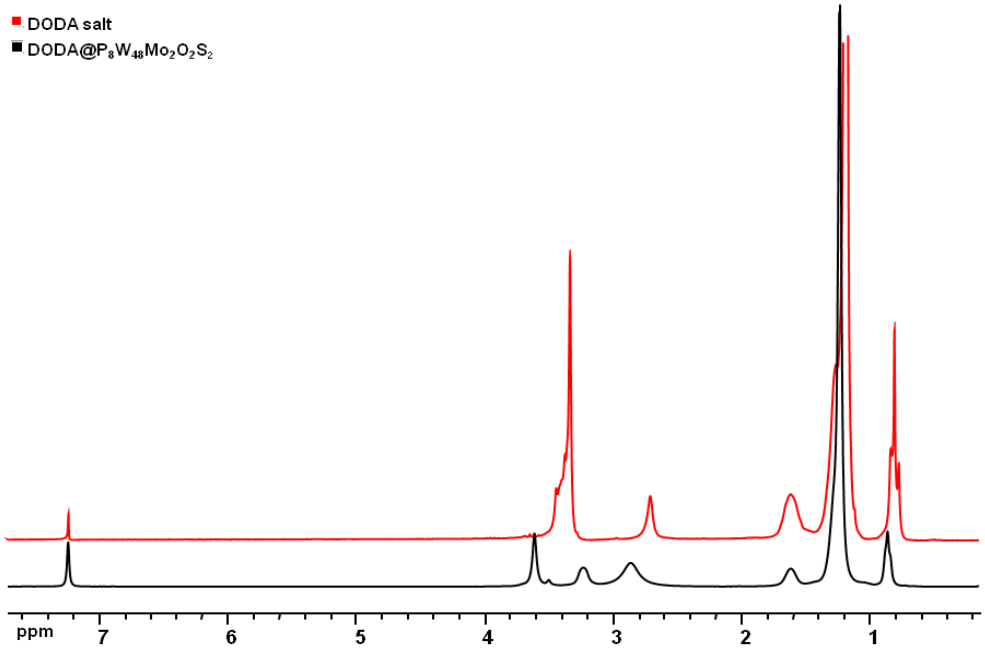

Figure A4.20. ^{1}H NMR spectra of DODACl (red) and $DODA_{19}$-1 (black) in $CDCl_3$.

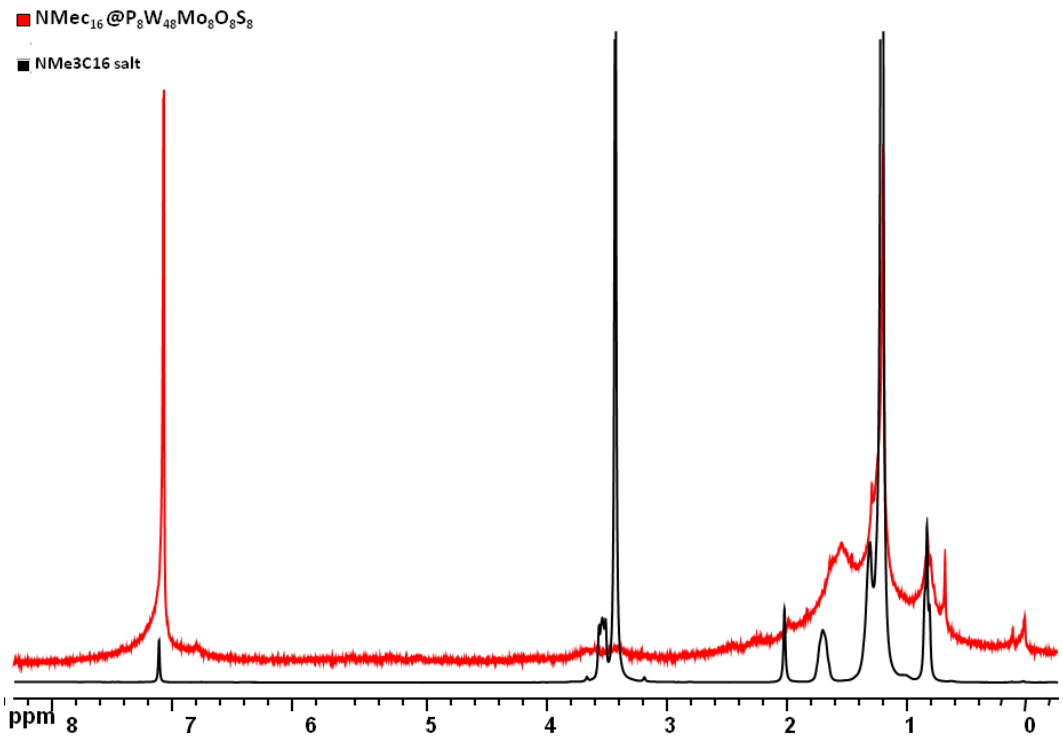

Figure A4.21. ^{1}H NMR spectra of $TMAC_{16}Cl$ (black) and **$(TMAC_{16})_{18}$-1** (red) in $CDCl_3$.

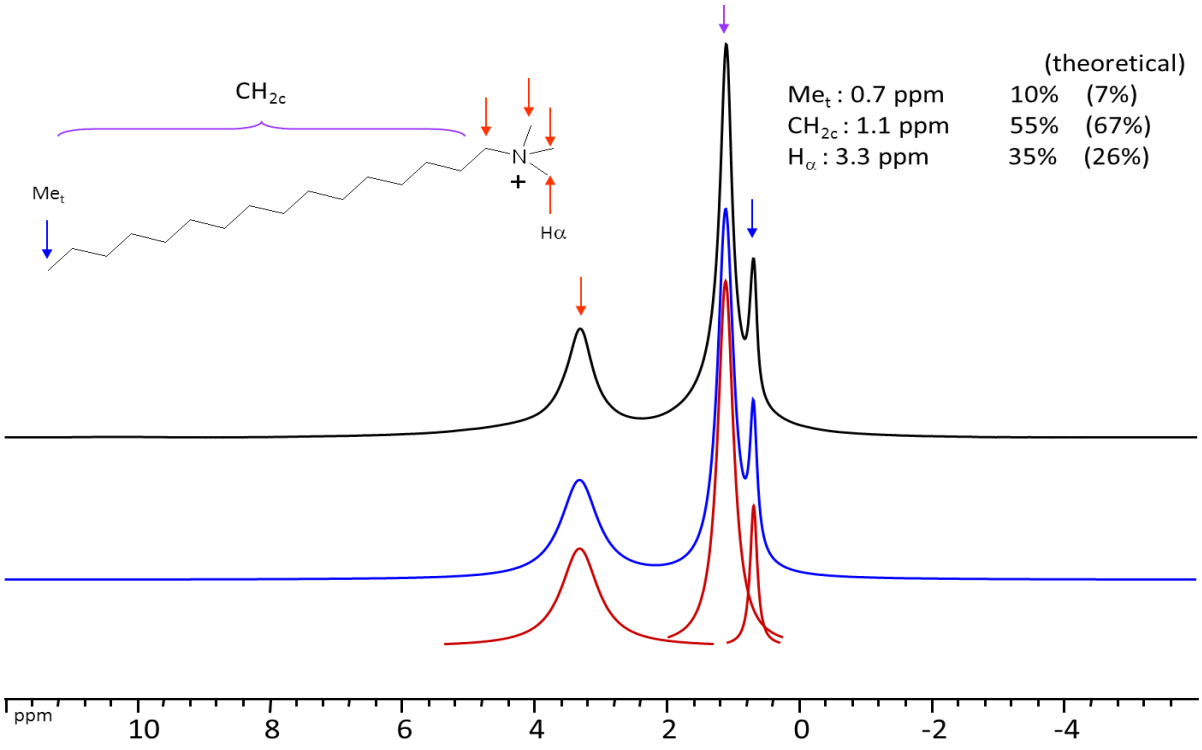

Figure A4.22. ^{1}H MAS (500.13 MHz, 20 kHz) NMR spectrum of **$(TMAC_{16})_{18}$-1**. Experimental spectrum in black, deconvolved spectra in red and complete simulated spectrum in blue.

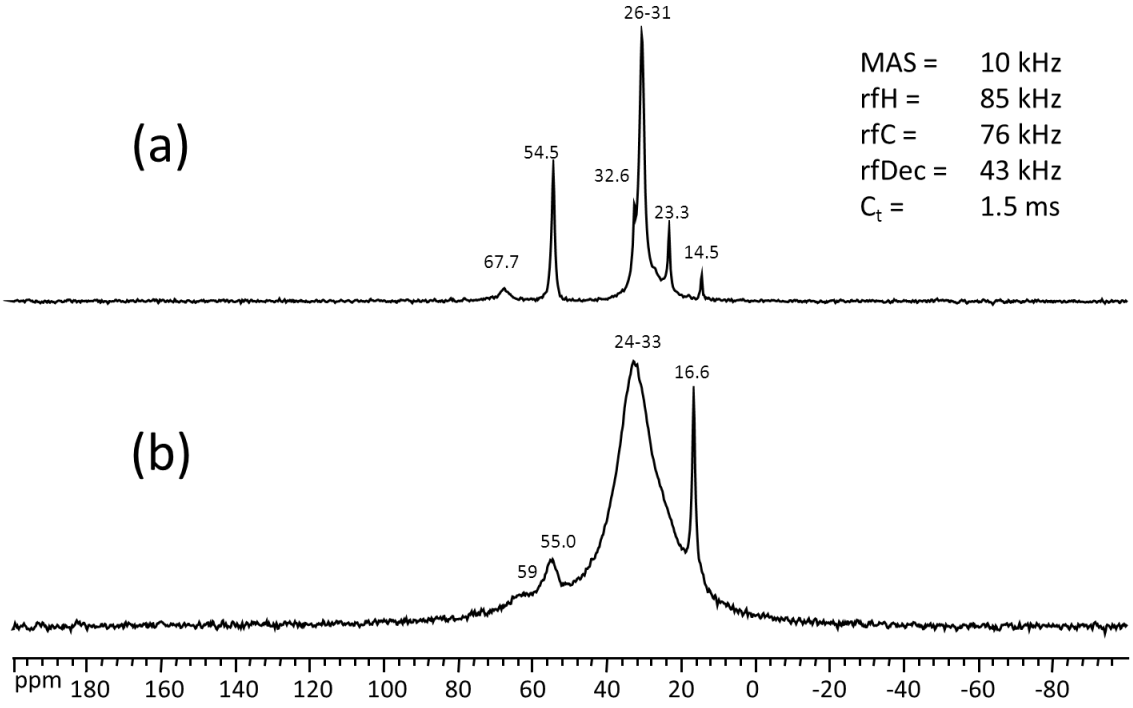

Figure A4.23. ^{13}C CPMAS NMR spectra of **$(TMAC_{16})_{18}$-1** (a) and **$TMAC_{16}Cl$** (b).

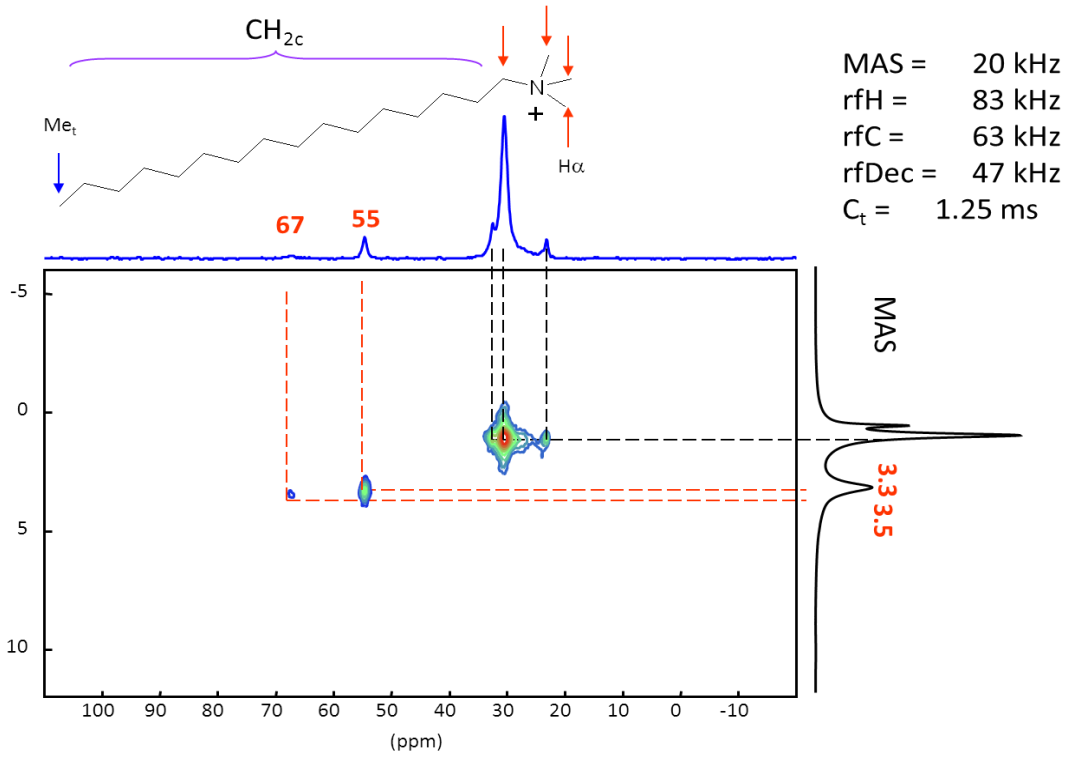

Figure A4.24. $^{13}C\{^{1}H\}$ HETCOR CPMAS NMR spectrum of **$(TMAC_{16})_{18}$-1**. The ^{13}C NMR signals at 67 and 55 ppm are assigned to the $-CH_2-$ and the three CH_3 groups attached to the ammonium head, respectively. These correlations confirm that the ^{1}H NMR lines at 3.3-3.5 ppm belong to these groups.

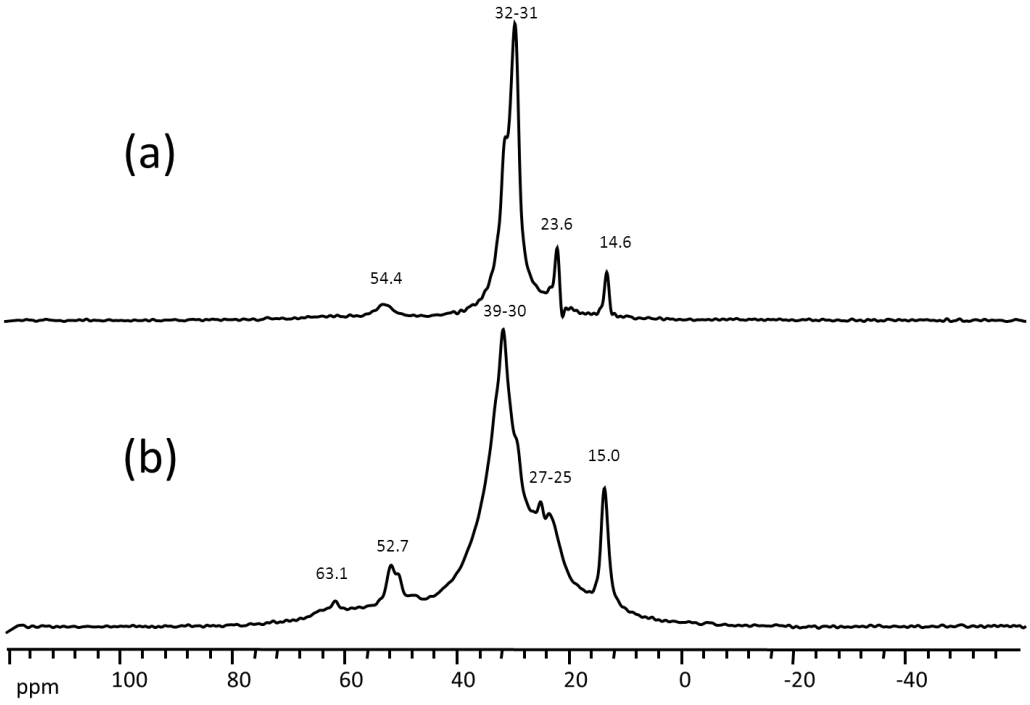

Figure A4.25. ^{13}C CPMAS NMR spectra of **(DODA)$_{19}$-1** (a) and **DODACl** (b).

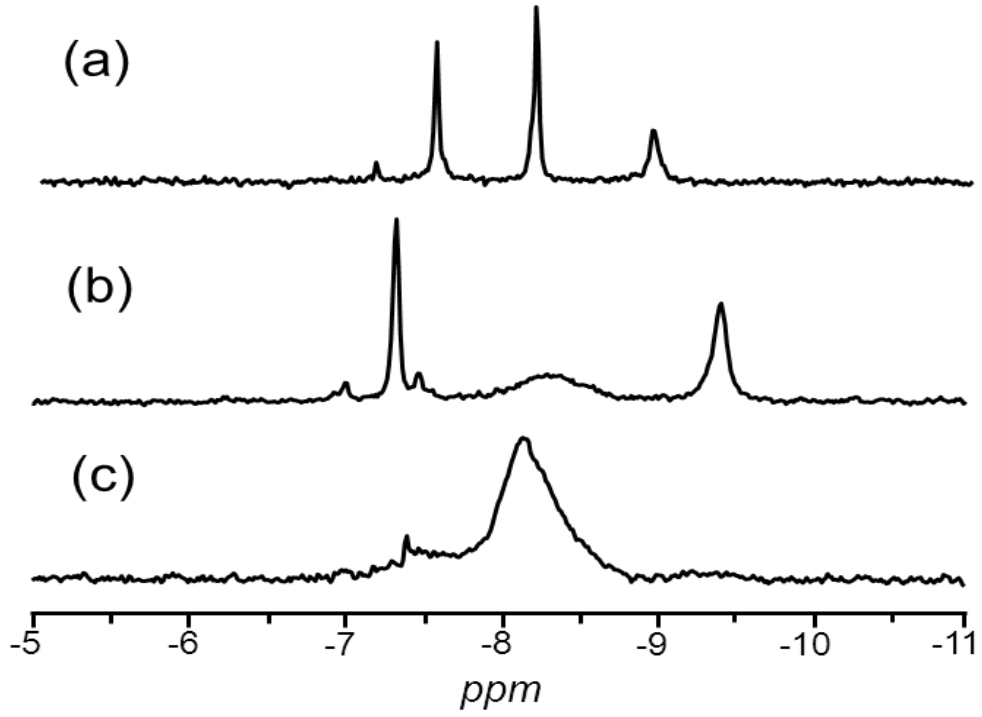

Figure A4.26. ^{31}P NMR spectrum of the precursor compound **1** in aqueous medium containing LiCl 1M as a function of the counter cations. (a) crystals of a potassium salt: the central peak corresponds to the trans isomer whereas the peripheral peaks refer to the *cis* isomer; (b) a mixed Na^+/K^+ salt: both isomers are also present with different chemical shifts and the signal of the *trans* isomer is broadened; (c) crystalline powder mainly containing Na^+ as counter ions which was employed as precursor in this study.

Table A4.1. Indexation at a Given Temperature for the Reflections Detected in the Liquid-Crystalline Phase by SA-XRD for **$DODA_{19}$-1**. Values are Given for the Second Heating and Cooling.

T /°C	$d_{hkl\ (mes)}$ /Å	*I* /a.u.	*00l*	$d_{hkl\ (calc)}$ /Å	
180°C	39.94	VS(Sh)	001	39.97	h = 39.97 Å
	20.00	S(Sh)	002	19.99	a_{Hex} = 33.83 Å
Cooling	-	-	003	-	
	13.5	W(Br)			
	11.4	W(Br)			
	-*	-			
160°C	39.76	VS(Sh)	001	39.89	h = 39.89 Å
	20.01	S(Sh)	002	19.95	a_{Hex} = 33.87 Å
Cooling	-	-	003	-	
	13.5	W(Br)			
	11.4	W(Br)			
	-*	-			
140°C	39.75	VS(Sh)	001	39.92	h = 39.92 Å
	20.04	S(Sh)	002	19.96	a_{Hex}= 33.86 Å
Cooling	-	-	003	-	
	13.5	W(Br)			
	11.4	W(Br)			
	-*	-			
120°C	40.25	VS(Sh)	001	40.33	h = 40.33 Å
	20.20	S(Sh)	002	20.16	a_{Hex}= 33.68 Å
Cooling	-	-	003	-	
	13.5	W(Br)			
	11.4	W(Br)			

	-*	-			
100°C	40.02	VS(Sh)	001	40.17	h = 40.17 Å
	20.16	S(Sh)	002	20.09	a_{Hex}= 33.75 Å
Cooling	-	-	003	-	
	13.5	W(Br)			
	11.4	W(Br)			
	-*	-			
80°C	40.19	VS(Sh)	001	40.30	h = 40.30 Å
	20.20	S(Sh)	002	20.15	a_{Hex}= 33.7 Å
Cooling	-	-	003	-	
	13.5	W(Br)			
	11.4	W(Br)			
	-*	-			
60°C	40.21	VS(Sh)	001	40.32	h = 40.32 Å
	20.21	S(Sh)	002	20.16	a_{Hex}= 33.69 Å
Cooling	-	-	003	-	
	13.5	W(Br)			
	11.4	W(Br)			
	-*	-			
40°C	40.17	VS(Sh)	001	40.29	h = 40.29 Å
	20.20	S(Sh)	002	20.14	a_{Hex}= 33.7Å
Cooling	-	-	003	-	
	13.5	W(Br)			
	11.4	W(Br)			
	-*	-			

60°C	40.26	VS(Sh)	001	40.34	h = 40.34 Å
	20.21	S(Sh)	002	20.17	a_{Hex}= 33.68 Å
Heating	-	-	003	-	
	13.5	W(Br)			
	11.4	W(Br)			
	-*	-			
80°C	40.41	VS(Sh)	001	40.48	h = 40.48 Å
	20.27	S(Sh)	002	20.24	a_{Hex} = 33.62Å
Heating	-	-	003	-	
	13.5	W(Br)			
	11.4	W(Br)			
	-*	-			
100°C	40.28	VS(Sh)	001	40.34	h = 40.34 Å
	20.20	S(Sh)	002	20.17	a_{Hex}= 33.68 Å
Heating	-	-	003	-	
	13.5	W(Br)			
	11.4	W(Br)			
	-*	-			
120°C	40.12	VS(Sh)	001	40.22	h = 40.22 Å
	20.16	S(Sh)	002	20.11	a_{Hex} = 33.73Å
Heating	-	-	003	-	
	13.5	W(Br)			
	11.4	W(Br)			
	-*	-			

140°C	39.94	VS(Sh)	001	40.01	h = 40.01 Å
	20.04	S(Sh)	002	20.01	a_{Hex}= 33.82 Å
Heating	-	-	003	-	
	13.5	W(Br)			
	11.4	W(Br)			
	-*	-			
160°C	39.74	VS(Sh)	001	39.78	h = 39.78 Å
	19.91	S(Sh)	002	19.89	a_{Hex}= 33.92 Å
Heating	-	-	003	-	
	13.5	W(Br)			
	11.4	W(Br)			
	-*	-			
180°C	39.30	VS(Sh)	001	39.53	h = 39.53 Å
	19.88	S(Sh)	002	19.77	a_{Hex} = 34.02 Å
Heating	-	-	003	-	
	13.5	W(Br)			
	11.4	W(Br)			
	-*	-			

$d_{hkl\ (mes)}$ and $d_{hkl\ (calc)}$ are the measured and calculated diffraction spacing ; h is the lattice parameter of the smectic phase ; I corresponds to the intensity of the reflections (VS : very strong. S : strong. W : weak ; br and sh stand for broad and sharp) ; h and $d_{hkl\ (calc\ )}$ are respectively calculated according the formula : $h = 1/3\ (d_{001(exp)} + 2d_{002\ (exp)} + 3d_{003\ (exp)})$ and $d_{hkl\ (calc)} = h/l$; a_{Hex} is the local hexagonal organization within the layers calculated with eq. 1 of the main text. * The reflection corresponding to the molten aliphatic chains (usually ~ 4.5 Å) is too broad to be measured.

Table A4.2. Indexation at a Given Temperature for the Reflections Detected in the Liquid-Crystalline Phase by SA-XRD for **$(mimC_{12})_{25}$-1**. Values are Given for the Second Cooling.

T /°C	$d_{hkl\,(mes)}$ /Å	*I* /a.u.	*00l*	$d_{hkl\,(calc)}$ /Å	
200°C	35.01	VS(Sh)	001	35.15	h = 35.15 Å
	22.15	W(Sh)			a_{Hex}=32.75 Å
Cooling	17.64	S(Sh)	002	17.57	h' = 22.15 Å
	13	W(Br)			
	11	W(Br)			
	-*	-			
180°C	35.46	VS(Sh)	001	35.55	h = 35.55 Å
	22.36	W(Sh)			a_{Hex}= 32.57 Å
Cooling	17.82	S(Sh)	002	17.78	h' = 22.36 Å
	13	W(Br)			
	11	W(Br)			
	-*	-			
160°C	35.52	VS(Sh)	001	35.59	h = 35.59 Å
	21.99	W(Sh)			a_{Hex} = 32.55 Å
Cooling	17.83	S(Sh)	002	17.80	h' = 21.99 Å
	13	W(Br)			
	11	W(Br)			
	-*	-			
140°C	35.47	VS(Sh)	001	35.63	h = 35.63 Å
	22.00	W(Sh)			a_{Hex} = 32.53 Å
Cooling	17.89	S(Sh)	002	17.81	h' = 22.00 Å
	13	W(Br)			

	11	W(Br)			
	-*	-			
120°C	35.58	VS(Sh)	001	35.69	h = 35.69 Å
	21.98	W(Sh)			a_{Hex} = 32.5 Å
Cooling	17.90	S(Sh)	002	17.85	h' = 21.98 Å
	13	W(Br)			
	11	W(Br)			
	-*	-*			
100°C	35.62	VS(Sh)	001	35.57	h = 35.57 Å
	21.82	W(Sh)			a_{Hex} = 32.56 Å
Cooling	17.76	S(Sh)	002	17.79	h' = 21.82 Å
	13	W(Br)			
	11	W(Br)			
	-*	-			
80°C	35.73	VS(Sh)	001	35.75	h = 35.75 Å
	22.01	W(Sh)			a_{Hex} = 32.47 Å
Cooling	17.88	S(Sh)	002	17.87	h' = 22.01 Å
	13	W(Br)			
	11	W(Br)			
	-*	-			
60°C	35.38	VS(Sh)	001	35.59	h = 35.59 Å
	22.62	W(Sh)			a_{Hex} = 32.55 Å
Cooling	17.90	S(Sh)	002	17.80	h' = 22.62 Å
	13	W(Br)			
	11	W(Br)			

	-*	-			
40°C	35.27	VS(Sh)	001	35.30	h = 35.30 Å
	21.98	W(Sh)			a_{Hex} = 32.68Å
Cooling	17.66	S(Sh)	002	17.65	h' = 21.98 Å
	13	W(Br)			
	11	W(Br)			
	-*	-			

$d_{hkl\ (mes)}$ and $d_{hkl\ (calc)}$ are the measured and calculated diffraction spacing ; h is the lattice parameter of the smectic phase ; I corresponds to the intensity of the reflections (VS : very strong. S : strong. W : weak. VW : very weak ; br and sh stand for broad and sharp) ; h and $d_{hkl\ (calc\ )}$ are respectively calculated according the formula : $h = 1/2\ (d_{001(exp)} + 2d_{002\ (exp)})$ and $d_{hkl\ (calc)} = h/l$; a_{Hex} is the local hexagonal organization within the layers calculated with eq. 1 of the main text. * The reflection corresponding to the molten aliphatic chains (usually ~ 4.5 Å) is too broad to be measured.

Table A4.3. Indexation at a Given Temperature for the Reflections Detected in the Liquid-Crystalline Phase by SA-XRD for **$(mimC_{14})_{26}$-1**. Values are Given for the Second Cooling.

T /°C	$d_{hkl\ (mes)}$ /Å	*I* /a.u.	*00l*	$d_{hkl\ (calc)}$ /Å	
200°C	38.39	VS(Sh)	001	38.44	h = 38.44 Å
	-	-			a_{Hex} = 32.10 Å
Cooling	19.24	S(Sh)	002	19.22	
	13	W(Br)			
	11	W(Br)			
180°C	38.25	VS(Sh)	001	38.28	h = 38.28 Å
	-	-			a_{Hex} =32.17 Å
Cooling	19.15	S(Sh)	002	19.14	
	13	W(Br)			
	11	W(Br)			
160°C	38.51	VS(Sh)	001	38.44	h = 38.44 Å
	-	-			a_{Hex} = 32.10 Å
Cooling	19.18	S(Sh)	002	19.22	
	13	W(Br)			
	11	W(Br)			
140°C	38.32	VS(Sh)	001	38.24	h = 38.24 Å
	-	-			a_{Hex} = 32.10 Å
Cooling	19.08	S(Sh)	002	19.12	
	13	W(Br)			
	11	W(Br)			
120°C	38.17	VS(Sh)	001	38.14	h = 38.14 Å
	-	-			a_{Hex} = 32.22 Å

Cooling	19.05	S(Sh)	002	19.07	
	13	W(Br)			
	11	W(Br)			
100°C	37.95	VS(Sh)	001	37.95	h = 37.95 Å
	-	-			a_{Hex} = 32.31 Å
Cooling	18.97	S(Sh)	002	18.97	
	13	W(Br)			
	11	W(Br)			
80°C	37.91	VS(Sh)	001	37.98	h = 37.98 Å
	-	-			a_{Hex} = 32.29 Å
Cooling	19.02	S(Sh)	002	18.99	
	13	W(Br)			
	11	W(Br)			
60°C	37.74	VS(Sh)	001	37.67	h = 37.67 Å
	-	-			a_{Hex} = 32.43 Å
Cooling	18.80	S(Sh)	002	18.84	
	13	W(Br)			
	11	W(Br)			
40°C	37.12	VS(Sh)	001	37.06	h = 37.06 Å
	-	-			a_{Hex} = 32.69 Å
Cooling	18.50	S(Sh)	002	18.53	
	13	W(Br)			
	11	W(Br)			

$d_{hkl\ (mes)}$ and $d_{hkl\ (calc)}$ are the measured and calculated diffraction spacing ; h is the lattice parameter of the smectic phase ; I corresponds to the intensity of the reflections (VS : very strong. S : strong. W : weak. VW : very weak ; br and sh stand for broad and sharp) ; h and $d_{hkl\ (calc\ )}$ are respectively calculated according the formula : $h = 1/2\ (d_{001(exp)} + 2d_{002\ (exp)})$ and $d_{hkl\ (calc)} = h/l$; a_{Hex} is the local hexagonal organization within the layers calculated with eq. 1 of the main text. * The reflection corresponding to the molten aliphatic chains (usually ~ 4.5 Å) is too broad to be measured.

Table A4.4. Indexation at a Given Temperature for the Reflections Detected in the Liquid-Crystalline Phase by SA-XRD for **$(mimC_{16})_{23}$-1**. Values are Given for the Second Cooling.

T /°C	$d_{hkl\ (mes)}$ /Å	*I* /a.u.	*00l*	$d_{hkl\ (calc)}$ /Å	
200°C	41.09	VS(Sh)	001	40.96	h = 40.96 Å
	-	-			a_{Hex} = 30.97 Å
Cooling	20.41	S(Sh)	002	20.48	
	12	W(Br)			
	-*	-			
180°C	40.09	VS(Sh)	001	40.46	h = 40.46 Å
	-	-			a_{Hex} = 31.16 Å
Cooling	20.41	S(Sh)	002	20.23	
	12	W(Br)			
	-*	-			
160°C	40.09	VS(Sh)	001	40.46	h = 40.46 Å
	-	-			a_{Hex} = 31.16 Å
Cooling	20.41	S(Sh)	002	20.23	
	12	W(Br)			
	-*	-			
140°C	40.09	VS(Sh)	001	40.41	h = 40.41 Å
	-	-			a_{Hex} = 31.18 Å
Cooling	20.36	S(Sh)	002	20.20	
	12	W(Br)			
	-*	-			
120°C	40.09	VS(Sh)	001	40.41	h = 40.41 Å
	-	-			a_{Hex} = 31.18 Å

Cooling	20.36	S(Sh)	002	20.20	
	12	W(Br)			
	-*	-			
100°C	40.71	VS(Sh)	001	40.67	h = 40.67 Å
	-	-			a_{Hex} = 31.08Å
Cooling	20.31	S(Sh)	002	20.33	
	12	W(Br)			
	-*	-			
80°C	40.52	VS(Sh)	001	40.48	h = 40.48 Å
	-	-			a_{Hex} = 31.15 Å
Cooling	20.22	S(Sh)	002	20.24	
	12	W(Br)			
	-*	-			
60°C	40.34	VS(Sh)	001	40.34	h = 40.34 Å
	-	-			a_{Hex} = 31.20 Å
Cooling	20.17	S(Sh)	002	20.17	
	12	W(Br)			
	-*	-			
40°C	40.16	VS(Sh)	001	40.16	h = 40.16 Å
	-	-			a_{Hex} = 31.28 Å
Cooling	20.08	S(Sh)	002	20.08	
	12	W(Br)			
	-*	-			
20°C	39.44	VS(Sh)	001	39.31	h = 39.31 Å

	-	-			a_{Hex} = 31.16 Å
Cooling	19.59	S(Sh)	002	19.66	
	12	W(Br)			
	-*	-			
10°C	38.92	VS(Sh)	001	38.54	*h* = 38.54 Å
	-	-			a_{Hex} = 31.93 Å
Cooling	19.08	S(Sh)	002	19.27	
	12	W(Br)			
	-*	-			
0°C	38.58	VS(Sh)	001	38.29	*h* = 38.29 Å
	-	-			a_{Hex} = 32.03 Å
Cooling	19.00	S(Sh)	002	19.15	
	12	W(Br)			
	-*	-			
-10°C	38.58	VS(Sh)	001	38.29	*h* = 38.29 Å
	-	-			a_{Hex} = 32.03 Å
Cooling	19.00	S(Sh)	002	19.15	
	12	W(Br)			
	-*	-			
-20°C	38.58	VS(Sh)	001	38.29	*h* = 38.29 Å
	-	-			a_{Hex} = 32.03 Å
Cooling	19.00	S(Sh)	002	19.15	
	12	W(Br)			
	-*	-			

-30°C	38.58	VS(Sh)	001	38.29	h = 38.29 Å
	-	-			a_{Hex} = 32.03 Å
Cooling	19.00	S(Sh)	002	19.15	
	12	W(Br)			
	-*	-			
-40°C	38.58	VS(Sh)	001	38.29	h = 38.29 Å
	-	-			a_{Hex} = 32.03 Å
Cooling	19.00	S(Sh)	002	19.15	
	12	W(Br)			
	-*	-			

$d_{hkl\ (mes)}$ and $d_{hkl\ (calc)}$ are the measured and calculated diffraction spacing ; h is the lattice parameter of the smectic phase ; I corresponds to the intensity of the reflections (VS : very strong. S : strong. W : weak. VW : very weak ; br and sh stand for broad and sharp) ; h and $d_{hkl\ (calc\ )}$ are respectively calculated according the formula : $h = 1/2\ (d_{001(exp)} + 2d_{002\ (exp)})$ and $d_{hkl\ (calc)} = h/l$; a_{Hex} is the local hexagonal organization within the layers calculated with eq. 1 of the main text. * The reflection corresponding to the molten aliphatic chains (usually ~ 4.5 Å) is too broad to be measured.

Table A4.5. Indexation at a Given Temperature for the Reflections Detected in the Liquid-Crystalline Phase by SA-XRD for **$(mimC_{18})_{24}$-1**. Values are Given for the Second Cooling.

T /°C	$d_{hkl\ (mes)}$ /Å	*I* /a.u.	*00l*	$d_{hkl\ (calc)}$ /Å	
200°C	43.30	VS(Sh)	001	43.28	*h* = 43.28 Å
	-	-			a_{Hex} = 30.81 Å
Cooling	21.63	S(Sh)	002	21.64	
	12	W(Br)			
	-*	-			
180°C	43.21	VS(Sh)	001	43.25	*h* = 43.25 Å
	-	-			a_{Hex}= 32.82 Å
Cooling	21.64	S(Sh)	002	21.62	
	12	W(Br)			
	-*	-			
160°C	43.25	VS(Sh)	001	43.23	*h* = 43.23 Å
	-	-			a_{Hex}= 30.83 Å
Cooling	21.60	S(Sh)	002	21.61	
	12	W(Br)			
	-*	-			
140°C	43.72	VS(Sh)	001	43.76	*h* = 43.76 Å
	-	-			a_{Hex} = 30.64 Å
Cooling	21.90	S(Sh)	002	21.88	
	12	W(Br)			
	-*	-			
120°C	43.73	VS(Sh)	001	43.70	*h* = 43.70 Å
	-	-			a_{Hex} = 30.66 Å

Cooling	21.83	S(Sh)	002	21.85	
	12	W(Br)			
100°C	43.55	VS(Sh)	001	43.58	h = 43.58 Å
	-	-			a_{Hex}= 30.7 Å
Cooling	21.80	S(Sh)	002	21.79	
	12	W(Br)			
80°C	43.62	VS(Sh)	001	43.59	h = 43.59 Å
	-	-			a_{Hex}= 30.7Å
Cooling	21.78	S(Sh)	002	21.80	
	12	W(Br)			
60°C	43.60	VS(Sh)	001	43.52	h = 43.52 Å
	-	-			a_{He} = 30.72 Å
Cooling	21.72	S(Sh)	002	21.76	
	12	W(Br)			
40°C	43.57	VS(Sh)	001	43.63	h = 43.63 Å
	-	-			a_{Hex} = 30.69 Å
Cooling	21.84	S(Sh)	002	21.84	
	12	W(Br)			

$d_{hkl\ (mes)}$ and $d_{hkl\ (calc)}$ are the measured and calculated diffraction spacing ; h is the lattice parameter of the smectic phase ; I corresponds to the intensity of the reflections (VS : very strong. S : strong. W : weak. VW : very weak ; br and sh stand for broad and sharp) ; h and $d_{hkl\ (calc\ )}$ are respectively calculated according the formula : $h = 1/2\ (d_{001(exp)} + 2d_{002\ (exp)})$ and $d_{hkl\ (calc)} = h/l$; a_{Hex} is the local hexagonal organization within the layers calculated with eq. 1 of the main text. * The reflection corresponding to the molten aliphatic chains (usually ~ 4.5 Å) is too broad to be measured.

Table A4.6. Indexation at a Given Temperature for the Reflections Detected in the Liquid-Crystalline Phase by SA-XRD for **$(mimC_{20})_{24}$-1**. Values are Given for the Second Cooling.

T /°C	$d_{hkl\ (mes)}$ /Å	*I* /a.u.	*00l*	$d_{hkl\ (calc)}$ /Å	
200°C	45.10	S(Sh)	001	45.03	*h* = 45.03 Å
	-	-			a_{Hex}= 30.68 Å
Cooling	22.48	S(Sh)	002	22.52	
	12	W(Br)			
	-*	-			
180°C	45.67	S(Sh)	001	45.64	*h* = 45.64 Å
	-	-			a_{Hex}= 30.47 Å
Cooling	22.80	S(Sh)	002	22.82	
	12	W(Br)			
	-*	-			
160°C	45.78	S(Sh)	001	45.81	*h* = 45.81 Å
	-	-			a_{Hex}= 30.41 Å
Cooling	22.92	S(Sh)	002	22.91	
	12	W(Br)			
	-*	-			
140°C	46.28	S(Sh)	001	46.30	*h* = 46.30 Å
	-	-			a_{Hex} = 30.25 Å
Cooling	23.16	S(Sh)	002	23.15	
	12	W(Br)			
	-*	-			
120°C	46.32	S(Sh)	001	46.34	*h* = 46.34 Å
	-	-			a_{Hex} = 30.24 Å

Cooling	23.18	S(Sh)	002	23.17	
	12	W(Br)			
100°C	46.10	S(Sh)	001	46.07	h = 46.07 Å
	-	-			a_{Hex} =30.33 Å
Cooling	23.02	S(Sh)	002	23.02	
	12	W(Br)			
80°C	46.85	S(Sh)	001	46.42	h = 46.42 Å
	-	-			a_{Hex} = 30.21 Å
Cooling	22.99	S(Sh)	002	23.21	
	12	W(Br)			
60°C	46.21	S(Sh)	001	46.12	h = 46.12 Å
	-	-			a_{Hex} = 30.31 Å
Cooling	23.01	S(Sh)	002	23.06	
	12	W(Br)			
40°C	43.72	VS(Sh)	001	43.70	h = 43.70 Å
	-	-		21.85	a_{Hex} =31.14 Å
Cooling	21.84	S(Sh)	002		
	12	W(Br)			

$d_{hkl\ (mes)}$ and $d_{hkl\ (calc)}$ are the measured and calculated diffraction spacing ; h is the lattice parameter of the smectic phase ; I corresponds to the intensity of the reflections (VS : very strong. S : strong. W : weak. VW : very weak ; br and sh stand for broad and sharp) ; h and $d_{hkl\ (calc\ )}$ are respectively calculated according the formula : $h = 1/2\ (d_{001(exp)} + 2d_{002\ (exp)})$ and $d_{hkl\ (calc)} = h/l$; a_{Hex} is the local hexagonal organization within the layers calculated with eq. 1 of the main text. * The reflection corresponding to the molten aliphatic chains (usually ~ 4.5 Å) is too broad to be measured.